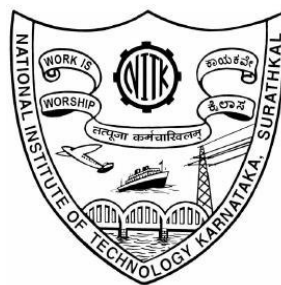


**CERIA-MANGANESE MIXED OXIDES
AS CATALYST FOR SOOT AND CO
OXIDATION ACTIVITY**

Thesis
Submitted in fulfillment of the requirements for the degree
of
DOCTOR OF PHILOSOPHY

by

ATMURI SHOURYA

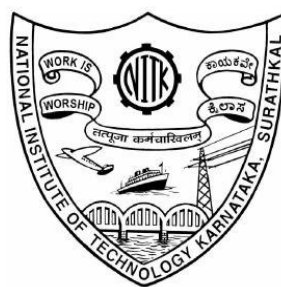


DEPARTMENT OF CHEMICAL ENGINEERING
NATIONAL INSTITUTE OF TECHNOLOGY KARNATAKA,
SURATHKAL, MANGALURU-575025
OCTOBER – 2024

CERIA-MANGANESE MIXED OXIDES AS CATALYST FOR SOOT AND CO OXIDATION ACTIVITY

Thesis
Submitted in fulfillment of the requirements for the degree
of
DOCTOR OF PHILOSOPHY
by
ATMURI SHOURYA

Under the guidance of
Prof. HARI PRASAD DASARI
Department
of
Chemical Engineering
NITK, Surathkal



DEPARTMENT OF CHEMICAL ENGINEERING
NATIONAL INSTITUTE OF TECHNOLOGY KARNATAKA,
SURATHKAL, MANGALURU-575025
OCTOBER – 2024

DECLARATION
By the Ph.D. Research Scholar

I hereby *declare* that the Research Thesis entitled **Ceria-Manganese Mixed Oxides as Catalyst for Soot and CO Oxidation Activity**, which is being submitted to the **National Institute of Technology Karnataka, Surathkal**, in fulfillment of the requirements for the award of the Degree of **Doctor of Philosophy** by **Department of Chemical Engineering** is a *bonafide report of the research work* carried out by me. The material contained in this Research Thesis has not been submitted to any University or Institution for the award of any degree.

Atmuri Shourya

187071 187CH001, ATMURI SHOURYA

Department of Chemical Engineering,

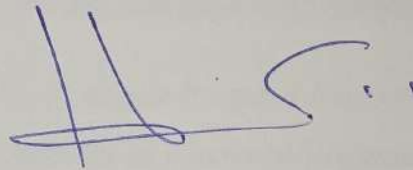
National Institute of Technology Karnataka, Surathkal, India

Place: NITK Surathkal

Date: 09/10/2024

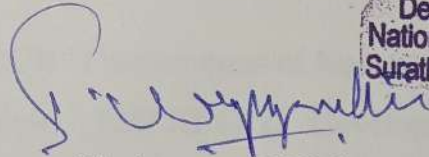
CERTIFICATE

This is to *certify* that the Research Thesis entitled **Ceria-Manganese Mixed Oxides as Catalyst for Soot and CO Oxidation Activity**, submitted by **ATMURI SHOURYA** (Register Number: 187071 187CH001) as the record of the research work carried out by him, is *accepted as the Research Thesis submission* in fulfillment of the requirements for the award of the degree of **Doctor of Philosophy**.



Prof. Hari Prasad Dasari

Research Guide



Chairman - DRPC
Head of the Department
विभागाध्यक्ष

Department of Chemical Engineering
रासायनिक अभियांत्रिकी विभाग

National Institute of Technology Karnataka - Surathkal
राष्ट्रीय प्रौद्योगिकी संस्थान कर्नाटक, सुरात्कल

PO Srinivasnagar, Mangalore - 575025 Karnataka
पी.ओ. श्रीनिवासनगर, मंगलौर - ५७५०२५ कर्नाटक

Department of Chemical Engineering

National Institute of Technology Karnataka, Surathkal, India

Dr. Hari Prasad Dasari
Professor
Department of Chemical Engineering
National Institute of Technology Karnataka
Surathkal, Mangalore -575 025, D.K. India

ACKNOWLEDGEMENTS

First and foremost, I thank Almighty for all the blessings in my life. I thank wholeheartedly my supervisor, **Prof. Hari Prasad Dasari**. My PhD has been a great learning experience because of his support, patience, and encouragement from the very beginning of my research work.

I thank the past Director of the NITK, **Prof. Karanam Umamaheshwar Rao**, and the present director, **Prof. B. Ravi**, for permitting me to use the institutional infrastructure. I thank **Prof. Hari Mahalingam**, **Prof. Prasanna B.D.**, **Prof. P.E. Jagadeeshbabu** the former Heads of the Department and the present Head of the Department, **Prof. I. Regupathi**, Department of Chemical Engineering, NITK, for permitting me to use the departmental facilities throughout my research work.

I am grateful to my Research Progress Assessment Committee members, **Prof. Keyur Raval**, Department of Chemical Engineering, NITK and **Prof. Anish S**, Department of Mechanical Engineering, NITK, for their critical evaluation and valuable suggestions during the progress of the work.

I thank **DST SERB ECR** “Development of Novel SOFC Electrolyte Materials with enhanced Ionic Conductivity”, **IMPRINT II** “Development and demonstration of solid oxide electrolysis cell technology for co-electrolysis of CO₂ and H₂O for the production of syngas”, and **SERB CRG** “Development of electrospun Ceria-based nanofibers for Diesel soot oxidation activity” for the funding. Without the support from the funding agency and my supervisor, it would be impossible for me to do my research.

My sincere thanks to **Dr. Mohammad Rizwanur Rahman** for the XRD data. Also, I acknowledge **Central Research Facility (CRF) NITK Surathkal** for Raman spectroscopy, SEM-EDS, XRD, BET, and BJH analysis conducted in their facilitation center and for the data provided. **SAIF, STIC Kochi** had provided me with the data related to TEM analysis, I thank them for their cooperation on time.

Without good peer group support, my journey would have never been this easy. I sincerely express my thanks for the timely help and support rendered by **Dr. Irfana Shahjahan, Mr. Lakhanlal, Mr. Rahulkumar Shirasangi, Dr. Sunaina Patil, Mrs. Gouri Pattanashetti, Mr. Aasif Ahmed Wagay, Ms. Madhura D.R., Mrs. Chaitra Shenoy, Mr. Govardhan P, Mr. Kunal Gajbhiye Ravindra, Ms. Pranathi Samineni, Mr. Avinash Suresh Nayak,** and other M.Tech students who were part of the research group.

I wholeheartedly thank my friends **Dr. Sanjith S. Anchan, Dr. Pragadeesh K.S., Mr. Sai Teja M.V., Mrs. Sahana Vijay Kumar, and Ms. Sedevino Sophia** for the support and comradeship throughout the doctoral journey. I sincerely acknowledge all the teaching staff and non-teaching staff, including **Mr. Sadashiva, Mrs. Thrithila Shetty, Mr. Janeshwar G.K., Ms. Vijyetha, Mrs. Bhavyashree, Mr. Suresh Shettigar, Mr. Hareesha Shetty, Mr. L Mahadeva, and Mrs. Sandhya** of the department for their support through my research. Also, I thank all other faculties, staff, and research scholars of the Department of Chemical Engineering and other departments of NITK Surathkal.

I thank the authors of all those research publications which have been referred in preparing this thesis. I also express my gratitude to the reviewers of the journals for their excellent input.

I thank all my dear friends who were there to support me and help me whenever needed. I extend my deepest and unconditional thanks to my mother, **A. Indira Devi,** my father, **A. Madhusudana Rao,** my sister, **A. Samatha,** my grandmother **A. Kusuma Kumari,** my wife **A. Snehal** and her family members.

Atmuri Shourya

Dedication

*To H.H. Shree Mataji Nirmala Devi and my family for all the support,
encouragement, and inspiration.*

ABSTRACT

Automobile exhaust catalysts, like three-way catalytic converters are known to use Ceria coating for the fine dispersion of Platinum Group Metals (PGM). The Ceria coating acts as an active support. PGMs have certain shortcomings, such as, high prices, sintering at relatively low temperatures, and fouling due to SO₂. Doping Ceria with other metals, like in the present work Manganese, boosts its catalytic properties while lessening or negating any determinantal effects. Manganese-doped Ceria catalysts have been widely studied as a catalyst for a variety of applications due to their attractive properties attained due to synergy achieved by favorable defects, physicochemical, and morphological features aiding in the oxidation processes. A systematic study has been carried out in the present work to study the effect of Manganese doping in Ceria and its soot oxidation activity from nanostructured powder to CO oxidation activity on structured catalysts, i.e., catalyst coated on to an Alumina wash-coated Cordierite honeycomb substrate. The EDTA-Citrate method was the choice of synthesis method for the powder catalyst. Since the variation in the atomic radius of both cations (Ce and Mn) is very large, phase difference and the existence of multiple oxidation states in Manganese, a complete solid solution is not feasible over the entire range of Manganese doping into the Ceria lattice. Consequently, two series of nanostructured powder catalysts were obtained, namely, Ceria-rich Ceria-Manganese and Manganese-rich Ceria-Manganese mixed oxides, with interesting morphological features attained due to the solubility limits. Ceria-Manganese mixed oxides (nanostructured powder catalysts) were examined by XRD, Raman spectroscopy, BET and BJH, FESEM, and TEM characterization techniques. A dip-coating technique was employed for coating of the Cordierite honeycomb substrate. The structured catalysts were utilized for CO oxidation. The adherence of the coating was tested by ultrasonication. XRD, Raman spectroscopy, and BET analysis probed the physicochemical parameters. Digital optical microscopy, and FESEM analysis analyzed the morphological features. Overall, the thesis concentrates on developing compositions of Ceria-Manganese oxides for soot and CO oxidation activity for a Catalyzed Diesel Particulate Filter (CDPF).

Keywords: Ceria-Manganese mixed oxides, Cordierite honeycomb substrate, Soot and CO oxidation, EDTA-Citrate, Dip-coating.

TABLE OF CONTENTS

DESCRIPTION	Page no.
LIST OF FIGURES	v
LIST OF TABLES	ix
ABBREVIATIONS	xi
UNITS AND NOTATIONS	xiii
1 INTRODUCTION	1
1.1 Background	1
1.2 Soot	3
1.3 Carbon Monoxide	5
1.4 Diesel Particulate Filter (DPF) and Diesel Oxidation catalyst (DOC)	7
1.5 Ceria	8
1.6 Manganese oxide	10
1.7 Coating Techniques for monolithic or structured catalysts	10
1.8 Scope and Objectives	11
1.8.1 Scope	11
1.8.2 Objectives	12
1.9 Organization of the Thesis	13
2 LITERATURE REVIEW	15
2.1 Ceria	15
2.2 Doped Ceria	23
2.3 Manganese doped Ceria and Manganese oxide	38
2.4 Soot oxidation by structured catalysts	51
2.5 Soot oxidation mechanism	63
2.6 CO oxidation	64
2.7 CO oxidation on structured catalysts	74
2.8 CO oxidation mechanism	75
2.9 Literature review conclusions	76

3	MATERIALS AND METHODOLOGY	79
3.1	Synthesis of nano-structured Ceria-Manganese mixed oxide powders	79
3.2	Synthesis of structured Ceria-Manganese mixed oxides	80
3.3	Characterization techniques	83
3.4	Soot oxidation activity	84
3.5	CO oxidation activity	85
4	STUDY ON NANOSTRUCTURED CERIA RICH CMX (X = 0 to 30) POWDER CATALYSTS FOR SOOT OXIDATION	89
4.1	XRD and BET surface area analysis	89
4.2	Raman spectra analysis	93
4.3	FESEM analysis	94
4.4	TEM analysis	96
4.5	Soot oxidation	100
4.6	Conclusions	106
5	STUDY ON NANOSTRUCTURED MANGANESE RICH CMX (X = 40 to 100) POWDER CATALYSTS FOR SOOT OXIDATION	109
5.1	XRD and BET surface area analysis	110
5.2	Raman spectra analysis	113
5.3	FESEM analysis	114
5.4	TEM analysis	117
5.5	Soot oxidation activity	121
5.6	Conclusions	131
6	CO OXIDATION OVER STRUCTURED CATALYSTS	133
6.1	XRD, BET, and BJH analysis	133
6.2	Raman Spectroscopy analysis	136
6.3	Adherence test and optical imaging analysis	138
6.4	FESEM analysis	140
6.5	CO oxidation activity	147

6.6	Conclusions	154
7	SUMMARY AND CONCLUSIONS	157
7.1	Summary	157
7.2	Conclusions	158
7.3	Future scope of work	159
	APPENDIX-I	161
	APPENDIX-II	165
	REFERENCES	169
	PUBLICATIONS	195
	BIODATA	197

LIST OF FIGURES

Figure no.	Caption	Page no.
1.1	Comparison between Bharath Stage IV and VI norms for diesel engines (PM).	3
1.2	Scale of soot particles.	4
1.3	Formation of soot schematic.	5
1.4	Mechanism and effects of CO on the tissue.	6
1.5	Schematic of a DPF.	7
1.6	Cubic fluorite structure of CeO ₂ .	9
3.1	Schematic of EDTA-Citrate synthesis method.	79
3.2	Schematic for pretreatment of cordierite.	81
3.3	Schematic of EDTA-Citrate sol-gel dip coating method.	82
3.4	Catalyst-coated cordierite samples calcined at 700 °C/2 h.	82
3.5	Schematic of the CO oxidation setup.	86
4.1	XRD pattern of CMX (X = 0, 5, 10, 20, 30) catalysts calcined at 600 °C/5 h.	90
4.2	Raman spectra of CMX (X = 0, 5, 10, 20, 30) catalysts calcined at 600 °C/5 h.	93
4.3	FESEM images of (a) CM0, (b) CM5, (c) CM10, (d) CM20, (e) CM30. Calcined at 600 °C/5 h.	95
4.4	TEM images (a to d) and (e) SAED pattern of CM0 catalyst calcined at 600 °C/5 h.	97
4.5	TEM images (a to d) and (e) SAED pattern of CM5 catalyst calcined at 600 °C/5 h.	98
4.6	TEM images (a to d) and (e) SAED pattern of CM30 catalyst calcined at 600 °C/5 h.	99
4.7	(a) Soot conversion (%) of CMX (X = 0 to 30) catalysts. (b) T ₅₀ (°C) triplicates error bar graph for CMX catalysts calcined at 600 °C/5 h.	101

4.8	Soot conversion (%) at ramp up rates of 5, 10, 15, and 20 °C/min over (a) CM0, (b) CM5, and (c) CM30, calcined at 600 °C/5 h.	103
4.9	Ozawa plots of (a) CM0, (b) CM5, and (c) CM30 catalysts calcined at 600 °C/5 h.	104
4.10	KAS plots of (a) CM0, (b) CM5, and (c) CM30 samples calcined at 600 °C/5 h.	105
5.1	XRD pattern of CMX (X = 40 to 100) catalysts calcined at 600 °C/5 h.	111
5.2	Raman spectra of CMX (X = 40 to 100) catalysts calcined at 600 °C/5 h.	113
5.3	FESEM images of (a) CM100, (b) CM90, (c) CM80, (d) CM70, (e) CM60, (f) CM50, and (g) CM40 calcined at 600 °C/5 h.	115
5.4	TEM images (a to d) and (e) SAED pattern of CM50 catalyst calcined at 600 °C/5 h.	118
5.5	TEM images (a to d) and (e) SAED pattern of CM70 catalyst calcined at 600 °C/5 h.	119
5.6	TEM images (a to d) and (e) SAED pattern of CM100 catalyst calcined at 600 °C/5 h.	120
5.7	(a) Soot conversion (%) of CMX (X = 40 to 100) catalysts. (b) T ₅₀ (°C) triplicates error bar graph for CMX catalysts calcined at 600 °C/5 h.	122
5.8	Soot conversion (%) at ramp-up rates of 5, 10, 15, and 20 °C/min over (a) CM50, (b) CM80, and (c) CM100 catalysts calcined at 600 °C/5 h.	126
5.9	Ozawa plots of (a) CM50, (b) CM80, and (c) CM100 catalysts calcined at 600 °C/5 h.	127
5.10	KAS plots of (a) CM50, (b) CM80, and (c) CM100 samples calcined at 600 °C/5 h.	128

6.1	XRD pattern of samples Cord to CM100/Al ₂ O ₃ /Cord calcined at 700 °C/2 h.	134
6.2	Raman spectra of Cord to CM100/Al ₂ O ₃ /Cord calcined at 700 °C/2 h.	137
6.3	Optical images of samples Cord to CM100/Al ₂ O ₃ /Cord calcined at 700 °C/2 h.	139
6.4	FESEM images of sample Cord calcined at 700 °C/2 h.	141
6.5	FESEM images of sample Al ₂ O ₃ /Cord calcined at 700 °C/2 h.	142
6.6	FESEM images of sample CM0/Al ₂ O ₃ /Cord calcined at 700 °C/2 h.	143
6.7	FESEM images of sample CM5/Al ₂ O ₃ /Cord calcined at 700 °C/2 h.	144
6.8	FESEM images of sample CM70/Al ₂ O ₃ /Cord calcined at 700 °C/2 h.	145
6.9	FESEM images of sample CM100/Al ₂ O ₃ /Cord calcined at 700 °C/2 h.	146
6.10	(a) CO oxidation over samples Cord to CM100/Al ₂ O ₃ /Cord; (b) T ₅₀ temperature triplicates of samples Cord to CM100/Al ₂ O ₃ /Cord.	148
6.11	Effect of heating rate on CO conversion (a) CM0/Al ₂ O ₃ /Cord; (b) CM5/Al ₂ O ₃ /Cord; (c) CM70/Al ₂ O ₃ /Cord; (d) CM100/Al ₂ O ₃ /Cord.	151
6.12	Ozawa plots of (a) CM0/Al ₂ O ₃ /Cord; (b) CM5/Al ₂ O ₃ /Cord; (c) CM70/Al ₂ O ₃ /Cord; (d) CM100/Al ₂ O ₃ /Cord.	152
6.13	Long-term CO oxidation stability studies (a) CM0/Al ₂ O ₃ /Cord; (b) CM5/Al ₂ O ₃ /Cord; (c) CM70/Al ₂ O ₃ /Cord; (d) CM100/Al ₂ O ₃ /Cord.	153

LIST OF TABLES

Table no.	Caption	Page no.
1.1	Composition of Model soot.	4
2.1	Soot oxidation by Ceria.	17
2.2	Soot oxidation by doped Ceria.	25
2.3	Soot oxidation activity by Manganese doped ceria and Manganese oxide.	40
2.4	Soot oxidation by using structured catalysts.	52
2.5	CO Oxidation activity by Ceria based materials.	66
4.1	Lattice parameter (a), Crystallite size (D), Lattice strain, Surface area, pore volume, and diameter average T_{50} of samples, Reactive planes, and Degree of agglomeration (ϕ) of CMX (X = 0 to 30) catalysts calcined at 600 °C/5 h.	92
4.2	EDS analysis of CMX (X = 5 to 30) catalysts calcined at 600 °C/5 h.	94
5.1	Lattice parameter (a), Crystallite size (D), Lattice strain, Surface area, pore volume and diameter, average T_{50} of samples, and Reactive planes of CMX (X = 40 to 100) catalysts calcined at 600 °C/5 h.	112
5.2	EDS analysis of CMX (X = 40 to 90) catalysts calcined at 600 °C/5 h.	116
6.1	CO oxidation, BET, and BJH results of samples Cord to CM100/Al ₂ O ₃ /Cord.	135
6.2	Adherence test of samples Al ₂ O ₃ /Cord to CM100/Al ₂ O ₃ /Cord.	138

ABBREVIATIONS

Abbreviation	Description
<i>a</i>	Lattice constant
BET	Brunauer–Emmett–Teller
BS	Bharath Stage
CI	Compression Ignition
CRDI	Common Rail Direct Injection
DOC	Diesel Oxidation Catalyst
DPF	Diesel Particulate Filter
CDPF	Catalyzed Diesel Particulate Filter
CMX	Ceria-Manganese Binary metal oxides (CMX (X = 0, 5, 10, 20, 30, 40, 50, 60, 70, 80, 90, and 100 corresponding to $\text{Ce}_{1-x}\text{Mn}_x\text{O}_{2-\delta}$ where, $x = 0, 0.05, 0.1, 0.2, 0.3, 0.4, 0.5, 0.6, 0.7, 0.8, 0.9,$ and 1 mol %)
CORD	Cordierite ($2\text{MgO} \cdot 2\text{Al}_2\text{O}_3 \cdot 5\text{SiO}_2$)
CRT	Continuously Regeneration Technique
<i>d</i>	Interplanar distance
D	Crystallite size
EDTA	Ethylene Diamine Tetra Acetic acid
EGR	Engine Gas Recirculation
FCC	Face Centered Cubic
IC	Internal Combustion
MvK	Mars and Van Krevelen mechanism
NO _x	Nitrous Oxides
O _{ads}	Surface adsorbed oxygen vacancy
OSC	Oxygen Storage Capacity
PAH	Poly Aromatic Hydrocarbons
PGM	Platinum Group Metal
PM	Particulate Matter
SI	Spark Ignition
SEM-EDS	Scanning Electron Microscopy-Energy Dispersive x-ray Spectroscopy

SCS	Solution Combustion Synthesis
SCR	Selective Catalytic Reduction
SOF	Soluble Organic Fraction
SOFC	Solid Oxide Fuel Cell
SO _x	Sulfur Oxides
T ₅₀	Temperature at 50% conversion
TEM	Transmission Electron Microscopy
TGA	Thermogravimetric analysis
TPR	Temperature Programmed Reduction
TWC	Three Way Catalytic convertors
V _o	Oxygen vacancy
VOC	Volatile Organic Compounds
XRD	X-ray Diffraction
ε	Lattice strain
φ	Degree of agglomeration

UNITS AND NOTATIONS

Symbol	Description
%	Percentage
°C	Degree Celsius
Å	Armstrong
a.u.	Arbitrary unit
Ce-NC	Ceria Nano Cubes
Ce-NR	Ceria Nano Rods
cps	Counts per second
cpsi	Cells per square inch
g	gram
h	Hour
K	Kelvin
kg	kilogram
kJ	kilo Joule
LC	Loose Contact (soot mixing)
m	Meter
mm	Millimeters
ml	Milliliter
m ² /g	Meter square per gram
min	Minutes
nm	Nanometer
PEG	Poly Ethylene Glycol
ppm	Parts per million
S/C	Soot to Catalyst ratio
T	Temperature (°C or K)
TC	Tight Contact (soot mixing)
W	Watt
W/m ²	Watt per Meter square
θ	degree
λ	Wavelength

CHAPTER 1

INTRODUCTION

1.1 Background

The modern world that we see around us is the manifestation of man's endeavor to fulfill the basic needs and his comforts. Thanks to the rapid industrialization, exploration, and advancements in the fields of science, engineering, and medicine, this endeavor of man seems to be attained. The consequences led to improving disparately socio-economic, financial, and technological wellness of people across the globe. This apparent disparity resulted in nations being categorized as developed, developing, and under-developed nations. Among many aspects of development, the transportation sector and its allied infrastructure play a crucial role directly or indirectly in improving the quality of life.

Transportation is the life blood of an economy; it has a direct and strong impact on the availability and pricing of goods and services in any given geographical location of a country. Transportation can be broadly classified into commercial and private; further commercial can be subdivided into Freight, people, and livestock transport. Freight consists of the movement of goods and commodities (inter and intra-nation) in bulk via air, water, and terrestrial/land modes of transportation. A cheaper and more efficient means of transport will result in reduced cost of goods and services, benefiting the consumer. In this regard, many solutions, such as efficient design and control of prime-movers, better pavements and transportation infrastructure planning, bulk transport by constructing larger vessels with better fuel economy, etc., were implemented. Inland transport is predominantly by road and railways, although waterways can also be considered if a region has natural or man-made motorable waterways to transport freight. In the context of India, the majority of the in-land transport is done via road ways and railways.

The transport of freight via roadways is done by heavy trucks, Light Motor Vehicles, and three-wheelers. Diesel engines are the prime movers of vehicles used for commercial transport for both freight and people; this is so because diesel/Compression Ignition (CI) engines have a higher power-to-volume ratio than their Spark Ignition (SI)/gasoline engines due to (1) higher compression ratio, (2) Lean and variable fuel mixture achievable by the CI engine for a given volume (Neeft et al. 1996b). Many advancements in CI technology, such as Common Rail Direct Injection (CRDI), turbocharging, etc., have helped improve its performance. The relatively lesser cost of diesel over petrol/gasoline, coupled with the better performance of CI over SI engines, has led to the proliferation of CI engines in the passenger segment. Diesel engines have certain undesirable aspects such as higher NO_x, particulate matter emissions, greenhouse gas emissions, SO_x, and Poly Aromatic Hydrocarbons (PAHs) (Zhang et al. 2010). NO_x, apart from forming photochemical smog, ground-level ozone formation, is a major culprit for acid rain; particulate matter, on the other hand, is an aerosol that has adverse health and environmental effects. Greenhouse gas emissions such as CO₂ and CO increase global warming by trapping heat; CO is more lethal to living things breathing oxygen as it binds to hemoglobin to form carboxyhemoglobin, reducing the ability of blood to bind with oxygen and may be fatal at higher concentrations of CO exposure (Raub et al. 2000). PAHs are known to be carcinogenic and also involve in secondary reactions with aerosols in the atmosphere tending to release active oxygen species which are potentially dangerous if inhaled (D'Anna 2009).

The introduction of stricter emission norms to curb the ill effects of the pollutants necessitated the development of NO_x, CO, and particulate matter abatement technologies. These emissions have been controlled by using better engine designs, like high-pressure fuel injection and swirl ratio. Small nozzle hole area, improvements in the combustion chamber shape, high response turbocharger, etc. (Fino 2007). Technologies like Diesel Particulate Filter (DPF), Selective Catalytic Reduction (SCR), Engine Gas Recirculation (EGR), Three Way Catalytic (TWC) convertors, fuel additives, etc., are also utilized for reducing diesel emissions. Although no one strategy

mentioned could possibly reduce the pollutant concentration to zero or to acceptable limits, in tandem, it is possible to achieve the emissions standards set to date (Bharath stage IV). A comparative figure of Bharath stage IV and VI norms (to be implemented) for diesel engines is shown in **Figure 1.1**. The reduction in PM will require better-tuned diesel engines in combination with other technologies and devices like EGR, SCR, DPF, etc.



Figure 1.1: Comparison between Bharath Stage IV and VI norms for diesel engines (PM) (IICT 2016).

1.2 Soot

Soot is formed due to incomplete combustion and pyrolysis (at high temperatures) of Hydrocarbons and fossil fuels (Stanmore et al. 2001)(Neeft et al. 1996b). It is an undesirable by-product of combustion that is a major health hazard to all living beings. Soot can travel great distances given suitable meteorological conditions. Soot also affects the climate of a region by altering the intensity of sunlight reaching the ground when suspended in the upper/lower atmosphere. When the sunlight is obstructed to reach the ground, it may cause temporary cooling. When the soot settles on ice and snow, it increases the rate of melting as soot is known to be very good at

absorbing the incoming radiation and causing quicker warming of the ice, thereby increasing the rate of melting of glaciers and polar ice caps (Sato et al. 2003)(Jacobson 2004)(Reddy and Boucher 2007)(Raj et al. 2013). Soot is an active component propelling climate change, as NASA had reported from their experiments and simulations. Soot may form due to natural phenomena like forest fires or anthropogenic means in the form of open burning, combustion of fossil fuels, burning of crop stubbles and biofuels, furnaces (non-electrical), boilers furnaces (non-electrical), internal combustion engines (Glaser et al. 2005). The finer the soot particles, the greater is the risk. Soot is linked directly or indirectly to cardiovascular and pulmonary diseases and deaths worldwide (Pope et al. 2004)(Lei et al. 2005). **Figure 1.2** shows the size range of soot particles in the atmosphere ranging from 10 nm to 100 nm.

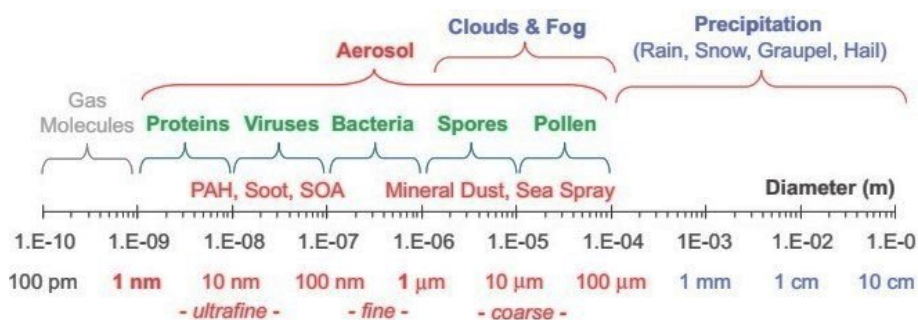


Figure 1.2: Scale of soot particles (Shiraiwa et al., 2012).

Table 1.1 gives the approximate composition of the model soot. Model soot is preferred for the evaluation of soot oxidation catalyst because it provides consistent and repeatable results due to the more homogenous nature of the soot in terms of size, shape, composition, and texture in comparison with real diesel soot particles. Nevertheless, real soot particles usually have a comparatively lesser soot combustion temperature due to the higher presence of Soluble Organic Fraction (SOF) (Ramdas et al. 2015).

Table 1.1: Composition of Model soot (Atribak et al. 2010).

Sample	C (%)	H (%)	N (%)	S (%)	O (%)
Printex-U	92.2	0.6	0.2	0.4	6.6
Vulcan XC-72R	98.0	0.1	0.1	0.5	6.6

Nucleation (secondary atmospheric reactions) of Volatile Organic Compounds (VOCs), vapors, and gases over the soot kernel causes the soot particle to grow to a higher size range (μm) (Kumar et al. 2012a). The exact formation of soot from gaseous fuel is still speculated upon. **Figure 1.3** shows the schematic of the soot formation. The soot formation mechanism is believed to be initiated by unsaturated hydrocarbons such as acetylene and its higher forms (C_{2n}H_2), PAH, and carbon vapors resulting from dehydrogenation of initial hydrocarbon molecules of the fuel as a by-product of pyrolysis/combustion/oxidation. The condensation of the above-unsaturated hydrocarbons leads to the formation of nascent soot particles ($d < 20\text{\AA}$). These nascent soot particles undergo surface growth by condensation of gas-phase polyacetylene and liquid-phase fuel, which forms the bulk of the soot (Lahaye 1990)(Haynes and Wagner 1981). The next step includes coagulation or aggregation, wherein the number of soot particles that nucleate on the surface to form the ‘fractal’ structure of the soot (Neeft et al. 1996b)

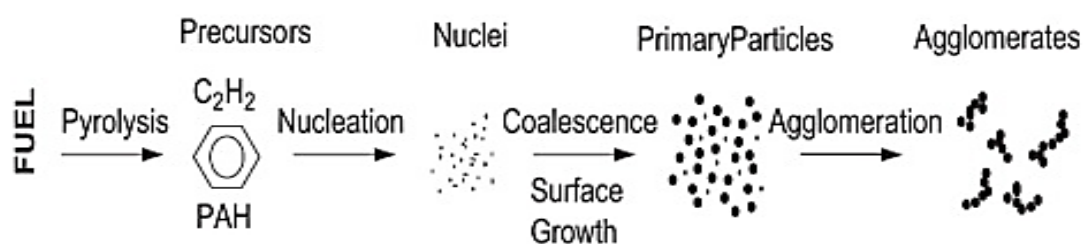


Figure 1.3: Formation of soot schematic (Haynes and Wagner 1981).

1.3 Carbon Monoxide

During the combustion of carbonaceous fuel, due to a lack of stoichiometry between the fuel and oxygen, soot, unburnt hydrocarbons, and CO are produced. CO is a colorless, odorless, tasteless, and non-irritant gas that is harmful to both the environment and living things, requiring oxygen for respiration (Raub 1999). Industrially, CO is used in steam reforming for the production of Hydrogen and is also used as a precursor for the formation of Synthetic fuel through the Fischer-Tropsch process (France et al. 2015)(Hubbard 2015). CO is lethal to human beings because it cannot be detected by sight, smell, taste, or any other cues and is rightly named a silent

killer. **Figure 1.4.** shows the possible mechanism of how CO affects the various tissues in different organs that are highly active in oxygen metabolism organs such as the heart, brain, kidneys, muscles, etc., As shown in **Figure 1.4**, CO binds with the Hemoglobin to form a COHb, reducing the amount of oxygen carried by blood, thereby causing shortness of breath and, at higher levels, leading to asphyxiation and death. CO stationary emission sources include the Iron and Steel industry, Petroleum refineries, and Chemical industries (synthesis gases, Methanol, Organic Acids, etc.). CO emission from IC engines is also a cause for concern; nonetheless, the usage of three-way catalytic converters has reduced CO emissions to acceptable limits. Catalytic oxidation of CO is one of the most favorable forms of CO abatement techniques.

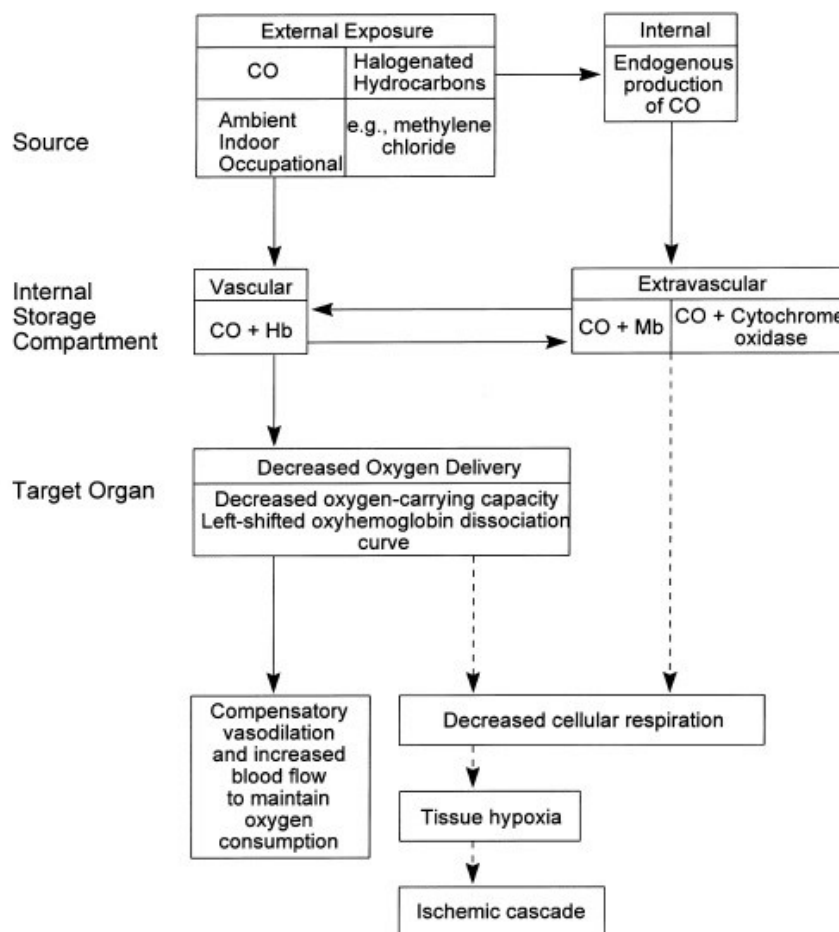


Figure 1.4: Mechanism and effects of CO on the tissue (Raub 1999).

1.4 Diesel Particulate Filter (DPF) and Diesel Oxidation catalyst (DOC)

DPF is an after-treatment device for reducing the emissions from Internal Combustion (IC) engines. It can be broadly classified into filtering and non-filtering types. Non-filtering catalyst or Diesel Oxidation Catalyst (DOC) consists of honeycomb monoliths that are adept at reducing the soluble/volatile organic fraction of the effluent emissions from an IC engine, whereas filtering type or are able to retain the PM apart from abating or reducing VOC content in the exhaust emissions of IC engines (Fino 2007)(Neeft et al. 1996b). **Figure 1.5** depicts the schematic of DPF; it can be seen that channels are plugged alternatively like a checkerboard, forcing the soot-laden exhaust gases to diffuse through the pores of the DPF channel walls, leaving behind the soot and ash. It prompts the build-up of soot on the walls of the channels and progressive blocking of the pores, consequently leading to an increase in back-pressure of the exhaust gases, triggering the reduction in performance and efficiency of the engine. If the DPF is not regenerated, then the engine may eventually stall due to a plugged filter.

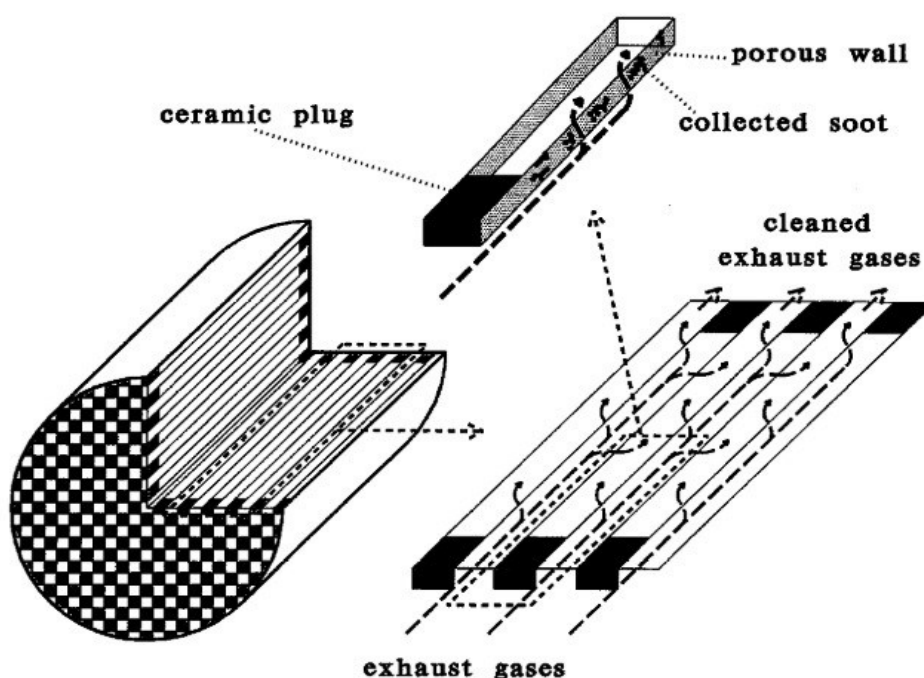


Figure 1.5: Schematic of a DPF (Neeft et al. 1996).

Regeneration of a DPF after regular intervals becomes inevitable to avoid poor engine performance. Usually, diesel soot combusts at 550 to 600 °C, which is higher than the engine operating temperatures of 250 to 400 °C. This calls for regeneration techniques that have to be incorporated/scheduled for the proper functioning of the DPF.

The regeneration techniques can be classified into two types: (1) Active. (2) Passive. The various active regeneration techniques include (1) fuel post-injection. (2) Fuel-borne catalyst. (3) external heating of the DPF by microwave or electric coil (Ma et al. 1997). The active regeneration strategy includes (1) Catalyzed DPF (CDPF). (2) Continuously Regenerated Trap (CRT) consisting of Diesel Oxidation Catalyst (DOC) & a wall flow trap (Fino et al. 2016). Commercially available technologies patented by automakers include the PSA (Peugeot-Citröen Societé d'Automobiles) system, CRT (Johnson Matthey), and Toyota Motors system DPNR (Diesel Particulate & NO_x Reduction) are able to oxidize soot into CO₂ in the temperature range of 200 to 400 °C (Shuang et al. 2015).

The materials used to manufacture the DPF are usually ceramic honeycomb monoliths (Pannone and Mueller 2001) and metallic wire meshes (Chen et al. 2019). Extruded ceramic honeycomb commercially are Cordierite (2MgO.2Al₂O₃.5SiO₂) (Nascimento and Serra 2016a) and SiC (Oi-Uchisawa et al. 2003). Ceramic monoliths have the following properties that make them attractive for an automobile manufacturer: (1) High melting point and thermal shock resistance. (2) Low coefficient of thermal expansion. (3) Sufficient porosity and pore size distribution. (4) Compatibility with the wash-coat and catalyst (Williams 2001)(Neyertz et al. 2014).

1.5 Ceria

Cerium ((Xe) 4f²5d⁰6s²) is a metal (atomic no 58; atomic mass 140.116 a.u.) belonging to the lanthanide series, which are termed rare earth metals. The oxide form of Cerium is called Ceria. It has a Calcium fluorite structure, as shown in **Figure 1.6**,

with space group $Fm\bar{3}m$ from room temperature to the melting point (Mogensen et al. 2000). In the Calcium fluorite structure, Ce atoms occupy the FCC positions, and Oxygen ions occupy the voids as shown in the **Figure 1.6** (Trovarelli 1996). Ceria can form a non-stoichiometric CeO_{2-x} oxide ($0 < x \leq 0.5$) at higher temperatures in a reducing atmosphere (Trovarelli 1996).

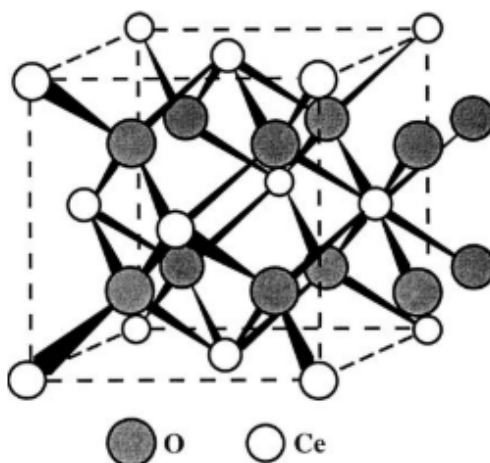


Figure 1.6: Cubic fluorite structure of CeO_2 (Trovarelli 1996).

Ceria's redox capabilities coupled with OSC (Trovarelli 1999) has propelled it to excel in various field and applications such as three-way catalytic convertor in automobiles (Kleitz et al. 2003), DPF (Di Sarli et al. 2016a) to oxidation catalyst for CO (Mukherjee and Reddy 2018), VOC (Wang et al. 2019), soot (Shuang et al. 2015), Methanol (Capdevila-Cortada et al. 2016), SOFCs (Rushton and Chronos 2014) (Capdevila-Cortada et al. 2016). When the particle size is ultra-fine, i.e., in nanoscale with high surface area, the redox capability enhances Oxygen Storage Capacity (OSC), and internal defects profoundly improve the oxygen transfer capability. This factor catapults Ceria as an excellent catalyst material for oxidation reactions. But with all such perks, there is a catch: Ceria sinters easily at high temperatures and loses the benefits it possesses when at the nanoscale (K. Krishna, A. Bueno-López, M. Makkee n.d.). Doping of Ceria with rare earth as well as transition metals has been done to overcome the sintering and thermal stability issues (Kašpar et al. 1999)(Aneggi et al. 2006)(Mukherjee and Reddy 2018). Optimized doping of Ceria increases the surface oxygen defects and other lattice defects, which, while improving the catalytic activity, also does not necessarily compromise the thermal stability issues (Mukherjee et al. Ceria-Manganese Mixed Oxides as Catalyst for Soot and CO Oxidation Activity.

2016a). Also, the doped Ceria, especially by multivalent dopants, have a favorable effect on the redox properties, OSC, and consequently active oxygen species (Rico-Pérez et al. 2016)(Katta et al. 2010).

1.6 Manganese

Manganese (Mn) is a transition metal that can exist in multiple oxidation states, such as MnO_2 , Mn_2O_3 , and Mn_3O_4 (Ji et al. 2019a). Manganese oxides are environmentally friendly, economical, and have been utilized as catalysts to oxidize VOC (Kim and Shim 2010), chlorinated VOC (Piumetti et al. 2015b), soot (Wagloehner et al. 2015), etc., Mn is easily reducible and imparts extrinsic oxygen vacancies in Ceria on doping. Manganese-doped ceria has been reported to have higher surface-active oxygen species than ceria alone (Li et al. 2011a)(Pérez and Bueno-López 2015)(Mukherjee et al. 2016a). This is attributed to the synergistic effect between Mn and ceria leading to the ease of redox behavior of the solid solution (Venkataswamy et al. 2014). Manganese oxide can store nitrates at low temperatures and release NO_2 at high temperatures, which will help in oxidizing soot (Tikhomirov et al. 2006). This phenomenon is associated with the synergistic effect between Manganese and Ceria, leading to the ease of redox behavior of the solid solution (Venkataswamy et al. 2014)(Liu et al. 2013).

1.7 Coating Techniques for monolithic or structured catalysts

The attractive advantages include superior mass transfer, modest pressure dip, high melting point, and excellent thermal, chemical, and mechanical stability of structured catalysts (Stegmayer et al. 2022a)(Nascimento et al. 2018a)(Guan et al. 2015)(Govender and Friedrich 2017)(Tomašić and Jović 2006) compared to powder and pellet type, have greatly heightened the demand for structured catalysts in industries in the past few decades. The structured catalyst usually consists of a substrate or a monolith structure or foams made up of ceramic or metallic material. Prior to the coating of the active catalyst, a secondary coating or wash coating of the monolith is

done for (1) Improvement in the monolith surface area, (2) Better dispersion of the active catalyst over the secondary coating or wash coating, (3) Improved adherence of the coated layers. Conventionally, the techniques employed in particular to the coating of catalyst on ceramic honeycomb monoliths include impregnation/wet impregnation, dip coating (slurry and sol-gel), and deposition precipitation,

Wet impregnation involves dipping or wetting the monolith surface in the precursor solution, removing or blowing out the excess solution, followed by drying and calcination. Wet impregnation is a very simple method of coating with the drawback that the distribution and thickness of the coating may be non-uniform (Vergunst et al. 2001). Deposition-precipitation or precipitation method involves the precipitation of metal salt solution in the channels or on the surface of the monolith by using urea. The drawback of the method is that there may be issues with the homogeneity of the catalyst layer coated on the monolith (Barrio et al. 2005). The dip coating by slurry method involves the dispersion of the catalyst powder by utilizing a suitable dispersant. Size reduction techniques may be used to reduce the size and narrow the distribution of particles. In comparison with other techniques, the dip coating by slurry method gives high loading rates per cycle. The downside is that the coating may lack high adherence, additional binders may be required for improving the adherence, for applications requiring porosity for example DPF, the pores of the substrate or monolith channels may be completely blocked. The sol-gel dip coating addresses the issues with that of the slurry dip coating by not fully blocking the pores and produces secondary or active catalyst layer with high adherence.

1.8 Scope and Objectives

1.8.1 Scope

The implementation of stricter emission norms with respect to enforcing BS VI, the need to develop an optimized catalyst composition so as to reduce the soot combustion temperature in the range of the CI engine exhaust temperatures (150 – 400

°C) to be adopted in DPF and DOC after treatments assume more importance. The current work will seek to address the challenges of developing a low-cost, effective, and efficient catalyst for Diesel engine working temperatures. The implementation of a ceramic monolith-coated catalyst for CO oxidation activity will mimic the real-time responses more closely than a powder catalyst. The outcomes of this study may pave the way for developing a product based on the Ceria-Manganese mixed oxides DPF and DOC.

1.8.2 Objectives

The objective of the study is to use Ceria-Manganese mixed oxides as catalyst for soot and CO oxidation activity,

The objectives of the study are as follows,

1. Synthesis of Ceria-Manganese mixed oxide catalysts using EDTA-Citrate method.
2. Characterization analyses of the Ceria-Manganese mixed oxide catalysts by XRD, BET, Raman spectroscopy, FESEM, TEM, and its diesel soot oxidation activity.
3. Fabrication of Ceria-Manganese mixed oxide catalysts coated on ceramic Cordierite using dip coating method.
4. Characterization analyses of the Ceria-Manganese mixed oxide coated Cordierites using XRD, BET, Raman spectroscopy, Optical imaging, FESEM, and testing for CO oxidation activity.

1.9 Organization of the Thesis

The remainder of the thesis is organized in the following manner,

Chapter 2 contains the literature review of soot and CO oxidation of Ceria and doped Ceria-based materials. The soot and CO oxidation mechanisms is also briefly explained.

Chapter 3 describes the materials utilized, synthesis of Ceria-Manganese nanostructured powder catalyst, dip coating technique to obtain Ceria-Manganese structured catalysts, characterization techniques utilized for nano structured powder and structured catalysts, and soot loading procedures. The soot and CO oxidation setup is also briefly discussed.

Chapter 4 reveals the soot oxidation and characterization results of Ceria-rich Ceria-Manganese mixed oxides (CMX (X = 0, 5, 10, 20, 30) corresponding to $Ce_{1-x}Mn_xO_{2-\delta}$, where x = 0, 0.05, 0.1, 0.2, and 0.3 mole %). The central focus of this chapter is to study the effect of modest Manganese doping in Ceria and its effect on soot oxidation activity.

Chapter 5 deals with the soot oxidation and characterization results of Manganese-rich Ceria-Manganese mixed oxides (CMX (X = 40, 50, 60, 70, 80, 90, and 100) corresponding to $Ce_{1-x}Mn_xO_{2-\delta}$, where x = 0.4, 0.5, 0.6, 0.7, 0.8, 0.9, and 1 mole %). The primary focus of this chapter is to examine the effects of phase separation and its allied effects on the soot oxidation activity.

Chapter 6 reveals the CO oxidation activity of the best performing (based on soot oxidation activity results from **Chapters 4 and 5**) Ceria and Manganese rich Ceria-Manganese mixed oxides coated onto Cordierite, i.e., CO oxidation activity on structured catalysts.

Chapter 7 contains the overall summary of the thesis highlighting the prominent findings, conclusions, and future scope of the present work.

CHAPTER 2

LITERATURE REVIEW

Heterogenous catalysts have been a boon to many chemical industries. They have improved the production rate, selectivity, energy efficiency, and environmentally friendly processes utilized by the chemical production industries. In the present context, soot oxidation, in the past two decades, has been widely studied, and rightly so, due to the menacing effect of soot on both biotic and abiotic organisms. Before delving into soot oxidation catalysts, one must understand the basic properties of heterogeneous catalysts to be utilized for selective oxidation. The parameters include the following: (1) lattice oxygen mobility (2) Strength of Metal-oxygen bond (3) Host structure (4) Redox capability (5) Multifunctionality of active sites (6) Site isolation (7) cooperation of phases (Grasselli 2003). Ceria has hogged the limelight as a crucial constituent for heterogenous catalysts utilized for various applications and processes due to possessing most of the favorable parameters.

2.1 Ceria

Ceria has been used as a catalyst for various applications ranging from three-way catalytic converters in automobiles (Kleitz et al. 2003), DPF (Di Sarli et al. 2016a) to oxidation catalysts for CO (Mukherjee and Reddy 2018), VOC (Wang et al. 2019), Soot (Shuang et al. 2015), Methanol (Capdevila-Cortada et al. 2016). When the particle size is ultra-fine, i.e., in nanoscale with high surface area, the redox capability enhances Oxygen Storage Capacity (OSC), and internal defects profoundly improve the oxygen transfer capability. This factor catapults Ceria as an excellent catalyst material for soot oxidation. From the literature, it is known that by tailoring the morphology of Ceria, the soot oxidation capabilities can be drastically improved by virtue of better contact points between the catalyst and soot particles (Bensaid et al. 2013)(Miceli et al. 2014). Also, exposing the reacting planes by tailored nanostructures having high surface area

helps in improving low-temperature soot oxidation (lower T_{10} temperatures) (Piumetti et al. 2015a). Soot oxidation under loose contact not only depends on the active oxygen species but also on the morphology, such as an ordered microporous structure for improving production and transfer of active oxygen species and long-range soot oxidation mechanism involving NO_2 (Alcalde-Santiago et al. 2018). Some of the soot oxidation literature on Ceria is shown in **Table 2.1**.

Table 2.1 gives the details of the number of compositions of Ceria, synthesis method utilized to obtain Ceria in different forms, the calcination temperature utilized, the specific surface area obtained after calcination, the T_{50} temperature for the type of contact for soot and catalyst reported, and the inferences given by the authors. The effect of different morphologies like nanorods, nanosticks, nanoflakes, nanofibers, etc., are summarized. The main objective was to tailor the morphologies of Ceria to expose the highly active planes as much as possible to aid in the combustion of soot at lower temperatures as much as possible.

Although, surface area helps in the overall soot oxidation activity by increasing the availability of contact points for better interaction of soot with the adsorbed gases (in the case of tight contact as well as loose contact type soot oxidation), its criticality isn't as much when compared with the exposed active planes that readily help in improving the soot oxidation activity of the Ceria. The morphology also plays a crucial role in the number of soot-catalyst contact points (especially true for loose contact type of soot oxidation).

The purpose of the engineered morphologies is to tailor in defects that aid in the soot oxidation activity positively than to destabilize the structure or have an unfavorable effect on the soot oxidation activity. Engineered morphologies with intention to form a specific shape of the Ceria catalysts seem to do better at soot oxidation than the Ceria produced by methods wherein the formation of Ceria catalyst with most stable planes being exposed are favored.

Table 2.1: Soot oxidation by Ceria.

Sno	Sample/Synthesis	Calcination temperature	Soot used/ratio	Surface area (m ² /g)	T ₅₀ (°C)		Remarks	Reference
					Tight contact	Loose contact		
1	Co-precipitation (NanoFibers -NF) (NaOH/citric acid) CeO ₂ - NF (0.3) CeO ₂ - NF (0.5) CeO ₂ - NF (0.8) CeO ₂ - NF (1) CeO ₂ - SCS	300 °C/3 h	Printex-U; S/C 1:9; LC; 200 to 700 °C at 5 °C /min 100 ml/min of 10% O ₂ in N ₂	-- -- -- -- --	400 399 401 397 408	440 445 447 438 465	Nano-fibers were adept at reducing the soot combustion temperature, especially the soot ignition/onset temperature. Morphology plays a critical role in soot oxidation activity when the contact is limited/loose.	(Kumar et al. 2012a)
2	Commercial Ceria calcined at different temperatures CeO ₂ ⁴⁵⁰ CeO ₂ ⁶⁰⁰	450 °C/2 h 600 °C/2 h	Soot obtained from burning commercial diesel fuel; TC; S/C 1:20;	20 20	480 480	520 --	The higher concentration of superoxide (O ₂ ⁻) and peroxide (O ₂ ²⁻) in CeO ₂ ⁸⁰⁰ sample led to better soot oxidation activity in tight contact conditions. A combustion mechanism of spillover takes place in loose contact conditions.	(Gross et al. 2012)

	CeO ₂ ⁸⁰⁰	800 °C/2 h	40 ml/min of 5% O ₂ /N ₂	20	380	515		
3	Hydrothermal CeO ₂ -fibers CeO ₂ -flakes CeO ₂ -sticks CeO ₂ -SCS	600 °C/5 h	Printex-U; S/C 1:9; LC and TC; 200 to 700 °C at 5 °C /min in 100 ml/min of 10 % O ₂ in N ₂	09.8 03.9 03.4 52.4	372 420 445 365	533 552 537 525	The soot and the catalyst contact plays a major role in lowering the soot combustion temperature, as seen for CeO ₂ nano-fibers that have comparable activity to high surface area SCS catalysts. The morphology of fiber catalysts maximizes the no. of contact of points between soot and catalyst.	(Bensaid et al. 2013)
4	Ce-NC (hydrothermal) Ce-NR (hydrothermal) Ce-M (template-assisted method)	550 °C/4 h 550 °C/4 h 450 °C/4 h and	Printex-U; S/C 1:9; LC and TC; 100 ml/min of 10 % O ₂ /N ₂	004 004 075	400 416 464	477 536 538	Exposed reactive planes in Ceria {100} and {110} help in better overall performance and are surface-sensitive at higher temperatures.	(Piumetti et al. 2015)

	Ce-NC/ZSM-5 (1:1 wt. ratio)	550 °C/4 h	from 200 to 700 °C at 5 °C/min.	425	439	525	High surface area helps in lowering T ₁₀ values, and soot oxidation is surface sensitive at low temperatures.	
	Ce-SCS	600 °C/0.3 h		069	476	580		
	Printex-U				620			
5	EDTA-Citrate method	600 °C/5 h	Printex-U; S/C 1:4; TC; 200 to 800 °C at 10 °C/min in 100 ml/min of synthetic air				Among the redox metal oxides, Mn performed the best by virtue of its lower Oxygen binding energy and reduction temperature. Among the non-redox metal oxides, higher BET surface area, lattice strain, relative surface oxygen ratio, and smaller ionic radius played an important role in soot oxidation activity. Among the non-redox metal oxides, HfO ₂ had the favorable characteristics mentioned above and thus fared better.	(Anantharaman et al. 2017)
	CeO ₂ (redox)			41.2	530	--		
	SnO ₂ (redox)			00.8	576	--		
	Pr ₆ O ₁₁ (redox)			03.6	485	--		
	Mn ₃ O ₄ (redox)			46.9	483	--		
	Gd ₂ O ₃ (non-redox)			16.3	533	--		
	La ₂ O ₃ (non-redox)			29.9	505	--		
	ZrO ₂ (non-redox)			12.3	494	--		
	HfO ₂ (non-redox)	09.4	483	--				

6	Hydrothermal method Ce-NC Ce-NR Ce-NO (nano octahedron)	550 °C/4 h 550 °C/4 h 550 °C/4 h	Printex-U; S/C 1:10; LC; 100 ml/min of 10% O ₂ /N ₂ ; 150 to 700 °C at 5 °C/min	03.9 69.7 07.4	-- -- --	459 539 541	Nano-cubes have abundant {100} planes that are beneficial for oxidation reactions. {100} planes have high surface energy. The reactivity of ceria nanostructured catalysts follows {100} > {110} > {111}. Ceria Nano-cubes had high TOF due to a greater amount of {100} planes.	(Jian et al. 2020)
7	CeO ₂ CeO ₂ (NR) CeO ₂ -A (aged) CeO ₂ (NR)-A (aged)	600 °C/3 h 600 °C/3 h 900 °C/8 h 900 °C/8 h	Printex-U, Degussa AG. S/C 1:9; TC 500 ml/min of 10% O ₂ , 7% vapour/N ₂ ; r.t. to 700 °C at 5 °C/min.	-- -- -- --	-- -- -- --	415 394 489 467	CeO ₂ -NR has more O ₂ vacancies than CeO ₂ nanoparticles. Comparatively, CeO ₂ -NR has better lattice oxygen mobility. CeO ₂ -NR has better high-temperature stability (high aging resistance).	(Chen et al. 2020)

8	One pot Urea Combustion synthesis of CeO ₂ .	400, 600, 800, and 1000 °C for 4h	Charcoal particulates; S/C 1:4; TC; r.t. to 1000 °C at 20 °C/min	--	CeO ₂ (800): 460 °C	--	<p>Increasing calcination temperature resulted in increased particle size.</p> <p>Oxygen vacancies increased with increasing the calcination temperature to 800 °C.</p> <p>An increase in oxygen vacancies consequently improved the catalytic activity.</p> <p>Higher temperature calcination improves the efficiency of oxygen transport by virtue of the denser packing obtained.</p>	(Ratnayake et al. 2021)
9	Hydrothermal method CeO ₂ -cubes CeO ₂ -rods, CeO ₂ -octahedra CeO ₂ -polyhedra	350 °C/3h	Printex-U; S/C 20/1; TC; 50 to 550 °C at 10 °C/min in 50 ml/min of 10% O ₂ /N ₂	29.0 12.0 64.0 06.6	398 415 411 458	-- -- -- --	<p>{100} and {110} planes of Ceria inherently more reactive than {111} plane for soot oxidation.</p> <p>It is easier to form oxygen vacancies in {100} and {110}.</p>	(Garcia et al. 2021)

							<p>The Peroxide and superoxide oxygen species are formed when interacting with oxygen vacancies.</p> <p>Nano-cubes of Ceria expose principally expose {100} planes</p> <p>Soot oxidation follows Mars-Van-Krevelen (MvK) mechanism.</p>	
10	Commercial CeO ₂ BCL-CeO ₂		Printex-U (orion); S/C: 1:9); LC; 100 ml/min of 20.5 % O ₂ /N ₂ from 150 °C to 700 °C at 5 °C/min	-- --	363 --	420 514	<p>One of the crucial factors of catalysts for soot oxidation is structure and surface properties.</p> <p>The bundled nanofibers, resembling broccoli (BCL), possess a higher amount of oxygen vacancies.</p>	(Tsai et al. 2022)

2.2 Doped Ceria

Ceria sinters easily at high temperatures and loses the benefits it possesses when at the nanoscale (K. Krishna, A. Bueno-López, M. Makkee n.d.). Doping of Ceria with rare earth as well as transition metals has been done to overcome the sintering and thermal stability issues (Kašpar et al. 1999)(Aneggi et al. 2006)(Mukherjee and Reddy 2018). Optimized doping of Ceria increases the surface oxygen defects and other lattice defects, while improving the catalytic activity, also do not necessarily compromise the thermal stability issues (Mukherjee et al. 2016a). Also, the doped Ceria, especially by multivalent dopants, have a favorable effect on the redox properties, OSC, and consequently active oxygen species (Rico-Pérez et al. 2016)(Katta et al. 2010).

Doping Zirconia in the Ceria lattice improves thermal stability by curbing the crystallite growth (Zhu et al. 2007)(Aneggi et al. 2012). However, Aneggi et al. reported that if a minimum threshold of surface area (around 40 m²/g) for a catalyst is not met, it may lead to a negative effect on the soot oxidation activity (Aneggi et al. 2012). Doping of Ceria with trivalent dopants improves the number of Oxygen vacancies, surface area, and reducibility of the doped catalyst and decreases the crystallite size (Rangaswamy et al. 2015). The addition of Mn into the Ceria lattice improves the soot oxidation activity by the enhanced availability of abundant active oxygen species both from the surface and lattice (due to weakly/loosely bound lattice Oxygen)(Mukherjee et al. 2016b). The multiple oxidation states of the dopant atom also promote synergistic effects between Ceria and the dopant element(Mukherjee et al. 2016b). The doped Ceria with different nanostructures like nano-rods and nano-cubes have been reported to have abundant low index planes (100) and (110) that are highly active in soot oxidation. Also, the morphology of nano-rods and nano-cubes have excellent lattice Oxygen mobility and reducibility of the surface in general (Andana et al. 2016).

Doped Ceria with three-dimensionally Ordered Mesoporous structures are reported to have good low-temperature reducibility of the catalyst, helping in better

low-temperature soot oxidation activity (Cheng et al. 2017b). Likewise, the addition of Co to the Ceria lattice improves its nitrate storage ability and Oxidation of NO to NO₂ in the presence of NO_x. Also, Co₃O₄ reduces itself to CoO to facilitate the active Oxygen species at high temperatures (Kumar et al. 2012b). The synergistic effects between Ceria and dopant elements, namely rare-earth metals, transition metals, alkali, and alkali earth metals, were lucidly described by Di Sarli et al. (Di Sarli et al. 2021). The doping of Ag into the Ceria lattice reduced the Metal-Oxygen bond strength and provided more active sites (Di Sarli et al. 2021). The variation of the doping methodology and its effect on the soot oxidation activity was also emphasized to cause changes in the synergy and soot oxidation activity (Di Sarli et al. 2021).

Table 2.2 gives a brief literature survey of doped Ceria catalysts used for soot oxidation activity. As earlier stated, the solution for Ceria that has sintering and stability issues at high temperatures, lower light of temperatures or T₁₀ temperatures, modest ability to form active oxygen species and long range oxidizing molecules like NO₂ in the presence of NO in the reactive gas feed, limited Oxygen Storage Capacity (OSC), is doping it with alkali, alkali earth, transition and rare earth elements to bring in favourable defects to improve the soot oxidation activity of the doped Ceria catalyst.

The synergy between the aliovalent and iso-valent dopants with Ceria helps in improving the redox capabilities boosting the oxygen mobility, OSC and also augmenting the active sites on the interface where in the soot oxidation reaction is to take place. The addition of certain multivalent dopants like Co, Fe, Pr, etc., reportedly increased the catalytic activity of the doped catalysts for soot oxidation. The addition of Ag has also been reported to have generated more active oxygen species helpful in reducing the light off temperatures and peak temperatures for combustion of soot. Also the deactivating effects of sulphur dioxide also can be negated/reduced by doping Ceria with Cobalt. Doping Zr into Ceria helps in improving the thermal stability at high temperatures. The dopants like Co and Mn reportedly also improve the nitrate storage at low temperatures and oxidation of NO to NO₂.

Table 2.2: Soot oxidation by doped Ceria.

Sno	Samples	Calcination temperature	Soot used & conditions	Surface area (m ² /g)	T ₅₀ (°C)		Remarks	Reference
					Tight	Loose		
1	Co-precipitation method CeO ₂ Ce _{0.7} Zr _{0.3} O ₂ Ce _{0.5} Zr _{0.5} O ₂ Ce _{0.3} Zr _{0.7} O ₂ ZrO ₂	700 °C/4 h	Printex-U; S/C 1:10; LC; 30 to 700 °C at 10 °C/min in 500 ml/min 10% O ₂ in N ₂	058.22 130.82 132.61 121.80 030.90	-- -- -- -- --	573 543 525 559 595	The addition of Zirconia improves Oxygen vacancies, thermal stability, and reduces the crystallite size. The concentration of O ₂ in the gas phase determines the rate-limiting step in the soot oxidation reaction.	(Zhu et al. 2007)
2	Sol-gel method Mn/Ce Ba, Mn/Ce Mn-Ce Ba/Mn-Ce	500 °C/3 h; (thermal ageing 800 °C/10 h)	Printex-U; S/C 1:10; LC; r.t. to 650 °C at 10 °C/min in 1000 ppm NO in 10% O ₂ /N ₂	43(1) 27(2) 62(4) 25(8)	-- -- -- --	414(532) 415(466) 400(500) 405(429)	Barium inhibited sintering but couldn't prevent phase separation in Mn-Ce solid solution. Doping of Mn in Ceria lattice refines crystallite size.	(Wu et al. 2011)

							Thermal aging drastically reduces surface area and soot oxidation activity.	
3	Coprecipitation/ ripening method CeO ₂ (0.8) 1% Co/CeO ₂ (0.8) 5% Co/CeO ₂ (0.8) 10% Co/CeO ₂ (0.8) 10% Co/CeO ₂ (0.8) aged at 800 °C/12 h in air. 10 % Co/CeO ₂ (0.8) aged at 800 °C/12 h in SO ₂ (1030 ppm) for 12 h.	600 °C/3 h	Printex-U; S/C 1:9; TC and LC, 200 to 700 °C at 5 °C/min in 100 ml/min of NO _x (500 ppm) in 10 % O ₂ /N ₂	21.5 11.4 09.2 07.5 03.5 3.1	445 390 400 410 416 506	With NO _x 412 381 369 357 375 485	The capability of fibrous CeO ₂ is further enhanced by Cobalt doping. The mobility of Oxygen species was further improved by Cobalt doping. The Co doped catalyst had better dispersed Co ₃ O ₄ particles that have superior oxidation capacity. The oxidation of NO to NO ₂ was more pronounced with the increase in Cobalt doping during NO _x assisted soot oxidation. The reduction in the activity of the Cobalt-doped ceria catalyst under SO ₂ aging is due to the conversion of Cobalt oxide particles to cobalt sulfate.	(Kumar et al. 2012c)

4	Coprecipitation method CeO ₂ Ce _{0.73} Zr _{0.27} O ₂ Ce _{0.9} Nd _{0.1} O ₂ Ce _{0.64} Zr _{0.27} Nd _{0.09} O ₂	800 °C/90 min	S/C 1:4; LC; r.t. to 700 °C at 10 °C/min in 500 ml/min of 500 pm NO in 5% O ₂ /N ₂	01 35 05 37	-- -- -- --	610 580 610 570	The mobility of oxygen species is improved in both Ceria and Zr doped Ceria by doping Nd into them. Nd doped Ceria sample has poor soot oxidation activity due to sintering.	(Hernández-Giménez et al. 2013)
5	Coprecipitation method CeO ₂ CeO ₂ -La ₂ O ₃ CeO ₂ -Sm ₂ O ₃	500 °C/5 h	Printex-U; S/C 1:4; TC and LC; r.t. to 500 °C at 10 °C/min in 100 ml/min of air	41 66 84	561 467 417	591 570 517	Trivalent dopants improve O ₂ vacancies, crystallite size, BET surface area, and reducibility of Ceria. In this, Sm ³⁺ had better of all the above properties when compared with La ³⁺ .	(Rangaswamy et al. 2015)
6	Coprecipitation method CeO ₂ – (C) CeO ₂ – ZrO ₂ (CZ)	500 °C /5 h	Printex-U; S/C 1:4; TC; 300 to 1000 °C at	41 84	552 522	-- --	Surface-confined oxygen species perform a key role in controlling the rate of soot oxidation activity.	(Mukherjee et al. 2016b)

	CeO ₂ – La ₂ O ₃ (CL) CeO ₂ – Pr ₂ O ₃ (CP) CeO ₂ – HfO ₂ (CH) CeO ₂ – Fe ₂ O ₃ (CF) CeO ₂ –Mn ₂ O ₃ (CM)		10 °C/min in 100 ml/min of air	66 72 78 68 58	467 438 409 513 396	-- -- -- -- --	CM had the highest amount of surface oxygen species. The synergistic effect of Ce and Mn assisted in better redox properties and, thereby, better soot oxidation activity.	
7	Hydrothermal Ce50Pr50 Ce75Pr25 Ce90Pr10 Ce100 Ce50Pr50-SCS Ce75Pr25-SCS Ce90Pr10-SCS Ce100-SCS	550 °C/4 h 650 °C/0.3 h (SCS)	S/C 1:9; TC and LC; 100 to 700 °C at 5 °C /min in 50% vol. air and 50% vol. N ₂	20 12 09 06 14 16 33 43	408 412 430 435 472 460 435 440	527 537 555 561 579 571 569 569	Better soot oxidation activity was seen in the hydrothermally synthesized sample due to well-defined nanostructure (high lattice Oxygen mobility and redox capability) and synergistic effect (redox capacity) of Ce and Pr. The well-defined nanostructures (Nano Rods (NR) and Nano Cubes (NC)) of CePr catalysts had (100) and (110) low index planes in abundance.	(Andana et al. 2016)

							SCS method had surface area overshadowing the positive effects of Pr.	
8	CTAB assisted Coprecipitation method $M_{0.1}Ce_{0.9}O_2$ (M = Mn, Fe, Co, Cu) CeO ₂ -co CeO ₂ MnCe FeCe CoCe CuCe	550 °C/6 h	S/C 1:9; TC in 100 ml/min of 5 % O ₂ /He and 1000 ppm NO in 5% O ₂ /He r.t. to 700 °C at 4 °C/min.	057 105 121 100 068 121	460 448 375 421 441 382	430 422 358 398 386 362	<p>The doping of transition metals enhances the redox properties by creating more oxygen vacancies. These parameters are also helpful in the favourable oxidation of NO to NO₂ and NO_x storage.</p> <p>In O₂ assisted soot oxidation, improved redox properties coupled with the high surface area are favourable parameters for soot oxidation. Active oxygen mechanism is followed for the O₂ assisted soot oxidation.</p> <p>MnCe has a superior mesoporous structure that plays a crucial role in improving the soot oxidation activity both in the presence and absence of NO_x.</p>	(Zhu et al. 2017a)

9	Coprecipitation with 2 wt% Cu loaded through incipient wetness, coprecipitation, and physical mixing CZ (20 mol% Zr) CZCu-CP Cu ₂ /CZ Cu ₂ /AL Cu ₂ CZ-LO Cu ₂ CZ-TI Cu ₂ CZ-TI-500	500 °C/1 h	S/C 1:4; LC; diluted with 320 mg of SiC,					The degree of dispersion of Cu species on the surface of CZ determines the activity of the catalyst, as Cu is highly active for NO oxidation to NO ₂ .	(Giménez-Mañogil and García-García 2017)
			Printex-U;	96	--	509	NO _x	Finely dispersed Cu on the surface of CZ increases the magnitude of contact points to soot, resulting in better activity at lower temperatures.	
			500 ml/min	72	--	510			
			(GHSV = 30000 h ⁻¹) of	71	--	513			
			500 ppm NO	67	--	550			
			5% O ₂ /N ₂ ; r.t.	75	--	520		The synergistic effect of Cu with base, i.e., Ce, plays a crucial role in both the catalytic and NO oxidation activity.	
			to 700 °C at 10 °C/min	77	--	500			
				70	--	521		Bulk Cu augments catalytic activity at high temperatures and finely dispersed Cu at lower temperatures, respectively.	

10	Microwave-assisted solution combustion method. CeO ₂ Ce_Fe3 Ce_Fe6	800 W at 2450 MHz for 3 min.	Printex-U (Degussa) TC; S/C 1:9; r.t. to 700 °C at 5 °C/min in 100 ml/min of 10 % O ₂ /N ₂	25.0 05.0 02.5	413 461 487	-- -- --	A Very low specific surface area of the Fe doped Ceria resulted in a lesser number of contact points with soot. The specific surface area is very much applicable in tight contact mode, wherein the solid-solid-gas interface reaction has the number of contact points as a crucial parameter.	(Sahoo et al. 2017)
11	EDTA-Citrate method CeO ₂ CS10 CS20 CS30 CS40 CS50 CS60 CS70	600 °C/5 h	Printex-U; S/C 1:4; TC; 200 to 700 °C at 10 °C/min in	24 38 45 35 29 24 18 16	530 480 500 511 502 512 531 537	-- -- -- -- -- -- -- --	Phase segregation in this system doesn't help in improving the soot oxidation activity. Comparatively higher oxygen vacancy concentration, low band energy, and degree of agglomeration propelled CS10 to have the best soot oxidation activity among the catalysts.	(Anantharaman et al. 2018)

	CS80 CS90 Sm ₂ O ₃		100 ml/min of synthetic air	14 10 08	542 538 537	-- -- --	The T ₅₀ trend is similar to the band gap energy trend, suggesting a direct influence of the band gap energy and the soot oxidation activity.	
12	SCS method 0NDC 1NDC 3NDC 5NDC 10NDC 20NDC 30NDC	600 °C/2 h	S/C 1:10; TC (TC) in r.t. to 600 °C at 10 °C/min in 100 ml/min of Synthetic air.	19 23 32 21 15 27 18	435 427 440 450 456 460 461	-- -- -- -- -- -- --	Nd doping into the Ceria lattice improved the redox potential and surface-active oxygen species. At lower temperatures, active surface oxygen species participate, and at higher temperatures, both surface active and lattice oxygen participate in the soot oxidation activity.	(Patil et al. 2019)
13	EDTA-Citrate method (9:1) CeO ₂ (C) CeO ₂ - SnO ₂ (CT) CeO ₂ -Sm ₂ O ₃ (CS) CeO ₂ -Gd ₂ O ₃ (CG)	600 °C/5 h	Printex-U; S/C 1:4; TC; 200 to 600 °C at	-- -- -- --	530 450 480 490	-- -- -- --	The crucial descriptors for the soot oxidation (binary metal oxide) were reported to the optical band gap.	(Anantharaman et al. 2019)

Ceria-Manganese Mixed Oxides as Catalyst for Soot and CO Oxidation Activity.

	CeO ₂ -La ₂ O ₃ (CL) CeO ₂ -ZrO ₂ (CZ) CeO ₂ -HfO ₂ (CH)		10 °C/min in 100 ml/min of synthetic air	-- -- --	450 425 430	-- -- --	The optical band gap relies upon the nature of the dopant, i.e., the charge of the dopant and its ionic radius. The smaller the ionic radius of the dopant, the lower the energy required for the oxygen vacancy formation.	
14	Hydrothermal synthesis CeO ₂ Ce ₉₅ Cu ₅ Ce ₉₅ Mn ₅ Ce ₉₅ Cu _{2.5} Mn _{2.5}	550 °C/4 h	Printex-U (Degussa); S/C 1:40; TC; 45 ml/min of air.	09 46 17 52	418 407 365 390	-- -- -- --	Copper and Manganese oxide doping ensured the formation of intrinsic and extrinsic defects in the Ceria lattice. CeO ₂ and Ce ₉₀ Mn ₅ samples displayed remarkable regeneration of defect sites after soot oxidation. Mn doping improves the textural and physical properties, favoring higher soot oxidation reaction by means of a stable distribution of defect sites.	(Sartoretti et al. 2019)

15	Coprecipitation and Direct Calcination CeO ₂ -500 CeO ₂ -1000 Ce _{0.8} Pr _{0.2} O _{2-δ} -500 Ce _{0.8} Pr _{0.2} O _{2-δ} -1000 Ce _{0.5} Pr _{0.5} O _{2-δ} -500 Ce _{0.5} Pr _{0.5} O _{2-δ} -500-CAL Ce _{0.5} Pr _{0.5} O _{2-δ} -1000 Ce _{0.2} Pr _{0.8} O _{2-δ} -500 Ce _{0.2} Pr _{0.8} O _{2-δ} -1000 PrO _{2-δ} -500 PrO _{2-δ} -1000	500 and 1000 °C/1 h	S/C 1:4; LC; 500 ml/min of 500 ppm NO _x in 5 % O ₂ /N ₂ (or) O ₂ /N ₂ from r.t. to 700 °C at 10 °C/min.	-- 54 01 67 04 28 37 -- 03 -- -- --	Loose O ₂ /N ₂ 580 594 547 589 542 562 592 560 592 560 586	Loose (NO _x) 501 602 502 589 485 477 589 480 589 486 587	The synthesis method plays a key role in the doping of dopants as the procedure determines the dopant's insertion into the parent lattice (<i>majority</i>) or dispersion on the surface or segregation of phases. Pr doping for 500 °C calcination improved the generation of anionic vacancies. The introduction of Pr into the Ceria lattice improved reduction potential at lower temperatures and also improved surface and subsurface O ₂ mobility in the Ceria lattice.	(Guillén-Hurtado et al. 2020)		
16	Incipient wet impregnation CZ Mn/CZ Fe/CZ	600 °C/3 h	Printex-U; S/C 1:10; TC and LC; 30 to 700 °C at	66.7 58.5 57.4	O ₂ 380 358 385	NO 388 360 388	O ₂ 628 609 619	NO 551 531 546	Doping Mn and CO in CZ enhanced the soot oxidation activity by comparatively abundant O ₂ species, excellent mobility	(He et al. 2021)

	Co/CZ		10 °C/min in 500 ml/min of 10 % O ₂ /N ₂ and 600 ppm NO in 10 % O ₂ /N ₂	58.6	361	350	607	531	of lattice oxygen, and oxygen vacancies. Textural properties had minimal impact on the catalytic activity for all samples. Mn and Co doped CZ has superior oxidation of NO to NO ₂ . NO ₂ has a better oxidizing ability than O ₂ .	
17	Hydrothermal method and impregnation CeO ₂ -R CeO ₂ -C CeO ₂ -O Ag/CeO ₂ -R Ag/CeO ₂ -C Ag/CeO ₂ -O	500 °C/4 h	Printex-U (Degussa) 200 ml/min of 8 % O ₂ /Ar. 100 to 550 °C at 5 °C/min	115 015 006 104 012 006	377 402 484 370 334 468	513 452 517 509 363 495	Silver's chemical state and O ₂ activation depend on support interaction and morphology. Oxygen activation is the formation of oxygen vacancy. Weak interaction of Ag on CeO ₂ gives rise to Ag ⁰ , which is more effective than silver oxide in terms of soot catalyst contact and		(Wang et al. 2021)	

							thereby improves the soot oxidation activity. Ag/CeO ₂ -C have high oxygen vacancies that help in the production of active oxygen species. The lattice oxygen is also pumped out to cater to soot oxidation activity.	
18	Co-precipitation and impregnation CeO ₂ La(1)-CeO ₂ La(3)-CeO ₂ La(5)-CeO ₂ La(9)-CeO ₂ Ag/CeO ₂ Ag/La(1)-CeO ₂ Ag/La(3)-CeO ₂ Ag/La(5)-CeO ₂ Ag/La(9)-CeO ₂	550 °C/4 h	Printex-U; LC; S/C 1:10; r.t. to 800 °C at 10 °C/min in 100 ml/min of 10% O ₂ and H ₂ O in He	-- -- -- -- -- 46 48 50 34 32	-- -- -- -- -- -- -- -- -- --	620 604 577 569 551 529 504 473 481 514	There is an increase in reducibility and O ₂ vacancies of La-CeO ₂ with the increase in La doping. Ag promotes the generation of active oxygen species. Excess of La in Ag/CeO ₂ promotes the sintering of silver particles. Excess La doping reduces O ₂ vacancies and the reducibility of the catalyst.	(Lee et al. 2021)

19	Co-precipitation (Microwave assisted) 0Ag/PDC 5Ag/PDC 10Ag/PDC 15Ag/PDC 20Ag/PDC	600 °C/5 h	Printex-U; S/C 1:10; TC; r.t. to 650 °C at 10 °C/min in 100 ml/min of 21 % O ₂ /N ₂	24 27 28 33 10	422 388 394 388 395	-- -- -- -- --	Ag loading onto CePr oxide improved oxygen vacancies. The introduction of Ag into the Ceria lattice improved the reducibility on the surface of the catalyst. The Mars-van-Krevelen mechanism was followed for the soot oxidation in tight contact conditions.	(Govardhan et al. 2022)
20	Wet chemical method and impregnation method (equal volume) Cu@Ce Cu@Ag/Ce Ag/Cu Ag/Ce	500 °C/2 h	S/C 1:10; LC; r.t. to 700 °C at 5 °C/min at 100000 h ⁻¹ GSHV of 1 % O ₂ /N ₂ .	091.9 100.4 -- --	-- -- -- --	516 464 506 494	The core-shell structure establishes a secondary oxygen delivery channel. CuO core encapsulated by CeO ₂ polycrystals and onto Ag metallic NPs dispersed on CeO ₂ Abundant surface oxygen species are generated over the Cu@Ag/Ce catalyst through lattice and gaseous oxygen. Ag helps in the generation of O ⁻² species over surface oxygen species	(Wan et al. 2022)

2.3 Manganese doped Ceria and Manganese oxide

Ceria Manganese solid solution in various compositions have been reportedly used for oxidation/decomposition of CO (Zhang et al. 2013), soot (Venkataswamy et al. 2014), toluene (Liao et al. 2013), benzene (Chen et al. 2018), VOC (Azalim et al. 2011), ethanol (Li et al. 2011a), formaldehyde and ozone (Zhang et al. 2019). Mukherjee et al. (Mukherjee et al. 2016a) reported from their research that doping manganese in ceria promoted the soot oxidation activity by low binding energy of lattice oxygen, high concentration of surface active species and synergistic effect of ceria manganese redox couples.

He et al. (He et al. 2018a) reported the effects of repeated soot oxidation with the help of in-situ Raman on $Mn_{0.4}Ce_{0.6}O_{2-\Delta}$ catalyst, found a decline of soot oxidation activity after the 1st run was attributed to the irreversible segregation of a minute amount of Mn in the form of Mn_3O_4 and consequently decrease in the no. of surface active species (He et al. 2018a). Liang et al. (Liang et al. 2008) synthesized doped Cerium oxide samples by the citric acid method. A T_{50} temperature of 503 °C was reported for the Mn-Ce (10 mol % Mn and 90 mol % Ce) sample under loose contact conditions, attributing a ‘spillover’ mechanism for the enhanced soot oxidation activity.

Wu et al. (Wu et al. 2010) reported a T_{50} temperature of 463 °C for MnO_x - CeO_2 (15 mol % Mn and 85 mol % Ce) sample under loose contact conditions in a NO_x atmosphere. Venkataswamy et al. (Venkataswamy et al. 2014) prepared doped Cerium oxide by coprecipitation method. The highest soot oxidation activity was reported for $Ce_{0.7}Mn_{0.3}O_{2-\delta}$ with a T_{50} temperature of 392 °C for soot oxidation temperature under tight contact conditions, citing high synergy and redox capability coupled with weak Metal-Oxygen bond due to incorporation of Mn in the Cerium oxide lattice.

Wang et al. (Wang et al. 2020) reported in their work that adding Mn to Ceria improves its soot oxidation activity through the synergistic effect. Tikomirov et al., 2005 (Tikhomirov et al. 2006) and Wu et al. 2013 (Wu et al. 2013) reported the NO_x

assisted soot oxidation by Mn doped ceria. It was noticed that Mn doped Ceria had a high affinity to store nitrates on the surface and release the nitrates in the form of NO₂ at low temperatures. NO₂ is known to be a better oxidative agent than O₂ and thus reduces the soot combustion temperature. Tikomirov et al., 2005 (Tikhomirov et al. 2006) reported the poisoning effect of SO₂ on the catalytic activity due to less NO₂ yield. Wu et al. 2013 (Wu et al. 2013) investigated the synergistic effects between Ce and Mn and attributed the same to the redox nature of both Ce and Mn. The redox reactions yield active oxygen species that oxidize NO to NO₂ in the following reactions,



Where O* is the active oxygen species.

Table 2.3 lists out briefly Manganese doped Ceria soot oxidation catalysts synthesized by varied methods under varying conditions and precursors to achieve proper synergy between Ceria and Manganese oxides such that the combustion of soot occurs at as low a temperature as possible. Manganese oxides exist in multiple oxidation states and this property helps in producing lot more oxygen vacancies than those elements that do not exhibit multiple oxidation states. The very same reason is responsible for Manganese oxides used for multiple component oxidation as mentioned earlier. The size of Manganese atom is also quite smaller when compared to the Cerium atom, this induces lattice strain in the Ceria lattice if complete solid solution is formed. The lattice strain and oxygen vacancies in tandem will help in better oxygen ion mobility and transport through the lattice. Apart from the above benefits Manganese doping improves the NO_x storage capacity of the Ceria Manganese mixed oxides as nitrates at lower temperatures and also generates NO₂ by oxidation of NO (when NO is present in the feed gas). This tremendously helps in improving the soot oxidation activity of Manganese doped Ceria in both tight and loose contact conditions (especially true for loose contact conditions).

Table 2.3: Soot oxidation activity by Manganese doped ceria and Manganese oxide.

Sno	Samples	Calcination temperature	Soot used and conditions	Surface area (m ² /g)	T ₅₀ (°C)		Remarks	Reference
					Tight	Loose		
1	Citric acid sol-gel method CeO ₂ Mn-CeO ₂ (10:90) Cu-CeO ₂ (10:90)	500 °C/3 h	Printex-U; S/C 1:10; TC and LC 10% O ₂ in N ₂	61.8 68.4 72.5	390 368 356	553 503 522	The active surface oxygen species and lattice oxygen mobility improve with the addition of Mn and Cu, respectively.	(Liang et al. 2008)
2	Sol-gel method (Citric acid) CeO ₂ Mn-CeO ₂ (15:85) MnO _x	500 °C/3 h	Printex-U; S/C 1:10; TC; 500 ml/min of 1000 ppm NO/10% O ₂ in N ₂	63 96 22	445 384 441	-- -- --	Mn-CeO ₂ has a smaller crystallite size, higher surface area, and low-temperature redox capability. Also, the storage and further oxidation of NO _x species to NO ₂ and the formation of surface oxygen complexes help in soot oxidation activity.	(Wu et al. 2010)
3	Co-precipitation method Ce-Mn (70:30)		Printex-U; S/C 1:4; TC air	58	392	--	Doping transition metals curbs the crystallite growth. A strong synergistic effect between Mn and Ce is responsible	(Venkataswamy et al. 2014)

Ceria-Manganese Mixed Oxides as Catalyst for Soot and CO Oxidation Activity.

	Ce-Fe (70:30) CeO ₂	800 °C/5 h		55 41	512 587	-- --	for better soot oxidation activity by virtue of more defects, improving oxygen vacancies and transport, and better redox properties.	
4	Hydrothermal (CeO ₂ Nanocubes) and wet impregnation (Mn precursor soln.) CeO ₂ MnO _x /CeO ₂	500 °C/4 h	Printex-U; S/C 1:4; TC; r.t to 1273 K at 10 K/min in 100 ml/min of air	30 37	450 387	-- --	CeO ₂ Nano cubes have a high defect plane (100) more exposed. Multiple oxidation states of Mn help in the effortless redox behavior at lower temperatures Interface sites have a wide influence over the redox properties and, in general, activity of the catalyst. Well-dispersed manganese oxide over Ceria nano cubes further improves the already high synergistic effects between both the metal oxides.	(Putla et al. 2015)

							Diverse nanostructures imbibe the catalyst with beneficial catalytic activity by enhancing favorable parameters such as oxygen vacancies, contact points, redox properties, and reducibility.	
5	Surfactant-assisted colloidal crystal template $Mn_xCe_{1-x}O_2$ and $Mn_xCe_{1-x-0.1}Nd_{0.1}O_2$ ($0.1 \leq x \leq 0.5$), MnO_x and CeO_2	550 °C/4 h & 800 °C/12 h for aged catalyst	S/C 1:10; LC; Printex-U 10% O ₂ in N ₂ & 1000 ppm NO in 10% O ₂ in N ₂	57.22 53.49	$Mn_{0.3}Ce_{0.69}Nd_{0.01}O_2$ with 307 °C & 331 °C in the presence & absence of NO. $Mn_{0.3}Ce_{0.7}O_2$ with 353 °C & 328 °C in the presence & absence of NO.	Doping Nd has a double effect of improving oxygen vacancies and better-sintering resistance during aging. Mn solubility is a maximum of 30%, and doping Mn improves the redox behavior of the catalyst.	(Tang et al. 2018)	
6	citric acid complex method $Ce_{1-x}Mn_xO_{2-\Delta}$ (x=0, 0.1, 0.2, 0.3, 0.4, 0.5, 0.6, 1)	550 °C/5 h	Printex-U; S/C 1:9; LC; diluted with silica; 10% O ₂ /Ar	125.2	299 °C for $Ce_{0.6}Mn_{0.4}O_{2-\delta}$.	Doping Mn favored Oxygen vacancies and improved redox behavior. Intrinsic Oxygen Vacancy (IOV) and Frenkel Oxygen Vacancy (FOV) were critical in the role of improving the soot oxidation activity.	(Xueting et al., 2018)	

Ceria-Manganese Mixed Oxides as Catalyst for Soot and CO Oxidation Activity.

							IOV creates the oxygen vacancy in the lattice by means of the escape of interstitial oxygen (in octahedral voids) to the surface, thus creating voids. FOV is formed due to Oxygen anions migrating to the interstitial voids (octahedral voids).	
7	Citric acid complex method Ce _{0.6} Mn _{0.4} O _{2-Δ} for repeated soot activity 1 st run 2 nd run 3 rd run	550 °C/5 h	Printex-U S/C 1:9; LC; diluted with silica; 10% O ₂ /Ar	89.08 (fresh) 58.07 55.25 52.58	-- -- --	-- 307.7 323.5 323.3	Sintering is observed after the very 1 st run, and the Mn ₃ O ₄ phase segregates. Sintering reduces surface area and active surface oxygen and promotes growth in crystallite size. Frenkel type oxygen is said to be spectators and participatory.	(He et al. 2018)

							The participatory type is regenerated after every soot oxidation run, but the spectator type doesn't get regenerated.	
8	Co-precipitation method Mn/(Mn + Ce) = 0, 0.05, 0.1, 0.2, 0.3, 0.4, 0.5 with Ag loading in the range of 3 to 4 wt %	500 °C/5 h	Printex-U, LC, S/C 1:10 with 0.1%NO/5% O ₂ balanced with Ar	63	AgCe _{0.9} Mn _{0.1} O _{2-δ} : 321 °C		Redox properties improvement of ceria is due to doping Mn and Ag. AgCe _{0.9} Mn _{0.1} O _{2-Δ} had high surface and bulk oxygen vacancies. The stability of AgCe _{0.9} Mn _{0.1} O _{2-Δ} is attributed to the effective incorporation of Ag ⁺ ions in the ceria lattice, increasing not only the surface-active oxygen but also the improved redox capability of the catalyst.	(Li et al. 2019)
9	Solvothermal method α -Mn ₂ O ₃ -Cubic (C)	500 °C/5 h	LC; S/C 1:10; 5% O ₂ , 0.25% NO in N ₂ .	30.3	--	435	α -Mn ₂ O ₃ -C has (001) facet with higher uncoordinated surface Oxygen sites, enabling better redox capability and oxidation of NO to NO ₂ , a powerful	Cheng et al. 2017

	α -Mn ₂ O ₃ - <i>Octahedral Truncated</i> (OT)			02.5	--	494	oxidant that decreases the soot combustion temperature. The kinetic study supports the idea that exposed crystal facets have a major role in soot oxidation activity compared to only having a higher surface area.	
	α -Mn ₂ O ₃ - <i>Octahedral</i> (O)			01.0	--	540		
10	Inverse micelle templating method Meso-Mn-A Meso-Mn ₂ O ₃ Meso-MnO ₂	450 °C/1 h	Printex-U; LC; Ar+10% air & Ar+10% air+1000 ppm NO ₂	165 088 094	442 334 (NO ₂) 436 323 (NO ₂) 355 305 (NO ₂)	Mesoporous MnO _x has 100% selectivity for CO ₂ . Mesoporous MnO _x has good redox behavior and is good at storing NO ₂ in the form of surface nitrates that reduce the ignition temperature of the soot. NO ₂ is a more powerful oxidant than O ₂ and helps in low-temperature soot ignition and combustion.	(Wasalathanthri et al. 2017)	

	Meso-OMS-2			150	358 316 (NO ₂)			
11	Co-precipitation method Mn ₃ O ₄ - <i>Octahedral Nano Plates</i> Mn ₃ O ₄ -Nano Particles Mn ₃ O ₄ -Hex Nano plates (HNS)	500 °C/3 h	LC; S/C 1:10; 2500 ppm NO+5% O ₂ +N ₂ (vol%)	28.5 08.6 18.6	-- -- --	427.8 454.6 407.7	Mn ₃ O ₄ -HNS had superior low-temperature reducibility, abundant surface reactive oxygen species, and high NO oxidation comparatively. This activity is also ascribed to the exposed (112) & (101) facets of Mn ₃ O ₄ -HNS. NO oxidation to NO ₂ is the key to reduction in the soot combustion temperatures as NO ₂ is a more powerful oxidant than O ₂ .	Men et al., 2019
12	Hydrothermal method Soot CeO ₂	600 °C/5 h	Printex-U; LC; S/C 1:9; 200 to 700 °C at 2 °C/min in		O ₂ 581 491	NO 582 467	Synergistic interaction between the trepang Ce and nano rod MnO ₂ responsible for better redox activity,	(Feng et al. 2020)

Ceria-Manganese Mixed Oxides as Catalyst for Soot and CO Oxidation Activity.

	MnO ₂ CeO ₂ @MnO ₂		5% O ₂ /N ₂ and 500 ppm NO in 5% O ₂ /N ₂ .		447 403	411 373	resulting in augmented active oxygen species. Soot-catalyst contact is vastly enhanced by the trepang morphology and nano rod structure on it.	
12	Hydrothermal synthesis of Mn _x Ce _{1-x} O ₂ (x = 0, 0.02, 0.06, 0.09, 0.13, and 0.17) Mn _{0.00} Ce _{1.00} O ₂ Mn _{0.02} Ce _{0.98} O ₂ Mn _{0.06} Ce _{0.94} O ₂ Mn _{0.09} Ce _{0.91} O ₂ Mn _{0.13} Ce _{0.87} O ₂ Mn _{0.17} Ce _{0.83} O ₂	500 °C/2 h	0.6 cm dia. quartz tube, LC, S/C 1:10; 80 ml of 0.05% NO/5.0% O ₂ /N ₂ ; 300 to 650 °C at 2 °C /min	53 57 74 68 65 64	-- -- -- -- -- --	521 508 495 481 501 515	Addition of Mn into Ceria drastically improves catalytic activity by heightened redox capability, active oxygen species due to synergistic effects of Mn doping into Ceria. Mesoporous materials possess tremendous exterior surface area and reactive sites compared to internal surface area.	(Wang et al. 2020)

							NO _x storage and oxidation ability of Mn doped samples were very much high compared to the undoped one.	
13	Hydrothermal method CeO ₂ MC-0.05 MC-0.10 MC-0.15 MC-0.20 MC-0.25 MC-0.30 MC-0.35 MC-0.40 MC-0.40used MC-0.45	550 °C/3 h	LC; 100 ml/min of 10% O ₂ /N ₂ and 500 ppm NO in 10% O ₂ /N ₂ ; 45 °C to 800 °C at 10 °C/min.	-- -- -- -- -- -- -- -- -- -- --	T _p (O ₂ /N ₂) 615 620 625 615 608 569 597 600 565 578 596	T _p (NO) -- 602 505 507 472 484 387 352 340 -- 578	Mn doped samples perform well in the presence of NO, as they can store NO as nitrates and also oxidize NO to NO ₂ , which is a powerful oxidant. The presence of ash in soot severely degrades the catalytic activity of the catalyst. They delay soot combustion by increasing the soot ignition temperature and decreasing the reaction rate. The suitable soot to catalyst ratio was reported to be 1:9 to 1:13 for lowering the soot combustion temperature.	(Yang et al. 2022)

14	Hydrothermal and impregnation method None CeO ₂ Mn _{0.03} Ce _{0.97} O ₂ Mn _{0.19} Ce _{0.81} O ₂ Mn _{0.32} Ce _{0.68} O ₂	300 °C/3 h	Printex-U; LC; S/C 1:10; 10% O ₂ /N ₂ ; 350 to 650 °C.	--	--	550 393 376 356 362	The soot-catalyst contact due to the morphology of the catalyst rendered a crucial role in improving the soot oxidation activity. Apart from contact, the formation of active oxygen species by adsorption and activation on the surface of the catalyst also played a key role in improving the soot oxidation activity.	(Zhu et al. 2022a)
15	Coprecipitation method Blank Ce _{0.16} Mn _{0.84} Ce _{0.43} Mn _{0.57} Ce _{0.64} Mn _{0.36} Ce _{0.80} Mn _{0.20} Ce _{0.94} Mn _{0.06} CeO ₂	600 °C/3 h	Printex-U; TC; S/C 1:10; 500 ml/min of 10 vol % O ₂ /Ar; 200 to 700 °C at 5 °C/min.	--	578 333 316 306 310 328 354	-- -- -- -- -- -- --	The highly dispersed Manganese oxide formed due to partial solid solution is the leading factor for improvement in the soot oxidation activity. Porosity is observed when complete solid solution is formed and are absent when phase separation occurs. Contact points are lost in phase separation leading to reduction in catalytic activity.	(Zhu et al. 2022b)

							<p>External surface area favorable than pores, since diameter of the soot particles are greater than the pore.</p> <p>After the active oxygen species reaches a threshold value on the surface of the catalyst, their role reduces in improvement of the soot oxidation activity.</p>	
--	--	--	--	--	--	--	---	--

2.4 Soot oxidation by structured catalysts

Structured catalysts are extensively used for heterogeneous catalysis, specifically catalytic reactions involving gaseous or vapor phase reactants (Zhou et al. 2010). The monolithic supports conventionally are made from Zeolites, Cordierite, Silicon Carbide, and also metal substrates. These metal supports can be made into any shape as required. The advantages of using structured catalysts are, low pressure drop across the catalyst (unlike fixed bed catalysts or catalysts in the form of pellets, where the pressure drop across the bed is high), considerably better mass transfer, and better mechanical strength compared to pelletized catalysts. Cordierite has been used extensively as an automotive exhaust catalyst support material for its superior thermal stability at elevated temperatures, relatively very low Coefficient of Thermal Expansion (CTE) (El-Shobaky et al. 2011), low-pressure drop, and superior mechanical strength (Yuan et al. 2016) (Chae et al. 2021). Structured catalysts can be synthesized broadly in two ways: (1) Coating monolithic supports with catalyst by using an appropriate coating technique, (2) Extruding the catalyst as a monolith. The ease of fabrication and robust nature of the monolithic supports for the structured catalysts make it more attractive to be used for various catalysis reactions in industries

Structured catalysts using cordierite as a substrate have been reported in the oxidation of soot (Nascimento et al. 2016, 2018; Nascimento and Serra 2016; Neyertz et al. 2014; Stegmayer et al. 2022; Tang et al. 2019), NO_x (Zhou et al. 2015) (Tang et al. 2021), CO (Yuan et al. 2016) (Yan et al. 2013), CO-PROX (Gómez et al. 2012) (Gómez et al. 2011), VOC (Azalim et al. 2013; Deng et al. 2018; Lu et al. 2011; Tiscornia et al. 2020; Zhu et al. 2018), toluene (Gómez et al. 2014; Huang et al. 2012; Patil et al. 2020; Zhu et al. 2019), Chlorobenzene (Kan et al. 2017) (Zhu et al. 2019), benzene (Li et al. 2014), n-hexane (Díaz et al. 2020). **Table 2.4** gives a brief literature review of Structured catalysts used for soot oxidation reactions. The table lucidly explains the various aspects of the methodology, experimental procedure and the important inferences from the reported open literature.

Table 2.4: Soot oxidation by using structured catalysts.

Sno	Monolith material and coated catalyst	Dimensions of the reactor/tube and conditions	Soot loading and drying conditions	Best T ₅₀ (°C)	Inferences	reference
1	Hydrothermal process for in-situ production of ZnO, K, K/ZnO on Aluminium Titatante (AT), SiC, and Cordierite (Cor)	Φ = 8 mm; 100 mL/min of 5% O ₂ /He at 5 °C/min from 100 to 700 °C	Soot (Printex-U (Degussa)) dispersed in ethanol (10 min ultrasonication), drying overnight at 50 °C; after drying, cut into pieces and pretreated in He flow (100 ml/min) at 200 °C;	K/ZnO/Cor : 414 °C	ZnO nano-rods (uniformly and densely distributed) helped in better dispersion of K and soot, thereby improving the soot oxidation activity. Dispersion of K was critical in reducing the soot combustion temperature. K/ZnO/Cor had the best dispersion and CO ₂ selectivity among all other coated catalysts.	(Zhang et al. 2023)
2	Hydrothermal in-situ CeO ₂ nanofiber	Φ = 16 mm; 20 mL/min of 0.1% NO, 18% O ₂ /He at 5	10 s dipping in 600 ppm n-hexane soot (obtained from burning commercial	CeO ₂ nanofibers on	The amorphous portion of the carbon in soot oxidized more easily than the graphitic part.	(Stegmaye r et al. 2022a)

Ceria-Manganese Mixed Oxides as Catalyst for Soot and CO Oxidation Activity.

	synthesis on cordierite	°C/min from 200 to 600 °C	Diesel fuel) dispersion; Drying at 80 °C/24h	monolith M2: 428 °C	<p>Nanofiber morphology augments the soot-catalyst contact points, thereby improving the soot oxidation activity.</p> <p>High-temperature runs caused the sintering of the nanofibers.</p> <p>Successive runs up to 800 °C caused a slight reduction in the soot oxidation activity due to some hot spot formation at high temperatures.</p>	
3	Molten salt synthesis over cordierite	Cordierite ($\phi = 20 \text{ mm}$, $L = 110 \text{ mm}$); 25 °C to 750 °C at 9.6 °C/min	Atomizing soot (Carbon powder) ethanol in a flow of N ₂ (100 ml/min) and depositing on the monolithic catalyst.	$T_m \sim 490 \text{ °C}$	<p>The rugged interface of the potassium titanate whiskers improved the soot entrapping ability, i.e., ample soot-catalyst contacts.</p> <p>The structured catalysts were stable, with a slight increase in T_m of 23 °C after 5 consecutive TPO runs.</p>	(Du et al. 2021)

4	Hydrothermal and wet impregnation method on three-dimensional microporous (3-DM) Ni foam (nanosheets) substrate. Co-NS, Mn-NS, and Fe-NS and by wet impregnation of K on Co-NS, Mn-NS, and Fe-NS.	$\Phi = 8$ mm; 100 ml/min of 0 to 600 ppm NO 10% O ₂ /N ₂ ; 200 °C to 700 °C at 2 °C/min	Soot (0.5 mg/1 ml ethanol) ultrasonicated for 2-3h, 2 ml of dispersion dropped on prepared catalyst; Drying at 120 °C/6h	KCo-NS: 390 °C (without NO) and 333 °C (with NO)	The loading of transition metals on 3-DM Ni foam (nanosheets) reduced the T ₅₀ temperature for soot oxidation. Further decrease in the T ₅₀ was observed with the loading of K on the nanosheets loaded with metal (Mn, Fe, and Co) oxides. Potassium interacts better with Cobalt oxide and Ferrous oxide than Manganese oxide. KCo-Ns has the best NO _x oxidation and redox capabilities; it also has an ample amount of surface oxygen species comparatively.	(Cao et al. 2021)
5	Hydrothermal method synthesis for cobalt oxide	Fixed bed reactor; 100 ml/min of 10%	15 mg of Degussa model soot dispersed in 25 ml of ethanol;	8Co/Mn-NR: 487 °C (absence of	Macroporous voids benefit soot-catalyst contact characteristics. A fourfold increase in the contact area was observed.	(Yang et al. 2021)

	decorated Manganese Octahedron Molecular Sieves-2.	O ₂ /N ₂ (or) 600 ppm NO/10% O ₂ /N ₂ ; 600 ppm NO/10% H ₂ O/10% O ₂ /N ₂	soot suspension was injected into the channels using a pipette gun. Nothing was mentioned about drying conditions	NO and H ₂ O), 383 °C (absence of H ₂ O), 378 °C	The thickness of the coating was achieved by using 13 times less powder than conventionally prepared powder catalysts. The addition of Co to the Mn-NR OMS-2 increased the active sites by 3 times.	
6	Hydrothermal method on three-dimensional microporous (3-DM) Ni foam (nanosheets) substrate. Co-NS, Mn-NS, and Fe-NS	Φ = 8 mm; 100 ml/min of 0 to 600 ppm NO, 5% O ₂ /N ₂ ; 200 °C to 700 °C at 2 °C/min	2 ml of soot (printex-U Degussa) dispersion (0.5 mg/1 ml ethanol) dropped on the prepared catalyst. Gravity contact method; Drying at 60 °C/2h	Co-NS: 462 °C (0 ppm NO), 391 °C (600 ppm NO)	SEM images of Ni foam display linked macroporous structure. The macroporous structure of synthesized catalyst-loaded nanosheets improved the soot catalyst contact. NO at low temperatures (<330 °C) readily oxidized to NO ₂ . NO ₂ oxidizes the soot efficiently.	(Cao et al. 2017)

					<p>At higher temperatures (330 to 450 °C), soot oxidation was done by NO₂ (when NO was used) and active oxygen species.</p> <p>Co-NS had the best/highest redox properties, surface vacancies, active oxygen species, the capability of oxidizing NO to NO₂, and microporous structure to facilitate mass transfer.</p>	
7	<p>Direct impregnation method</p> <p>AC, Ce/AC, Mn/AC and Ce/Mn/AC</p>	<p>Φ = 23 mm;</p> <p>1000 cm³/min of air; r.t. to 500 °C at 25 °C/min.</p>	<p>10 wt% carbon black in ethanol, 30 s dip, excess suspension eliminated using centrifugation at 400 rpm, three immersions done; Drying at 120 °C/1h</p>	<p>Ce/Mn/AC: ~ 350 °C</p>	<p>Doping Mn into Ce improved the redox properties, active oxygen species, and acidity of the surface by means of synergy between Ceria and Manganese oxides.</p> <p>Multiple oxidation states of Mn had a prominent effect on the soot oxidation activity.</p>	<p>(COLMA N-LERNER et al. 2016)</p>

8	Modified dip coating (<i>forced circulation of suspension into channels using a peristaltic pump</i>)	Catalytic filter ($\phi = 1\text{ cm}$, $L = 3\text{ cm}$); 50 ml/min of 500 ppmv NO and 5% O ₂ /Ar at 5 °C/min from 250 °C to 650 °C	1 min dipping in a continuously stirred Model soot (<i>Elftex 430 Cabot</i>) dispersion (0.2g/100 ml of n-pentane); Dried at 65 °C/1h.	FeK/DL: ~ 500 °C (NO+O ₂)	The morphological characteristics of the coated catalyst layer depended upon the type of alumina wash-coat precursor used. The diffusion of potassium in a favorable morphology enhances the soot oxidation activity.	(Ascaso et al. 2014)
9	Sol-Gel modified method for CeZr. Slurry dip coated on cordierite and impregnated with K by dipping in KNO ₃ soln.	4% O ₂ /N ₂ at 12 °C/min from 200 to 700 °C	1 s dip in vigorously stirred in soot (obtained from burning diesel fuel) methanol suspension (7g/L)	M6 (K/CeO ₂): 425 °C (1 st run) to 531 °C (10 th run) M2(K/Ce _{0.65} Zr _{0.35} O ₂): 436 °C	The presence of K improved the soot oxidation activity, but deactivation of the catalyst was observed after 10 TPO runs due to the loss of K by sublimation. The initial very high loading of K in M2 helped it perform better and improve its soot oxidation activity at the 10 th TPO despite having the highest K weight loss percentage.	(Neyertz et al. 2014)

				(1 st run) to 414 °C (10 th run) M5(CeO ₂): 521 °C (1 st run) to 483 °C (10 th run)	The catalyst without K initially had modest activity, but the catalyst was activated after 10 TPO runs due to the beneficial restructuring of the coated microstructure.	
10	Sol-gel synthesis method, Fe/Al ₂ O ₃ , K/Al ₂ O ₃ , Fe/K/Al ₂ O ₃ Calcined at 450 and 650 °C on the cordierite monolith.	Catalytic filter (φ = 1 cm, L = 3 cm); 50 ml/min of 500 ppmv NO and 5% O ₂ /Ar at 5 °C/min from 250 °C to 650 °C	1 min dipping in a continuously stirred Carbon black (Elftex 430 Cabot) dispersion (0.2g/100 ml of n-pentane); Dried at 65 °C/1h.	FeK450_M: 510 °C (NO+O ₂)	The role of K (alkali metal is to enhance the soot and active sites on the catalyst. Calcination temperature influences the type of carbonate species present. At 450 °C, KNO ₃ species are present, and at 650 °C, K ₂ O species are present that become K ₂ CO ₃ when exposed to atmospheric air. Iron oxide improves the selectivity of CO ₂ for soot oxidation.	(Gálvez et al. 2014)

11	Dip coating from ZrO ₂ colloidal soln. for wash-coat and acetates of the Co, Ba, and K for active metals	20 ml/min of 18% O ₂ /He and 0.1% NO in 18% O ₂ /He at 5 °C/min from 250 to 600 °C.	1 min immersion in the soot suspensions (600, 3000, and 10000 ppm of soot in Hexane) and blow-dried at room temperature, 10000 ppm was chosen for soot oxidation as it gave a sharp peak.	Co, Ba, K/ZrO ₂ 400 °C. (0.1 % NO)	Utilization of higher concentration soot suspension yielded a sharper TPO profile with distinct maxima. The active components formed Barium carbonate, Potassium Nitrate, and Co ₃ O ₄ spinel on the channels of cordierite. Excellent adherence was achieved with not much change in the microstructure of the coated cordierite when compared to the bare cordierite.	(Banús et al. 2013)
12	Dip coating technique of K, Cu, V, and Co containing active metals in Al ₂ O ₃ suspension.	50 ml/min of 500 ppmv NO and 5% O ₂ /Ar at 5 °C/min from 250 °C to 650 °C	1 min dipping in a continuously stirred dispersion of Carbon black in 0.2g/100 ml of n-pentane. Dried at 65 °C/1h	Co-K catalyst	Higher viscosity suspensions resulted in thicker layers with cracks and holes. NO _x adsorption at low temperatures (250 to 425 °C) was observed in all catalysts.	(Gálvez et al. 2013)

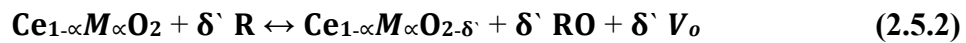
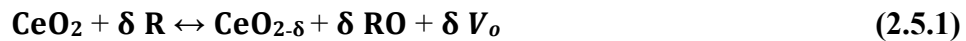
					Co-K generated higher amounts of NO ₂ , which is a powerful oxidizer.	
13	Impregnation method.	6% O ₂ /N ₂ at 12 °C/min from 100 to 600 °C.	Immersing monolith in soot (obtained from Burning commercial diesel fuel) suspension (Methanol) to obtain 1 mg of soot over 0.2 g monolith section.	K(from KNO ₃)/CeO ₂ or M ₂ : 443 °C	<p>K improves the soot-catalyst contact.</p> <p>Surface basicity is a critical factor for the interaction of active species. High basicity discourages the adsorption of gaseous oxygen onto the catalyst surface.</p> <p>The precursors of the potassium, according to the increasing order of soot oxidation activity, are KOH<K₂CO₃<KNO₃.</p> <p>A decrease in the Potassium content due to higher temperatures (>600 °C) causes a reduction in the soot oxidation activity.</p>	(Neyertz et al. 2012)
14	Dip coating of the wash-coat followed by	φ = 52 mm; 50 ml/min of 0.2 % NO in 5% O ₂ /Ar	Impregnation of soot (Printex-U	LaKCoO ₃ /γAl ₂ O ₃ /Cordierite:	γ-Al ₂ O ₃ wash coating on monoliths gives good adhesion to catalyst coating, negating the usage of binders.	(Tang et al. 2020)

	impregnation of active metals in their aqueous phase.	or 5% O ₂ /Ar at 2 °C/min from 100 to 700 °C	(Degussa)) from ethanol suspension.	314.6 °C	The usage of a one-step method wherein the catalyst was coated onto the cordierite without wash-coat resulted in poor adherence and uneven distribution of the catalyst in the channels/walls. γ-Al ₂ O ₃ wash-coat helps in improving the active component dispersion over a large surface area, thereby increasing the possibility of having more active sites. The result of this positively affects the soot oxidation activity.	
15	Dip coating of colloidal suspension of Ceria	φ = 2.54 cm; 47 L/h, 15 % O ₂ /N ₂	SiC (φ =1.3 cm; L = 3 cm) dipped in the soot (Printex-U (Degussa)) suspension (1g/100 ml of heptane), time varied to get	Catalyst to soot ratio of 98 (w/w): 525 °C	Soot, when loaded in loose contact, comes into contact with the catalyst in two modes: (1) internal zone, wherein the soot is in the crevices and pores of the catalyst, (2) external zone, wherein the soot forms a cake like layer on top of the catalyst.	(Di Sarli et al. 2016b)

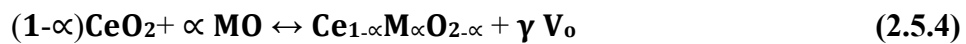
			different loading of soot; Dried for 1h at room temperature.		Thermal regeneration favors the selectivity of CO more than CO ₂ and catalytic regeneration vice-versa. For thermal regeneration, low catalyst-to-soot ratios are responsible, and for catalytic regeneration, high catalyst-to-soot ratios are responsible.	
--	--	--	--	--	--	--

2.5 Soot oxidation mechanism

Ceria loses the lattice oxygen and reduces itself to Ce^{3+} in reducing atmospheres with simultaneous formation of oxygen vacancy. This vacancy can travel or be mobile, leading to an interesting phenomenon of oxygen storage, transport, and release. Therefore, theoretically, by increasing these point defects, i.e., by doping, etc., the no of oxygen vacancy increases, prompting more oxygen mobility and Oxygen Storage Capacity (OSC), given that the following conditions are met, They being: (1) the chemical modification doesn't considerably diminish the no of active redox sites (2) defect concentration more than a particular threshold hinders the mobility of ions and diminishes thermal stability. (Trovarelli 1999)



Eq. 2.5.1 is the general mechanism wherein a reductant (R) reduces Ceria by oxidizing itself as RO, thereby creating an oxygen vacancy V_o . Eq. 2.5.2 is the expression when an iso-valent dopant (M) is added to the ceria lattice.

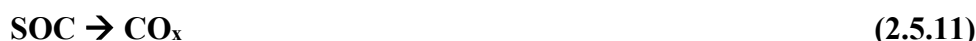


Divalent and Trivalent dopants in ceria introduce the oxygen vacancies due to charge compensation for incorporation of alien/foreign tri and divalent atoms into ceria lattice and are represented in Eq. 2.5.3 and Eq. 2.5.4 respectively (Trovarelli 1999). The soot oxidation mechanism includes spillover/active oxygen mechanism and NO_2 -assisted soot oxidation (Bueno-López 2014). In the spillover mechanism, the gaseous oxygen in the exhaust stream gets adsorbed onto the surface vacancy of the catalyst and becomes O_2^- species, which will then transfer onto the soot and oxidize it as seen in Eq. 2.5.5 to 2.5.7 (Zhu et al. 2017b)





In the NO₂-assisted soot oxidation mechanism, the catalyst oxidizes the NO present in the exhaust stream, and some of it forms nitrates on the surface of the catalyst. NO₂ is known to be a better oxidant than O₂ and will come in contact with soot in the gas phase and on the surface of the catalyst and oxidize the same. At higher temperatures, nitrates decompose to give NO₂, which helps in the oxidation of soot. The following reactions as shown in Eq. 2.5.8 to 2.5.11, occur in the NO₂-assisted soot oxidation mechanism (Zhu et al. 2017b)



2.6 CO Oxidation

From the literature, it is reported that a wide variety of materials have been used for CO oxidation. It is reported that Platinum group elements have been utilized for the CO oxidation. The Oxidation of CO has been done by using gold clusters supported on the oxides of Ce, La, and Zr (Russo et al. 2006). Gold with Zinc oxide support has also been reported to have been used for Co oxidation (Carabineiro et al. 2010). Ceria, as support for Au, has also been reported to be used for such catalytic activity (Tana et al. 2011). There has been research reported wherein Ceria doped with some transition and lanthanide group of metals such as Cu, Ti, Zr, Tb, Pr, Sm, Eu (Falcón et al. 2000) (Liu et al. 2010). Manganese doping with Ceria to improve its activity has been reported in the literature (Chang et al. 2007) (Mukherjee et al. 2016c) (Venkataswamy et al. 2015a) (Guo et al. 2016).

Soliman et al., 2019 (Soliman 2019) in his review explained lucidly the various factors that might affect the CO reaction over nanosized materials. The factors were

elucidated as follows (Soliman 2019),

- The CO oxidation catalyst must have high selectivity and high resistance to deactivation by H₂O and CO₂.
- Metal oxide nanoparticles were suitable and favorable for CO oxidation.
- The crystal size of the catalyst had a say in the CO oxidation activity. The activity increased with a decrease in the crystal size of the catalyst up to an extent, and a further decrease in the crystal size diminishes the CO oxidation activity.
- The synthesis method has an effect on the CO oxidation activity due to the varied surface area and dispersion of the nanoparticles obtained by different synthesis methods.

Some of the CO oxidation activity by various catalyst are tabulated in **Table 2.5**. The table explicitly explains the synthesis method utilized to obtain the different compositions of catalyst for CO oxidation, the experimental parameters, the T₅₀ temperature of the best performing catalysts, and briefly the inferences reported in the open literature. Ceria, doped Ceria, transition metal oxides, Three Dimensionally Ordered Macro porous catalysts, and rare earth metal oxides have been used for CO oxidation catalysts. Engineered or tailored catalysts have also been reported for CO oxidation, for example nano rod, nano cubes and in Octahedron morphologies of Ceria. The main aim of the researchers was to induce the catalyst to expose the comparatively higher active planes to reduce the T₅₀ temperature for the CO oxidation. The aim of the researchers is to bring down the T₅₀ temperature as much possible, preferably to the ambient temperatures (through the usage of Platinum Group Metals (PGM)) using non-PGM catalysts. The reduction in activation can be achieved by tailoring defects that favor the formation of active sites, production of active oxygen species, oxygen ion transport through the lattice of the catalyst and OSC to name a few. This particularly is beneficial for the automotive industry as the cold start emissions can be reduced or all together avoided. Apart from good catalytic activity the CO oxidation catalysts should good thermal stability, selectivity, and resistance to catalyst poisoning due to the presence of other pollutants and contaminants in the exhaust stream of the automobile.

Ceria-Manganese Mixed Oxides as Catalyst for Soot and CO Oxidation Activity.

Table 2.5: CO Oxidation activity by Ceria based materials.

Sno	Synthesis method	Conditions	Dimensions	T ₅₀ (best)	Inferences	reference
1	Precipitation CA, CB, and CC methods of preparing Ceria.	27<T<827 °C; 100 ml/min; 10 K/min; 2% CO, 1% O ₂ /N ₂ ; 100 ml/min; GSHV = 2 x 10 ⁵ h ⁻¹	Dia. :6 mm; L: 300 mm	CA473: 317 °C	The mechanism is Mars-Van Krevelen Mechanism is the prevalent mechanism. More oxygen vacancies are formed in (220) and (200) planes, and they are more reactive than (111).	(Aneggi et al. 2005)
2	Hydrothermal Ce _{0.9} M _{0.1} O _{2-δ} (M= Y, La, Zr, Pr, Sn)	50 mg catalyst; 150 to 400 °C; 2% CO, 1% O ₂ 95% N ₂ ; 50 ml/min	--	CeSnO: 205 °C	Mesoporous structure improves CO oxidation activity. Variable valency improves CO catalytic activity.	(Xiao et al. 2009)
3	Microwave-assisted gel combustion: LaMnO	0.1 g catalyst; 6.0 mol% CO 0.2 mol % C ₃ H ₈ in 10% O ₂ /N ₂ ; 50 ml/min (sccm)	Dia.: 7.0 mm ID	LaMn _{1.2} O _{3+δ} : 120 °C	The formation of separate highly dispersed amorphous phases of MnO _x enhances activity. Increased oxygen vacancies also improve catalytic activity.	(Esmaciln ejad-Ahranjani et al. 2011)
4	Microemulsion method used for CeFe series (Fe	80 mg catalyst, 100 μm < φ < 200 μm, R.T. to 400 °C, 5 °C/min; 3.4 vol% CO &	U-shaped quartz reactor	CeFe10: 205 °C	Substitution of Ce ⁴⁺ with Fe ³⁺ produced Oxygen vacancies. The synthesis method gives a better homogenous solid solution, resulting in better Ce-Fe interactions.	(Laguna et al. 2011)

Ceria-Manganese Mixed Oxides as Catalyst for Soot and CO Oxidation Activity.

	doping 0, 5, 10, 25, 50 and 100)	21 vol% O ₂ /He at 42 ml/min;				
5	Hydrothermal method: Ceria (rods, cubes and octahedron)	50 mg catalyst diluted with quartz sand; r.t. to 400 °C at 1 °C/min; 30 ml/min of 5% O ₂ /He + 10 ml/min 2% CO/2% Ar/He; O ₂ :CO = 7.5	U-shaped quartz tube (4 mm i.d.)	Ceria nano rods: 287 °C	{110} and {100} are more reactive towards CO oxidation than {111} Reducibility and lattice oxygen mobility follow the trend: rods>cubes>octahedra.	(Wu et al. 2012)
6	Glycine Nitrate Process (SCS) Ce _{0.75} Zr _{0.25} O _{2-δ} & Ce _{0.65} Zr _{0.25} RE _{0.1} O _{2-δ} (RE = Tb, Gd, Eu, Sm, Nd, Pr and La	100 mg of catalyst; 25 to 500 °C at 5 °C/min at 60 ml/min of 50 % CO & 50 % O ₂	Fixed bed reactor	Ce _{0.65} Zr _{0.25} Pr _{0.1} O _{2-δ} : 208 °C	The RE doped solid solution had more oxygen vacancies due to defective structure formation. Pr doped CZ had enhanced surface reduction at comparatively low temperatures, enabling augmented Oxygen mobility.	(Prasad et al. 2012)
7	Incipient wetness impregnation method (5%)Cu/CeO	100 mg catalyst (0.12 to 0.15 mm); 1% CO, 1% O ₂ in N ₂ ; 80 ml/min;	Tubular quartz microreactor 6 mm i.d.	CuO/Ce ₁ O ₂₄₋₅ : 95 °C	Synergistic effects between CuO and the Cu/CeO ₂ solid solution improved oxygen vacancies and reducibility of the catalyst for the formation of active oxygen species.	(Jia et al. 2012)

	calcined at different temperatures	48,000 ml $g_{cat}^{-1}h^{-1}$			The reaction pathway followed the Mars-Van-Krevelan mechanism.	
8	Incipient wetness impregnation method: CuO/MnO ₂	50 mg catalyst; 1% CO in 99% dry air; 20 ml/min; 24,000 ml $g_{cat}^{-1}h^{-1}$	Fixed bed flow reactor	1 to 40 % CuO/MnO ₂ : 60 °C MnO _x 350: 110 °C	The interface between the CuO and Mn is the active site for CO oxidation. The interfacial reaction mechanism is the proposed CO oxidation pathway.	(Qian et al. 2013)
9	Coprecipitation method (Ce _{0.7} Mn _{0.3} O _{2-δ}) CM	100 mg of catalyst+quartz particles; 9.98 % CO, 10.2% O ₂ in Ar; 27 to 500 °C at 5 °C/min	Reactor 2 mm i.d. 250 mm length	CM773K: 117 °C	Doping Mn into Ceria increased Oxygen vacancies. Synergistic Mn-Ce interactions, redox behavior, and highly dispersed MnO _x species were responsible for high CO oxidation activity.	(Venkataswamy et al. 2015)
10	Coprecipitation method (CZ(8:2), CL(8:2), CP(8:2), CH(8:2), CM(8:2), CF(9:1))	100 mg catalyst (250-355 μm sieve fraction) diluted with similar size quartz particles; 9.98% CO, 10.2% O ₂ in Ar.	Quartz reactor	CM: 117 °C	CM exhibited loosely bound lattice oxygen and more adsorbed oxygen species comparatively. High oxygen mobility is due to higher lattice strain. Surface area is not a predominant factor in CO oxidation.	(Mukherjee et al. 2016b)

		50 to 60 Nmlmin ⁻¹ ; 27-500 °C at 5 °C min ⁻¹			More extrinsic Oxygen vacancies formed due to the smaller ionic radius of Mn. The synergy between Ce and Mn promotes CO oxidation activity.	
11	Hydrothermal method Ce _x Zr _{1-x} O ₂ (x = 0.9, 0.8 and 0.7) NP	0.1g of pelletized catalyst; r.t. to 450 °C at 5 °C/min; 1000 ppm CO; 10 vol% O ₂ in He; W/F = 0.12 gs ⁻¹ cm ⁻³ .	Fixed-bed microreactor; quartz tube dia.: 4 mm.	Ce _{0.9} Zr _{0.1} O ₂ -NP: 224 °C	The presence of (100) and (110) improves CO oxidation. The surface area is not that important as compared to the structural features of solid catalysts.	(Piumetti et al. 2016)
12	PMMA-templating route and coprecipitation method for non-porous catalysts	100 mg catalyst; 1% CO, 10 vol% O ₂ in Ar at 50 ml/min; r.t. to 600 °C at 10 °C/min.	Quartz tube i.d. 6 mm	CZ600 (3-DOM): 255 °C	3-DOM materials having large pore size (>50 nm) have abundant accessible active sites benefiting catalytic activity. The {110} crystal plane and oxygen vacancy concentration play a key role in promoting CO oxidation.	(Zheng et al. 2016)
13	Low-temperature coprecipitation	50 mg catalyst; 1 vol% CO and 10 vol% O ₂ in	Quartz tubular	CuMn prepared by EG: 45 °C	High surface area, abundant active surface oxygen species, and strong synergistic interaction between Cu and Mn were	(Li et al. 2017)

	followed by a post-annealing process.	N ₂ at 20 mlmin ⁻¹ ; GSHV:24,000 mlg ⁻¹ h ⁻¹	fixed bed reactor		prominent factors positively influencing CO oxidation. The dumbbell-like shape with split ends promoted CO oxidation	
14	Impregnation (of CuO NP) by thermal decomposition (onto SiO ₂ NS prepared by hydrolysis method and CeO ₂ NR by Hydrothermal method)	25 mg catalyst and quartz wool; 30 to 350 °C; 1% CO – 20% O ₂ in He at 70 ml/min	Fixed bed plug flow reactor	CuO/CeO ₂ – 400: 88 °C	CeO ₂ Nano Rod (NR) had better reducibility than SiO ₂ Nano Spheres (NS) Doping Cu into CeO ₂ improved Oxygen mobility and redox capability. Support interaction also played a prominent role in the redox reaction.	(Hossain et al. 2018)
15	Hydrothermal method (CeO ₂ and CuO) and wet impregnation method (Cu/CeO ₂)	400 mg of catalyst; 2000 ppm CO & 1.0 vol% O ₂ in He at 500 cm ³ /min; GSHV: 39,000 h ⁻¹ .	Quartz fixed bed reactor (9 mm i.d.)	Cu/CeO ₂ - NR: 72 °C	Rod morphology has a greater concentration of weakly bound Oxygen species relating to Oxygen mobility and vacancy. Exposed facets {110} and {100} in Rod morphology have a significant role in CO	(Lykaki et al. 2018)

		Temperature to 500 °C at 25 °C steps up.			oxidation despite poor surface area and crystallite size.	
16	Hydrothermal method	100 mg catalyst; Vol%: 1% CO, 4% O ₂ in He; GSHV: 60,000 h ⁻¹ ; 23-600 °C	Fixed bed quartz reactor	20Mn ₃ O ₄ /CeO ₂ MSs: 103 °C	Strong synergistic interactions between Ce and Mn. Multiple oxidation states, redox capability, and oxygen vacancies are pivotal in reducing the T ₅₀ temperature of CO oxidation.	(Jampaiah et al. 2019)
17	Microwave-assisted synthesis method: Ni, Co, Fe, Zn, Ga, Sn oxides coated on OMS-2 nanoarray catalyst coated onto the cordierite	8*8*10 mm (W*H*L) cordierite piece; 100 sccm of 1% CO in 10% O ₂ /N ₂ .	Fixed bed quartz reactor	OMS-2@Co ₃ O ₄ -acac monolith: 110 °C	High surface oxygen and its mobility were present in Cobalt oxide coated OMS-2 monolith.	(He et al. 2019)
18	Hydrothermal method with citric acid as chelating agent: CeO ₂ , CuCe (nitrate precursor),	25 to 400 °C in 25 ml/min of 1 % CO in 22% O ₂ /He	Fixed bed reactor	CuCe (Cu ring precursor): 133 °C	The fine dispersal and interaction of Cu species with Ceria has an overwhelming positive effect on the activity of the catalyst.	(Papadopoulos et al. 2019)

	CuCe (Copper ring precursor)				Specific surface area and defect concentration had a lesser role comparatively.	
19	Coprecipitation method Gd _{0.05} Bi _{0.15} M _x Ce _{0.7} _{5-x} O ₂ (M=Cu, Zr, Ni, Co, Mn)	0.3 g of catalyst; 20 to 500 °C in 60 ml/min vol%: 1% CO in 2% O ₂ /97% N ₂ ;	U-shaped quartz	Gd _{0.05} Bi _{0.15} Mn _{0.2} Ce _{0.55} O ₂ : 165 °C	The catalyst with Mn doping has a greater oxygen vacancy population and augmented redox behavior. Mn simultaneously stabilized the solid solution while introducing more defects in the lattice compared to other catalysts.	(Zagaynov et al. 2021)
20	Coprecipitation method Mg doped CuO _x CeO _{2-δ}	0.2 g of catalyst mixed with silica gel; 300 ppm CO, 5% O ₂ /He at GSHV: 50000 mlg ⁻¹ h ⁻¹ ; r.t. to 110 °C	Glass reactor	6MgCuCe: 56 °C	Mg doping results in lattice expansion of Ceria (due to more Ce ³⁺) with greater oxygen vacancies.	(Waikar et al. 2021)
21	Coprecipitation method	50 mg of catalyst; 1000 ppm CO in 10 % O ₂ /He at 100 ml/min	U- quartz reactor (16 mm i.d.)	Cu ₂ CZ-IWI: 90 °C (2 wt% Cu on CeZr synthesized by	CuO is finely dispersed over CeO ₂ or reduced Cu species strongly interacting with CeO ₂ .	(Martínez-Munuera et al. 2022)

	Cu doped Ceria zirconia ($\text{Ce}_{0.8}\text{Zr}_{0.2}\text{O}_{2-\delta}$)	(90000 h^{-1}); r.t. to $300 \text{ }^\circ\text{C}$ at $5 \text{ }^\circ\text{C}/\text{min}$		incipient wet impregnation)		
22	Hydrothermal method Ce doped with La, and Ce doped with Nd	100 mg of catalyst; 50 ml of 1000 ppm CO in 10% O_2/N_2 ; temperature increased in steps of $50 \text{ }^\circ\text{C}$ after stabilization.	U tube reactor	Ce90Nd10: $290 \text{ }^\circ\text{C}$	Formation of more defect sites due to doping and reduced Ce-O bond strength. Higher doping leads to stronger basic sites that reduce CO conversion.	(Sartoretti et al. 2022)

2.7 CO oxidation on structured catalysts

Heterogeneous catalysis reactions employ structured catalysts greatly, specifically catalytic reactions involving gaseous or vapor phase reactants (Zhou et al. 2010). The automobile industry utilizes structured catalysts to abide by the strict pollution norms enforced on the sector. Cordierite has been extensively utilized as an automotive exhaust catalyst support material for its superior thermal stability at elevated temperatures, relatively very low Coefficient of Thermal Expansion (CTE) (El-Shobaky et al. 2011), low-pressure drop, and superior mechanical strength (Yuan et al. 2016) (Chae et al. 2021). Structured catalysts using cordierite as a substrate have been reported in the oxidation of soot (Nascimento et al. 2016, 2018b; Nascimento and Serra 2016b; Neyertz et al. 2014; Stegmayer et al. 2022a; Tang et al. 2019), NO_x (Zhou et al. 2015) (Tang et al. 2021), CO (Yuan et al. 2016) (Yan et al. 2013), CO-PROX (Gómez et al. 2012) (Gómez et al. 2011), VOC (Azalim et al. 2013; Deng et al. 2018; Lu et al. 2011; Tiscornia et al. 2020; Zhu et al. 2018), toluene (Gómez et al. 2014; Huang et al. 2012; Patil et al. 2020; Zhu et al. 2019), Chlorobenzene (Kan et al. 2017) (Zhu et al. 2019), benzene (Li et al. 2014), n-hexane (Díaz et al. 2020).

There are a few literatures pertaining to CO oxidation on structured catalysts, and some of them are briefly discussed below. Yan et al. (Yan et al. 2013) reported $\text{LaCo}_{0.5}\text{Mn}_{0.5}\text{O}_3$ had the best CO oxidation activity among the synthesized catalysts $\text{LaCo}_{0.5}\text{M}_{0.5}\text{O}_3$ ($M = \text{Mn}, \text{Cr}, \text{Fe}, \text{Ni}, \text{Cu}$) catalysts and $\text{LaCo}_{0.5}\text{Mn}_{0.5}\text{O}_3/\text{CC5}$ ($\text{LaCo}_{0.5}\text{Mn}_{0.5}\text{O}_3$ impregnated on cordierite and calcined at $500\text{ }^\circ\text{C}$) had further improved CO oxidation with the T_{50} of $\sim 80\text{ }^\circ\text{C}$. The factors that were reported to have a crucial role in the improvement of CO oxidation activity were attributed to the weakening of the Cobalt-Oxygen bond and the increase of the lattice oxygen due to more cations (Mn) doping into site b of the perovskite structure. Ren et al. (Ren et al. 2014) integrated $\text{M}_x\text{Co}_{3-x}\text{O}_4$ ($M = \text{Co}, \text{Ni}, \text{and Zn}$) nano array catalyst onto cordierite and reported the T_{50} of $\sim 155\text{ }^\circ\text{C}$ for CO oxidation by spinel Co_3O_4 . He et al. (He et al. 2019) synthesized the Mn OMS-2 nanoarray structure in situ in the channels of the cordierite and loaded metals of Ni, Co, Fe, Zn, Ga, and Sn onto the Mn OMS-2

nanoarray by microwave-assisted process. The CO oxidation of the best-structured catalyst reported was that of OMS-2@Co₃O₄-acac monolith with a T₅₀ of 110 °C and 40.3 kJ/mol of activation energy. The factors such as ample surface-active oxygen species, the synergy between MnO₂ and Co₃O₄ combined with interfacial effects, and the large amount of Co³⁺ on the surface of the OMS-2 and the synergy between MnO₂ OMS-2 and Cobalt oxide contributed to exceptional CO oxidation augmented the CO oxidation. Dong et al. (Dong et al. 2021) reported the CO oxidation of flexible TiO₂ mesh (curled into a monolith) coated with Mn₃O₄ with the best T₅₀ of 116 °C for the Mn/TiO₂ (10) sample. The excellent CO oxidation activity was attributed to the synergy between TiO₂ and Manganese oxide coated onto it. The other factors contributing to the CO oxidation activity at low temperatures were reported to be Manganese oxide's redox properties and the titanium sheets' ultrathin thickness. Chen et al. (Chen et al. 2016) synthesized cordierite coated with different Manganese oxide morphology (rods and nanowires) by hydrothermal method. It was reported that the sample HM-PSF (K₂S₂O₇ utilized in the hydrothermal in-situ deposition of Manganese oxide onto the cordierite) had the highest CO oxidation activity with a T₅₀ of ~160 °C and an activation energy of 28.7 kJ/mol.

To summarize, Parameters like facets or planes having higher oxygen vacancies (Aneggi et al. 2005) (Wu et al. 2012), the morphology of the catalyst promoting oxygen mobility and exposed facets (Wu et al. 2012) (Lykaki et al. 2018), mesoporous structure (Xiao et al. 2009), redox nature, and variable valency (Xiao et al. 2009), highly dispersed active phase (Venkataswamy et al. 2015a) (Esmaeilnejad-Ahranjani et al. 2011), synergy and oxygen vacancies (Jampaiah et al. 2019a)(Zagaynov et al. 2021) are known to promote CO oxidation.

2.8 CO oxidation Mechanism

CO oxidation on Ceria Ceria-based catalyst predominantly follows the Langmuir–Hinshelwood mechanism at low temperatures (110 to 220 °C) and the Mars–Van Krevelen mechanism at relatively higher temperatures (>190 °C). In the Langmuir–

Hinshelwood mechanism, adsorbed Oxygen on surface oxygen vacancies are instrumental in the CO oxidation activity. In the Mars-Van Kervelen mechanism, the lattice oxygen plays a critical role. The binding energy of the metal oxide bond assumes more importance as this dictates the release of the active oxygen for CO oxidation. The equations (Eq. 2.8.1 to 2.8.8) for both the mechanism are shown below (Xu et al. 2013a)



‘*’ represents an adsorption site on the catalyst. Eq. 2.8.1 and Eq. 2.8.2 represent the Langmuir-Hinshelwood mechanism. Eq. 2.8.3 and Eq. 2.8.4 represent the Mars-Van Krevelen mechanism of CO oxidation.

Also, the Mars-Van Krevelen for CO oxidation can explained with the following steps in a redox cycle (Mukherjee et al. 2016a).



Here * represents an adsorption site on the surface of the catalyst. ‘O_L’ and ‘V_L’ represent lattice oxygen and oxygen vacancy in the catalyst, respectively.

2.9 Literature review conclusions

The parameters that play a key role in soot oxidation by tight and loose contact in Ceria-based catalysts from the literature review can be summarised as follows (the criticality may not necessarily be in the order that they appear) (1) exposed reactive planes and morphology(nano-rods, nano-cubes, nano-fibers) (2) Lattice Oxygen mobility, metal-Oxygen bond, and availability of active Oxygen species on the surface (3) Synergistic effects between the dopant and Ceria (4) In the presence of NO_x, long-range NO₂ assisted soot oxidation and NO_x storage as surface complexes (5) Surface area and active sites (surface defects, Oxygen Vacancies, surface cracks and pores) (6)

Reducibility and multiple oxidation states of the dopant atom. In brief, the summary of the parameters that influence the CO oxidation in Ceria-based catalysts includes (1) Synergy and metal support interactions (when finely dispersed on the surface), (2) Morphology and exposed facets/planes, (3) Reducibility and redox capabilities (multiple oxidation states) of the dopant in Ceria, (4) High lattice Oxygen mobility, porosity of the catalyst (e.g. 3 DOM), metal-Oxygen bond strength, and Oxygen vacancies. The literature gap from the literature survey can be summarized as follows: Ceria-Manganese mixed oxides are some of the best-performing soot and CO oxidation catalysts, considering only the non-noble metal oxide catalysts. The important factors for enhanced oxidation activity may be summarised due to the following points: morphology of the catalyst (nanorods, nanocubes, etc.), Crystallite size, oxygen vacancies, and redox behavior, promoting and synergistic effects of doping iso-valent and aliovalent dopants, metal and oxygen binding energy in the oxide, exposed reactive planes and surface area to name a few. The shift of focus from the Platinum group of metals to other metal oxides in the late 1990s was due to the high cost and ease of being poisoned by sulfur. Manganese doped ceria materials have shown good catalytic activity for a number of pollutants, including soot and CO.

A vast and systematic examination of soot and CO oxidation has been done for catalysts in the powder form. Still, only a few studies are available where they are coated onto the cordierite honeycomb substrate utilized for Soot and CO oxidation. Further limited literature is available for Ceria-based materials coated onto DOC. So, a clear and systematic understanding of how Ceria-Manganese mixed oxides behave for soot and CO oxidation when coated onto ceramic monoliths is lacking. Based on the literature gap, the objectives of the present work were set, as shown in section **1.8.2** (chapter 1). In the context of the current work, Ceria-Manganese mixed oxide is one of the promising solutions for the oxidation of soot and CO. The forthcoming chapter, i.e., chapter 3 (Material and Methodology), will illustrate the synthesis method for powder and structure catalysts as well as the Characterization technique utilized for probing into the factors that influence soot and CO oxidation on powder and structured catalysts respectively.

CHAPTER 3

MATERIALS AND METHODOLOGY

3.1 Synthesis of nano-structured Ceria-Manganese mixed oxide powders

The samples of $Ce_{1-x}Mn_xO_{2-\delta}$ (where $x = 0, 0.05, 0.1, 0.2, 0.3, 0.4, 0.5, 0.6, 0.7, 0.8, 0.9,$ and 1) named as CM0, CM5, CM10, CM20 and CM30, CM40, CM50, CM60, CM70, CM80, CM90, and CM100 respectively were synthesized using EDTA-Citrate method (Prasad et al. 2012b) (Anantharaman et al. 2018a). Cerous nitrate hexahydrate (SRL extra pure AR Assay 99.9%, M.W. 434.22) and Manganese (II) Nitrate tetrahydrate (Sigma-Aldrich, purity $\geq 97.01\%$, M.W. 251.01) were the metal nitrate salts used for the synthesis. EDTA (SRL extra pure), Citric acid Monohydrate (SRL extra pure Assay), and Ammonium hydroxide solution (25% Extra pure Specific gravity 0.91 LOBA CHEMIE) was the chemical reagent used for the EDTA-Citrate method. **Figure 3.1** depicts the schematic of the EDTA-Citrate synthesis method.

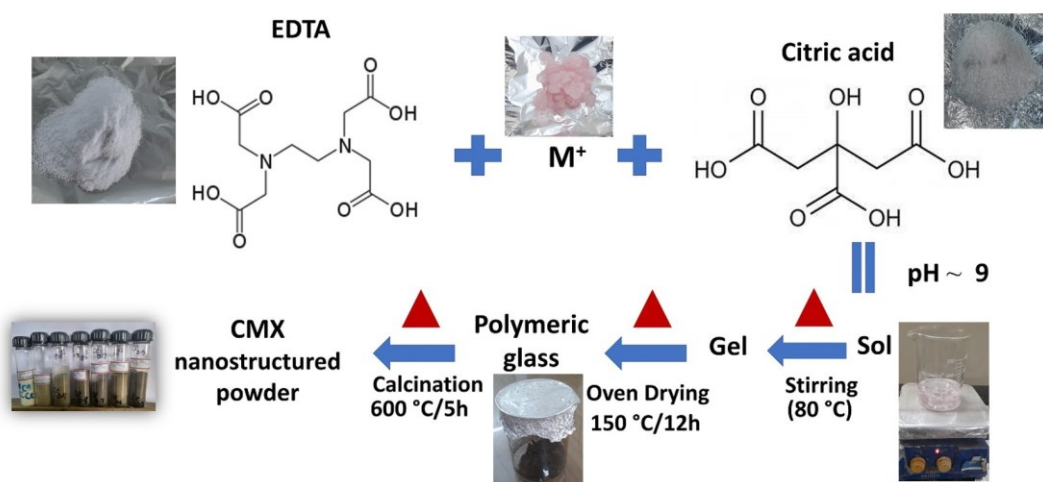


Figure 3.1: Schematic of EDTA-Citrate synthesis method.

The synthesis utilized Stoichiometric amounts of the mentioned Chemicals, with distilled water being the solvent. Metal nitrates were transferred into the EDTA

solution. A calculated amount of Citric acid was transferred to the EDTA-metal complex solution and allowed to stir for 30 minutes. Subsequently, the pH of the EDTA-complex solution was made alkaline (pH ~ 9) by using an ammonium hydroxide solution, and the solvent was evaporated by supplying heat to form a gel. The gel was dried for 12 h in a hot air oven at 150 °C and subsequently heat-treated at 350 °C/12 h. The dried residue was shifted to a crucible to be further calcined at 600 °C/5 h. The calcined powders of CMX catalysts were ground with a mortar pestle and sieved to be utilized further for characterizations and soot oxidation activity.

3.2 Synthesis of structured Ceria-Manganese mixed oxides

The honeycomb cordierite substrates (dia.: 25 mm, length: 50 mm, 400 cps) were used as received from Technistro, Nagpur, India. **Figure 3.2** shows the pictorial representation of the pretreatment process of the cordierite. The cleaning procedure involved the usage of physical and chemical treatments of the honeycomb cordierite substrates. The Physical treatment comprised of sonicating (40 kHz) the bare cordierite honeycomb monolith in the soap solution for 45 min (Patil et al. 2020), Washing with soap solution was done in order to remove dirt, grease, oil, etc. followed by thorough washing and rinsing the cordierite with distilled water and then sonicating the same in ethanol for 45 min to remove any leftover remnants if any. The chemical treatment involved sonicating the cordierite (*after the physical treatment*) in 50 % acetic acid solution for 45 min (Zhang and Wu 2016). The acetic acid solution treatment was utilized to help roughen the surface of the cordierite honeycomb substrate to facilitate better adherence of the subsequent coating layers. After the above step, the cordierite is thoroughly rinsed with distilled water and dried in a hot air oven at 150 °C overnight. The dried cordierite was finally calcined in the muffle furnace at 550 °C/2h (Zhang and Wu 2016)(Gao et al. 2011). CM0, CM5, CM70, and CM100 were the selected catalyst compositions for coating on the pretreated cordierites after γ -Al₂O₃ wash-coating.

The wash-coating of alumina was done by dip coating method wherein the cordierite was immersed in alumina (50 nm DLS) dispersion (20 wt. percentage of

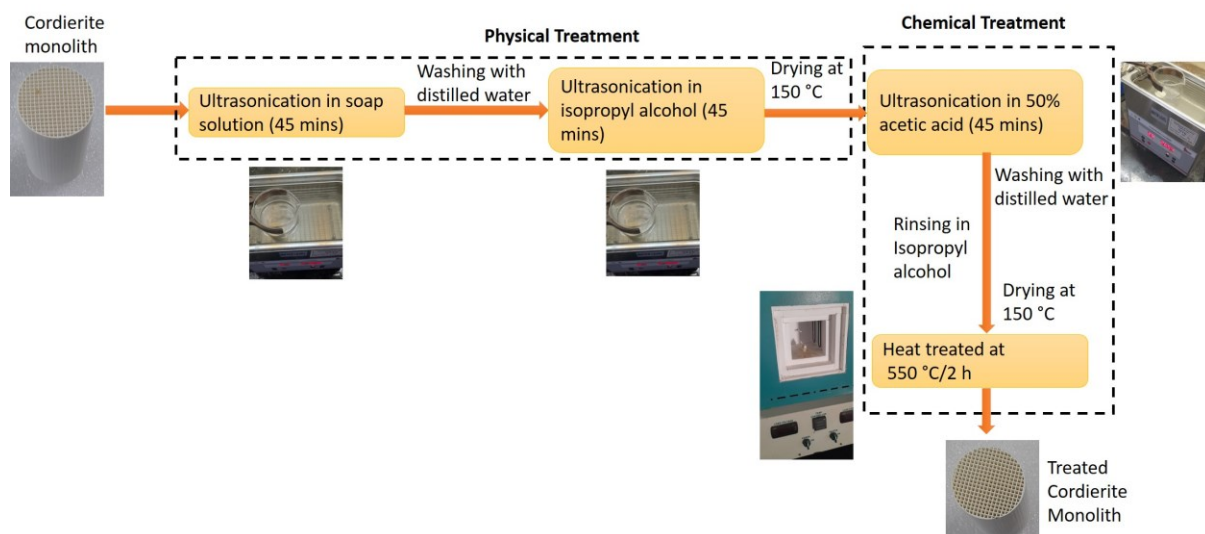


Figure 3.2: Schematic for pretreatment of cordierite.

Alumina in 100 gms of iso-propanol) containing 50 ml of 20 wt % alumina dispersed in isopropanol diluted with 50 ml of isopropyl alcohol in a 100 ml beaker for 5 min. Following the dip coating procedure, the alumina-coated cordierite was microwave-heated for 2 min at 540 W (Tang et al. 2020). Microwave (at 500 W) drying promotes homogeneity and negligible shrinkage stress, resulting in a coating that has less or no cracks compared to oven drying or room drying (Gao et al. 2011). The cordierite was transferred to a hot air oven at 390 °C/1 h. Later, the cordierite was weighed, and the dip coating procedure was repeated until 10 % of the alumina wash-coat was achieved. After achieving 10wt. % Alumina coating, the cordierite was further calcined at 700 °C/2 h to remove any undesired component used in the Alumina dispersion.

The catalyst coating was done by preparing a sol using the EDTA-Citrate method mentioned elsewhere (Shourya and Dasari 2022)(Shourya and Dasari 2023). The sol-gel dip coating of the catalyst is shown in the **Figure 3.3**. PEG 3350 (10 wt % of metal nitrates) was added to the EDTA-Citrate solution. It was reported that Poly Ethylene Glycol (avg. mol. wt. ~ 4000) improves the catalyst's thin film porosity (Sonawane et al. 2004). The solvent used for the sol was distilled water. The solution was kept for

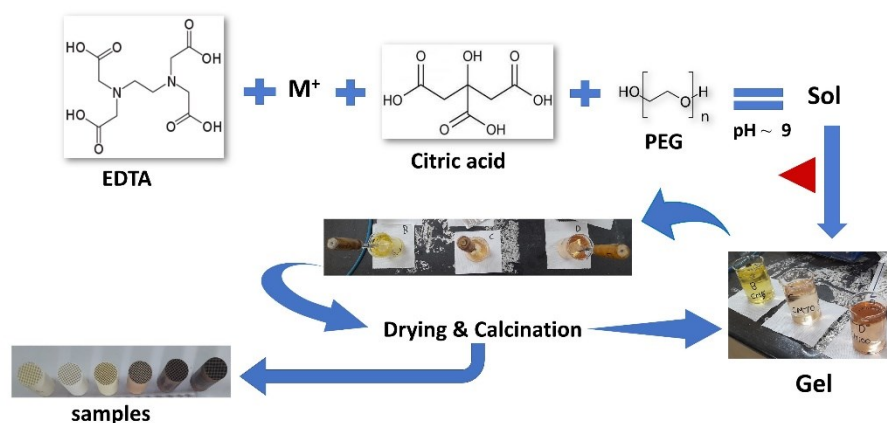


Figure 3.3: Schematic of EDTA-Citrate sol-gel dip coating method.

heating and stirring until the solution had decreased to around ~ 200 ml. The Alumina wash-coated cordierite was dipped into the sol solution for 5 min. Compressed air is blown to remove the excess sol on the surface of the Alumina-coated cordierite before transferring it to a hot air oven at 390 °C for 1 h. After the drying, the cordierite was transferred into the muffle furnace for calcination at 600 °C/1h. The dip, dry and calcination step was repeated until approximately 10 wt % of catalyst coating was achieved and finally calcined at 700 °C/2h. The Alumina wash-coated cordierites coated with the catalysts CM0, CM5, CM70, and CM100 are hereafter denoted as CM0/ Al_2O_3 /Cord, CM5/ Al_2O_3 /Cord, CM70/ Al_2O_3 /Cord and CM100/ Al_2O_3 /Cord respectively. **Figure 3.4** shows the prepared structured catalyst samples by two-step dip coating method.

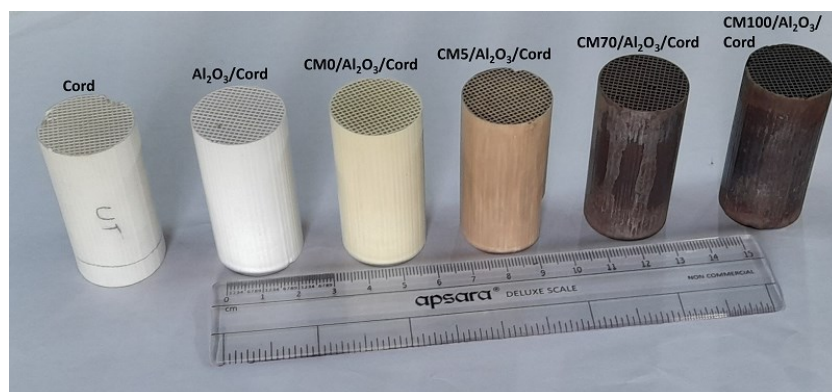


Figure 3.4: Catalyst-coated cordierite samples calcined at 700 °C/2 h.

3.3 Characterization techniques

The following were the characterizations that were utilized for probing into the Ceria-Manganese mixed oxides nanostructured catalysts and structured catalysts. X-ray Diffraction (XRD) (PANalytical Empyrean diffractometer, PANalytical Co., The Netherlands) with Cu K α ($\lambda = 1.54059 \text{ \AA}$) and the scanning range was from 10 to 80° with 0.02° as the scan step. The average crystallite size was obtained from the Debye-Scherrer equation (Dasari et al. 2014)

$$D = \frac{0.9\lambda}{\beta \cdot \cos\theta} \quad (3.3.1)$$

Crystallite size ' D ' (nm), X-Ray wavelength ' λ ' (\AA), peak position ' θ ' (°), and β (°) is peak width at half maximum intensity.

BET and BJH analysis (Quanta Chrome Novae-2200) was carried out to obtain information pertaining to the specific surface area, pore diameter, and pore volume of the synthesized CMX catalysts. Raman spectra (STR500 confocal micro-Raman spectrometer, Erik corporation, Japan) of the CMX ($X = 0$ to 0.3) samples were obtained with a 785 nm laser beam, and Raman spectra (LAB RAM HR Horiba France) of the CMX ($X = 0.4$ to 1) samples were obtained with a 532 nm laser beam. RAMAN spectra (Compact Raman Spectrometer, Renishaw, UK) analysis for the CMX/Cord samples were characterized by a 532 nm laser beam. FESEM (CARL ZIESS AG GeminiSEM 300) micrographs, elemental mapping, and compositional analysis through EDAX were obtained for the CMX and CMX/Cord samples. High-resolution TEM (HR-TEM - JEOL/JEM 2100) with SAED analysis was carried out to visualize the morphology, microstructure, distribution of agglomerates, and particles of the CMX samples.

The strength of the wash coat can be tested by methods such as ultrasonication, drop test, scratch test, abrasive test, etc. (Yang et al. 2016). Ultrasonication (Power: 100 W; Frequency: 40 kHz) was used in the present work to test the adherence strength of the wash coat. The weight (W_c) of the coated cordierite substrates is measured prior to

ultrasonication. Ultrasonication of the coated substrate was done for 30 minutes in isopropyl alcohol. The substrates were then oven-dried, and the weight (W_{us}) of the substrates was measured. The weight loss was calculated by measuring weight before and after the Ultrasonication using equation 1 (Azalim et al. 2013), shown below.

$$\% \text{ wt. loss} = \frac{W_c - W_{us}}{W_c} \times 100 \quad (3.3.2)$$

Weight loss < 5% indicates good wash-coat adherence (Tang et al. 2020). The adherence test was done after alumina wash-coating and after catalyst coating onto the alumina wash-coated cordierite honeycomb substrates.

3.4 Soot oxidation activity

The soot oxidation activity for the synthesized CMX nano-structured catalysts was conducted in a TGA (Sieko EXSTAR 6000) using Printex-U (Orion Engineered Chemicals) as model soot in tight contact conditions. The soot-to-catalyst ratio was 1:10, with a flow rate of 100 ml/min of air and a heating rate of 10 °C/min from room temperature to 630 °C. The conditions for all the soot oxidation activity were optimized to nullify heat and mass transfer constraints (Neeft et al. 1996a). The tests were done in triplicates to ensure repeatability and the reproducibility of the results obtained. T_{50} temperatures were recorded for the CMX catalysts. The soot conversion percentage was calculated using the equation (1) (Lee et al. 2013), as shown below.

$$\text{Soot conversion} = \frac{(M - M_T)}{(M - M_F)} \quad (3.4.1)$$

Where ‘ M ’ is the initial mass, ‘ M_T ’ is the mass at any temperature point, and ‘ M_F ’ is the mass at the final temperature point.”

The activation energy of soot oxidation activity was obtained by conducting soot oxidation experiments in TGA at diverse ramp-up rates ($\alpha = 5, 10, 15,$ and 20 °C/min), and the data from these experiments were utilized to calculate the activation energy by Ozawa method (Krishna et al. 2007a; Rajvanshi et al. 2020; Shenoy et al.

2019) and Kissinger-Akahira-Sunose (KAS) method (López-Fonseca et al. 2005, 2006; Nishu et al. 2021) as shown below in equation (2) and (4) respectively,

$$\frac{d(\log \phi)}{d(1/T\alpha)} = \frac{0.4567 E_a}{R} \quad (3.4.2)$$

Where,

‘ E_a ’ (kJ/mol) is the activation energy.

‘ R ’ (kJ/kg.K) is the universal gas constant.

‘ ϕ ’ (K/min (or) °C/min) is the fixed ramp-up rate.

‘ T_α ’ (K) is the absolute temperature at a given soot conversion percentage ‘ α .’

The mean activation energy was determined from the slope of the fit between the log (ϕ) and ($1/T_\alpha$).

$$\ln\left(\frac{\beta}{T^2}\right) = \ln\left(\frac{AE_a}{Rg(\alpha)}\right) - \frac{E_a}{RT} \quad (3.4.3)$$

Where,

‘ T ’ (K) is the absolute temperature,

‘ α ’ is the soot conversion percentage.

‘ β ’ (K/min or °C/min) is the linear heating rate.

‘ R ’ (kJ/kg.K) is the universal gas constant,

‘ E_a ’ (kJ/mol) is the activation energy.

‘ A ’ is the pre-exponential factor.

The mean activation energy is calculated from the slope of the plot between $\ln(\beta/T^2)$ and ($1/T$).

3.5 CO oxidation activity

Figure 3.5 shows the experimental setup utilized for the CO oxidation experiments. The CO oxidation was performed in a quartz tube ($\phi_{\text{inner}} = 27$ mm, $L = 1000$ mm) placed in a split tube furnace. The Structured catalysts (inserted in the quartz tube) were subjected to a reactant gas (0.1 % CO in 20.9 % O₂/N₂) at a rate of 10 °C/min in 100 ml/min from 40 °C to 450 °C. A CO gas analyzer (GA2211, Ambtronics Pvt. Ltd.

Mumbai, India) was used to monitor the concentration of CO in the reactant gas flowing in the quartz tube. The diameter of the honeycomb cordierite substrate is 25 mm, and the gap between the cordierite and quartz tube was plugged with quartz wool. Prior to each CO oxidation run, no pretreatment was done (Zagaynov et al. 2018)(Hossain et al. 2018)(Papadopoulos et al. 2020)(Piumetti et al. 2016).

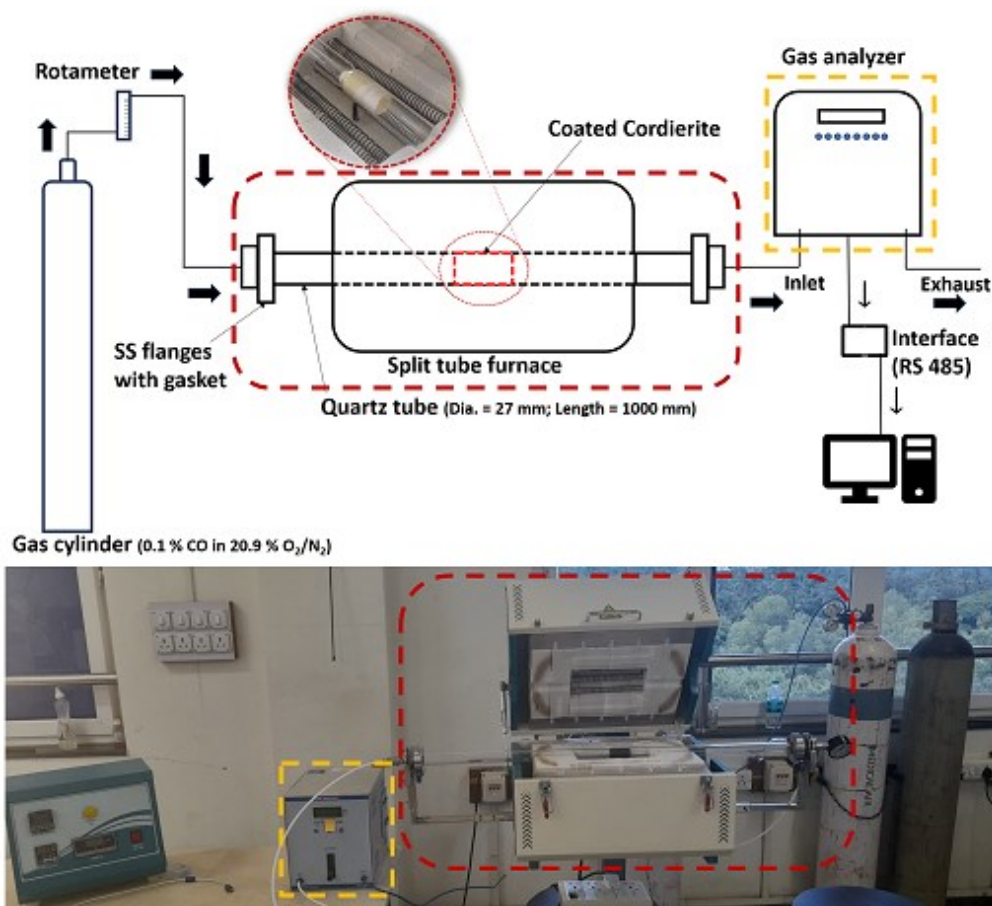


Figure 3.5: Schematic of the CO oxidation setup.

The CO conversion was calculated through the equation (Dey et al. 2019)(Prasad et al. 2012a)(Chang et al. 2007)(Li et al. 2019c)

$$CO \text{ conversion (\%)} = \frac{CO_i - CO_o}{CO_i} \times 100 \quad (3.5.1)$$

CO_i is the initial CO concentration (ppm), and CO_o is the reactor's outlet CO concentration (ppm).

The effect of heating rate was studied for CO oxidation on the coated catalysts. The gas composition remained the same as used for the CO oxidation. The activation energy for CO oxidation on all the catalyst-coated cordierites (samples CM0/Cord to CM100/Cord) was obtained by the Ozawa method (Ozawa 1992)(Krishna et al. 2007a)(Jampaiah et al. 2019b). The data from the effect of heating rate on CO oxidation were used to plot a graph between $\log\beta$ and $(1/T)$, where β and T are the heating rate and temperature. The activation energy (E_a) was calculated from the slope of the plot.

The next Chapter, i.e., Chapter 4, will discuss the soot oxidation activity of Ceria-rich Ceria-Manganese mixed Oxides and their characterization results. The EDTA-Citrate method, as discussed in section 3.1, was utilized for the synthesis process. The characterization techniques utilized are XRD, Raman spectroscopy, BET and BJH, FESEM, and TEM analysis. The soot oxidation activity was carried out in a TGA/DTA equipment.

CHAPTER 4

STUDY ON NANOSTRUCTURED CERIA RICH CMX (X = 0 to 30) POWDER CATALYSTS FOR SOOT OXIDATION

The CMX (X = 0, 5, 10, 20, 30) were synthesized by the EDTA-Citrate method and calcined at 600 °C/5h. The inclusion/doping of Mn in Ceria has excellent catalytic activity for oxidation reactions. The parameters that positively influence the soot oxidation known from literature are as follows, (1) Low lattice Oxygen binding energy or weak metal-Oxygen bond (Mukherjee et al. 2016a) (Venkataswamy et al. 2014) (2) synergistic effects redox capability (Mukherjee et al. 2016a) (Venkataswamy et al. 2014) (Wang et al. 2020) (3) high concentration of surface active oxygen species (Mukherjee et al. 2016a) (4) NO₂ assisted soot oxidation in presence of NO_x in the feed (Tikhomirov et al. 2006). The following sections will deal with the results and discussion of the characterizations and soot oxidation activity of CMX (X = 0 to 30) samples.

4.1 XRD and BET surface area analysis

Figure 4.1 shows the XRD spectra of the synthesized CMX (Ce_{1-x}Mn_xO_{2-δ}, where x = 0, 0.05, 0.1, 0.2, and 0.3 mole %, termed CM0, CM5, CM10, CM20, and CM30 respectively) catalyst samples calcined at 600 °C/5 h. It is evident from the spectra that the diffraction peaks obtained at 28.55°, 33.12°, 47.47°, 56.33°, 59.03°, 69.43°, 76.72°, and 79.09° pertain to the cubic fluorite structure of Ceria (Jampaiah et al. 2019b)(Mukherjee et al. 2016c). No additional peaks of Manganese oxide were seen in the XRD spectra, indicating substitution of the Mn ions into the Ceria lattice or MnO_x may exist in a highly non-crystalline or thoroughly dispersed state beyond the detection limits of the instrument (Zhao et al. 2017). From **Figure 4.1**, it can be observed that the peaks had a negligible apparent shift in the peaks, and the width of the peaks increased with progressive Manganese addition, indicating a decrease in the crystallinity of the

CMX catalysts. A similar kind of observation was made by Zhao et al. (Zhao et al. 2017) with wide diffraction peaks and no observable shift attributed to MnO_x existing in a highly dispersed phase. The doped Ceria catalysts had broader peaks, and the intensity of the Ceria fluorite phase diminished progressively with CMX samples as compared to the CM0 sample, indicating a shrinkage in the crystallite size (Du et al. 2018) (Zhou et al. 2018), which is corroborated by the values in **Table 4.1**. **Table 4.1** shows the lattice parameter and crystallite size of the synthesized CMX (X = 0 to 30) compositions. The lattice parameter varies from 5.4139 Å (CM10) to 5.3782 Å (CM30), and crystallite size varies from 5 nm (CM30) to 15 nm (CM0), the lattice strain ranges from 0.0182 (CM0) to 0.0652 (CM30). It can be noted that, with the inclusion of Mn ions into the Ceria cubic fluorite structure, there is a decrease in the crystallite size and, consequently, an increase in the lattice strain (Wu et al. 2010).

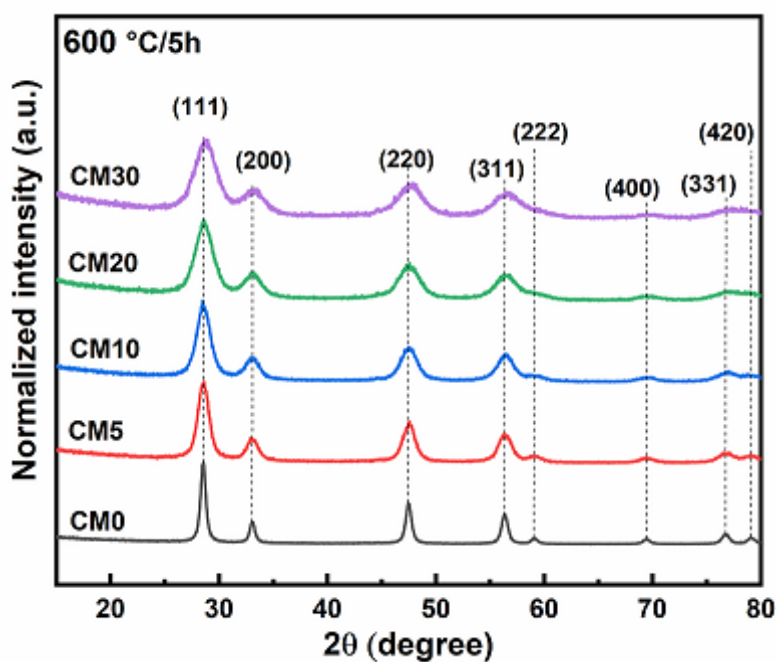


Figure 4.1: XRD pattern of CMX (X = 0, 5, 10, 20, 30) catalysts calcined at 600 °C/5 h.

The increased lattice strain may help improve oxygen mobility (Mukherjee et al. 2016b). It is noticed from **Table 4.1** that there is a minimal increase in the lattice parameter of CM10, which may be attributed to an increased amount of Ce^{3+} cations

due to the doping of Manganese ions into the Cerium oxide lattice. The unusual lattice expansion is since Ce^{3+} has a higher ionic radius than Ce^{4+} cations. Chen et al. (Chen et al. 2010) observed the phenomenon of lattice expansion in Ceria synthesized with three different methods. The lattice expansion was found to be dependent primarily on the synthesis methods. Putla et al. (Putla et al. 2015b) also observed a similar phenomenon of lattice expansion in the synthesized Ce-Mn catalyst when investigating the shift of the XRD peaks of $\text{MnO}_x/\text{CeO}_2$ to lower 2θ values instead of higher.

The doping of Manganese ions into Cerium oxide increased the magnitude of low index planes, as seen in **Table 4.1**. The reactive planes (220)/(111) ratio is the highest for CM5 (0.5169), and that of (200)/(111) is CM30. The higher the (220)/(111) and (200)/(111) ratio, the higher the exposed (220) and (200) planes, which are more reactive to soot oxidation and may result in lower T_{50} temperatures (Anantharaman et al. 2019). Dosa et al. (Dosa et al., 2018) reported a similar result for 5 mol % Mn-doped Ceria synthesized by the hydrothermal method.

The results of the BET and BJH analysis are in **Table 4.1**. It is observed that CM0 has a BET surface area of $43 \text{ m}^2/\text{g}$, pore volume of $0.111 \text{ cm}^3/\text{g}$, and pore dia. of 3.405 nm. From **Table 4.1**, the doping of Manganese ions into the Cerium oxide lattice reduces the crystallite size and improves the BET surface area (Venkataswamy et al. 2015a) compared to the CM0 sample. It can be noticed from **Table 4.1** that among all the synthesized samples, CM5 has the highest pore volume (0.128 cc/g) and BET surface area ($50 \text{ m}^2/\text{g}$) among the CMX catalyst samples. However, the same trend cannot be seen for pore diameter, which varies very slightly. The degree of agglomeration ' ϕ ' is obtained from the ratio of crystallite size to the particle size (Anantharaman et al. 2018c). It can be observed from **Table 4.1** that with the incorporation of the Manganese in the Ceria lattice, the ' ϕ ' reduces from 0.2293 for CM0 to 0.0843 for CM30 catalyst, and the range indicates all the CMX samples are agglomerated (Anantharaman et al. 2017). The N_2 sorption isotherm is in the **Figure A1.1** in the Appendix-I section.

Table 4.1: Lattice parameter (a), Crystallite size (D), Lattice strain, Surface area, pore volume, and diameter average T₅₀ of samples, Reactive planes, and Degree of agglomeration (φ) of CMX (X = 0 to 30) catalysts calcined at 600 °C/5 h.

Composition	Lattice parameter ^a (Å)	Crystallite size ^a (nm)	Lattice strain ^a	Reactive planes ^a		BET	BJH		Degree of agglomeration ^d φ	T ₅₀ average ^e (°C)
				(220)/ (111)	(200)/ (111)	Surface area ^b (m ² /g)	Pore volume ^c (cc/g)	Pore dia. ^c (nm)		
CM0	5.4110	15	0.0182	0.5070	0.2751	43	0.111	3.405	0.2293	405
CM5	5.4061	07	0.0361	0.5169	0.3118	50	0.128	3.422	0.1723	360
CM10	5.4139	06	0.0448	0.4334	0.3145	44	0.076	3.467	0.1059	369
CM20	5.4021	06	0.0558	0.4797	0.3757	45	0.089	3.439	0.1110	373
CM30	5.3782	05	0.0652	0.4661	0.3946	43	0.089	3.468	0.0843	391

a: values obtained from XRD analysis.; b: values obtained from BET analysis.; c: values obtained from BJH analysis.; d: ratio of crystallite size from XRD by particle size obtained from BET surface area; e: values obtained from TGA analysis.

4.2 Raman spectra analysis

Figure 4.2 depicts the Raman spectra of the CMX catalysts calcined at 600 °C/5 h. A strong F_{2g} peak is observed at 463 cm^{-1} ascribed to the first-order scattering and symmetric breathing of the oxygen atom in Ce-O-Ce (Anantharaman et al. 2018a)(Anantharaman et al. 2018b)(Li et al. 2017). On observing the spectra of the CMX samples in **Figure 4.2**, one can see a redshift of the F_{2g} peak to lower wavenumbers, and the peaks have become more diffuse (Hong et al. 2011). It may be due to the inclusion of Manganese ions into Cerium oxide cubic fluorite structure, distorting the structure, resulting in smaller crystallite size of the doped samples, confirming solid solution formation (Wheeler and Khan 2014).

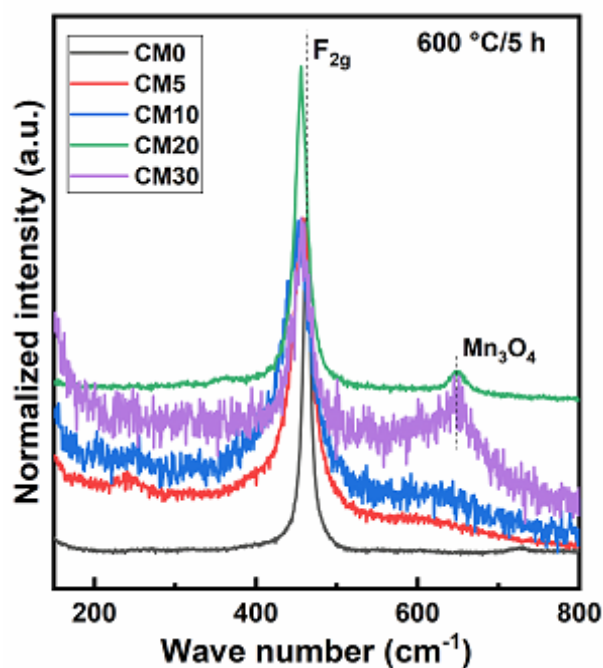


Figure 4.2: Raman spectra of CMX (X = 0, 5, 10, 20, 30) catalysts calcined at 600 °C/5 h.

From **Figure 4.2**, a relatively low intense peak appears at around 653 cm^{-1} from CM20 onwards and increases in intensity. This peak is attributed to the Mn_3O_4 crystalline phase stretching mode of Mn-O-Mn (Venkataswamy et al. 2015b). From the literature, Kapteijn et al. (Kapteijn et al. 1994), Han et al. (Han et al. 2006), Wu et al.

(Wu et al. 2011b), and He et al. (He et al. 2018c) observed the peak seen from about 645 to 653 cm^{-1} in the Raman spectra corresponding to Mn_3O_4 peak. The presence of the Mn_3O_4 phase implies that the solubility of Mn in the Ceria lattice may not be till CM30, as observed from XRD spectra in **Figure 4.1**, but the complete solubility is only till CM10. Kang et al.(Kang et al. 2006) reported the solubility of Mn-doped Ceria is between 5 to 10 mol %, and Li et al.(Li et al. 2011b) reported a solubility limit of 20 mol %. Tang et al. (Tang et al. 2018) reported that the upper limit of Manganese ions solubility in Cerium oxide is 30 mol %.

4.3 FESEM analysis

Figure 4.3(a to e) shows the FESEM micrographs of CMX (X = 0 to 30) catalysts. It can be observed from the micrographs that the images of CM0 to CM30 are flaky agglomerates, and CM5 has the smallest agglomerates. The elemental mapping and EDS of all the samples were done, and they suggest that the Cerium, Manganese, and Oxygen were homogeneously distributed throughout the samples.

Table 4.2: EDS analysis of CMX (X = 5 to 30) catalysts calcined at 600 °C/5 h.

Composition	Ce %	Mn %
CM5	96.21	03.79
CM10	91.75	08.25
CM20	83.91	16.09
CM30	72.69	27.31

This homogeneity can be attributed to the EDTA-Citrate synthesis method that has ensured uniformity of the elements throughout the synthesized CMX catalysts. The EDS of all the samples was done, and the results of the EDS from the FESEM analysis are in **Table 4.2**

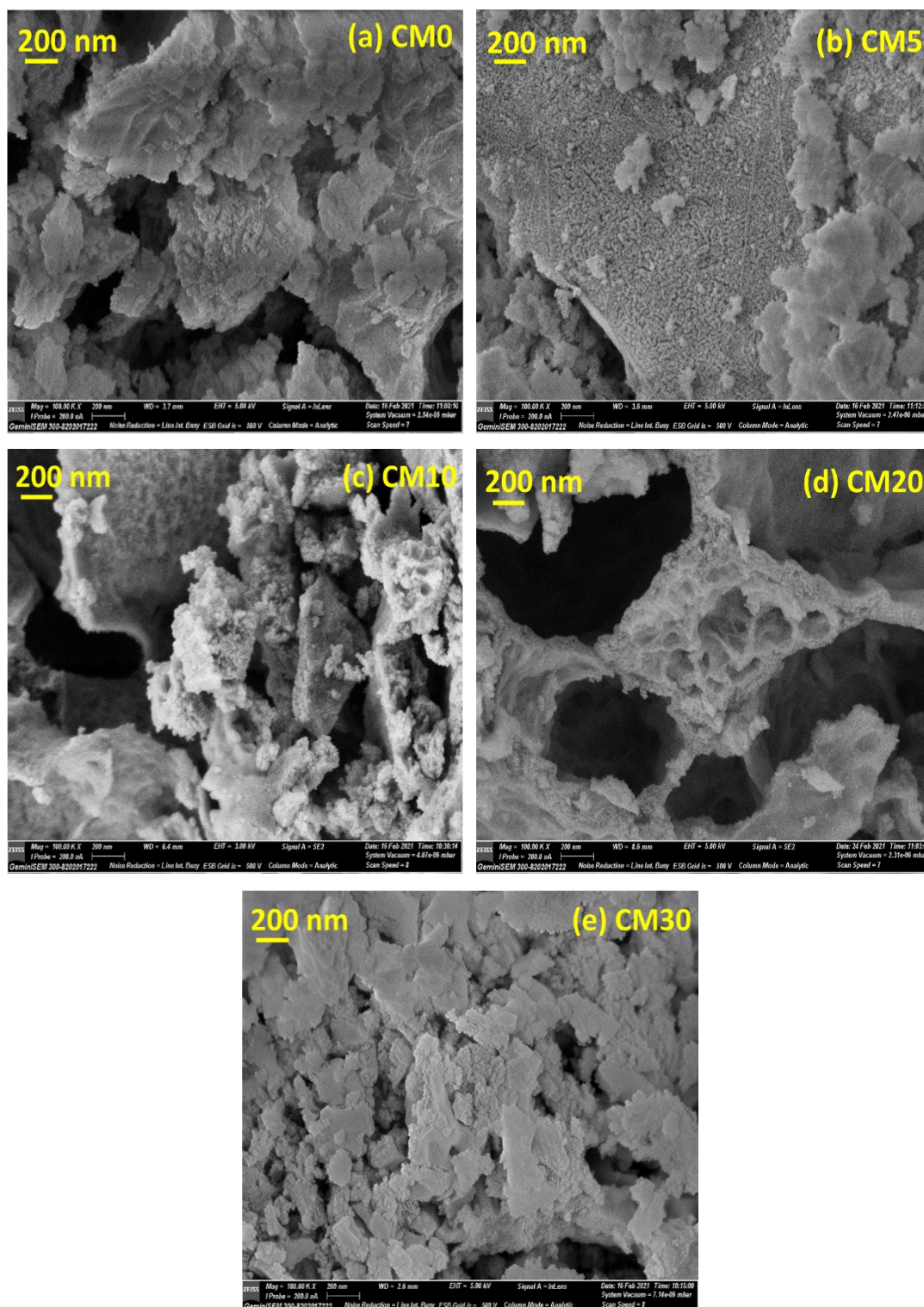


Figure 4.3: FESEM images of (a) CM0, (b) CM5, (c) CM10, (d) CM20, (e) CM30 calcined at 600 °C/5 h.

4.4 TEM analysis

The TEM images of CM0, CM5, and CM30 are shown in **Figure 4.4(a to d)**, **Figure 4.5(a to d)**, and **Figure 4.6(a to d)**, respectively. It can be observed that the particles are not spherical and agglomerated for all three CMX samples. As observed from the TEM images, the average particle size had reduced with Mn incorporation into Ceria; thus, these very fine particles easily agglomerated due to the high surface energy. The same can be observed in the FESEM micrographs, wherein the catalysts are agglomerated. The lattice fringes, as seen in **Figure 4.4(d)**, **4.5(d)**, and **4.6(d)**, were measured for their interplanar distance, and they were found to be the planes of Ceria, namely (111), (200), and (222).

SAED patterns for the CM0, CM5, and CM30 are shown in **Figure 4.4(e)**, **4.5(e)**, and **4.6(e)**. Debye characteristic rings and an absence of discrete patterns in SAED indicate the polycrystalline nature of the samples (Anantharaman et al. 2018b). It can be observed that the SAED pattern is discontinuous in the CM0, and a continuous pattern is observed for the CM5 and CM30 samples.

A continuous ring pattern in the SAED analysis indicates the presence of numerous smaller-sized polycrystalline particles. A discontinuous ring indicates comparatively larger size polycrystalline particles; this further suggests that the inclusion of Manganese ions into the Cerium oxide lattice resulted in finer particles (Putla et al. 2015a).

(Cont...)

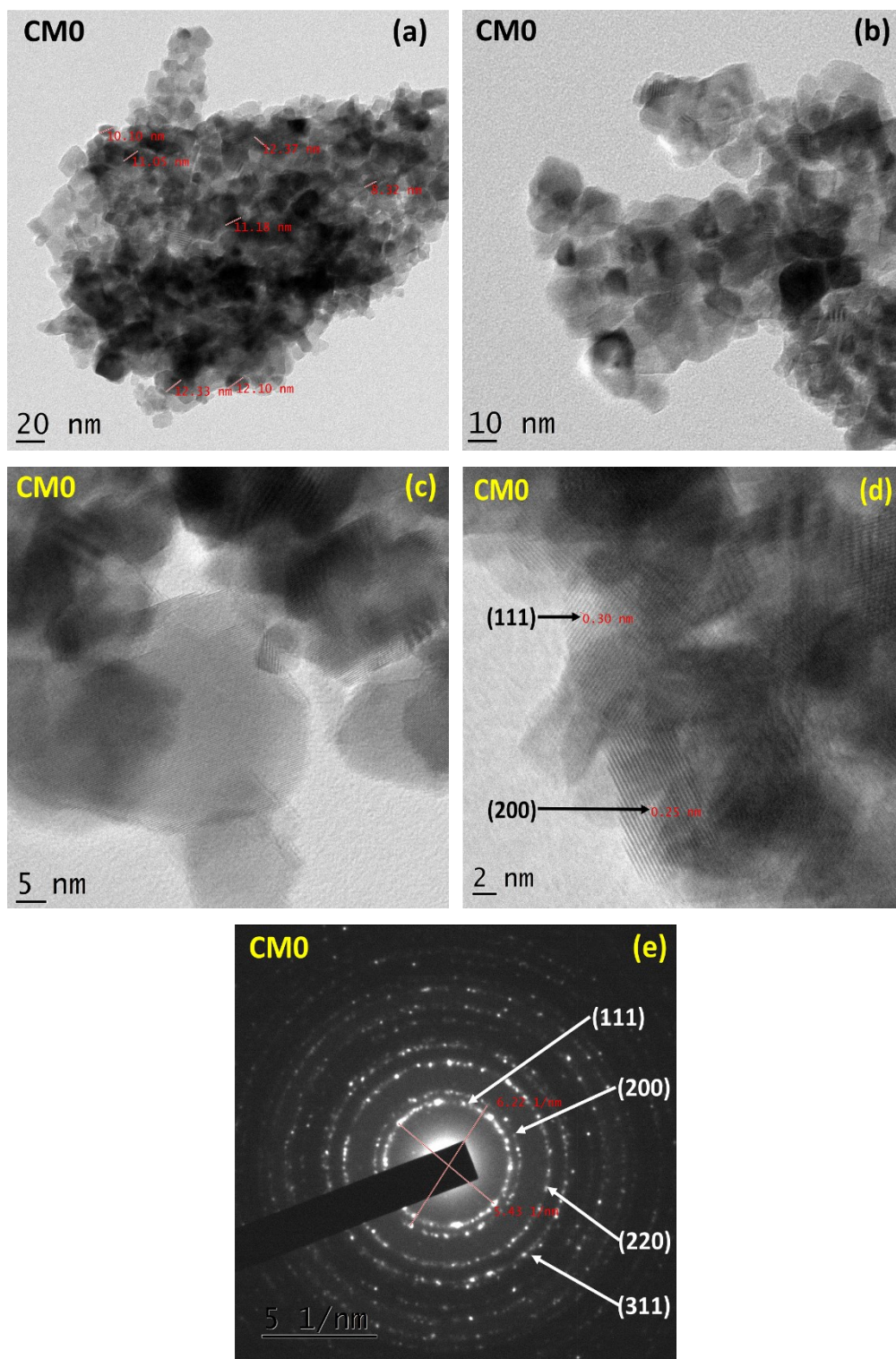


Figure 4.4: TEM images (a to d) and (e) SAED pattern of CM0 catalyst calcined at 600 °C/5 h.

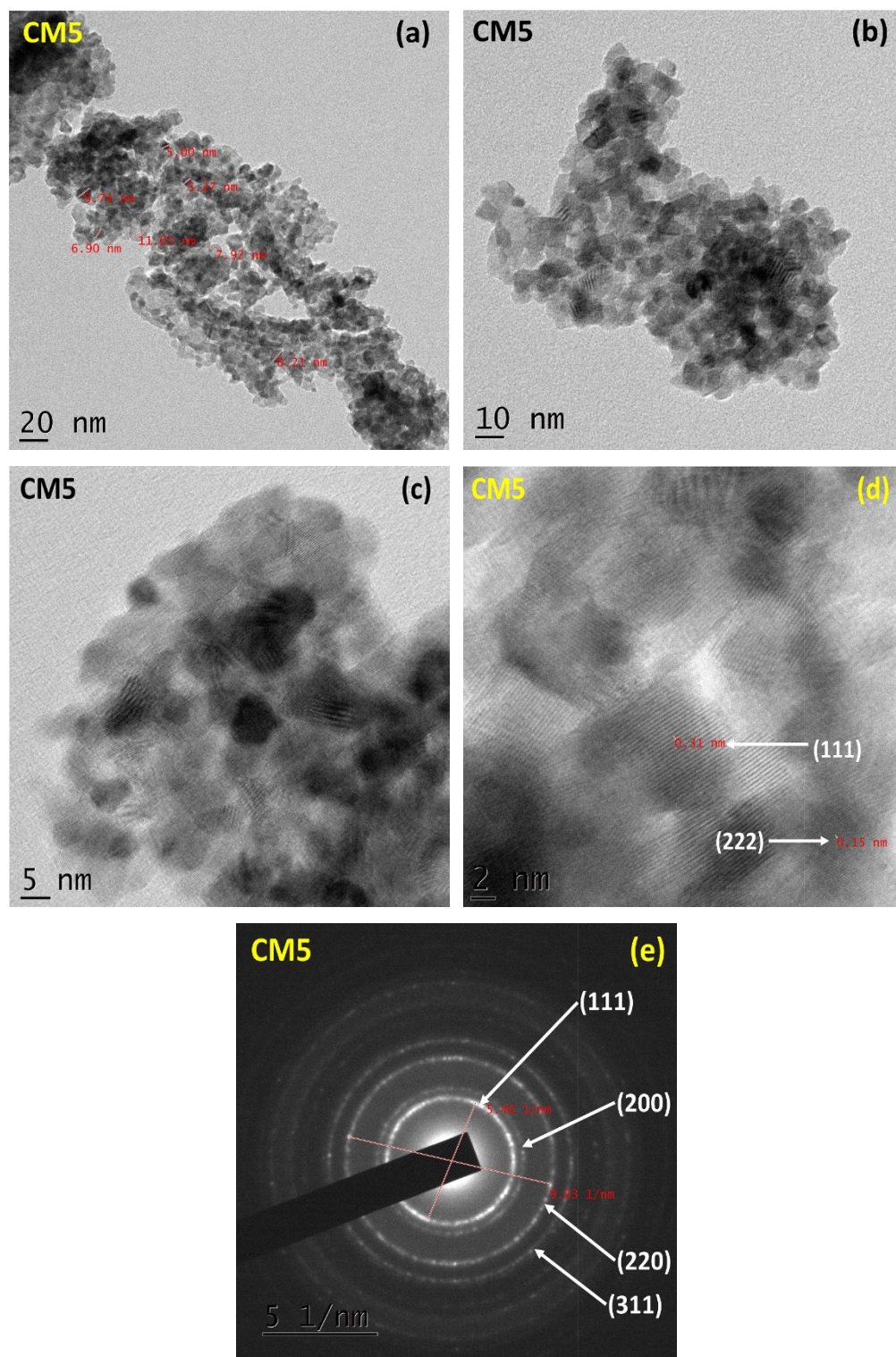


Figure 4.5: TEM images (a to d) and (e) SAED pattern of CM5 catalyst calcined at 600 °C/5 h.

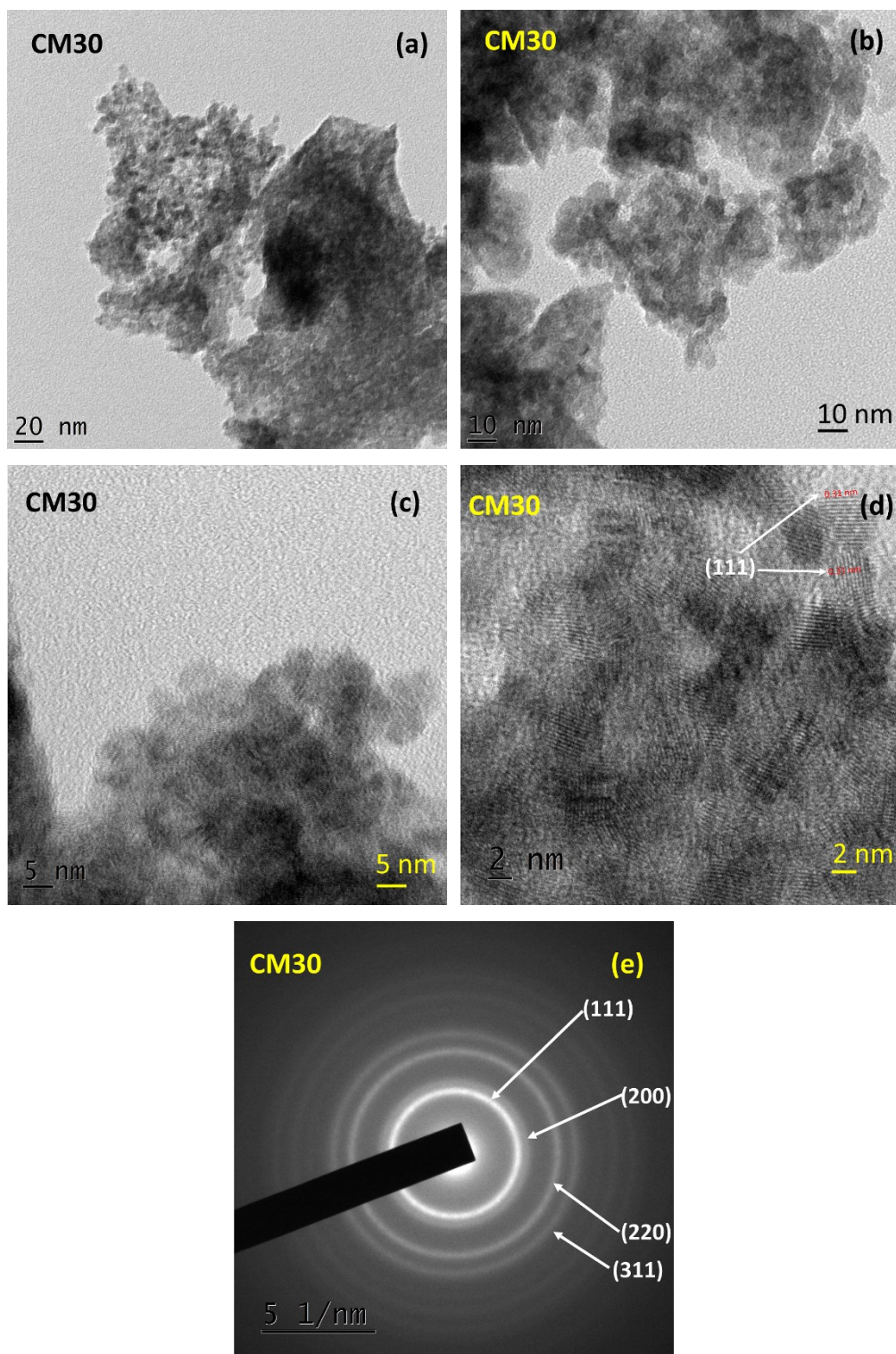


Figure 4.6: TEM images (a to d) and (e) SAED pattern of CM30 catalyst calcined at 600 °C/5 h.

4.5 Soot oxidation

Figure 4.7(a) shows the soot oxidation activity of the synthesized CMX catalysts from room temperature to 600 °C at 10 °C/min with Printex-U (Orion Engineered Chemicals) as model soot. Based on the T₅₀ temperatures, the descending order of the soot oxidation activity was as follows: CM5 (360 °C) > CM10 (369 °C) > CM20 (373 °C) > CM30 (391 °C) > CM0 (405 °C).

The Synergistic effects of doping Mn into the Ceria lattice and the consequent increase in the anionic vacancies due to the substitution of Ce⁴⁺ ions with Mn²⁺ and Mn³⁺ ions (Zhang et al. 2015)(Wu et al. 2013). The activity of CM5 (T₅₀ of 360 °C) may be credited to the augmented surface-active species due to the incorporation of Mn into the Ceria lattice, leading to a smaller crystallite size, high BET surface area, and high pore volume. It can be observed from XRD, BET, and BJH analysis, respectively (Lin et al. 2018a). Dosa et al. (Dosa et al. 2018) in their study had reported that Ce_{0.95}Mn_{0.05} prepared by the hydrothermal method was the best-performing catalyst composition for soot oxidation (tight contact conditions under air) with a T₅₀ temperature of 451 °C. The performance was attributed to the good lattice to surface oxygen mobility.

Zhou et al. (Zhou et al. 2018) reported soot oxidation activity (tight contact in the air) of Ce-Mn-based composition. In their synthesized composition, the least Mn-doped Ceria (10 mol % Mn-doped Ceria) performed best among the catalysts (T₅₀ of 389 °C & 399 °C) for two different synthesis methods in their study. It was inferred from the results obtained that the Ce-Mn catalyst had a greater amount of surface-active oxygen species (due to a greater number of lattice imperfections) that aided in comparatively low-temperature soot combustion. The CM5 and CM10 catalysts synthesized in this study perform better and have comparably less T₅₀ compared to the quoted literature. **Figure 4.7(b)** depicts the variation of T₅₀ temperature for the triplicates of the soot oxidation activity.

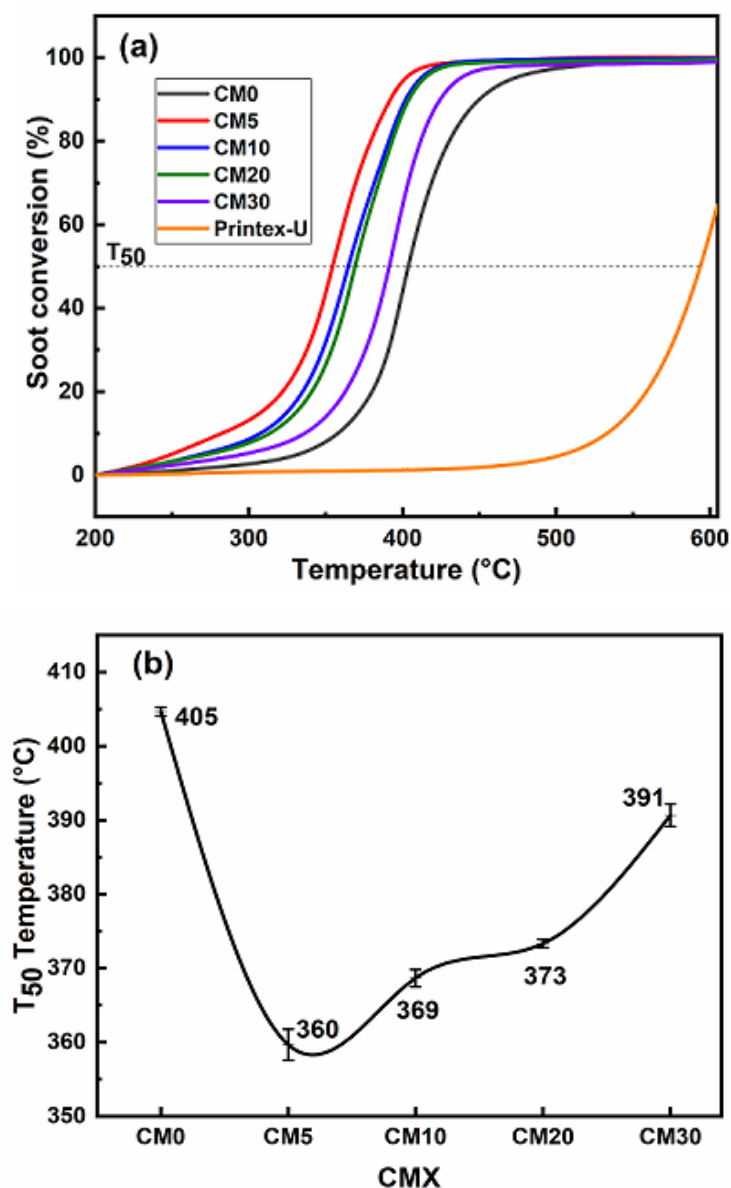


Figure 4.7: (a) Soot conversion (%) of CMX (X = 0 to 30) catalysts. (b) T₅₀ (°C) triplicates error bar graph for CMX catalysts calcined at 600 °C/5 h.

Three samples, namely the least T₅₀, i.e., CM5, the highest T₅₀ CM0, and CM30, were chosen for the soot oxidation activation energy studies. **Figure 4.8(a to c)** shows the soot oxidation activity of CM0, CM5, and CM30 at various heating rates (5, 10, 15, and 20 °C/min), respectively. The data from **Figure 4.8(a to c)** were used for Ozawa

and KAS plots to obtain the mean activation energy of CM0, CM5, and CM30, as shown in **Figure 4.9(a to c)** and **Figure 4.10(a to c)**, respectively. The mean activation energy, as calculated from the Ozawa method, was obtained to be 121 kJ/mol for CM0, 118 kJ/mol for CM5, and 120 kJ/mol for CM30. The mean activation energy obtained from the KAS method for the CMX catalysts namely CM0, CM5 and CM30 were 116 kJ/mol, 114 kJ/mol and 115 kJ/mol, respectively. According to the literature, the uncatalyzed soot oxidation activation energy varies from around 154 kJ/mol (Palmisano et al. 2006), 150 kJ/mol (Krishna et al. 2007b) to 161 kJ/mol (Kalogirou and Samaras 2010) for Printex-U soot. The soot oxidation activation energy of CeO₂ has been reported as 126 kJ/mol (Shimizu et al. 2010), 123.2 kJ/mol (Lee et al. 2015), 127 kJ/mol (Shimizu et al. 2011), and 114 kJ/mol (Palmisano et al. 2006). The obtained activation energy values are lower than the uncatalyzed soot oxidation reactions, and that of Ceria is close to the reported literature values as mentioned above.

Table 4.1 shows that for Mn-doped Ceria, a shrinkage in crystallite size led to a rise in the lattice strain. Too small a crystallite size invariably increases the surface area, grain boundary volume and induces higher lattice strain. It can be inferred from the literature that surface area doesn't have a major say after a particular threshold value in the soot oxidation activity (Aneggi et al. 2006) (Shuang et al. 2015) compared to that of the pore volume and pore diameter.

It can be seen from **Table 4.1** that although CM20 (45 m²/g) has a comparable BET surface area with that of CM5 (50 m²/g), there is some variation in the T₅₀ values between them. Sufficient pore size and volume facilitate intimate contact with the soot particles, resulting in better transfer of active and lattice oxygen species by virtue of an improved number of active sites (Cheng et al. 2018), thereby lowering the activation energy required for the soot oxidation activity. The soot oxidation mechanism among the synthesized catalysts may be due to the active oxygen mechanism (Gross et al. 2012) due to the spill-over of the adsorbed oxygen as well as the lattice oxygen on the surface of the CMX catalysts (Anantharaman et al. 2017).

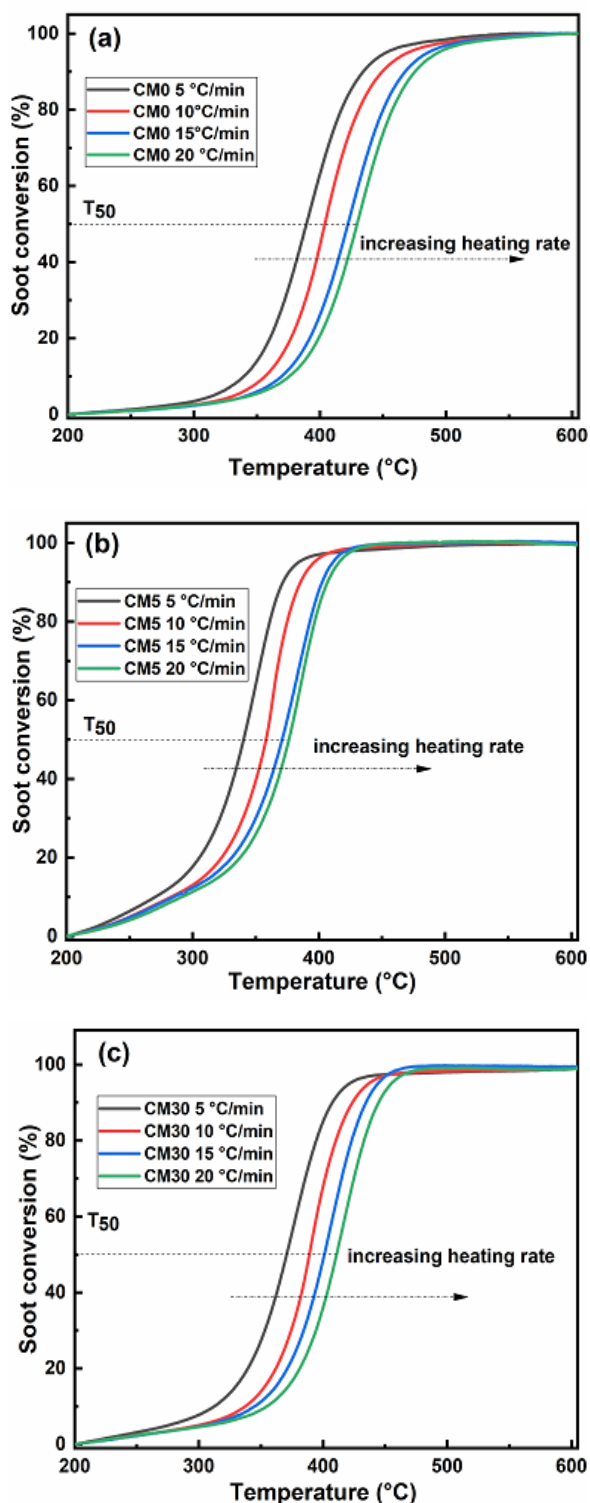


Figure 4.8: Soot conversion (%) at ramp up rates of 5, 10, 15, and 20 °C/min over (a) CM0, (b) CM5, and (c) CM30, calcined at 600 °C/5 h.

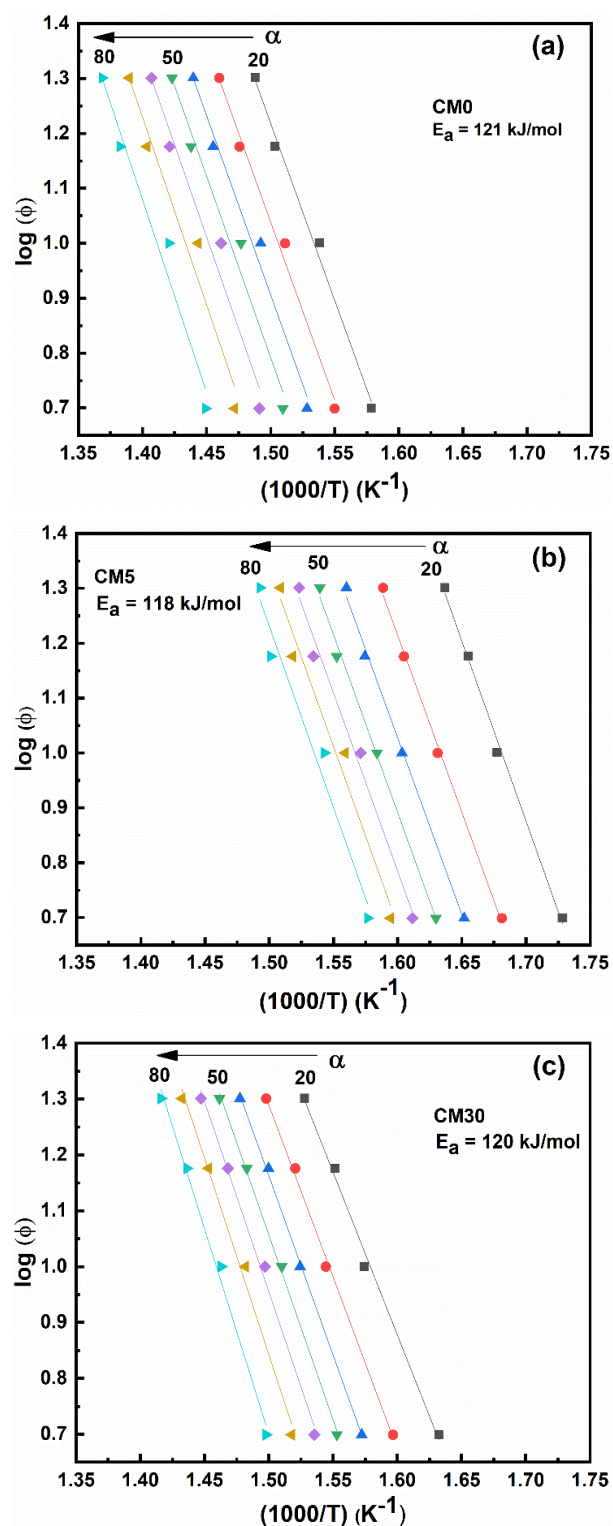


Figure 4.9: Ozawa plots of (a) CM0, (b) CM5, and (c) CM30 catalysts calcined at 600 °C/5 h.

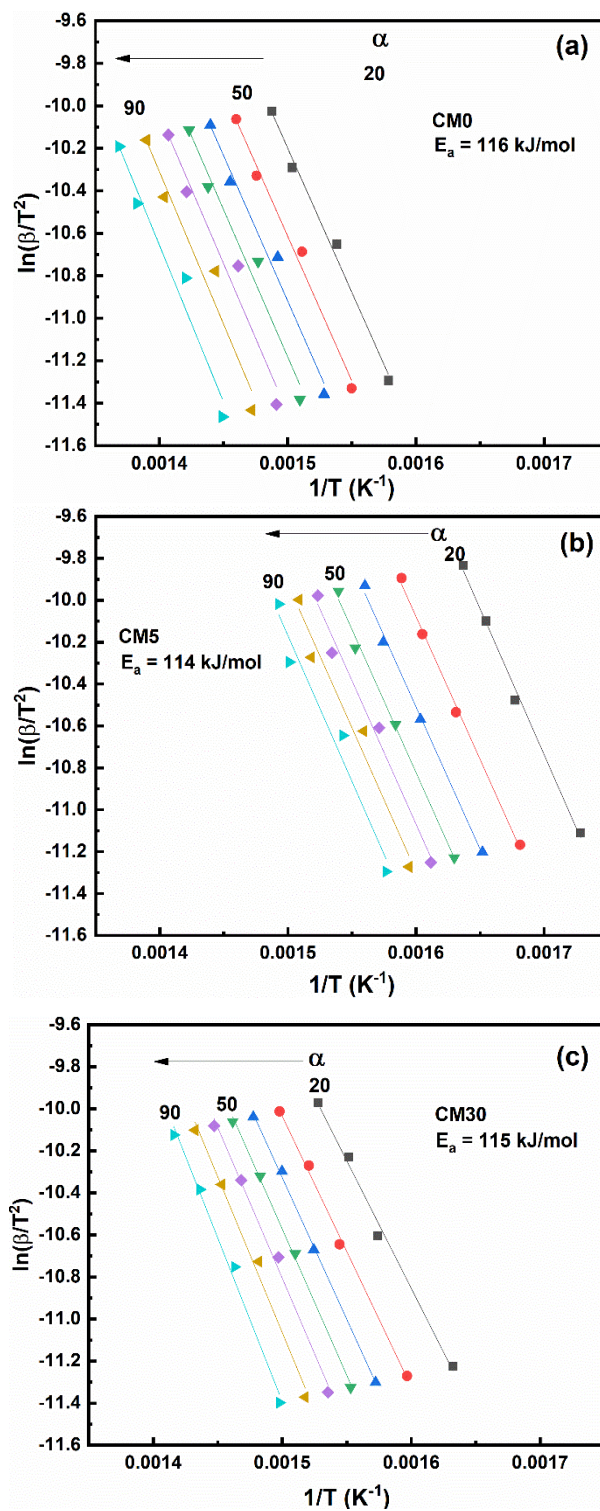


Figure 4.10: KAS plots of (a) CM0, (b) CM5, and (c) CM30 samples calcined at 600 °C/5 h.

The combined effects of synergy between Ce and Mn (Wang et al. 2020), lattice distortions resulting from doping of relatively smaller Mn ions in the Ceria lattice as seen in the XRD and Raman spectra, have a desirable effect on the oxygen vacancies and lowering the Metal-Oxygen bond energy, thereby improving the low-temperature catalytic activity by virtue of augmented availability of surface-active oxygen species, especially that of CM5 sample as seen in **Figure 4.7(a) & 4.8(b)**, improved surface area and pore volume, higher surface-active sites, therefore propelled CM5 catalyst to perform better than other CMX samples in the soot oxidation activity.

4.6 Conclusions

Ceria and doped Ceria (up to 30 mol % Mn) were successfully synthesized using the EDTA-citrate method. XRD revealed the complete solubility of Mn (Mn^{2+} and Mn^{3+}) with the Ceria lattice is till CM30. But Raman spectroscopy analysis revealed the Mn_3O_4 phases in CM20 and CM30, indicating that the complete solubility of Manganese ions in Cerium oxide is only till CM10. The crystallite size of the CMX catalysts decreased with an increase in the doping of Mn in the Cerium oxide lattice, while lattice strain followed an increasing trend for Mn doped Ceria samples, indicating that, with the increase in smaller size Mn^{2+} and Mn^{3+} ions replacing the relatively larger Ce^{4+} and Ce^{3+} ions by means of doping which led to the contraction of lattice and development of lattice strain. FESEM micrograph analysis shows that all the samples had agglomerates. The TEM images and SAED analysis indicated the presence of a polycrystalline nature of the synthesized CMX catalysts. Doping of Mn in Ceria resulted in improved specific surface area and an improvement in pore volume. CM5 had the least T_{50} (360 °C) and activation energy of 118 kJ/mol and 114 kJ/mol by Ozawa and KAS methods. With the virtue of better synergistic effects between Ceria and Manganese oxide and a relatively greater number of exposed reactive planes coupled with a high surface area that helps expose a greater number of reactive sites.

The Ceria-rich phase of Ceria Manganese mixed oxides had a partial solid solution from CM20 onwards, it will be interesting to study further doping of

Manganese (Mn > 30 mol. %) into Ceria lattice and its effect on soot oxidation activity. The forthcoming chapter, will delve into the issue and discuss the results of soot oxidation of Manganese-rich Ceria-Manganese mixed oxides synthesized by the EDTA-Citrate method (as discussed in section 3.1). The characterization techniques utilized were XRD, Raman spectroscopy, BET and BJH, FESEM, and TEM analysis. TGA/DTA equipment was used for the soot oxidation experiments.

CHAPTER 5

STUDY ON NANOSTRUCTURED MANGANESE RICH CMX (X = 40 to 100) POWDER CATALYSTS FOR SOOT OXIDATION

This chapter will deal with the CMX (X = 40 to 100) catalysts synthesized by the EDTA-Citrate method and calcined at 600 °C/5h. The Manganese-rich Ceria-Manganese oxides have been widely used as oxidation catalysts; for example, Ceria-Manganese ($3\text{MnO}_{x-1}\text{CeO}_2$) synthesized in three ways was used to oxidize benzene by Chen et al. (Chen et al. 2018). Azalim S et al. (Azalim et al. 2011), catalytical oxidized Oxygenated Volatile Organic Compounds (OVOC) with a series of metal oxides of $\text{Zr}_{0.4}\text{Ce}_{0.6-x}\text{Mn}_x\text{O}_2$ (x = 0, 0.12, 0.24, 0.36, 0.48, 0.60) synthesized by sol-gel method. Li et al. (Li et al. 2011a) synthesized $\text{Mn}_{0.6}\text{Ce}_{0.4}\text{O}_2$ by co-precipitation method, varied calcination time, and investigated its effect on ethanol oxidation. Zhang et al. (Zhang et al. 2019) synthesized MnCeO_x with citric acid, so the gel method with ethylene glycol, and examined the catalyst's impact on the oxidation of formaldehyde and ozone simultaneously.

In recent years, many researchers have synthesized nanoparticles of different morphologies tailored to cater to a specific purpose. Aneggi et al. (Aneggi et al. 2014) synthesized Ceria in polycrystalline and nano-rods, nano-cubes, and single crystalline form through hydrothermal methods to study their effect on soot oxidation activity. It was concluded that the morphology of the Ceria nanoparticles played a crucial role in improving the soot oxidation activity owing to higher reactive facets of {100} and {110} than {111}. Ceria nano-rods and nano-cubes had the best soot oxidation activity among the synthesized catalysts. Wang et al. (Wang et al. 2012) utilized the hydrothermal method to synthesize rod, wire, tube, and flower-like morphologies of MnO_2 on a nanoscale for toluene oxidation. The nano-rod structures yielded the best result. According to their study, factors such as good reducibility and considerable availability of active oxygen species aided in the low-temperature oxidation of toluene.

Putla et al. (Putla et al. 2015a) investigated the soot oxidation activity of dispersed MnO_x nanoparticles on Ceria nano-cubes. It was inferred that the interface sites had strong synergistic effects that had a major role in its excellent soot oxidation activity performance. Huang et al. (Huang et al. 2020) synthesized $\text{CeO}_2/\text{MnO}_x$ via the deposition-precipitation method in various morphologies of nano-rods, nano-cubes, and nano-octahedrons for the oxidation of N, N-Dimethyl Formamide(DMF). Huang et al. investigations yielded that the nano-rod morphology of the $\text{CeO}_2/\text{MnO}_x$ catalyst had the best catalytic activity among the synthesized samples due to excellent interactions between the two oxides. These interactions yielded a high specific area, leading to more oxygen defects and an ample amount of active oxygen species. The following sections will deal with the results and discussion of the characterizations and soot oxidation activity of CMX (X = 40 to 100) samples.

5.1 XRD and BET surface area analysis

The XRD spectra of CMX ($\text{Ce}_{1-x}\text{Mn}_x\text{O}_{2-\delta}$, where $x = 0.4$ to 1) catalysts are displayed in **Figure 5.1**; it is noticeable from the spectra that the diffraction peaks at 28.53° , 33.11° , 47.48° , 56.34° , 59.05° , 69.45° , 76.71° , and 79.08° associate to Ceria's cubic fluorite structure, corresponding to planes (111), (200), (220), (311), (222), (400), (331) and (420) respectively (Jampaiah et al. 2019b)(Mukherjee et al. 2016c). The diffraction peaks observed at 17.9° , 29° , 32.4° , 36.1° , 44.5° , 50.9° , 58.5° , 59.8° , and 64.6° pertain to the tetragonal hausmanite spinel structure of Mn_3O_4 corresponding to the planes (101), (112), (103), (211), (220), (105), (321), (224) and (440) (Ji et al. 2019b). The planes of Mn_2O_3 can be observed in **Figure 5.1**, the peaks observed at 23.1° , 33° , 38.2° , 45.2° , 49.3° , 55.2° , and 65.8° corresponding to the (211), (222), (400), (322), (431), (440) and (541) planes (Cheng et al. 2017a). From **Figure 5.1**, it can be observed that with the increase in the Ce content in the CMX (X = 100 to 40) catalysts, the cubic fluorite phase starts emerging and becomes incrementally dominant; simultaneously, the phases of Mn become secondary until CM50. The lattice parameter and crystallite size of the CMX samples are displayed in **Table 5.1**. The lattice parameter variation is from 5.3981 \AA (CM80) to 5.4034 \AA (CM40), the crystallite size

varies from 7 nm (CM50) to 12 nm (CM80), and the lattice strain fluctuates from 0.033 (CM40 and CM60) to 0.043 (CM50) for the CMX catalysts.

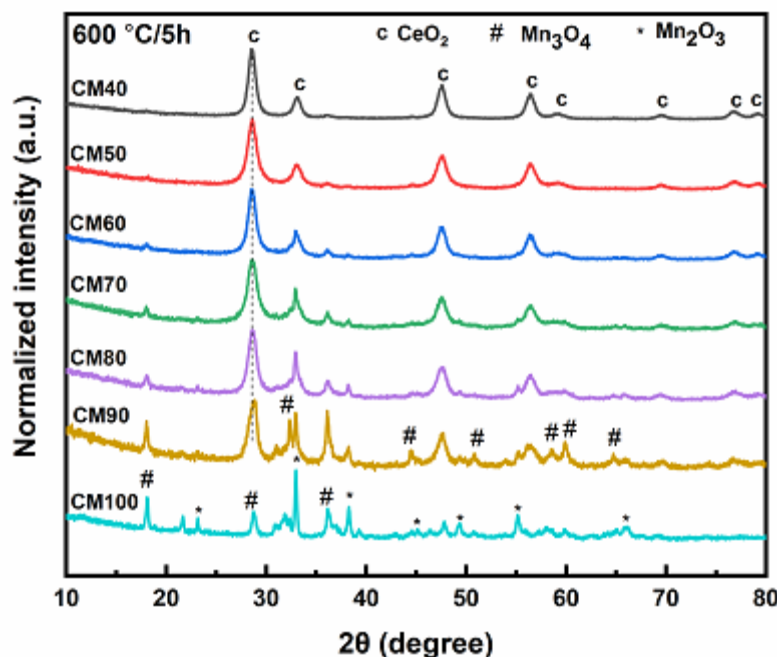


Figure 5.1: XRD pattern of CMX (X = 40 to 100) catalysts calcined at 600 °C/5 h.

The low index plane proportion has an increasing trend with the increase in the mol percentage of Manganese. The same can be seen from **Table 5.1** that CM80 has the highest reactive plane ratios of (220)/(111) (0.5087) and (200)/(111) (0.6886). Higher the (220)/(111) and (200)/(111) ratio, numerous the exposed (220) and (200) planes may have better soot oxidation reactivity, leading to lower T_{50} temperatures (Anantharaman et al. 2019). The results of the BET analysis are in **Table 5.1**. It can be perceived from **Table 5.1** that CM70 has the maximum pore volume (0.166 g/CC), CM60 has the best BET surface area (50 m²/g), and CM90 has the highest pore diameter among the CMX catalyst samples. From **Table 5.1**, it can be noticed that with the increase in the Ceria content, there is a steady increment in BET surface area. The pore diameter and volume increased steadily with an increase in Manganese content, except for pure Manganese oxide, which had the least pore volume (0.0539 cc/g) among the synthesized CMX catalysts. The N₂ isotherm is in **Figure A2.1** in the Appendix-II.

Table 5.1: Lattice parameter (a), Crystallite size (D), Lattice strain, Surface area, pore volume and diameter, average T₅₀ of samples, and Reactive planes of CMX (X = 40 to 100) catalysts calcined at 600 °C/5 h.

Composition	Lattice parameter ^a (Å)	Crystallite size ^a (nm)	Lattice strain ^a	Reactive planes ^a		BET Surface area ^b (m ² /g)	Pore diameter ^b (nm)	Pore volume ^b (cc/g)	Average T ₅₀ ^c (°C)
				(220)/ (111)	(200)/ (111)				
CM40	5.4034	09	0.033	0.4817	0.3294	30	12.9	0.0961	397
CM50	5.4011	07	0.043	0.5046	0.3945	28	16.2	0.1142	391
CM60	5.4014	09	0.033	0.4799	0.3982	50	12.5	0.1552	390
CM70	5.4004	09	0.038	0.4804	0.5393	43	14.4	0.1660	389
CM80	5.3981	12	0.035	0.5087	0.6886	31	21.1	0.1637	400
CM90	--	--	--	--	--	27	21.9	0.1493	408
CM100	---	--	--	--	--	12	18.5	0.0539	431

a: values obtained from XRD analysis.; b: values obtained from BET analysis.; c: values obtained from TGA analysis

5.2 Raman spectra analysis

Figure 5.2 shows the Raman spectra of the synthesized CMX (X = 40 to 100) catalysts. A weak F_{2g} peak is observed at 451 cm^{-1} from CM80 onwards, and its intensity increases as the Ceria content increases in the catalyst. This peak at 451 cm^{-1} is ascribed to the Raman active F_{2g} peak of cubic fluorite structure of Ceria pertaining to the $Fm\bar{3}m$ space group (Putla et al. 2015a) (Anantharaman et al. 2018c; a; Li et al. 2017a; Patil et al. 2019). A gradual blue shift in the F_{2g} peak from 451 cm^{-1} to 458 cm^{-1} for CM80 to CM40 due to comparatively less Mn (smaller ionic radius) getting doped into the Ceria lattice, inducing fewer distortions in the CeO_2 lattice, as observed in **Figure 5.2**.

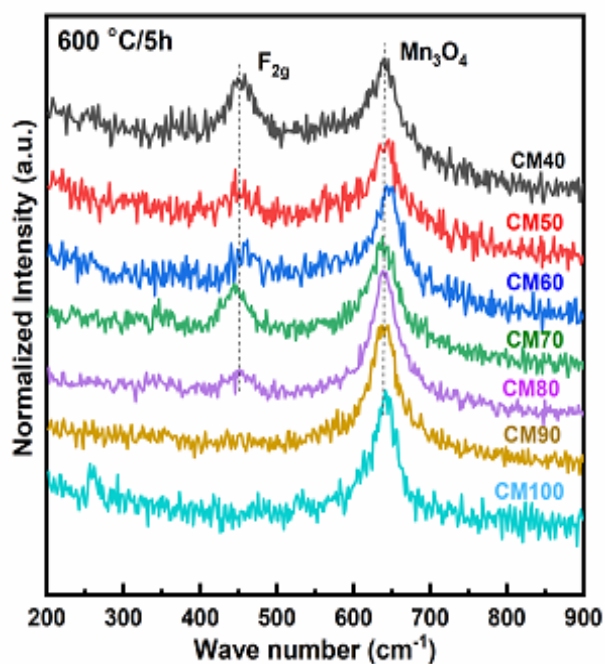


Figure 5.2: Raman spectra of CMX (X = 40 to 100) catalysts calcined at $600\text{ °C}/5\text{ h}$.

Usually, a redshift is observed when there is lattice deformation due to multivalent doping dopants having a relatively smaller ionic radius (Zhu et al. 2022a). A comparatively high intense peak develops around $640\text{ to }645\text{ cm}^{-1}$ from CM40 onwards and intensifies as the Manganese content increases in the CMX catalyst. This

peak could be associated with the Mn_3O_4 crystalline phase stretching mode of Mn-O-Mn. (Venkataswamy et al. 2015b). According to the literature, Wu et al. (Wu et al. 2011b), He et al. (He et al. 2018c), Han et al. (Han et al. 2006), and Kapteijn et al. (Kapteijn et al. 1994) have reported the peak observed in the range of 645 to 653 cm^{-1} in the Raman spectra corresponds to Mn_3O_4 phase.

5.3 FESEM analysis

Figures 5.3(a to g) depict the FESEM images of the CMX (X = 100 to 40) catalysts calcined at 600 °C/5 h. A glance at the images in **Figures 5.3(a to g)** shows the presence of nano-rods with the agglomerates, and it is present in all samples in different concentrations and sizes. Similar kind of results were obtained by Baria et al. (Barai et al. 2016) while synthesizing Manganese oxide via. Acid reduction of $KMnO_4$. The formation of three systems was reported by Baria et al. (Barai et al. 2016), and they are nanorods, nanorods-nanoparticles, and nanoparticles only; this was achieved by varying the concentration of K^+ . These systems were tested for superconductor application, and it was reported by the authors that the extraordinary/unique system of a mixture of nanorods and nanoparticles had a superior electrochemical performance by virtue of better reactive surface sites, high active surface area in the pores of nanoparticles and high surface to volume ratio of nanorods. The authors also reported that such kind of unique system of different morphology would have a beneficial effect on interfacial applications.

In the present study, the formation of the nano-rods, apart from the nano-structured agglomerates, is a very interesting phenomenon. No shape control or such technique was employed in the synthesis process of the CMX catalysts in the current study, making the formation of the nano-rods all the more intriguing. Nano-rods were obtained by a simple co-precipitation method by J. Han et al.; it was reported that the increase in Mn concentration resulted in the further growth of the nano-rods (Xu et al. 2010).

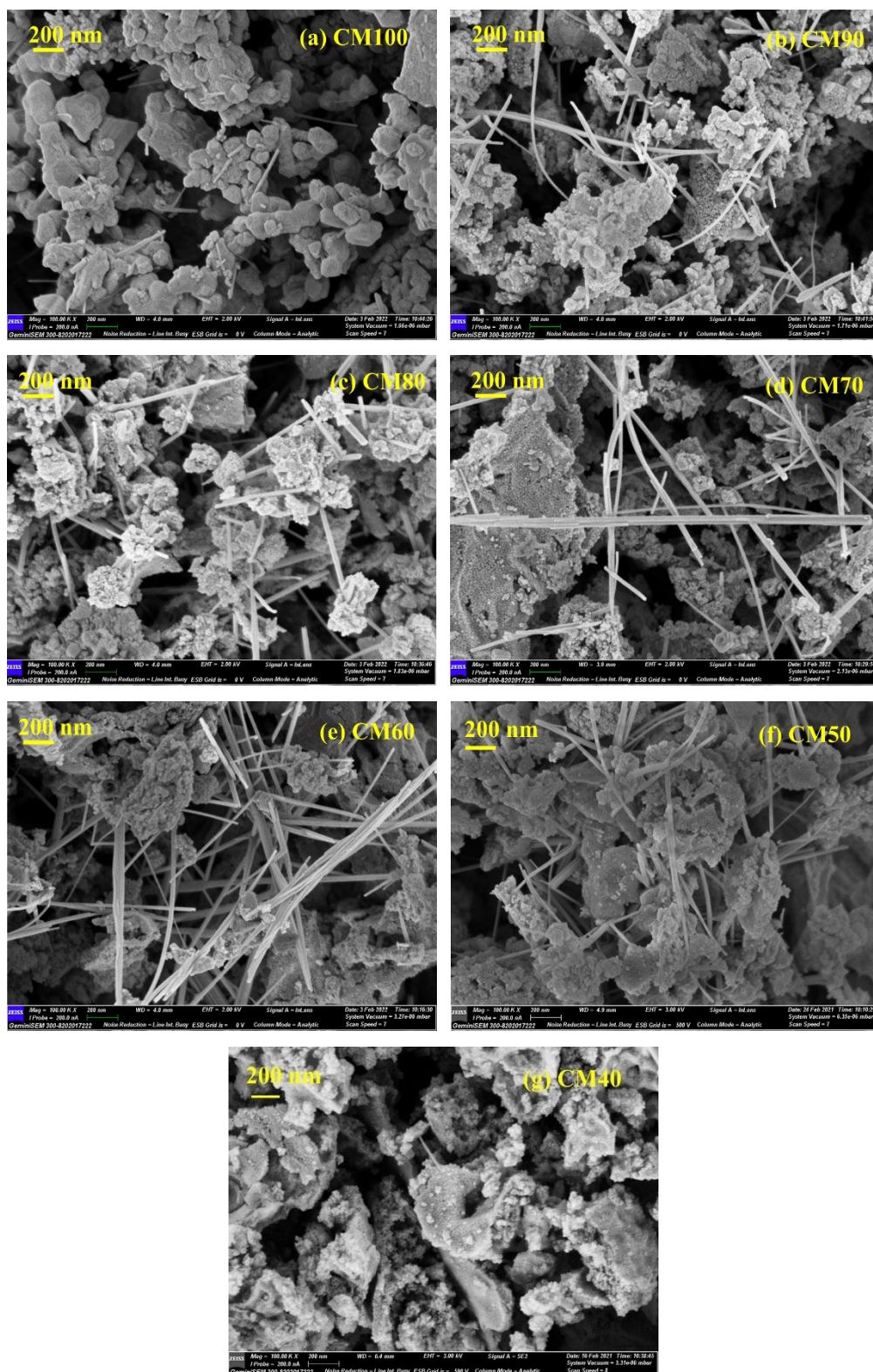


Figure 5.3: FESEM images of (a) CM100, (b) CM90, (c) CM80, (d) CM70, (e) CM60, (f) CM50, and (g) CM40 calcined at 600 °C/5 h.

Table 5.2: EDS analysis of CMX (X = 40 to 90) catalysts calcined at 600 °C/5 h.

Composition	Ce (%)	Mn (%)
CM40	61.47	38.53
CM50	54.09	45.91
CM60	33.57	66.43
CM70	32.90	67.10
CM80	--	--
CM90	--	--

Such a hybrid system (both agglomerates and nano-rods) has not been reported in the literature for the EDTA-Citrate method. The formation of such a hybrid system is observed when the partial solid solution is formed, which can be confirmed by the XRD spectra from **Figure 5.1**. It can be observed that such hybrid formation is also seen in CM100 (only oxide of Manganese) from **Figure 5.3(a)**; with the addition of Ceria, the nano-rods have grown in numbers and size, as seen in **Figures 5.3(b to f)**. Visually it was observed from Figure 5.3(a) (CM100) with incremental addition of 10 mol % of Ceria, the count and the length of the nano-rods increased steadily peaking at Figure 5.3(d) (CM70) and Figure 5.3(e) (CM60) until Figure 5.3(f) (CM50). It is interesting to note that the presence of Ceria may also have encouraged the flourishing of the hybrid phase (nano-rods) up to an extent. On further 10 mol % addition of Ceria to Manganese phase, the system becomes Ceria rich phase. A drastic decrease in the count and length of the nano-rods is observed. This can be attributed to the scarcity of segregated Manganese oxide (specifically MnO₂) due to the lesser mol % of Mn and also relatively more mol % of Ceria being present for the Manganese to get doped into as the catalyst becomes Ceria rich. The scant availability of free Manganese oxide (undoped or segregated) resulted in reduction in the numbers of nano rods and subsequently no hybrid phase existed (from CM30 to CM0). The spectroscopy analysis was done using EDS, and the values as seen in **Table 3**; as seen from the spectroscopy analysis, the composition of the nano-rods consists of oxides of Cerium and

Manganese. No impurities were responsible for forming the nano-rods, as observed in the CMX catalysts synthesized by the EDTA-Citrate method. It would be interesting to know how this hybrid system will affect the soot oxidation activity of these catalysts.

5.4 TEM analysis

Figures 5.4(a to d), 5.5(a to d), and 5.6(a to d) depict the TEM images of CM50, CM70, and CM100, respectively. A look at the TEM images will prove that apart from near-spherical particles, there are also elongated particles in the form of nano-rods, as seen in FESEM images. The SAED patterns of CM50, CM70, and CM100 are shown in **Figures 5.4(e), 5.5(e), and 5.6(e)**, respectively, confirming that the phases of Manganese oxide and Ceria are present in the catalyst samples; no other phases or impurities are present. Also, from **Figures 5.5(a), 5.5(b), and 5.6(b)**, the fringe width has been calculated, and it was found to be that of the α -MnO₂ (0.68 to 0.72 nm) (Lee et al. 2011) (Wang et al. 2007) (Meng et al. 2014).

The TEM images and the SAED patterns of the catalyst samples further add to the evidence seen in the XRD pattern and FESEM analysis that no impurity phase is responsible for forming the nano-rod structures in the CMX samples synthesized by the EDTA-Citrate method. Among the three SAED patterns, CM100 has the most discontinuous pattern, indicating the presence of large polycrystalline particles.

Another striking feature that can be observed from the sample CM50 in **Figure 5.4(c)** and CM70 in **Figure 5.5(c)** is the well-defined grain boundaries, indicating that the grains' sintering might have occurred. Sintering may be attributed to the oxides of Manganese, which are known to be good sintering agents (Zhang et al. 2002) (Zhang et al. 2020).

(Cont...)

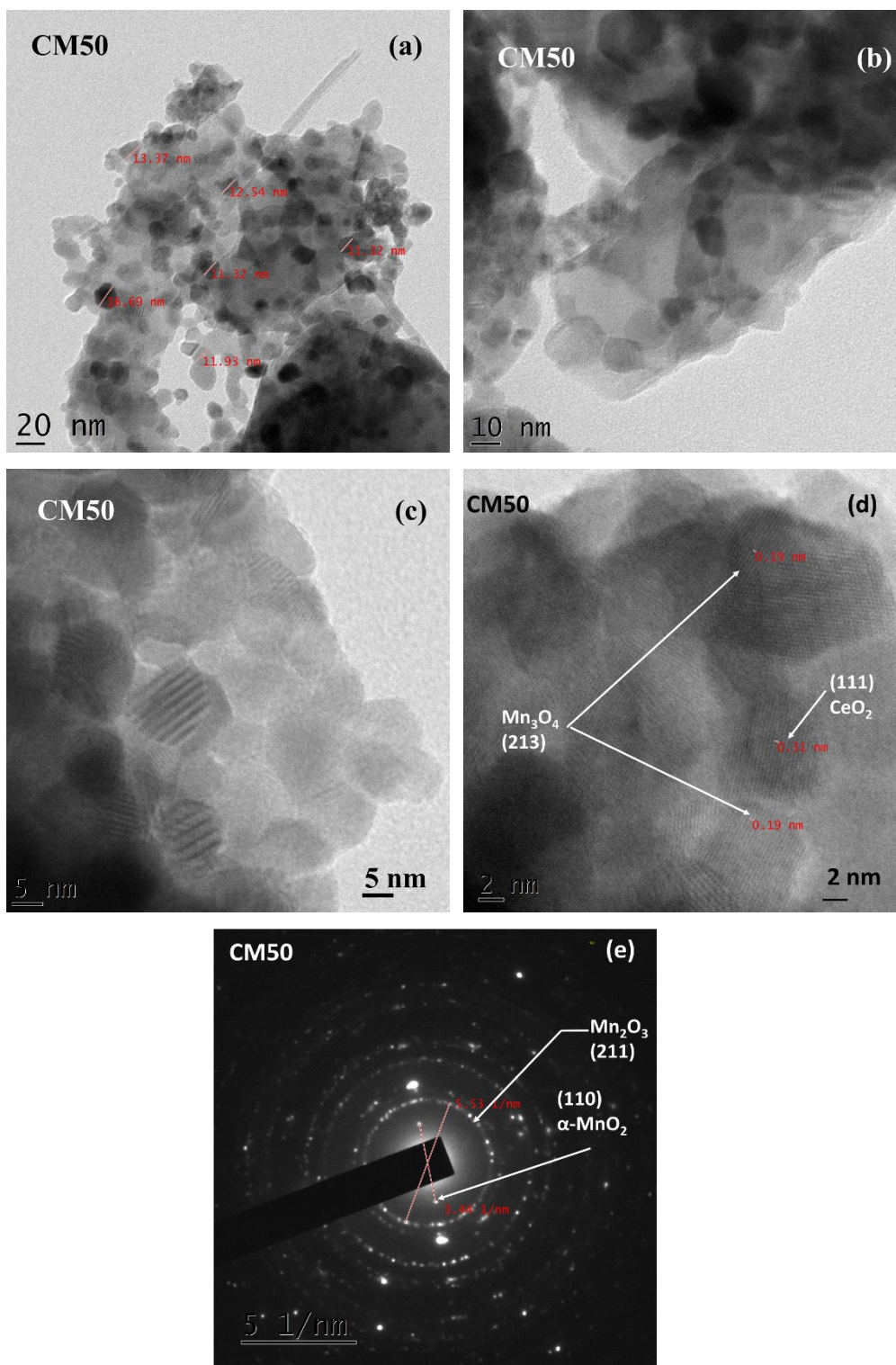


Figure 5.4: TEM images (a to d) and (e) SAED pattern of CM50 catalyst calcined at 600 °C/5 h.

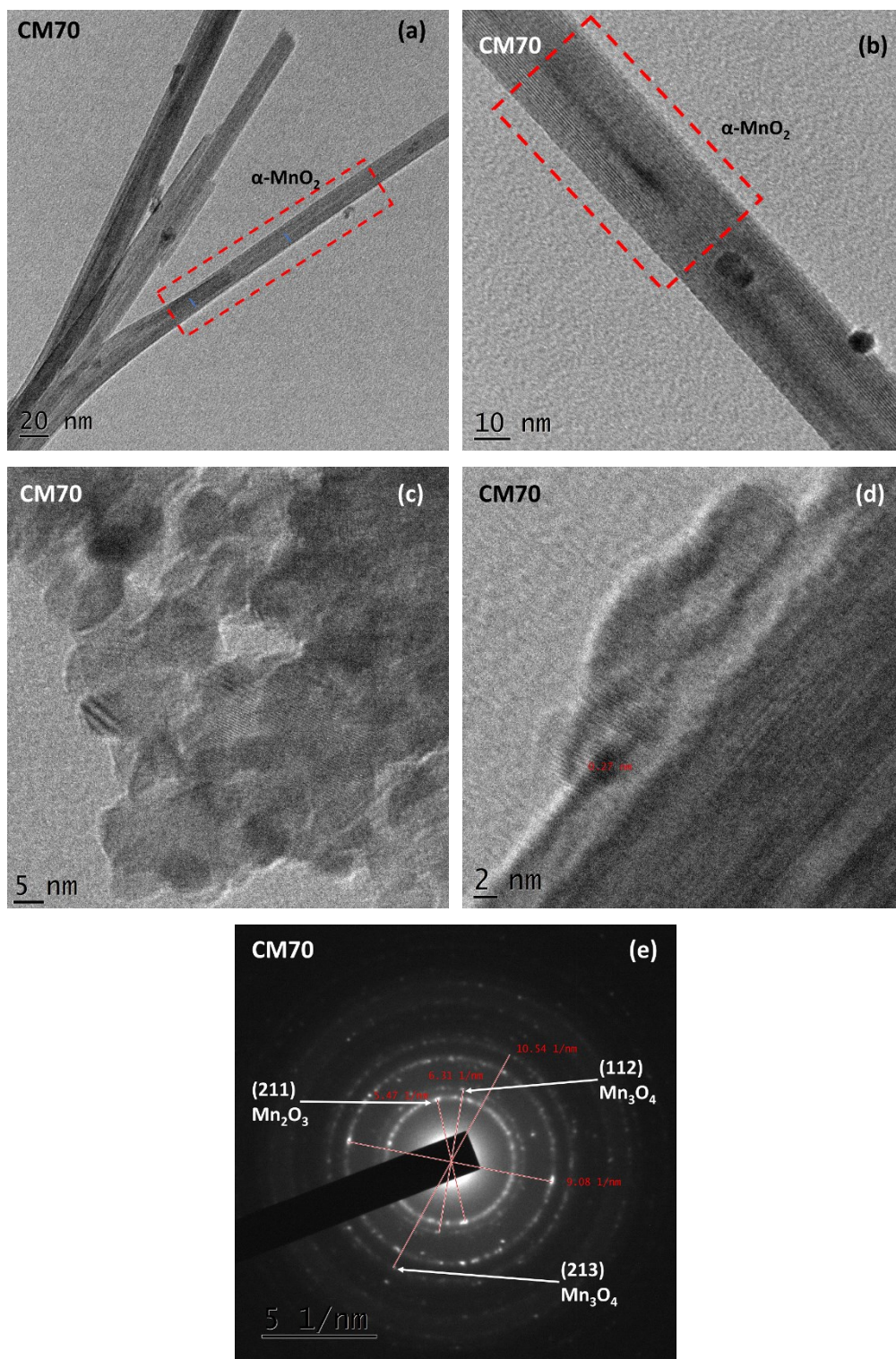


Figure 5.5: TEM images (a to d) and (e) SAED pattern of CM70 catalyst calcined at 600 °C/5 h.

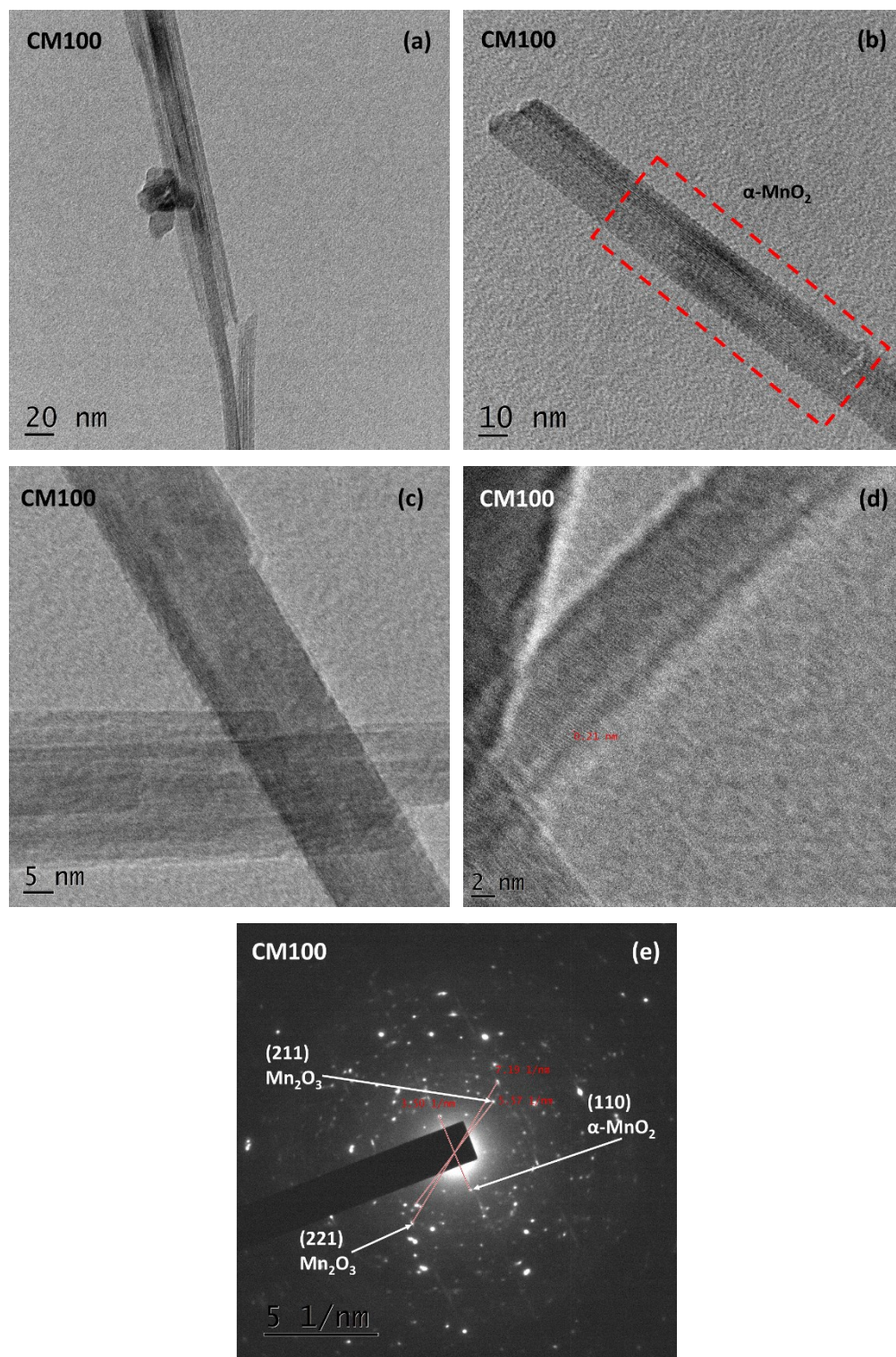


Figure 5.6: TEM images (a to d) and (e) SAED pattern of CM100 catalyst calcined at 600 °C/5 h.

5.5 Soot oxidation activity

Figure 5.7(a) depicts the soot combustion of the CMX catalysts from 200 °C to 630 °C in an air atmosphere at 10 °C/min. The sample mass was adjusted to negate diffusional effects and heat mass transfer constraints. Maini et al. (Maini et al. 2022) had reported usage of very less sample (4 to 5 mg) from the literature for the very same reason. Also, Li et al. (Li et al. 2019a) reported the usage of very less sample for conducting catalytic tests using the TGA. The average T_{50} temperature in increasing order is as follows, CM70 (389 °C) < CM60 (390 °C) < CM50 (391 °C) < CM40 (397 °C) < CM80 (400 °C) < CM90 (408 °C) < CM100 (431 °C). Triplicates of the soot oxidation experiments were performed, and the mean and variance of the T_{50} temperature are shown in **Figure 5.7(b)**.

The introduction of the Ceria into the Manganese oxide had a beneficial effect of decreasing the soot oxidation activity up to CM70, as seen in **Figures 5.7(a)** and **5.7(b)**. From Literature, Sacco et al. (Sacco et al. 2022) synthesized samples of pure Ceria to Manganese of the Ceria Manganese oxide by the citric acid complexation method. It was reported that the presence of Manganese oxide was in Mn^{2+} and Mn^{3+} ions, and Ceria existed in Ce^{3+} and Ce^{4+} ions in the as-synthesized samples. The redox couple of Ceria is well known to bolster oxygen mobility, and doping multivalent Mn ions into Ceria will further improve its oxygen vacancies.

It was also observed through the XPS analysis that the surface of the higher Mn doped Ceria samples was enriched in segregated Mn species of higher oxidation states on the surface of Ceria. The ample presence of higher oxidation state Mn species on the surface of Mn75Ce25(1-CA) catalyst helped it to perform the best ($T_{50} = 325$ °C) among the synthesized catalyst samples. Also, the surface enriched with Mn^{3+} and Ce^{3+} had been reported to have more amount of adsorbed oxygen species on the surface.

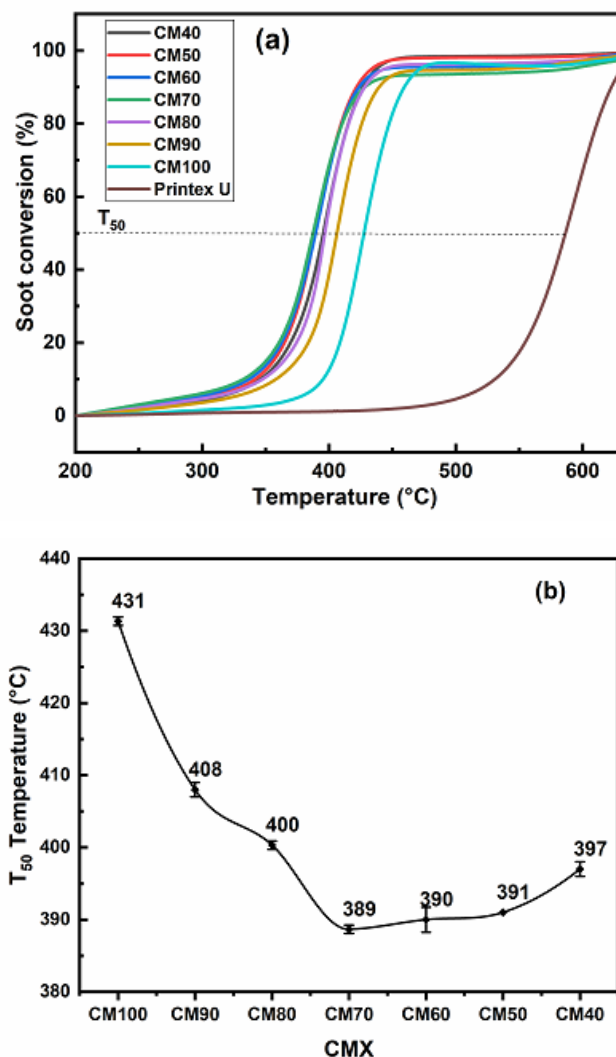


Figure 5.7: (a) Soot conversion (%) of CMX (X = 40 to 100) catalysts. (b) T₅₀ (°C) triplicates error bar graph for CMX catalysts calcined at 600 °C/5 h.

Yang et al. (Yang et al. 2022) reported the presence of Ce³⁺ and Mn⁴⁺ influenced the amount of surface-adsorbed oxygen species of the Ceria-rich Ceria Manganese oxides. It was reported that the higher the magnitude of Ce³⁺ and Mn⁴⁺, the higher the percentage of surface-adsorbed Oxygen species. The presence of a higher amount of adsorbed Oxygen species had a direct effect on the soot oxidation activity of the catalysts. It was reported that MC-0.40 had the best soot oxidation activity (T₅₀ = 565 °C), and coincidentally, the same composition had the highest adsorbed oxygen species. Jampaiah et al. (Jampaiah et al. 2019a) reported a T₅₀ of 350 °C for 20 Mn₃O₄/CeO₂ Microspheres (MSs), and the presence of the highest amount of Chemisorbed Oxygen

species known through XPS analysis was the reason for the best soot oxidation activity among the flower-like Ceria- Manganese oxides MSs. Lin et al. (Lin et al. 2018b) reported that the presence of reactive adsorbed oxygen species and the redox couple set in the oxidation states of Ceria (Ce^{3+} and Ce^{4+}) and Manganese oxide (Mn^{2+} , Mn^{3+} , and Mn^{4+}) are the crucial parameters influencing the soot oxidation reaction. Mukherjee et al. (Mukherjee et al. 2016b) conducted the soot and CO oxidation analysis on varied dopants (Zr, La, Mn, Fe, Hf, and Pr) in Ceria. It was reported that CM (Cerium Manganese oxide) performed the best in soot oxidation ($T_{50} = 390\text{ }^{\circ}\text{C}$ or 663 K) and CO conversion ($T_{50} = 117\text{ }^{\circ}\text{C}$ or 390 K) as it possessed surface adsorbed species (O_{β}) compared to other doped Ceria samples.

The occurrence of the nano-rods has undeniably augmented the soot oxidation activity, as seen from the T_{50} temperatures of CMX catalysts. Huang et al. (Huang et al. 2017) synthesized $\text{Ce}_{1-x}\text{Mn}_x\text{O}_2$ by sol-gel method and reported their lowest T_{50} temperature as $383\text{ }^{\circ}\text{C}$ for $\text{Ce}_{0.5}\text{Mn}_{0.5}\text{O}_2$. The T_{50} of CM50 in the present study is close to the reported value of $391\text{ }^{\circ}\text{C}$. The soot oxidation activity of Ce-Mn mixed oxide catalysts synthesized through the co-precipitation method by Zhu et al. (Zhu et al. 2022b) yielded the lowest T_{50} temperature of $306\text{ }^{\circ}\text{C}$ for $\text{Ce}_{0.64}\text{Mn}_{0.36}$ and $310\text{ }^{\circ}\text{C}$ for $\text{Ce}_{0.80}\text{Mn}_{0.20}$ sample.

Li et al. (Li et al. 2019b) reported The least T_{50} temperature among the Ceria and Fe doped Ceria samples as $371\text{ }^{\circ}\text{C}$ for $\text{Fe}_5\text{Ce}_{95}$ synthesized by Solution Combustion Synthesis (SCS) method and reported a T_{50} temperature of $476\text{ }^{\circ}\text{C}$ for $\text{Fe}_{30}\text{Ce}_{70}$. The best performance of 5% Fe doped Ceria sample was attributed to the ample amount of contact points due porous structure of the sample. The relatively modest performance of $\text{Fe}_{30}\text{Ce}_{70}$ by the SCS method was due to low surface area (2 to 3 m^2/gm). Govardhan et al. (Govardhan et al. 2022) reported the least T_{50} temperature of $387\text{ }^{\circ}\text{C}$ (660 K) for the 5% Ag loaded $\text{Ce}_{0.8}\text{Pr}_{0.2}\text{O}_{2-\delta}$. The activity reported was attributed to the surface concentration of Ce^{3+} and Ag^+ coupled with rich adsorbed surface oxygen species. The T_{50} temperatures of CM50 to CM70 in the present study are very close, and the concentration of nano-rods is higher when compared to other CMX catalysts. Although

there is a variation in BET-specific surface area, pore diameter, and pore volume in the CM50 to CM70 samples, the soot oxidation activity remains almost similar. From the literature, Li et al. (Li et al. 2019a) reported the findings of the soot oxidation activity (tight contact mode) of Fe doped Ceria by co-precipitation (CP) and Solution Combustion Synthesis (SCS). The sample prepared by the SCS method performed better than the one prepared by CP. The better performance was attributed to the porous structure of the SCS sample. Although the surface area of the CP sample was more than SCS, the SCS sample had high porosity with a larger pore diameter that increased the contact points and mobility of the adsorbed active oxygen species. The trend changed with higher doping of Fe into Ceria, as the surface area reduced drastically, resulting in fewer contact points. The similarity can be credited to the greater concentration of nano-rods in these catalysts since nano-rods have more contact points, more reactive planes exposed, and oxygen vacancies, and overall improves the catalytic activity compared to near spherical particles/agglomerates (Chen et al. 2020).

Wang et al. (Wang et al. 2021) reported that the Ceria nano-rods have better soot oxidation activity due to their exposed reactive facets/planes. Lykaki et al. (Lykaki et al. 2018), while investigating the Catalytic activity (CO oxidation) of nano-rod morphology of Cu/CeO₂, reported that the rod morphology has more concentration of weak/loosely bound Oxygen species, aiding in better mobility and vacancy of Oxygen. **Figures 5.8(a to c)** show the soot oxidation activity of CM50, CM80, and CM100 at varied ramping rates (5, 10, 15, and 20 °C/min), respectively. Ozawa and KAS methods calculated the activation energy of the CM50, CM80, and CM100 from the data obtained through **Figures 5.9(a to c)** and **5.10(a to c)**.

Both Ozawa and KAS methods have shown quite a similar trend in the activation energy of the evaluated samples. The average activation energy evaluated from the Ozawa method for CM50, CM80, and CM100 is 131 kJ/mol, 132 kJ/mol, and 137 kJ/mol, respectively, and that of the KAS method is 127 kJ/mol, 128 kJ/mol, and 133 kJ/mol. Herein, it can be noticed that the activation energy of CM50 is similar to the CM70 sample. This may be due to the fact that both CM50 and CM70 have very close

(difference of less than 10 °C) T₅₀ temperatures for the soot oxidation runs conducted at different heating rates (5, 10, 15, and 20 °C). The same cannot be said for the activation energy of CM100, whose difference (30 to 40 °C) in T₅₀ is quite significant when compared to CM80 and CM50. CM50 has the least activation energy of 131 kJ/mol (Ozawa method) and 127 kJ/mol (KAS method). CM50 (391 °C) T₅₀ temperature too is quite close to the best performing catalyst CM70 (389 °C) and can be considered as one of the best performing CMX among the synthesized CMX (X = 40 to 100) samples.

The CM100 Catalyst performed modestly among all the samples in the soot oxidation activity with a T₅₀ temperature of 431 °C and activation energy of 137 kJ/mol (Ozawa) and 133 kJ/mol (KAS). From the literature, it can be seen that there is not a clear and direct trend between activation energy and T₅₀ temperature (soot oxidation activity), Maini et al. (Maini et al. 2022) reported the activation energy of Ceria for soot oxidation as 133 kJ/mol (non-isothermal Kissinger method) and that of uncatalyzed soot reaction as 170.5 kJ/mol.

Shourya and H.P. Dasari (Shourya and Dasari 2022) reported CM5 with a T₅₀ of 360 °C and activation energy of the soot oxidation activity of CM5 to be 118 kJ/mol (Ozawa) and 114 kJ/mol (KAS). The catalytic activity of the modestly performing sample was CM0 with a T₅₀ temperature of 405 °C and activation energy of 121 kJ/mol (Ozawa) and 116 kJ/mol (KAS). Govardhan et al. (Govardhan et al. 2022) reported an activation energy of 149.86 kJ/mol for 5Ag/PDC (T₅₀ = 387 °C or 660 K) and 140.06 kJ/mol for 0Ag/PDC (T₅₀ = 458 °C or 731 K). Jampaiah et al. (Jampaiah et al. 2017) reported the soot oxidation activity of Cu and Co bi-doped α -MnO₂ nanowires with a T₅₀ temperature of 279 °C and an activation energy of 121 kJ/mol (Ozawa method).

(Cont...)

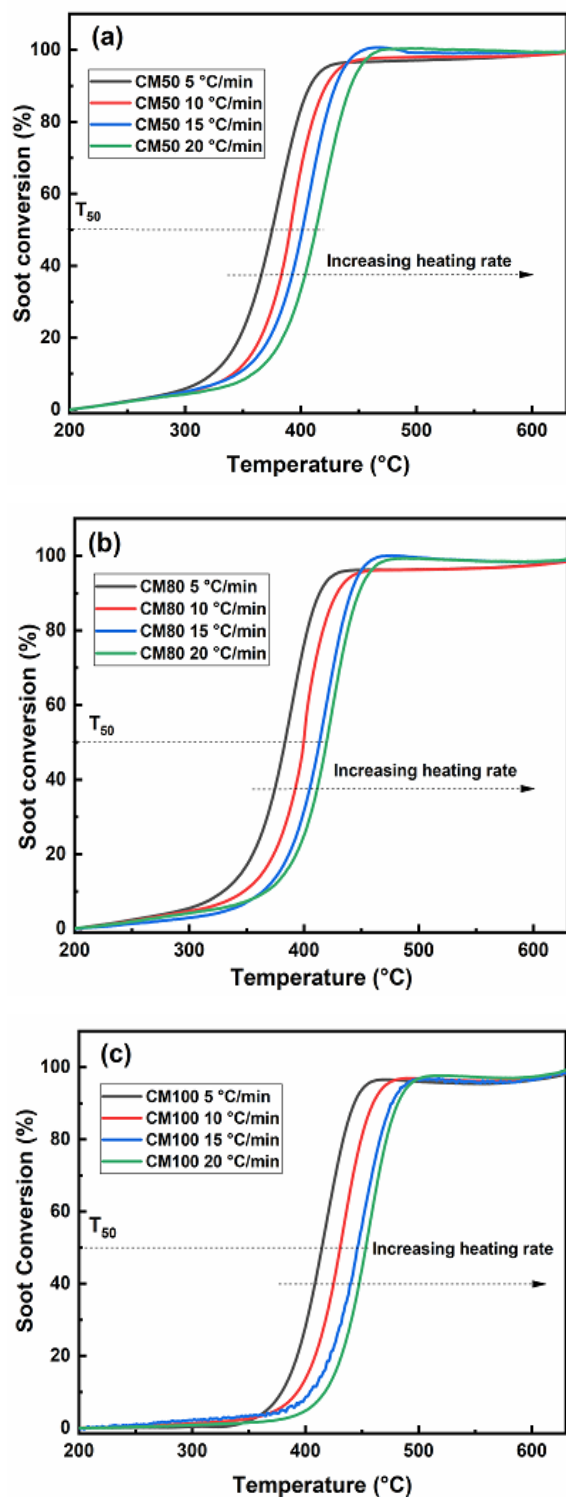


Figure 5.8: Soot conversion (%) at ramp-up rates of 5, 10, 15, and 20 °C/min over (a) CM50, (b) CM80, and (c) CM100 catalysts calcined at 600 °C/5 h.

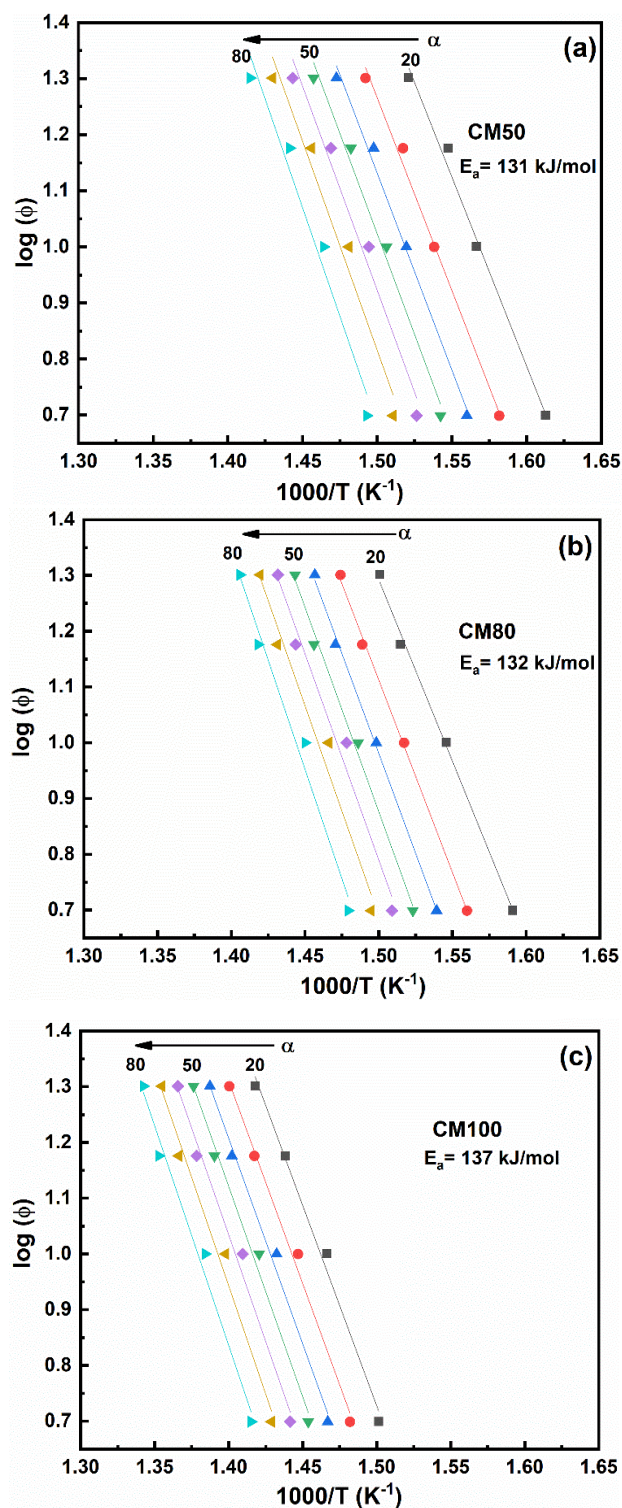


Figure 5.9: Ozawa plots of (a) CM50, (b) CM80, and (c) CM100 catalysts calcined at 600 °C/5 h.

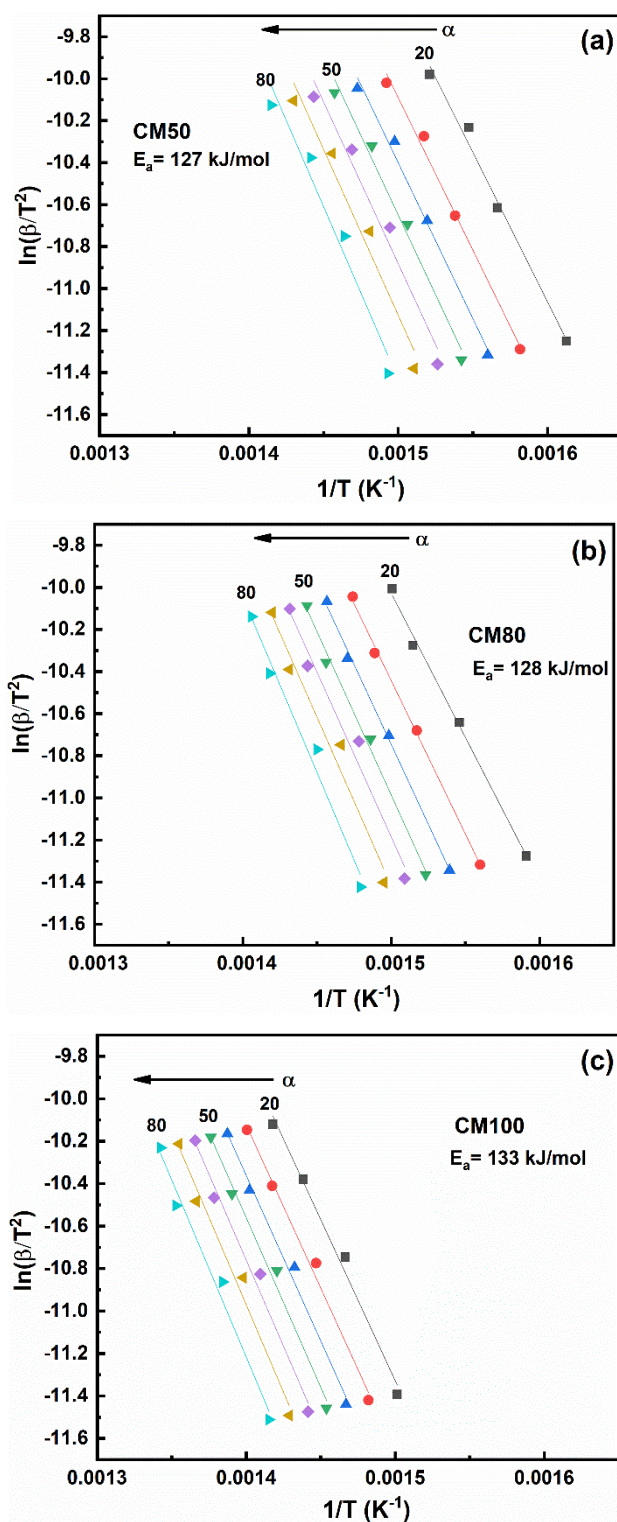


Figure 5.10: KAS plots of (a) CM50, (b) CM80, and (c) CM100 samples calcined at 600 °C/5 h.

Lee et al. (Lee et al. 2015) synthesized Ag loaded Ceria electrospun nano-fibers soot oxidation activity. It was reported that the Ag/CeO₂-500 and CeO₂-500 had the lowest T₅₀ temperature of 429 °C (tight contact), but the activation energy was 112.1 kJ/mol (Ag/CeO₂-500) and 123.2 kJ/mol (CeO₂-500). Therefore, from the literature, one cannot make a direct relationship between T₅₀ temperature and the activation energy of soot oxidation of a particular composition of a catalyst. There are more parameters in play that influence both the catalytic activity and activation energy. There is a considerable decrease in the activation energy of soot oxidation in comparison with the activation energy of uncatalyzed soot (Printex-U) oxidation that fluctuates from around 154 kJ/mol (Palmisano et al. 2006), 150 kJ/mol (Krishna et al. 2007b) to 161 kJ/mol (Kalogirou and Samaras 2010).

The incremental addition of Ceria into Manganese oxide has visually given evidence from **Figures 5.3(a to g)** that the concentration of nano-rods has increased, and the increasing trend can be observed until CM50. The further increase in the Ceria's addition into Manganese oxide showed reduced nano-rod concentration. This phenomenon may indicate that more Manganese is getting doped into Ceria, as noticed from the XRD spectra in **Figure 5.1**, wherein the cubic fluorite structure peaks were seen predominantly with the increasing addition of Ceria into Manganese oxide from CM80. **Figure 5.7(b)** shows a similar trend to the concentration of nano-rods. The T₅₀ temperature initially reduces as the concentration of nano-rods increases. Then, it is almost constant, followed by a slight increase in the T₅₀ temperature.

Raman spectroscopy analysis reveals that the Mn₃O₄ phase has formed in CM100 at around 640 cm⁻¹. As the Ceria content increased in the CMX catalysts, a weak F_{2g} peak of Ceria was observed from CM80 onwards, and the peak's intensity increased as the Ceria content increased. Soot oxidation activity revealed that CM70 had the lowest T₅₀ temperature (389 °C) among the synthesized catalysts, although CM50 and CM60 had their T₅₀ temperatures close to the CM70, as seen in **Figure 5.7(b)**. This behavior can be associated with the nano-rods formed in these samples.

Furthermore, to investigate the crucial nature of contact points and morphology from the literature, Li et al. (Li et al. 2019b) investigated the soot oxidation reaction using an Environmental Transmission Electron Microscope (ETEM) to visualize the real-time soot oxidation reaction of commercial Ceria and 5, 10, 20, and 30 % Fe doped Ceria samples. The best performance of the 5% Fe doped Ceria sample was attributed to the abundant amount of contact points due to porous structure of the sample. The relatively modest performance of Fe₃₀Ce₇₀ by the SCS method was due to low surface area (2 to 3 m²/g). The contact dynamics of the soot and catalyst were examined thoroughly. The visual evidence proved without any doubt that the porous structure (pore diameter and volume) and morphology, in general, do help in better soot oxidation activity by means of providing numerous contact points and its lower density, aiding in its mobility towards the soot particles under tight contact conditions. They also found that the dispersed ultrafine catalyst particles also improve the soot oxidation activity as a result of contact area/points for the carbon particles to interact and oxidize.

Maini et al. (Maini et al. 2022) studied the catalyzed and non-catalyzed soot oxidation reactions using TGA/DSC and Environmental Scanning Transmission Electron Microscope (ESTEM) techniques. The soot oxidation kinetics were studied by using TGA/DSC, and the kinetic parameters were evaluated for catalyzed and uncatalyzed soot oxidation reactions. The visualization gave a critical point regarding the contact points and proximity/contact mode of the soot particles with the catalyst. The Nano rods obtained in the synthesis of the CMX catalyst have a higher number of contact points than the agglomerated particles, and this plays a key role in the soot oxidation activity. The number and concentration of the nano-rods have a prominent factor in the reduction and proximity of the T₅₀ temperatures obtained. The reactive planes, especially (220)/(111), pore diameter, pore volume, and BET surface area, seem to influence the soot oxidation activity. It can be observed from **Table 5.1** that even though CM80 has one of the least surface areas, it has the highest Reactive plane ratios, pore diameter, and volume among all the synthesized CMX catalysts that propel its soot oxidation activity.

5.6 Conclusions

The CMX (X = 40 to 100) catalysts were successfully synthesized by the EDTA-Citrate method. XRD analysis has shown the formation of Mn²⁺ and Mn³⁺ for the synthesized CM100 sample and, subsequently, the formation of partial solid solution and Ceria diffraction peaks until CM40. There was little variation in the lattice parameter (~ 5.4 Å). The reactive planes improved the soot oxidation activity, primarily the (220) planes, and the CMX catalysts from CM40 up to CM80 had their T₅₀ temperature (390 to 400 °C) in a close range. There isn't considerable change in the crystallite size with increasing Ceria's content. However, with an increase in Ceria content, there was a drastic enhancement in specific surface area from 12 m²/g (CM100) to 50 m²/g (CM60), and after that, there was a sudden decrease. This trend coincides with the observed FESEM images, where the concentration of nano-rods has increased from CM100 to CM60.

Further, the Energy Dispersive Spectroscopy (EDS) analysis shows that the composition of the nano-rods is oxides of Cerium and Manganese and not of any impurity. The results from HRTEM images and SAED analysis further reinforce this fact. The T₅₀ temperature of the CM80 (400 °C) catalyst is relatively close to the lowest T₅₀ temperature (390 °C), implying the fact stated earlier that the combination of availability (concentration and number) of nano-rods, high pore characteristics (pore volume and pore diameter), and high reactive plane ratios. The same can be comprehended for the better performance of the CM50, CM60, and CM70 catalysts. The unintended formation of the nano-rods has an incredible enhancing outcome on the soot oxidation activity of the CMX catalyst synthesized via the EDTA-Citrate method. The next Chapter will discuss the CO oxidation and characterization of Structured catalyst (catalyst coated on Alumina wash-coated Cordierite). The characterization techniques utilized are XRD, Raman spectroscopy, BET, Optical Imaging, and FESEM analysis.

CHAPTER 6

CO OXIDATION OVER STRUCTURED CATALYSTS

Structured catalysts have been extensively utilized for heterogeneous catalytic reactions. The success of structured catalysts in reducing automobile exhaust emissions has garnered interest among the scientific community to utilize the same concept for chemical catalytic reactions. Cordierite is one of the materials commonly used as a substrate for structured catalysts. As observed from the literature review and summary, CO oxidation on structured catalysts reported are few. The following sections deal with Ceria-Manganese coated structured (Cordierite) catalysts characterization, and CO oxidation results with appropriate discussion.

RESULTS AND DISCUSSION

6.1 XRD, BET, and BJH analysis

Figure 6.1 shows the XRD spectra of samples Cord to CM100/Al₂O₃/Cord calcined at 700 °C/2h. The Cordierite (2MgO.2Al₂O₃.5SiO₂) peaks are shown with a ‘*’, and they follow the trend as seen in the literature (Lu et al. 2011)(Ai et al. 2022; Lu et al. 2017; Zhou et al. 2017). The peaks of Cordierite are sharp, indicating good crystallinity as they are sintered at relatively high temperatures (>1000 °C) after extrusion. The γ -Alumina characteristic peaks were seen in the Al₂O₃/Cord spectra indicated with ‘ γ ’. L. Tang et al. (Tang et al. 2017) observed similar γ -Al₂O₃ peaks in their investigation of coating LaCoO₃ catalyst on Alumina wash-coated cordierite.

It is evident from the spectra of CM0/Al₂O₃/Cord (from **Figure 6.1**) that the diffraction peaks obtained at 28.55°, 33.12°, 47.47°, and 56.33° pertain to cubic fluorite structure of ceria corresponding to planes (111), (200), (220), and (311) respectively (Jampaiah et al. 2019b)(Mukherjee et al. 2016c). It can be observed that with the

increase in Mn doping, there is a reduction in the peak intensity in samples CM0/Al₂O₃/Cord to CM70/Al₂O₃/Cord. No diffraction peaks of Mn were observed in the CM5/Al₂O₃/Cord, indicating a complete solid solution. Zhao et al. (Zhao et al. 2017) observed wide diffraction peaks and no observable shift in the XRD spectra, attributed to MnO_x existing in a highly dispersed phase.

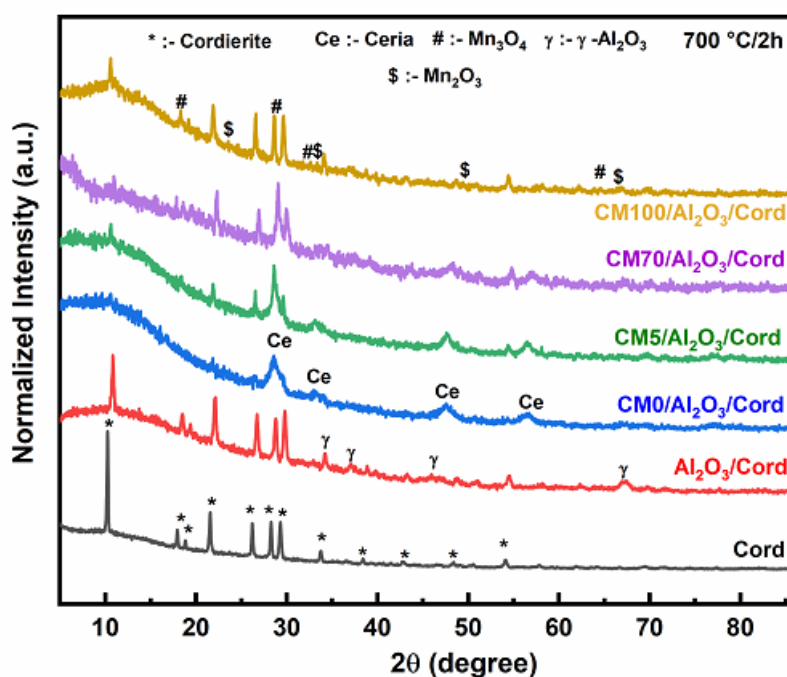


Figure 6.1: XRD pattern of samples Cord to CM100/Al₂O₃/Cord calcined at 700 °C/2 h.

The diffraction peaks observed in CM100/Al₂O₃/Cord of **Figure 6.1** at 17.9°, 29°, 32.4°, and 64.6° pertain to the tetragonal hausmanite spinel structure of Mn₃O₄ corresponding to the planes (101), (112), (103), and (440) (Ji et al. 2019b)(Jampaiah et al. 2019b). Also, the planes of Mn₂O₃ can be observed from the peaks observed at 23.1°, 33°, 49.3°, and 65.8, corresponding to the (211), (222), (431), and (541) planes (Cheng et al. 2017a). Wang et al. (Wang et al. 2017) reported that doping manganese into ceria increased oxygen vacancies due to the defects induced by the smaller Mn⁺ ions. It was reported that the created oxygen vacancies might act as active sites (Zhou et al. 2014). But with an increase in the Mn content from samples CM5/Al₂O₃/Cord to CM100/Al₂O₃/Cord, the diffraction pattern of Mn is observed pointing to the formation

Ceria-Manganese Mixed Oxides as Catalyst for Soot and CO Oxidation Activity.

of partial solid solution and separation of phases. Another observation that can be made from the XRD spectra from **Figure 6.1** is the intensity of cordierite peaks diminished or were absent in the spectra of coated cordierite. It can be observed that some cordierite reflections diminished in Al₂O₃/Cord. The CM0/Al₂O₃/Cord sample has hardly any reflections of the cordierite phase in its spectra. Samples CM5/Al₂O₃/Cord and CM70/Al₂O₃/Cord have highly diminished reflections of cordierite peaks. The characteristic peaks of cordierite as observed from the XRD spectra in **Figure 6.1**, comparative to all the coated catalyst samples (as in CM0/Al₂O₃/Cord, CM5/Al₂O₃/Cord, and CM100/Al₂O₃/Cord) were more pronounced in the CM100/Al₂O₃/Cord. The diminishing or absence of the cordierite phases may indicate the formation of layer of coating on top of the cordierite honeycomb substrate. The idea of uniformity, thickness, and the strength of the Alumina and catalyst coating can be better ascertained by visual inspection and adherence test.

Table 6.1: CO oxidation, BET, and BJH results of samples Cord to CM100/Al₂O₃/Cord.

Sample	CO conversion		BET and BJH		
	T ₅₀ (°C)	T ₉₀ (°C)	SSA (m ² /g)	Pore size (nm)	Pore volume (cc/g)
Cord	784	829	8.34	3.17	0.013
Al₂O₃/Cord	622	664	36.14	8.96	0.162
CM0/Al₂O₃/Cord	311	367	28.37	5.01	0.071
CM5/Al₂O₃/Cord	195	233	19.89	6.11	0.067
CM70/Al₂O₃/Cord	157	195	24.52	7.99	0.098
CM100/Al₂O₃/Cord	181	220	14.84	7.30	0.054

The BET and BJH analysis results are shown in **Table 6.1**. On wash coating the Cord with γ -Al₂O₃, there is a dramatic increase in the average specific surface area accompanied by a consequent increase in the average pore size and volume, respectively. γ -Al₂O₃ was utilized for increasing the substrates' surface area so that the catalyst's active component could be finely dispersed over its surface. The catalyst

Ceria-Manganese Mixed Oxides as Catalyst for Soot and CO Oxidation Activity.

coating on the surface visibly reduces the surface area, pore size, and volume characteristics. From **Table 6.1**, it can be known that CM70/Al₂O₃/Cord has the highest surface area (24.52 m²/g), pore size (7.99 nm), and pore volume (0.098 cc/g) compared to the other samples.

6.2 Raman Spectroscopy analysis

Figure 6.2 shows the Raman spectra of the samples Cord to CM100/Al₂O₃/Cord calcined at 700 °C/2h. The Raman spectra of Cord and Al₂O₃/Cord are similar in pattern, but the intensity of sample Al₂O₃/Cord is lesser. The slight diminishing of the intensity may be due to the wash-coating of Alumina on the surface of the Cordierite. The intensity of the cordierite phase drastically diminishes in the catalyst-coated samples (namely samples CM0/Al₂O₃/Cord to CM100/Al₂O₃/Cord), further augmenting the observation made in the XRD spectra (as observed in **Figure 6.1**) that the catalyst has been coated onto the cordierite honeycomb. The intense peak F_{2g} peak seen at 462.53 cm⁻¹ in the Raman spectra of CM0/Al₂O₃/Cord to CM70/Al₂O₃/Cord corresponds to the first-order scattering and symmetric breathing of the oxygen atom in Ce-O-Ce (Shourya and Dasari 2022)(Anantharaman et al. 2017)(Li et al. 2017a).

On observing the Raman spectra of the doped ceria samples in **Figure 6.2**, a redshift of the F_{2g} peak to lower wavenumbers was observed, indicating the formation of Ce-Mn solid solution and defects (O₂ vacancies and lattice defects) (Kan et al. 2017), and also the peaks had become more diffuse/broadened (Hong et al. 2011). The redshift may be due to variations in the ionic radius of Ce and dopant atoms (Wheeler and Khan 2014). Also, with increased Mn doping, the intensity and sharpness/broadness of F_{2g} decrease, indicating the formation of Oxygen vacancies and solid solution (Venkataswamy et al. 2015a)(Tang et al. 2018).

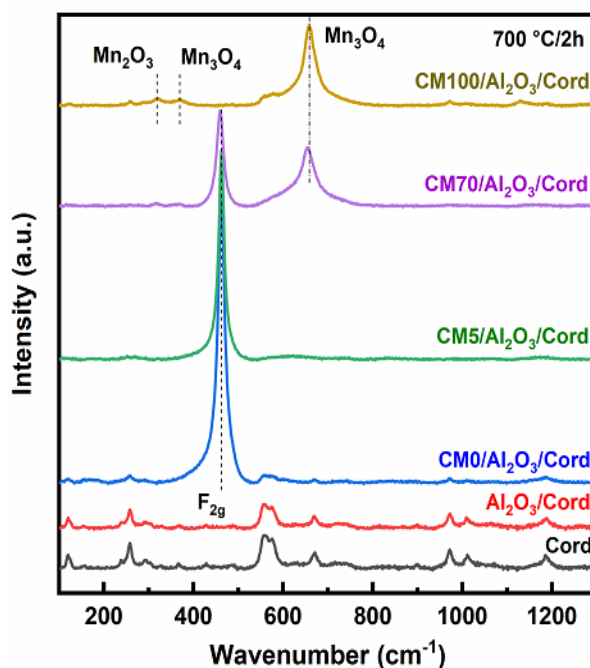


Figure 6.2: Raman spectra of Cord to CM100/Al₂O₃/Cord calcined at 700 °C/2 h.

From **Figure 6.2**, a peak appears at around 658 cm⁻¹ from sample CM70/Al₂O₃/Cord onwards and increases in intensity. This peak can be attributed to the Mn₃O₄ crystalline phase stretching mode of Mn-O-Mn. (Venkataswamy et al. 2015b)(Kaplin et al. 2019). From the literature, Kaplin et al. (Kaplin et al. 2019), Kapteijn et al. (Kapteijn et al. 1994), Han et al. (Han et al. 2006), Wu et al. (Wu et al. 2011b), and He et al. (He et al. 2018c) have reported the peak seen from about 645 to 660 cm⁻¹ in the Raman spectra corresponds to the Mn₃O₄ phase. The appearance of the Mn peak in CM70/Al₂O₃/Cord provides evidence that phase separation is taking place and a partial solid solution has formed. Further small peaks at around 319 cm⁻¹ and 369 cm⁻¹ observed from CM70/Al₂O₃/Cord correspond to Mn₂O₃ and Mn₃O₄ bending modes of Mn-O-Mn, respectively (Venkataswamy et al. 2015b). The inference augments the observation made in XRD analysis regarding the partial solid solution. Observing the effect of separation of phase (or) formation of partial solid solution on the CO oxidation activity will be interesting.

6.3 Adherence test and optical imaging analysis

The samples Al₂O₃/Cord to CM100/Al₂O₃/Cord were subjected to an adherence test after Alumina wash-coat and catalyst coating. It was observed that a very minute amount of Alumina (< 40 mg) and catalyst (~ 10 to 70 mg) was lost.

Table 6.2: Adherence test of samples Al₂O₃/Cord to CM100/Al₂O₃/Cord.

Sample	Alumina Wash-coat			Catalyst coating		
	Before (g)	After (g)	Wt. loss (%)	Before (g)	After (g)	Wt. loss (%)
Al ₂ O ₃ /Cord	17.4472	17.4144	0.19	--	--	--
CM0/Al ₂ O ₃ /Cord	17.6549	17.6433	0.07	19.3589	19.3430	0.08
CM5/Al ₂ O ₃ /Cord	16.9069	16.9010	0.03	18.6267	18.6068	0.11
CM70/Al ₂ O ₃ /Cord	17.5774	17.5695	0.04	19.3318	19.3015	0.16
CM100/Al ₂ O ₃ /Cord	17.6578	17.6459	0.07	19.2960	19.2224	0.38

The maximum loss of ~70 mg accounts for 0.38 %, as observed from **Table 6.2**, i.e., the coating has very good adherence. The optical images of the samples Cord to CM100/Al₂O₃/Cord captured digitally are shown in **Figure 6.3(a to f)** in magnifications of 400 μm. The coating is observed by a clear increase in the channels' width and rounding/filleting of the corners seen in **Figure 6.3** for samples Al₂O₃/Cord to CM100/Al₂O₃/Cord, proving the observation made from the diminishing of cordierite peaks in the XRD (**Figure 6.1**) and Raman Spectra (**Figure 6.2**). The coating seems to be slightly non-uniform, given that some rough edges are seen to increase with the increase in Mn doping progressively. Still, it is visually evident that the coating has been achieved. Further investigation regarding the nature of the agglomerates/particles has to be analyzed using FESEM imaging.

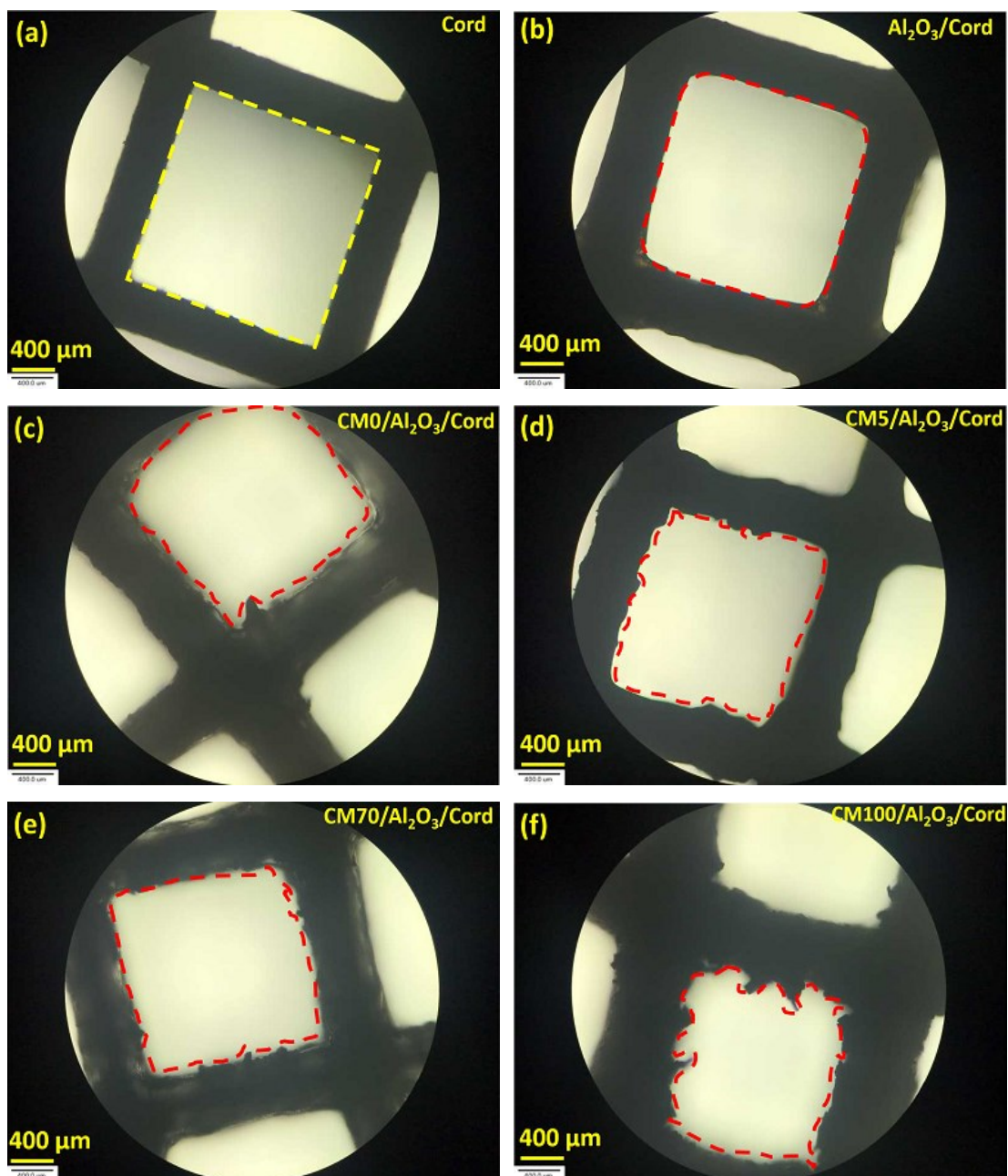


Figure 6.3: Optical images of samples Cord to CM100/Al₂O₃/Cord calcined at 700 °C/2 h.

6.4 FESEM analysis

The FESEM images of samples Cord, Al₂O₃/Cord, CM0/Al₂O₃/Cord, CM5/Al₂O₃/Cord, CM70/Al₂O₃/Cord, and CM100/Al₂O₃/Cord are shown in **Figures 6.4(a to d), 6.5(a to d), 6.6(a to d), 6.7(a to d), 6.8(a to d), and 6.9(a to d)** respectively. A glance at these figures will show that the wash-coating of Alumina and coating of the catalyst is successfully done. In comparison to **Figures (6.4 and 6.5)**, the rough surface of the Cord (as observed in **Figure 6.4**) has a smooth and uniform coating of Alumina with very few cracks (as observed in **Figure 6.5**). The cracks may have appeared while drying and calcination due to shrinkage and differences in the thermal expansion coefficient (Tang et al. 2017)(Gómez et al. 2012). Novak et al. (Novák et al. 2013) reported that cracks form in the coated layer during the drying and calcination steps. The cracks may be useful to increase the diffusivity and improve catalytic activity if it doesn't impede mechanical stability (Novák et al. 2013).

The adherence test has shown that the Alumina wash-coating has very good anchorage to the honeycomb Cordierite substrate. In the catalyst-coated samples, namely CM0/Al₂O₃/Cord to CM100/Al₂O₃/Cord in **Figures (6.6 to 6.9)**, the catalyst coating can be observed as smooth large chunks with comparatively more cracks than Alumina wash-coating as seen in **Figure 6.5**. The other observation that can be made is the increase in coating layer thickness with the increase in Mn doping, as seen in **Figure 6.6(a), Figure 6.7(a), Figure 6.8(a), and Figure 6.9(a)** from 0 to 100 %. Also, progressively, with increased Mn doping, the coating thickness accumulation/rounding of the edges has increased visibly.

The Adherence test for the catalyst-coated samples CM0/Al₂O₃/Cord to CM100/Al₂O₃/Cord has shown that a maximum of 0.38 % of the catalyst is lost, i.e., indicating a very good and strong adherence of the catalyst coating to the Alumina wash-coat layer. The Alumina wash-coat layer is very well seen in **Figures 6.6(b) and 6.8(b)**, wherein the chunk of catalyst layer may have chipped off or come off during the adherence test.

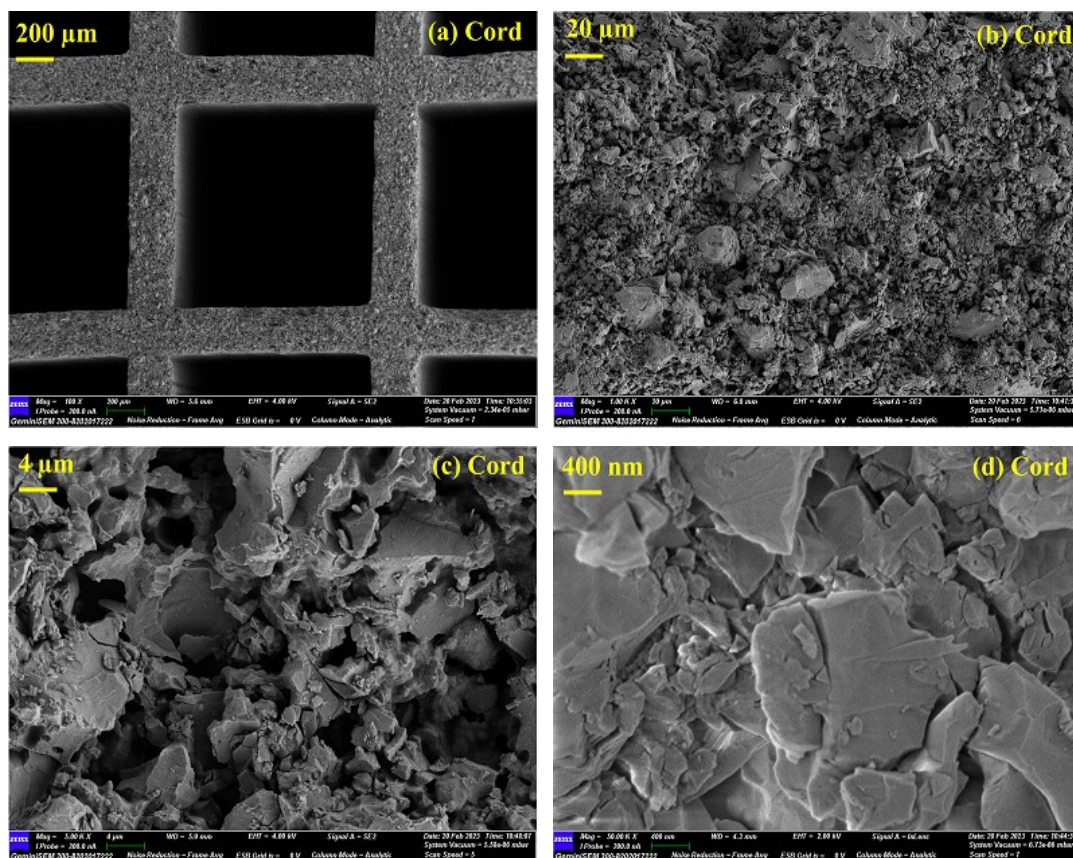


Figure 6.4: FESEM images of sample Cord calcined at 700 °C/2 h.

(Cont...)

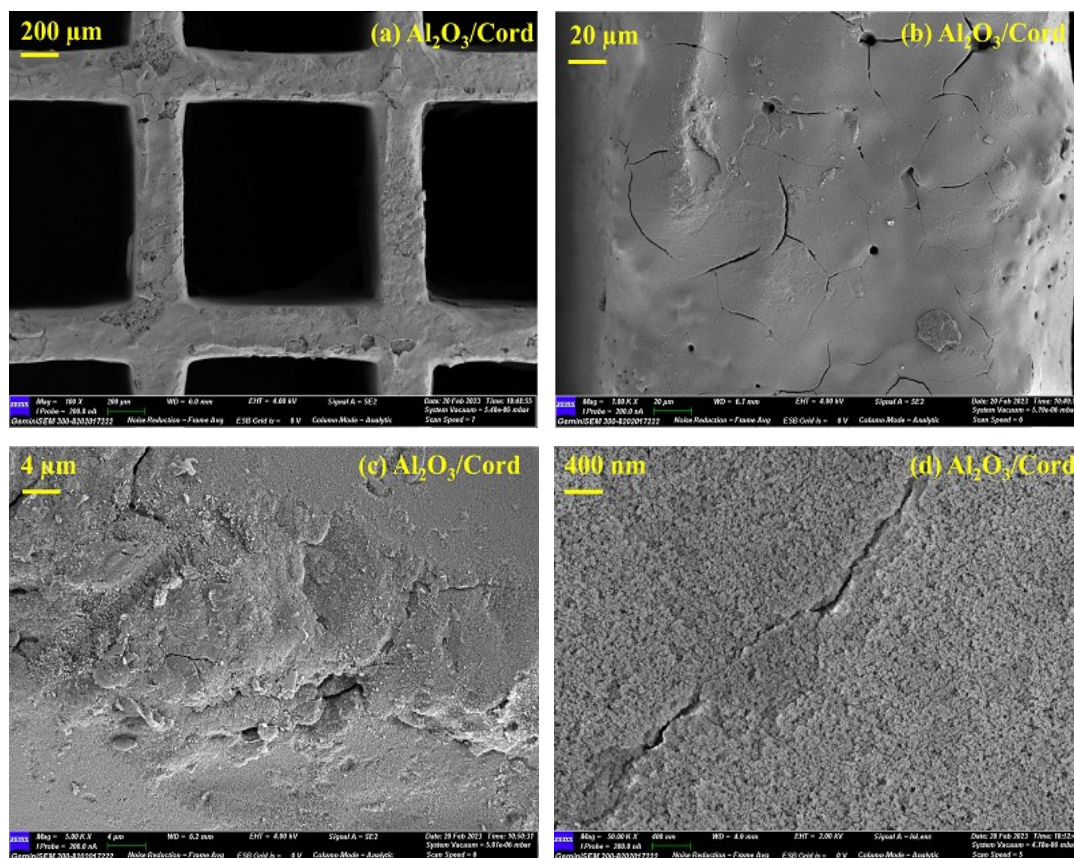


Figure 6.5: FESEM images of sample $\text{Al}_2\text{O}_3/\text{Cord}$ calcined at $700^\circ\text{C}/2\text{ h}$.

(Cont...)

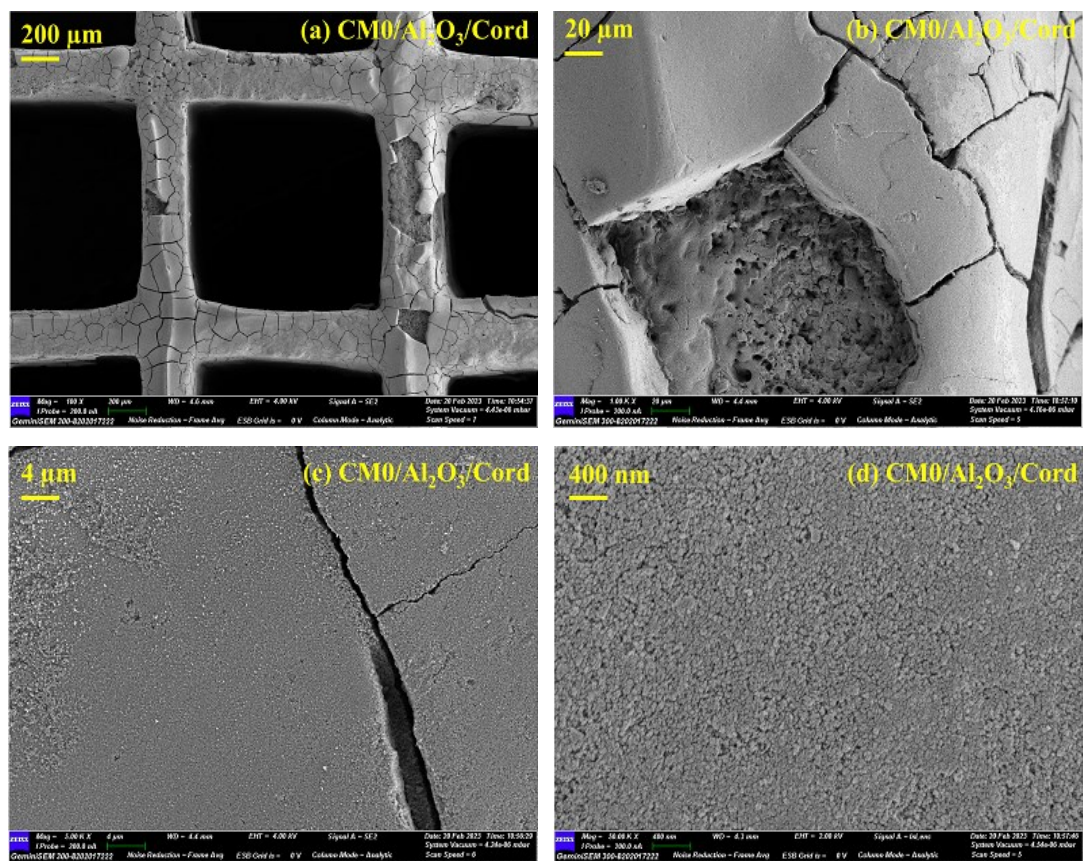


Figure 6.6: FESEM images of sample CM0/Al₂O₃/Cord calcined at 700 °C/2 h.

(Cont...)

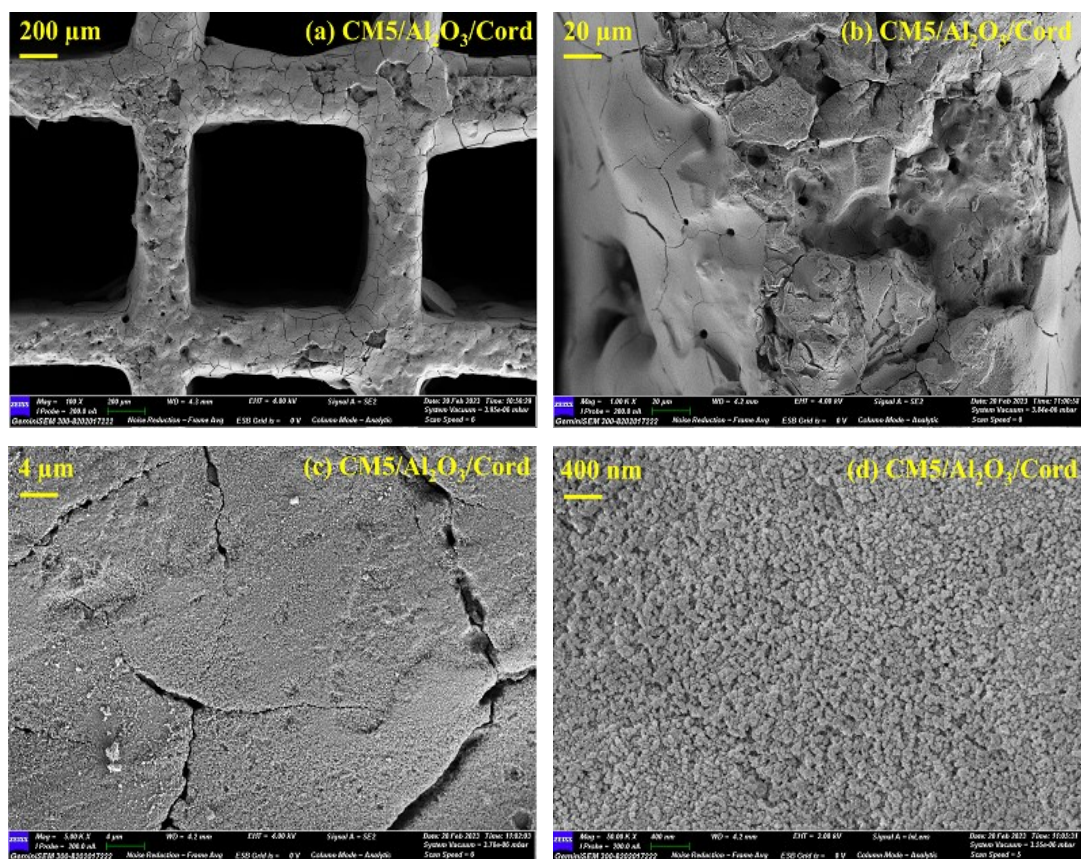


Figure 6.7: FESEM images of sample CM5/Al₂O₃/Cord calcined at 700 °C/2 h.

(Cont...)

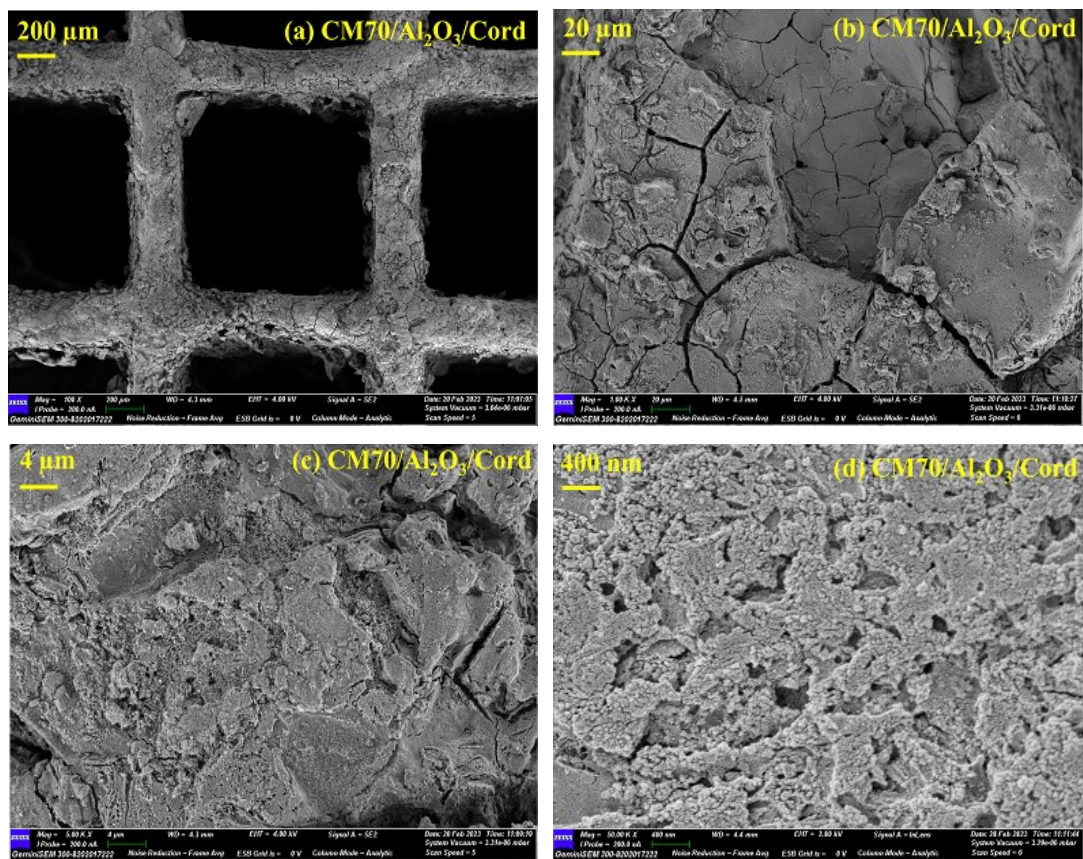


Figure 6.8: FESEM images of sample CM70/Al₂O₃/Cord calcined at 700 °C/2 h.

(Cont...)

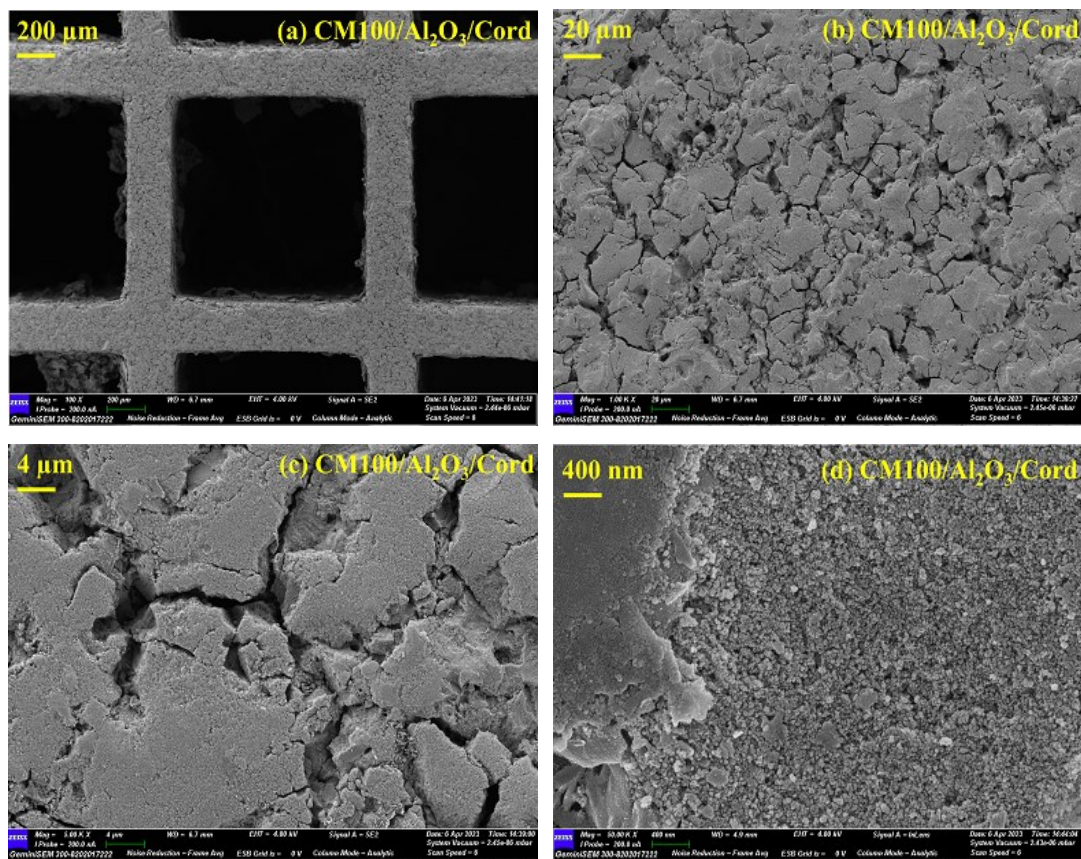


Figure 6.9: FESEM images of sample CM100/Al₂O₃/Cord calcined at 700 °C/2 h

(Cont...)

An interesting observation can be made in the FESEM images of 400 nm scale in the catalyst-coated samples of CM0/Al₂O₃/Cord to CM100/Al₂O₃/Cord **Figure (6.6, 6.7, 6.8, and 6.9)d** that a uniform coating of nearly spherical particles (size < 100 nm) is observed. Samples CM70/Al₂O₃/Cord and CM100/Al₂O₃/Cord have very high porous structures and cracks compared to samples CM0/Al₂O₃/Cord and CM5/Al₂O₃/Cord. It is highly evident from the optical imaging and FESEM images that the coating has been successful; although not completely uniform, the coatings of all samples have good mechanical strength and stability, as observed from the adherence test.

6.5 CO oxidation activity

Figure 6.10(a) depicts the CO oxidation activity on samples Cord to CM100/Al₂O₃/Cord from around 40 to 900 °C at 10 °C/min in 100 ml/min. The Cord sample is Chemically inert substance and has negligible CO oxidation activity. A very obvious observation one can make is the decrease in T₅₀ temperature between Cord and Al₂O₃/Cord being around 162 °C, and that of samples Al₂O₃/Cord and CM0/Al₂O₃/Cord is around 311 °C. The T₅₀ temperature dropped further by 116 °C on doping of Mn into Ceria, as seen in the difference of T₅₀ temperatures observed between CM0/Al₂O₃/Cord and CM5/Al₂O₃/Cord. For the latter sample, i.e., CM70/Al₂O₃/Cord, a decrease of around 38 °C compared with sample CM5/Al₂O₃/Cord. The T₅₀ temperature increases by 24 °C for CM100/Al₂O₃/Cord compared with CM70/Al₂O₃/Cord. The T₅₀ temperatures of all the catalyst samples for CO oxidation are shown in **Figure 6.10(b)**.

A considerable improvement in the CO oxidation activity was seen with the coating of the catalyst, and CM70/Al₂O₃/Cord has the best CO oxidation activity among all the coated samples. Compared with the literature, Yan et al. (Yan et al. 2013) reported LaCo_{0.5}Mn_{0.5}O₃ had one of the best CO oxidation activity among the synthesized catalysts LaCo_{0.5}M_{0.5}O₃ (M = Mn, Cr, Fe, Ni, Cu) catalysts and LaCo_{0.5}Mn_{0.5}O₃/CC5 (LaCo_{0.5}Mn_{0.5}O₃ impregnated on cordierite and calcined at

Ceria-Manganese Mixed Oxides as Catalyst for Soot and CO Oxidation Activity.

500 °C) had further improved CO oxidation with the T_{50} of 80 °C. The factors that were reported to have a crucial role in the improvement of CO oxidation activity were attributed to the weakening of the Cobalt-Oxygen bond and the increase of the lattice oxygen due to more cations (Mn) doping into site b of the perovskite structure.

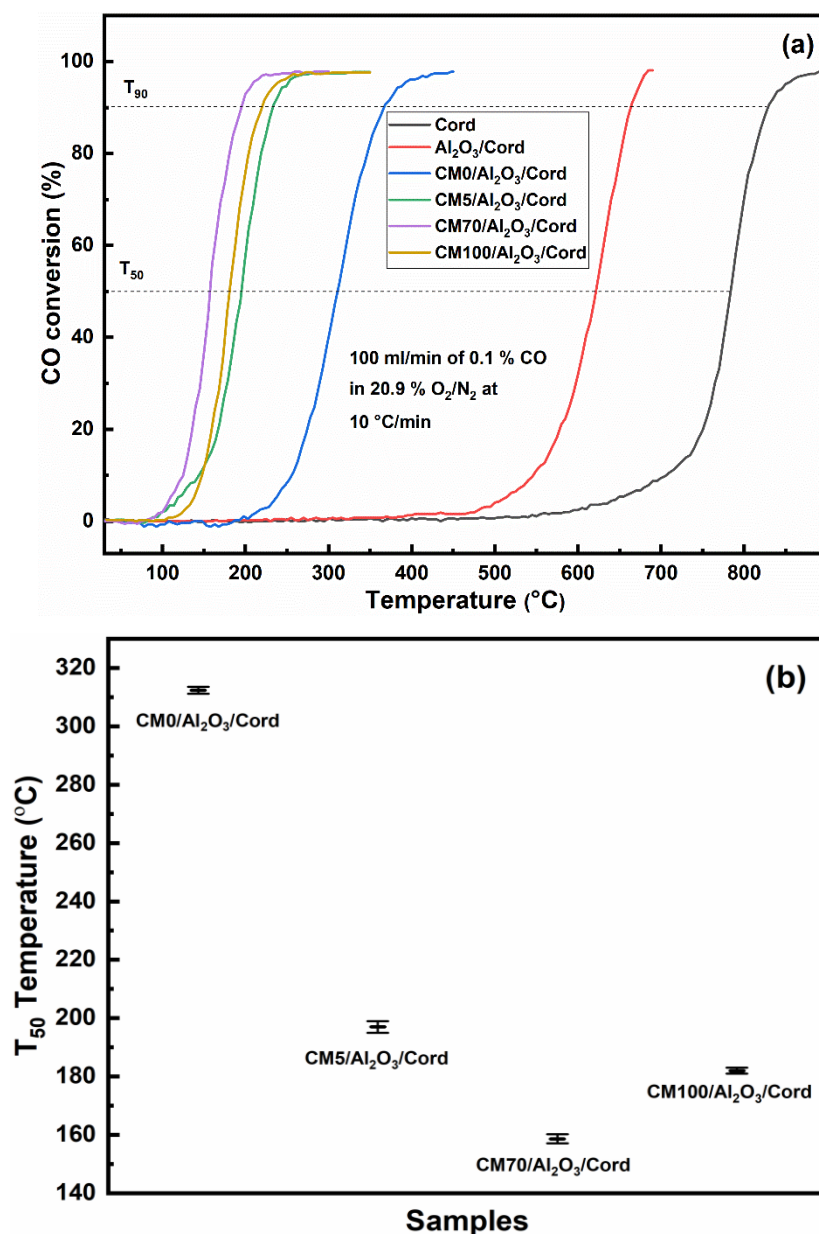


Figure 6.10: (a) CO oxidation over samples Cord to CM100/Al₂O₃/Cord; (b) T_{50} temperature triplicates of samples Cord to CM100/Al₂O₃/Cord.

Ren et al. (Ren et al. 2014) integrated $M_x\text{Co}_{3-x}\text{O}_4$ ($M = \text{Co}, \text{Ni}, \text{and Zn}$) nano array catalyst onto cordierite and reported the T_{50} of ~ 155 °C for CO oxidation by spinel Co_3O_4 . He et al. (He et al. 2019) synthesized the Mn OMS-2 nanoarray structure in situ in the channels of the cordierite and loaded metals of Ni, Co, Fe, Zn, Ga, and Sn onto the Mn OMS-2 nanoarray by microwave-assisted process. The CO oxidation of the best-structured catalyst reported was that of OMS-2@ Co_3O_4 -acac monolith with a T_{50} of 110 °C and 40.3 kJ/mol of activation energy. The factors such as ample surface-active oxygen species, the synergy between MnO_2 and Co_3O_4 combined with interfacial effects, and the large amount of Co^{3+} on the surface of the OMS-2 and the synergy between MnO_2 OMS-2 and Cobalt oxide contributed to exceptional CO oxidation augmented the CO oxidation.

Dong et al. (Dong et al. 2021) reported the CO oxidation of flexible TiO_2 mesh (curled into a monolith) coated with Mn_3O_4 with the best T_{50} of 116 °C for the Mn/ TiO_2 (10) sample. The excellent CO oxidation activity was attributed to the synergy between TiO_2 and Manganese oxide coated onto it. The other factors contributing to the CO oxidation activity at low temperatures were reported to be Manganese oxide's redox properties and the titanium sheets' ultrathin thickness. Chen et al. (Chen et al. 2016) synthesized cordierite coated with different Manganese oxide morphology (rods and nanowires) by hydrothermal method. It was reported that the sample HM-PSF ($\text{K}_2\text{S}_2\text{O}_7$ utilized in the hydrothermal in-situ deposition of Manganese oxide onto the cordierite) had the highest CO oxidation activity with a T_{50} of ~ 160 °C and an activation energy of 28.7 kJ/mol. Wu et al. [20] synthesized Ceria nano-rods by the Hydrothermal method with a T_{50} for CO oxidation at 287 °C. Aneggi et al. (Aneggi et al. 2005) reported the T_{50} of Ceria around 317 °C. Papadopoulos et al. (Papadopoulos et al. 2020) reported the CO oxidation on ceria as 316°C. Spezzati et al. (Spezzati et al. 2019) reported the CO oxidation on rod morphology of CeO_2 and cube morphology of CeO_2 as ~ 260 °C and ~ 285 °C, respectively. The CO oxidation activity of Ceria in the form of Nano-rods, Nanoparticles, and Nano-cubes was reported by Lykaki et al. (Lykaki et al. 2018) was 320 °C, 350 °C, and 385 °C respectively. Venkataswamy et al. (Venkataswamy et al. 2015a) reported a T_{50} of $\text{Ce}_{0.7}\text{Mn}_{0.3}\text{O}_{2-\delta}$ synthesized by the coprecipitation method at

Ceria-Manganese Mixed Oxides as Catalyst for Soot and CO Oxidation Activity.

117 °C. The T_{50} obtained for CM0/Al₂O₃/Cord, CM5/Al₂O₃/Cord, and CM70/Al₂O₃/Cord are comparable to the literature.

The effect of heating rate (3, 5, 7, and 10 °C/min) on the CO oxidation activity for samples CM0/Al₂O₃/Cord to CM100/Al₂O₃/Cord are depicted in **Figures 6.11(a to d)**. The increase in heating rate offset the T_{50} to higher values. **Figures 6.12(a to d)** are the Ozawa plots of samples CM0/Al₂O₃/Cord to CM100/Al₂O₃/Cord. The activation energy calculated from the Ozawa method for samples CM0/Al₂O₃/Cord, CM5/Al₂O₃/Cord, CM70/Al₂O₃/Cord, and CM100/Al₂O₃/Cord was 70.5 kJ/mol, 48.5 kJ/mol, 42.1 kJ/mol, and 35.1 kJ/mol, respectively. The activation energy from literature for CO oxidation on ceria was reported to be 83.8 kJ/mol (Kim et al. 2017). Ren et al. reported the activation energy for CO oxidation by Co₃O₄ supported on cordierite as 23.7 kJ/mol. (Ren et al. 2014). Zheng et al. (Zheng et al. 2016b) reported the CO oxidation activation energy of Ceria calcined at different temperatures of 450 °C, 600 °C, and 800 °C to be 62 kJ/mol, 92 kJ/mol, and 112 kJ/mol, respectively.

In the present work, the activation energy of the equivalent ceria, i.e., CM0/Al₂O₃/Cord on a honeycomb substrate, is within the range compared to the literature. Kharlamova et al. (Kharlamova et al. 2022) reported the CO activation energy of Ce-Mn(20/1) as 49-51 kJ/mol. Jampaiah et al. (Jampaiah et al. 2019c) reported the CO oxidation activation energy of Ceria microspheres (Mss) at 63 ± 2 kJ/mol, 20Mn₃O₄/CeO₂ Mss at 50 ± 3 kJ/mol, and 72 ± 3 kJ/mol for Mn₃O₄. The activation energy of Mn₂O₃ has been reported to be 57.9 ± 2.0 kJ/mol (Ramesh et al. 2008) and 61.0 kJ/mol (Buciuman et al. 1999), and that of α -Mn₂O₃ is 37.0 kJ/mol (Wang et al. 2008) and 60.0 kJ/mol (Xu et al. 2013b). He et al. (He et al. 2019) reported the CO oxidation activity of Mn OMS-2 (Octahedron Molecular Sieve) coated with Cobalt to have the best T_{50} of 110 °C and an activation energy of 40.3 kJ/mol. The activation energies obtained in the present work for the samples CM70/Al₂O₃/Cord and CM100/Al₂O₃/Cord are in the range compared to the literature.

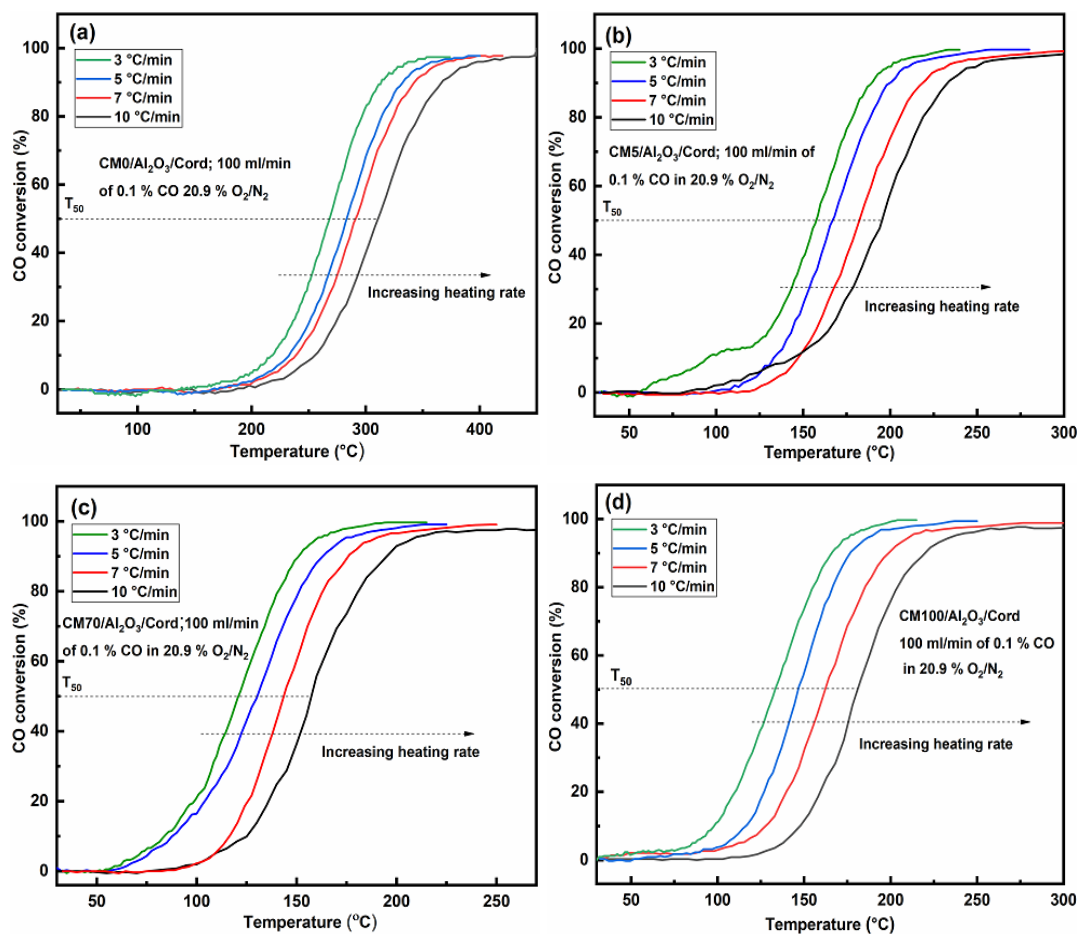


Figure 6.11: Effect of heating rate on CO conversion (a) CM0/Al₂O₃/Cord; (b) CM5/Al₂O₃/Cord; (c) CM70/Al₂O₃/Cord; (d) CM100/Al₂O₃/Cord.

The long-term stability of all the cordierite-coated catalysts, i.e., samples CM0/Al₂O₃/Cord to CM100/Al₂O₃/Cord, are shown in **Figure 6.13(a to d)**. The samples CM0/Al₂O₃/Cord to CM100/Al₂O₃/Cord were tested for CO conversion activity at their respective T_{90} for 50 h. The result, as seen in **Figure 6.13(a to d)**, shows no thermal deactivation of the catalysts, indicating good thermal stability of the coated catalysts. From the literature, studies have been conducted on the stability of the catalyst for CO oxidation. Jampaiah et al. (Jampaiah et al. 2019c) reported that the 20Mn₃O₄/CeO₂ Mss at 200 °C ($\sim T_{90}$) for 48 h and observed no significant deactivation. Yan et al. (Yan et al. 2013) reported the CO oxidation of LaCo_{0.5}Mn_{0.5}O₃ (M = Mn, Cr, Fe, Ni, and Cu) coated on cordierite. During the long-term CO oxidation study over cordierite coated with LaCo_{0.5}Mn_{0.5}O₃/CC5 for 20 h, Yan et al. (Yan et al. 2013) *Ceria-Manganese Mixed Oxides as Catalyst for Soot and CO Oxidation Activity*.

reported that the presence of water vapor at lower temperatures (~ 150 °C, i.e., T_{100}) was detrimental to the CO oxidation as it competes with CO for the active sites on the catalyst. However, it was reported that the effect of water vapor was nullified at higher temperatures (~ 200 °C) as it gets removed from the surface of the catalyst (coverage is reduced).

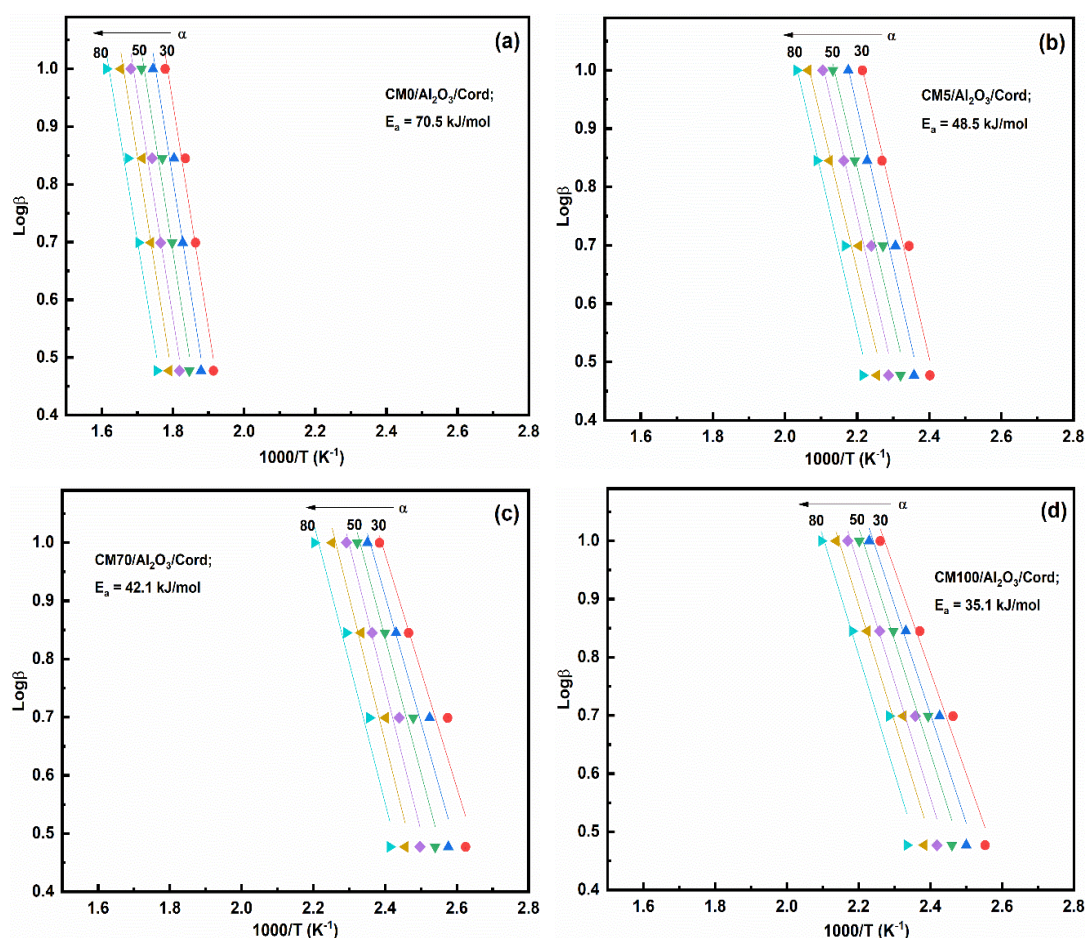


Figure 6.12: Ozawa plots of (a) CM0/Al₂O₃/Cord; (b) CM5/Al₂O₃/Cord; (c) CM70/Al₂O₃/Cord; (d) CM100/Al₂O₃/Cord.

Xiao et al. (Xiao et al. 2009) synthesized doped ceria with dopants (10 mol %) such as Y, Sn, Zr, Pr, and La via the hydrothermal method and subjected them to CO oxidation activity. It was reported that the obtained nano-structured powder was flowerlike and had mesoporous pores (pore size ~ 3.9 nm). The mesoporous pores were

reported to have contributed significantly to improving CO oxidation. Xiao et al. (Xiao et al. 2009) reported the T_{50} (CO oxidation) of Ceria as ~ 253 °C.

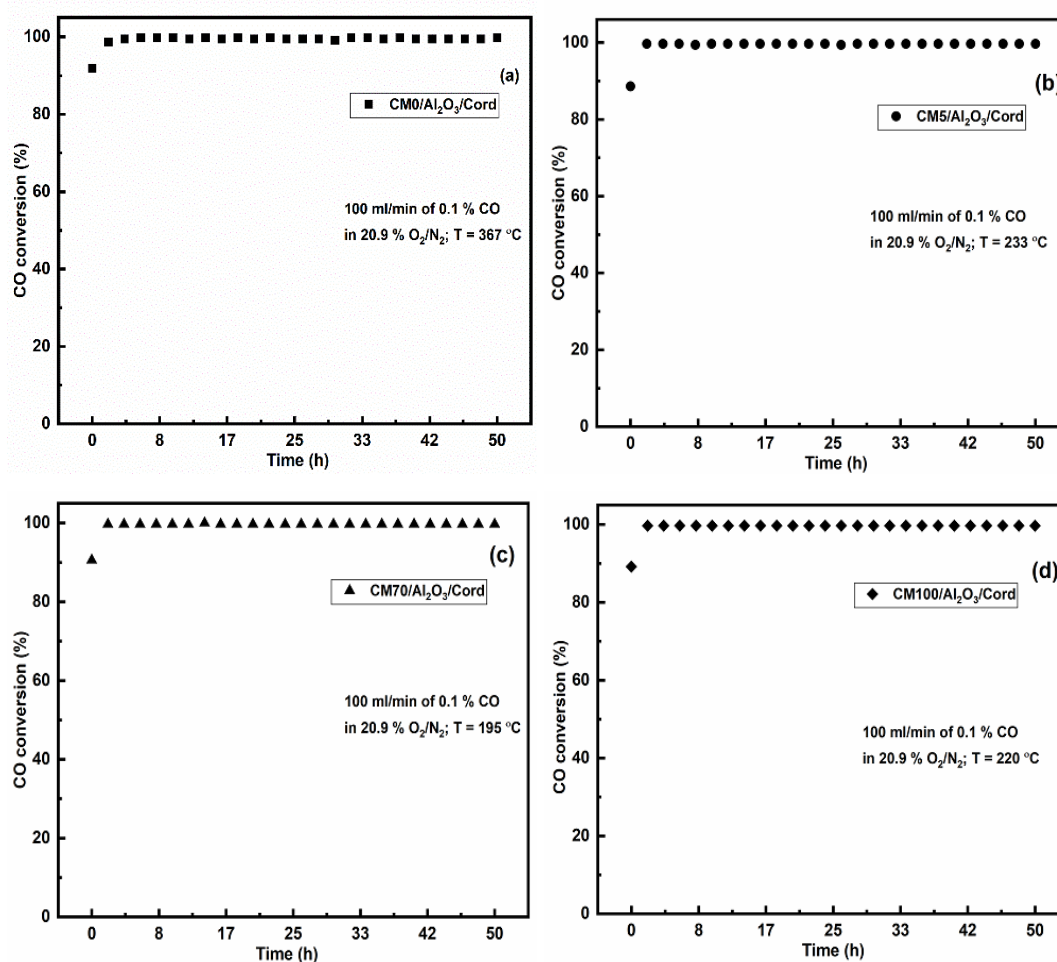


Figure 6.13: Long-term CO oxidation stability studies (a) CM0/Al₂O₃/Cord; (b) CM5/Al₂O₃/Cord; (c) CM70/Al₂O₃/Cord; (d) CM100/Al₂O₃/Cord.

Esmailnejad-Ahramjani et al. (Esmailnejad-Ahramjani et al. 2011) reported that a highly dispersed phase MnO_x was beneficial for CO and propane oxidation utilizing non-stoichiometric LaMn_{1+x}O_{3+δ} (x = 0.05 to 0.4) synthesized by gel combustion (microwave-assisted) method. Venkataswamy et al. (Venkataswamy et al. 2015a) Ceria-Manganese oxide (30 mol % Mn-doped) by coprecipitation method and utilized the catalyst for CO oxidation. The T_{50} temperature reported was 117 °C. Venkataswamy et al. (Venkataswamy et al. 2015a) reported that the oxygen vacancies increased by

Ceria-Manganese Mixed Oxides as Catalyst for Soot and CO Oxidation Activity.

doping of the Mn into Ceria. Other factors that reportedly influenced the CO oxidation were synergistic Mn-Ce interactions, redox properties, and highly dispersed MnO_x species on the catalyst. Mukherjee et al. (Mukherjee et al. 2016a) reported CM(8:2) (Ceria-Manganese oxide) synthesized through the coprecipitation method as the least T₅₀ temperature of 117 °C for CO oxidation among the CM catalyst. The factors attributing to the excellent performance of CM catalyst were reported to be as follows: (1) high oxygen mobility; (2) loosely bound oxygen atoms; (3) Synergy between Ce and Mn. It was reported that surface area, although it matters, doesn't play a crucial role in enhancing the CO oxidation activity as compared to the mentioned parameters. Another study reported by Piumetti et al. (Piumetti et al. 2016) also reiterated that the higher surface area does not necessarily translate into higher CO oxidation activity. Jampaiah et al. (Jampaiah et al. 2019c) reported that synergy between ceria and manganese oxide, Multiple oxidation states resulting in redox nature, further manifesting into oxygen vacancies between the two oxides (Ce and Mn) were the critical factors for 20Mn₂O₃/CeO₂ synthesized by hydrothermal method to have a T₅₀ temperature of 103 °C for CO oxidation activity.

In the present study, (1) The porous nature of the obtained coatings and the cracks that improve diffusivity and likely catalytic activity. (2) The fine dispersion of particles due to partial solid solution or phase separation (3) The metal support interactions, synergy, reducibility, and redox properties together manifesting into oxygen vacancies (4) The good adhesion and coverage of the wash coat and catalyst layer on the honeycomb cordierite substrate, are crucial factors in reducing the T₅₀ temperature for CO oxidation activity and for excellent long-term stability of the coated cordierite catalysts.

6.8 Conclusions

The cordierites were successfully wash-coated with γ -Al₂O₃, and then the catalyst was coated by the sol-gel dip coating. XRD and Raman spectra analysis provided evidence of the formation of γ -Al₂O₃, CeO₂, Mn₂O₃, and Mn₃O₄ phases in Ceria-Manganese Mixed Oxides as Catalyst for Soot and CO Oxidation Activity.

coatings. The dip coating yielded good adhesion and anchorage of the wash-coat and catalyst to the honeycomb cordierite substrate (wt. loss ≤ 0.38 % in the adherence test). The optical imaging visually confirmed the increase in the width of the honeycomb channels, indicating the coating was successful. Furthermore, FESEM analysis confirmed a very fine and porous coating of γ -Al₂O₃ and large agglomerated chunks of catalyst on top of the wash coat layer with cracks that may have formed due to the difference in the coefficient of thermal expansion of the wash coat layer and catalyst layer. However, the cracks seen in the FESEM images don't seem to affect the coating adhesion much, as seen from the result of the adherence test. The cracks may assist in the low-temperature oxidation of the CO on the catalyst surface. FESEM images of sample CM70/Al₂O₃/Cord display very finely dispersed particles on the agglomerated chunks of the catalyst that may act as active sites for the CO oxidation reaction. CM70/Al₂O₃/Cord had the lowest T₅₀ (157 °C) temperature for CO oxidation and the highest pore size and volume among the catalyst-coated samples. The activation energy of sample CM0/Al₂O₃/Cord to CM100/Al₂O₃/Cord was estimated by the Ozawa method to be 70.5 kJ/mol, 48.5 kJ/mol, 42.1 kJ/mol, and 35.1 kJ/mol, respectively. The 50 h long-term CO oxidation stability studies were carried out for samples CM0/Al₂O₃/Cord to CM100/Al₂O₃/Cord. All samples performed well, with no deactivation seen in the entire study. The fine dispersion of catalyst particles combined with comparatively large pore size, pore volume, and synergy between Ceria and Manganese oxide have enhanced the CO oxidation activity of CM70/Al₂O₃/Cord.

CHAPTER 7

SUMMARY AND CONCLUSION

7.1 Summary

The present thesis focuses on Ceria-Manganese mixed oxides in powder (nanostructured) form and as a structured catalyst (coated onto an Alumina wash-coated Cordierite) for soot and CO oxidation activity. EDTA-Citrate synthesis method was utilized for the synthesis of the nanostructured Ceria-Manganese mixed oxides (CMX ($X = 0, 5, 10, 20, 30, 40, 50, 60, 70, 80, 90,$ and 100) corresponding to $Ce_{1-x}Mn_xO_{2-\delta}$ (where $x = 0, 0.05, 0.1, 0.2, 0.3, 0.4, 0.5, 0.6, 0.7, 0.8, 0.9,$ and 1)) and tested for soot oxidation in tight contact conditions. The nanostructured Ceria-Manganese powder catalysts were further segregated into Ceria and Manganese-rich Ceria-Manganese oxides and their effect on the soot oxidation in tight contact conditions. Various Characterization techniques like XRD, Raman spectroscopy, BET and BJH, FESEM, and TEM analysis were utilized to study the physicochemical and morphological features of the Ceria-Manganese mixed oxides. The soot oxidation experiments were conducted in a TGA-DTA.

The structured catalyst was obtained by first wash-coating a pretreated Cordierite (honeycomb substrate) with Alumina and dip-coated with sol-gel obtained via the EDTA-Citrate method (with the addition of Polyethylene Glycol to improve coating characteristics). The structured catalysts were tested for CO oxidation in a quartz tube placed in a split tube furnace. The outlet of the quartz tube was connected to the CO/CO₂ gas analyzer. The gas mixture utilized for the CO oxidation had a composition of 0.1% CO in 20.9% O₂/N₂, imitating the CO concentration at the outlet conditions of a diesel engine. Long-term (50 h) CO oxidation studies were conducted on the catalyst-coated Cordierite.

7.2 Conclusions

The inferences of the characterization and soot oxidation activity by nanostructured powder catalyst in tight contact are as follows,

- EDTA-Citrate synthesis method yielded homogenously distributed fine nanostructured Ceria-Manganese mixed oxides powders.
- The solubility limit of Mn in Ceria is only 10 mole % of Mn, as observed in Raman spectroscopy analysis (although XRD hadn't revealed any secondary phase up until 40 mole % of Mn doping in Ceria).
- The best performing Ceria-Manganese mixed oxide was CM5 with a T_{50} of 360 °C and an activation energy of 114 kJ/mol (Ozawa method).
- The best soot oxidation performance of CM5 is attributed to the better synergy between Mn and Ceria, leading to better redox capabilities, coupled with high surface area and a greater number of active sites for active Oxygen species on the surface of the catalyst.
- The partial solid solution formation led to the formation of an unintended hybrid nanostructure, i.e., a mixture of agglomerates and nano-rods/sticks.
 - The increase in Mn doping further leads to the increase in the number of nano-rods/sticks
 - Pure Manganese oxide, too, had such a hybrid system but with comparatively fewer numbers of nano-rods/sticks.
 - The presence of Ceria has a role in the abundance of the nano-rods/sticks until 40 mole % of Mn; below 40 mole % of Mn, no such hybrid system was observed.
 - The soot oxidation activity of the hybrid system had T_{50} values closer to each other, indicating the positive effect of the nano-rods/sticks on the soot oxidation activity.

The conclusions from the characterizations and CO oxidation activity on structured catalysts are as follows,

- The dip coating technique yielded a strongly adhered Alumina wash-coat and catalyst coating (catalyst wt. loss ≤ 0.38 %).
- The Alumina wash-coat primarily consisted of γ -Al₂O₃, revealed through XRD analysis.
- The catalyst coating was slightly non-uniform with cracks, and non-uniformity moderately increased with an increase in Manganese doping in the Ceria lattice.
- CM70/Al₂O₃/Cord had a finely dispersed layer of particles on the surface of the catalyst and also had the highest pore size and volume among the structured catalysts.
- CM70/Al₂O₃/Cord performed the best among the structured catalysts with a T₅₀ of 157 °C.
- The better CO oxidation performance of CM70/Al₂O₃/Cord was due to relatively large pore size, pore volume, fine dispersion of particles on the surface of the catalyst, and synergy between Ceria and Manganese oxide.
- 50 h long-term CO oxidation test revealed all the structured catalysts to have no deactivation.

7.3 Future scope of work

- NO_x assisted soot oxidation on the structured catalyst can be conducted.
- The individual and collective effect of H₂O, NO_x, and SO_x on structured catalysts for CO oxidation can be studied.
- The effect of decorating/impregnating other transition metal oxides on structured catalysts for soot, CO, and NO_x oxidation can be studied.
- Soot and CO oxidation runs may be conducted on an actual diesel engine rig with variations in engine load, thereby with the dynamic exhaust characteristics.

APPENDIX-I

Table A1.1: Calculations for Ceria-Manganese mixed oxides CMX (X = 0 to 100) synthesized by EDTA-Citrate method.

sample (10 g)	Cerium Nitrate hexahydrate (g)	Manganese Nitrate tetrahydrate (g)	EDTA (g)	Citric Acid monohydrate (g)
CM0	30.9900	0.0000	20.8577	22.4964
CM5	30.3634	0.9238	21.5116	23.2016
CM10	29.6963	1.9074	22.2078	23.9525
CM20	28.2235	4.0788	23.7446	25.6101
CM30	26.5317	6.5731	25.5101	27.5142
CM40	24.5681	9.4681	27.5591	29.7242
CM50	22.2615	12.8687	29.9661	32.3203
CM60	19.5135	16.9203	32.8337	35.4132
CM70	16.1838	21.8293	36.3082	39.1607
CM80	12.0661	27.9002	40.6051	43.7952
CM90	06.8429	35.6010	46.0557	49.6739
CM100	00.0000	45.6896	53.1963	57.3755

N₂ sorption isotherm for CM0 to CM30 catalysts

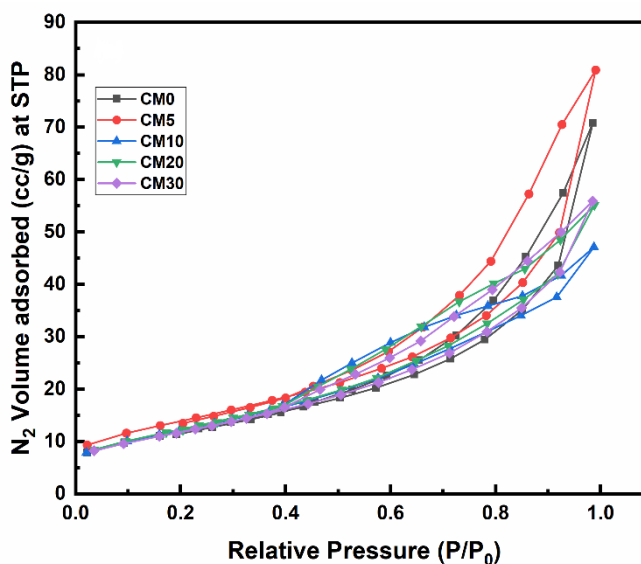


Figure A1.1: N₂ adsorption-desorption isotherm of samples CM0 to CM30 calcined at 600 °C/5 h.

The N_2 adsorption and desorption isotherm for CM0 to CM30 are shown in the **Figure A1.1**. The isotherms of all the samples follow type IV isotherm from relative pressure of 0.45 to 1, following H3 hysteresis pattern (Du et al. 2018) (Yu et al. 2022). The type IV isotherm and H3 hysteresis indicates that samples CM0 to CM30 are predominantly mesoporous structured coatings and sporadic in nature (Zhu et al. 2022a) (Li et al. 2022).

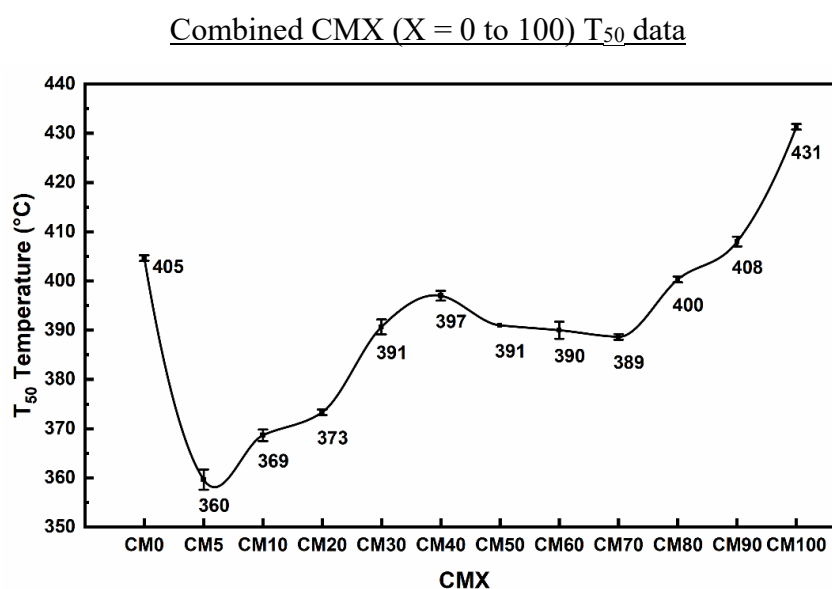


Figure A1.1: T_{50} (°C) triplicates error bar graph for CMX (X = 0 to 100) catalysts calcined at 600 °C/5 h.

The above **Figure A1.1** shows the T_{50} profile of all of the CMX catalysts (done in triplicates) in a combined way. It can be roughly divided into four trends, (1) a steep decrease in T_{50} from CM0 to CM5; (2) A steep increase in the T_{50} from CM10 to CM40; (3) A constant T_{50} trend from CM50 to CM70; (4) Finally a steep increase in the T_{50} from CM80 to CM100. It can be observed that the least T_{50} was achieved by CM5 among all the CMX catalysts and it can be said that a minute amount of dopant had multi fold benefit in improving the soot oxidation activity. The phase separation from CM20 (as observed from Raman spectra) up to CM40. had a determinantal effect on the soot oxidation activity. The formation of nano rods had a beneficial effect on the soot oxidation activity of the CM50 to CM70 where the T_{50} is almost very similar.

Ceria-Manganese Mixed Oxides as Catalyst for Soot and CO Oxidation Activity.

Further increase in the Manganese content didn't have the same augmenting effect, this can be attributed to the determinantal effects due to phase separation outweighing the beneficial effect of the nano rod structures in the hybrid phase. This can be particularly observed from the trend of T_{50} of CM80 to CM100 that steeply increased when compared to that of CM50 to CM70.

APPENDIX-II

Table A2.1: Sol-Gel dip coating method calculations

SAMPLE (10 gms)	Cerium Nitrate hexahydrate (g)	Manganese Nitrate tetrahydrate (g)	EDTA (g)	Citric Acid (g)	Total metal nitrates (g)	Total
CM0/Al₂O₃/Cord	30.9900	00.0000	20.8577	22.4964	30.9900	074.3441
CM100/Al₂O₃/Cord	00.0000	45.6896	53.1963	57.3755	45.6896	156.2615
CM5/Al₂O₃/Cord	30.3634	00.9238	21.5116	23.2016	31.2872	076.0004
CM70/Al₂O₃/Cord	16.1838	21.8293	36.3082	39.1607	38.0131	113.4820
Total	77.5373	68.4427	131.8738	142.2342		

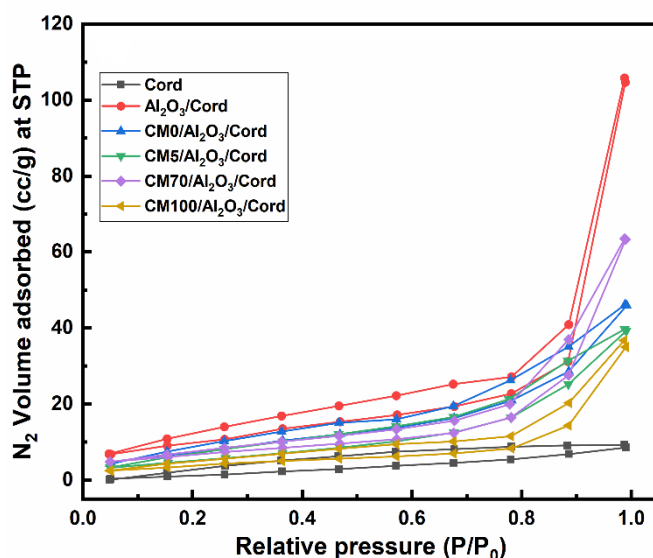
N₂ sorption isotherm for Cord to CM100/Al₂O₃/Cord catalysts

Figure A2.1: N₂ adsorption-desorption isotherm of samples Cord to CM100/Al₂O₃/Cord calcined at 700 °C/2 h.

The N₂ adsorption and desorption isotherm for Cord to CM100/Al₂O₃/Cord are shown in the **Figure A2.1**. The isotherms of all the samples except the bare cordierite (Cord) follow type IV isotherm from relative pressure of 0.75 to 1, following H3 hysteresis pattern (Du et al. 2018)(Chen et al. 2018)(Yu et al. 2022). The type IV isotherm and H3 hysteresis indicates that samples Al₂O₃/Cord to CM100/Al₂O₃/Cord are predominantly mesoporous structured coatings and sporadic in nature (Zhu et al. 2022a)(Thommes et al. 2015)(Li et al. 2022). The Cord sample has type I adsorption isotherm indicating the sample to have modest surface area (*microporous in nature*)(Thommes et al. 2015) as evidenced from Table 1.

Details of optical images sub figures

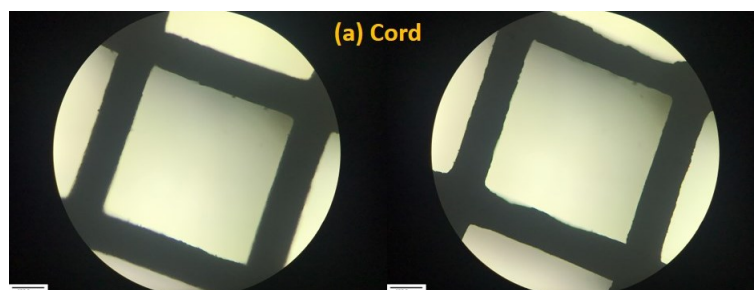


Figure A2.2(a): Optical images of Cord.

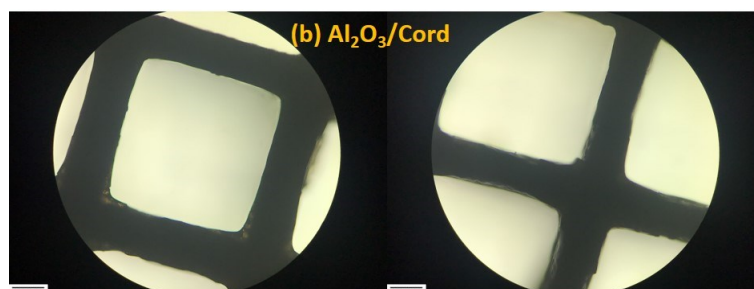


Figure A2.2(b): Optical images of Al₂O₃/Cord.

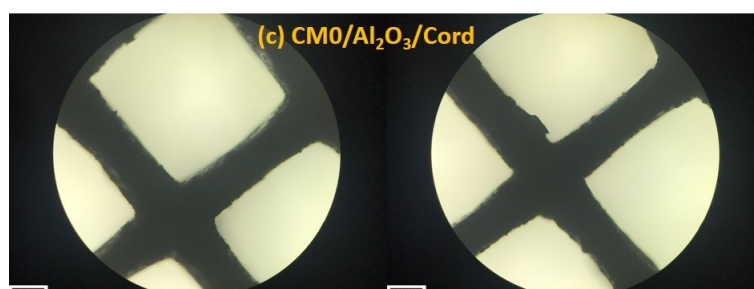


Figure A2.2(c): Optical images of CM0/Al₂O₃/Cord.

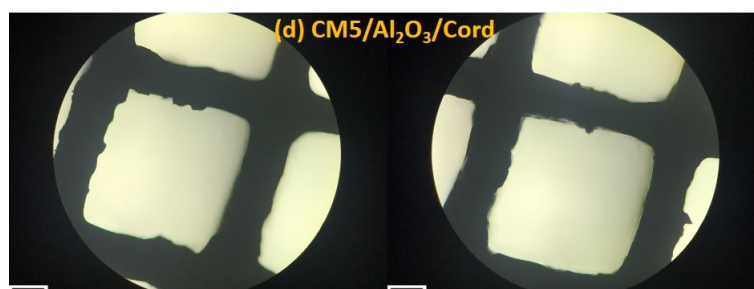


Figure A2.2(d): Optical images of CM5/Al₂O₃/Cord.

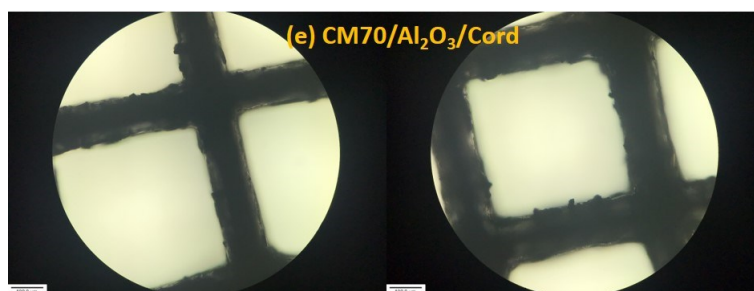


Figure A2.2(e): Optical images of CM70/Al₂O₃/Cord.

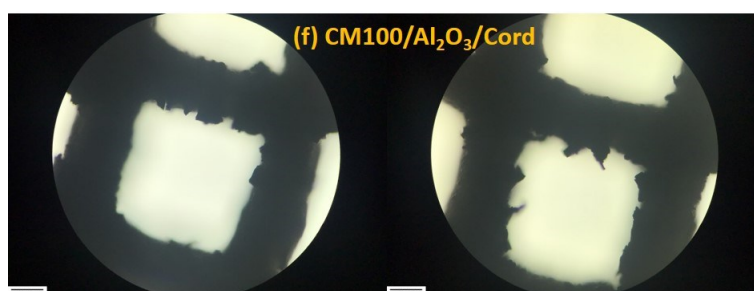


Figure A2.2(f): Optical images of CM0/Al₂O₃/Cord.

REFERENCES

- Ai, C., Du, Y., Wen, B., Shu, R., Cao, L., and Wang, W. (2022). "Preparation and characterization of diesel particle filter (DPF) with hierarchical microstructure for catalytic combustion of soot." *Ceram. Int.*, 48(7), 9304–9312.
- Alcalde-Santiago, V., Davó-Quiñonero, A., Lozano-Castelló, D., and Bueno-López, A. (2018). "On the soot combustion mechanism using 3DOM ceria catalysts." *Appl. Catal. B Environ.*, 234, 187–197.
- Anantharaman, A. P., Dasari, H. P., Dasari, H., and Babu, G. U. B. (2018a). "Surface morphology and phase stability effect of Ceria-Hafnia (CHx) binary metal oxides on soot oxidation activity." *Appl. Catal. A Gen.*, 566, 181–189.
- Anantharaman, A. P., Dasari, H. P., Dasari, H., and Babu, G. U. B. (2019). "Effect of ionic radius on soot oxidation activity for ceria-based binary metal oxides." *Asia-Pacific J. Chem. Eng.*, wiley asia-pacific journal of chemical engineering.
- Anantharaman, A. P., Dasari, H. P., Lee, J. H., Dasari, H., and Babu, G. U. B. (2017). "Soot Oxidation Activity of Redox and Non-Redox Metal Oxides Synthesised by EDTA–Citrate Method." *Catal. Letters*, 147(12), 3004–3016.
- Anantharaman, A. P., Gadiyar, H. J., Surendran, M., Rao, A. S., and Prasad, H. (2018b). "Effect of synthesis method on structural properties and soot oxidation activity of gadolinium - doped ceria." *Chem. Pap.*, 72, 3179-3188.
- Anantharaman, A. P., Geethu, J., P, M. R., Dasari, H. P., Lee, J. H., Dasari, H., and Bhaskar Babu, G. U. (2018c). "Ceria-samarium binary metal oxides: A comparative approach towards structural properties and soot oxidation activity." *Mol. Catal.*, 451, 247–254.
- Andana, T., Piumetti, M., Bensaid, S., Russo, N., Fino, D., and Pirone, R. (2016). "Nanostructured ceria-praseodymia catalysts for diesel soot combustion." *Appl. Catal. B Environ.*, 197, 125–137.
- Aneggi, E., Leitenburg, C. de, Dolcetti, G., and Trovarelli, A. (2006). "Promotional effect of rare earths and transition metals in the combustion of diesel soot over CeO₂ and CeO₂-ZrO₂." *Catal. Today*, 114(1), 40–47.
- Aneggi, E., Leitenburg, C. De, and Trovarelli, A. (2012). "On the role of lattice/surface Ceria-Manganese Mixed Oxides as Catalyst for Soot and CO Oxidation Activity."

oxygen in ceria-zirconia catalysts for diesel soot combustion.” *Catal. Today*, 181(1), 108–115.

Aneggi, E., Llorca, J., Boaro, M., and Trovarelli, A. (2005). “Surface-structure sensitivity of CO oxidation over polycrystalline ceria powders.” *J. Catal.*, 234(1), 88–95.

Aneggi, E., Wiater, D., Leitenburg, C. De, Llorca, J., and Trovarelli, A. (2014). “Shape-dependent activity of ceria in soot combustion.” *ACS Catal.*, 4(1), 172–181.

Ascaso, S., Gálvez, M. E., Costa, P. Da, Moliner, R., and Lázaro, M. J. (2014). “On the influence of the alumina precursor in Fe-K/Al₂O₃ structured catalysts for the simultaneous removal of soot and NO_x: From surface properties to reaction mechanism.” *Comptes Rendus Chim.*, 17(7), 681–686.

Azalim, S., Brahmi, R., Agunaou, M., Beaurain, A., Giraudon, J. M., and Lamonier, J. F. (2013). “Washcoating of cordierite honeycomb with Ce-Zr-Mn mixed oxides for VOC catalytic oxidation.” *Chem. Eng. J.*, 223, 536–546.

Azalim, S., Franco, M., Brahmi, R., Giraudon, J. M., and Lamonier, J. F. (2011). “Removal of oxygenated volatile organic compounds by catalytic oxidation over Zr-Ce-Mn catalysts.” *J. Hazard. Mater.*, 188(1–3), 422–427.

Banús, E. D., Milt, V. G., Miró, E. E., and Ulla, M. A. (2013). “Catalytic coating synthesized onto cordierite monolith walls. Its application to diesel soot combustion.” *Appl. Catal. B Environ.*, 132–133, 479–486.

Barai, H. R., Banerjee, A. N., Hamnabard, N., and Joo, S. W. (2016). “Synthesis of amorphous manganese oxide nanoparticles-to-crystalline nanorods through a simple wet-chemical technique using K⁺ ions as a ‘growth director’ and their morphology-controlled high performance supercapacitor applications.” *RSC Adv.*, 6(82), 78887–78908.

Barrio, I., Legórburu, I., Montes, M., Domínguez, M. I., Centeno, M. A. N., and Odriozola, J. A. (2005). “New redox deposition-precipitation method for preparation of supported manganese oxide catalysts.” *Catal. Letters*, 101(3–4), 151–157.

Bensaid, S., Russo, N., and Fino, D. (2013). “CeO₂ catalysts with fibrous morphology for soot oxidation: The importance of the soot-catalyst contact conditions.” *Catal. Today*, Elsevier B.V., 57–63.

Ceria-Manganese Mixed Oxides as Catalyst for Soot and CO Oxidation Activity.

- Buciuman, F. C., Patcas, F., and Hahn, T. (1999). "A spillover approach to oxidation catalysis over copper and manganese mixed oxides." *Chem. Eng. Process. Process Intensif.*, 38(4–6), 563–569.
- Bueno-López, A. (2014). "Diesel soot combustion ceria catalysts." *Appl. Catal. B Environ.*, 146, 1–11.
- Cao, C., Xing, L., Yang, Y., Tian, Y., Ding, T., Zhang, J., Hu, T., Zheng, L., and Li, X. (2017). "The monolithic transition metal oxide crossed nanosheets used for diesel soot combustion under gravitational contact mode." *Appl. Surf. Sci.*, 406, 245–253.
- Cao, C., Yang, H., Xiao, J., Yang, X., Ren, B., Xu, L., Liu, G., and Li, X. (2021). "Catalytic diesel soot elimination over potassium promoted transition metal oxide (Co/Mn/Fe) nanosheets monolithic catalysts." *Fuel*, 305.
- Capdevila-Cortada, M., Vilé, G., Teschner, D., Pérez-Ramírez, J., and López, N. (2016). "Reactivity descriptors for ceria in catalysis." *Appl. Catal. B Environ.*, 197, 299–312.
- Carabineiro, S. A. C., MacHado, B. F., Bacsa, R. R., Serp, P., Draić, G., Faria, J. L., and Figueiredo, J. L. (2010). "Catalytic performance of Au/ZnO nanocatalysts for CO oxidation." *J. Catal.*, 273(2), 191–198.
- Chae, K. W., Son, M. A., Park, S. J., Kim, J. S., and Kim, S. H. (2021). "Effect of sintering atmosphere on the crystallizations, porosity, and thermal expansion coefficient of cordierite honeycomb ceramics." *Ceram. Int.*, 47(14), 19526–19537.
- Chang, L. H., Sasirekha, N., Rajesh, B., and Chen, Y. W. (2007). "CO oxidation on ceria- and manganese oxide-supported gold catalysts." *Sep. Purif. Technol.*, 58(1), 211–218.
- Chen, J., Chen, X., Chen, X., Xu, W., Xu, Z., Jia, H., and Chen, J. (2018). "Homogeneous introduction of CeO_y into MnO_x-based catalyst for oxidation of aromatic VOCs." *Appl. Catal. B Environ.*, 224, 825–835.
- Chen, L., Fleming, P., Morris, V., Holmes, J. D., and Morris, M. A. (2010). "Size-related lattice parameter changes and surface defects in ceria nanocrystals." *J. Phys. Chem. C*, 114(30), 12909–12919.
- Chen, L., Liu, G., Feng, N., Yu, J., Meng, J., Fang, F., Zhao, P., Wang, L., Wan, H., and Guan, G. (2019). "Effect of calcination temperature on structural properties and Ceria-Manganese Mixed Oxides as Catalyst for Soot and CO Oxidation Activity."

catalytic soot combustion activity of MnO_x/wire-mesh monoliths.” *Appl. Surf. Sci.*, 467–468, 1088–1103.

Chen, S. Y., Song, W., Lin, H. J., Wang, S., Biswas, S., Mollahosseini, M., Kuo, C. H., Gao, P. X., and Suib, S. L. (2016). “Manganese Oxide Nanoarray-Based Monolithic Catalysts: Tunable Morphology and High Efficiency for CO Oxidation.” *ACS Appl. Mater. Interfaces*, 8(12), 7834–7842.

Chen, Z., Chen, L., Jiang, M., Gao, X., Huang, M., Li, Y., Ren, L., Yang, Y., and Yang, Z. (2020). “Controlled synthesis of CeO₂ nanorods and their promotional effect on catalytic activity and aging resistibility for diesel soot oxidation.” *Appl. Surf. Sci.*, 510, 145401.

Cheng, L., Men, Y., Wang, J., Wang, H., An, W., Wang, Y., Duan, Z., and Liu, J. (2017a). “Crystal facet-dependent reactivity of α -Mn₂O₃ microcrystalline catalyst for soot combustion.” *Appl. Catal. B Environ.*, 204, 374–384.

Cheng, Y., Liu, J., Zhao, Z., Song, W., and Wei, Y. (2017b). “Highly efficient and simultaneously catalytic removal of PM and NO_x from diesel engines with 3DOM Ce_{0.8}M_{0.1}Zr_{0.1}O₂ (M = Mn, Co, Ni) catalysts.” *Chem. Eng. Sci.*, 167(x), 219–228.

Cheng, Y., Liu, J., Zhao, Z., Song, W., and Wei, Y. (2018). “A new 3DOM Ce-Fe-Ti material for simultaneously catalytic removal of PM and NO_x from diesel engines.” *J. Hazard. Mater.*, 342, 317–325.

COLMAN-LERNER, E., PELUSO, M. A., SAMBETH, J., and THOMAS, H. (2016). “Cerium, manganese and cerium/manganese ceramic monolithic catalysts. Study of VOCs and PM removal.” *J. Rare Earths*, 34(7), 675–682.

D’Anna, A. (2009). “Combustion-formed nanoparticles.” *Proc. Combust. Inst.*, 32 I(1), 593–613.

Dasari, H. P., Ahn, J. S., Ahn, K., Park, S. Y., Hong, J., Kim, H., Yoon, K. J., Son, J. W., Lee, H. W., and Lee, J. H. (2014). “Synthesis, sintering and conductivity behavior of ceria-doped Scandia-stabilized zirconia.” *Solid State Ionics*, 263, 103–109.

Deng, L., Huang, C., Kan, J., Li, B., Chen, Y., Zhu, S., and Shen, S. (2018). “Effect of coating modification of cordierite carrier on catalytic performance of supported NiMnO₃ catalysts for VOCs combustion.” *J. Rare Earths*, 36(3), 265–272.

Dey, S., Dhal, G. C., Mohan, D., and Prasad, R. (2019). “Synthesis of highly active Ceria-Manganese Mixed Oxides as Catalyst for Soot and CO Oxidation Activity.”

- Cobalt catalysts for low temperature CO oxidation.” *Chem. Data Collect.*, 24, 100283.
- Díaz, C. C., Pilar Yeste, M., Vidal, H., Gatica, J. M., Cadús, L. E., and Morales, M. R. (2020). “In situ generation of $Mn_{1-x}Ce_x$ system on cordierite monolithic supports for combustion of n-hexane. Effects on activity and stability.” *Fuel*, 262, 116564.
- Dong, S., Wang, J., Tang, X., Li, J., Zhang, X., and Liu, B. (2021). “Low-temperature and stable CO oxidation of in-situ grown monolithic Mn_3O_4/TiO_2 catalysts.” *J. Alloys Compd.*, 855, 157444.
- Dosa, M., Piumetti, M., Bensaid, S., Andana, T., Novara, C., Giorgis, F., Fino, D., and Russo, N. (2018). “Novel Mn–Cu-Containing CeO_2 Nanopolyhedra for the Oxidation of CO and Diesel Soot: Effect of Dopants on the Nanostructure and Catalytic Activity.” *Catal. Letters*, 148(1), 298–311.
- Du, J., Qu, Z., Dong, C., Song, L., Qin, Y., and Huang, N. (2018). “Applied Surface Science Low-temperature abatement of toluene over Mn-Ce oxides catalysts synthesized by a modified hydrothermal approach.” *Appl. Surf. Sci.*, 433, 1025–1035.
- Du, Y., Wen, B., Shu, R., Cao, L., and Wang, W. (2021). “Potassium titanate whiskers on the walls of cordierite honeycomb ceramics for soot catalytic combustion.” *Ceram. Int.*, 47(24), 34828–34835.
- El-Shobaky, G. A., El-Shobaky, H. G., Badawy, A. A. A., and Fahmy, Y. M. (2011). “Physicochemical, surface and catalytic properties of nanosized copper and manganese oxides supported on cordierite.” *Appl. Catal. A Gen.*, 409–410, 234–238.
- Esmailnejad-Ahranjani, P., Khodadadi, A., Ziaei-Azad, H., and Mortazavi, Y. (2011). “Effects of excess manganese in lanthanum manganite perovskite on lowering oxidation light-off temperature for automotive exhaust gas pollutants.” *Chem. Eng. J.*, 169(1–3), 282–289.
- Falcón, H., Martínez-Lope, M. J., Alonso, J. A., and Fierro, J. L. G. (2000). “Large enhancement of the catalytic activity for CO oxidation on hole doped $(Ln,Sr)NiO_3$ ($Ln = Pr, Sm, Eu$) Perovskites.” *Solid State Ionics*, 131(3), 237–248.
- Fino, D. (2007). “Diesel emission control: Catalytic filters for particulate removal.” *Sci. Technol. Adv. Mater.*, 8(1–2), 93–100.
- Fino, D., Bensaid, S., Piumetti, M., and Russo, N. (2016). “A review on the catalytic combustion of soot in Diesel particulate filters for automotive applications: From Ceria-Manganese Mixed Oxides as Catalyst for Soot and CO Oxidation Activity.”

- powder catalysts to structured reactors.” *Appl. Catal. A Gen.*, 509, 75–96.
- France, L. J., Edwards, P. P., Kuznetsov, V. L., and Almegren, H. (2015). *Chapter 10 - The Indirect and Direct Conversion of CO₂ into Higher Carbon Fuels. Carbon Dioxide Util.*, Elsevier B.V.
- Gálvez, M. E., Ascaso, S., Moliner, R., and Lázaro, M. J. (2013). “Me (Cu, Co, V)-K/Al₂O₃ supported catalysts for the simultaneous removal of soot and nitrogen oxides from diesel exhausts.” *Chem. Eng. Sci.*, 87(715), 75–90.
- Gálvez, M. E., Ascaso, S., Stelmachowski, P., Legutko, P., Kotarba, A., Moliner, R., and Lázaro, M. J. (2014). “Influence of the surface potassium species in Fe-K/Al₂O₃ catalysts on the soot oxidation activity in the presence of NO_x.” *Appl. Catal. B Environ.*, 152–153(2), 88–98.
- Gao, X., Zhao, Y., Wang, S., Yin, Y., Wang, B., and Ma, X. (2011). “A Pd-Fe/ α -Al₂O₃/cordierite monolithic catalyst for CO coupling to oxalate.” *Chem. Eng. Sci.*
- Garcia, X., Soler, L., Casanovas, A., Escudero, C., and Llorca, J. (2021). “X-ray photoelectron and Raman spectroscopy of nanostructured ceria in soot oxidation under operando conditions.” *Carbon N. Y.*, 178, 164–180.
- Giménez-Mañogil, J., and García-García, A. (2017). “Identifying the nature of the copper entities over ceria-based supports to promote diesel soot combustion: Synergistic effects.” *Appl. Catal. A Gen.*, 542, 226–239.
- Glaser, B., Dreyer, A., Bock, M., Fiedler, S., Mehring, M., and Heitmann, T. (2005). “Source apportionment of organic pollutants of a highway-traffic-influenced urban area in Bayreuth (Germany) using biomarker and stable carbon isotope signatures.” *Environ. Sci. Technol.*, 39(11), 3911–3917.
- Gómez, D. M., Gatica, J. M., Hernández-Garrido, J. C., Cifredo, G. A., Montes, M., Sanz, O., Rebled, J. M., and Vidal, H. (2014). “A novel CoO_x/La-modified-CeO₂ formulation for powdered and washcoated onto cordierite honeycomb catalysts with application in VOCs oxidation.” *Appl. Catal. B Environ.*, 144, 425–434.
- Gómez, L. E., Tiscornia, I. S., Boix, A. V., and Miró, E. E. (2011). “Co/ZrO₂ catalysts coated on cordierite monoliths for CO preferential oxidation.” *Appl. Catal. A Gen.*, 401(1–2), 124–133.
- Gómez, L. E., Tiscornia, I. S., Boix, A. V., and Miró, E. E. (2012). “CO preferential Ceria-Manganese Mixed Oxides as Catalyst for Soot and CO Oxidation Activity.”

oxidation on cordierite monoliths coated with Co/CeO₂ catalysts.” *Int. J. Hydrogen Energy*, 37(19), 14812–14819.

Govardhan, P., Anantharaman, A. P., Patil, S. S., Dasari, H. P., Dasari, H., and Shourya, A. (2022). “Effect of Ag loading on praseodymium doped ceria catalyst for soot oxidation activity.” *Korean J. Chem. Eng.*, 39(2), 328–342.

Govender, S., and Friedrich, H. B. (2017). “Monoliths: A review of the basics, preparation methods and their relevance to oxidation.” *Catalysts*.

Grasselli, R. K. (2003). “Fundamental Principles of Selective Heterogeneous Oxidation Catalysis.” *ChemInform*, 34(20), 79–88.

Gross, M. S., Ulla, M. A., and Querini, C. A. (2012). “Diesel particulate matter combustion with CeO₂ as catalyst. Part I: System characterization and reaction mechanism.” *J. Mol. Catal. A Chem.*, 352, 86–94.

Guan, B., Zhan, R., Lin, H., and Huang, Z. (2015). “Review of the state-of-the-art of exhaust particulate filter technology in internal combustion engines.” *J. Environ. Manage.*, 154, 225–258.

Guillén-Hurtado, N., Giménez-Mañogil, J., Martínez-Munuera, J. C., Bueno-López, A., and García-García, A. (2020). “Study of Ce/Pr ratio in ceria-praseodymia catalysts for soot combustion under different atmospheres.” *Appl. Catal. A Gen.*, 590(November 2019), 117339.

Guo, X., Li, J., and Zhou, R. (2016). “Catalytic performance of manganese doped CuO-CeO₂ catalysts for selective oxidation of CO in hydrogen-rich gas.” *Fuel*, 163, 56–64.

Han, Y. F., Chen, F., Zhong, Z. Y., Ramesh, K., Widjaja, E., and Chen, L. W. (2006). “Synthesis and characterization of Mn₃O₄ and Mn₂O₃ nanocrystals on SBA-15: Novel combustion catalysts at low reaction temperatures.” *Catal. Commun.*, 7(10), 739–744.

Haynes, B. S., and Wagner, H. G. (1981). “Soot formation.” *Prog. Energy Combust. Sci.*, 7(4), 229–273.

He, H., Lin, X., Li, S., Wu, Z., Gao, J., Wu, J., Wen, W., Ye, D., and Fu, M. (2018a). “The key surface species and oxygen vacancies in MnO_x(0.4)-CeO₂ toward repeated soot oxidation.” *Appl. Catal. B Environ.*, 223, 134–142.

He, J., Chen, S. Y., Tang, W., Dang, Y., Kerns, P., Miao, R., Dutta, B., Gao, P. X., and Suib, S. L. (2019). “Microwave-assisted integration of transition metal oxide Ceria-Manganese Mixed Oxides as Catalyst for Soot and CO Oxidation Activity.”

nanocoatings on manganese oxide nanoarray monoliths for low temperature CO oxidation.” *Appl. Catal. B Environ.*, 255, 117766.

He, J., Yao, P., Qiu, J., Zhang, H., Jiao, Y., Wang, J., and Chen, Y. (2021). “Enhancement effect of oxygen mobility over $Ce_{0.5}Zr_{0.5}O_2$ catalysts doped by multivalent metal oxides for soot combustion.” *Fuel*, 286(P1), 119359.

Hernández-Giménez, A. M., Xavier, L. P. D. S., and Bueno-López, A. (2013). “Improving ceria-zirconia soot combustion catalysts by neodymium doping.” *Appl. Catal. A Gen.*, 462–463, 100–106.

Hong, W. J., Iwamoto, S., Hosokawa, S., Wada, K., Kanai, H., and Inoue, M. (2011). “Effect of Mn content on physical properties of CeO_x - MnO_y support and BaO - CeO_x - MnO_y catalysts for direct NO decomposition.” *J. Catal.*, 277(2), 208–216.

Hossain, S. T., Almesned, Y., Zhang, K., Zell, E. T., Bernard, D. T., Balaz, S., and Wang, R. (2018). “Support structure effect on CO oxidation: A comparative study on SiO_2 nanospheres and CeO_2 nanorods supported CuO_x catalysts.” *Appl. Surf. Sci.*, 428, 598–608.

Huang, F., Ye, D., Guo, X., Zhan, W., Guo, Y., Wang, L., Wang, Y., and Guo, Y. (2020). “Effect of ceria morphology on the performance of MnO_x/CeO_2 catalysts in catalytic combustion of N, N -dimethylformamide.” *Catal. Sci. Technol.*, 10(8), 2473–2483.

Huang, H., Liu, J., Sun, P., Ye, S., and Liu, B. (2017). “Effects of Mn-doped ceria oxygen-storage material on oxidation activity of diesel soot.” *RSC Adv.*, 7(12), 7406–7412.

Huang, Q., Zhang, Z. Y., Ma, W. J., Chen, Y. W., Zhu, S. M., and Shen, S. B. (2012). “A novel catalyst of Ni-Mn complex oxides supported on cordierite for catalytic oxidation of toluene at low temperature.” *J. Ind. Eng. Chem.*, 18(2), 757–762.

Hubbard, W. G. (2015). *Chapter 4 - Wood Bioenergy. Bioenergy*, Anju Dahiya.

Jacobson, M. Z. (2004). “Climate response of fossil fuel and biofuel soot, accounting for soot’s feedback to snow and sea ice albedo and emissivity.” *J. Geophys. Res. D Atmos.*, 109(21), 1–15.

Jampaiah, D., Velisoju, V. K., Devaiah, D., Singh, M., Mayes, E. L. H., Coyle, V. E., Reddy, B. M., Bansal, V., and Bhargava, S. K. (2019a). “Flower-like Mn_3O_4/CeO_2 Ceria-Manganese Mixed Oxides as Catalyst for Soot and CO Oxidation Activity.”

microspheres as an efficient catalyst for diesel soot and CO oxidation: Synergistic effects for enhanced catalytic performance.” *Appl. Surf. Sci.*, 473, 209–221.

Jampaiah, D., Velisoju, V. K., Venkataswamy, P., Coyle, V. E., Nafady, A., Reddy, B. M., and Bhargava, S. K. (2017). “Nanowire Morphology of Mono- and Bidoped α -MnO₂ Catalysts for Remarkable Enhancement in Soot Oxidation.” *ACS Appl. Mater. Interfaces*, 9(38), 32652–32666.

Ji, F., Men, Y., Wang, J., Sun, Y., Wang, Z., Zhao, B., Tao, X., and Xu, G. (2019b). “Promoting diesel soot combustion efficiency by tailoring the shapes and crystal facets of nanoscale Mn₃O₄.” *Appl. Catal. B Environ.*, 242, 227–237.

Jia, A. P., Hu, G. S., Meng, L., Xie, Y. L., Lu, J. Q., and Luo, M. F. (2012). “CO oxidation over CuO/Ce_{1-x}Cu_xO_{2- δ} and Ce_{1-x}Cu_xO_{2- δ} catalysts: Synergetic effects and kinetic study.” *J. Catal.*, 289, 199–209.

Jian, S., Yang, Y., Ren, W., Xing, L., Zhao, D., Tian, Y., Ding, T., and Li, X. (2020). “Kinetic analysis of morphologies and crystal planes of nanostructured CeO₂ catalysts on soot oxidation.” *Chem. Eng. Sci.*, 226, 115891.

Kalogirou, M., and Samaras, Z. (2010). “Soot oxidation kinetics from TG experiments: Can they be used reliably in diesel particulate filter modelling tools?” *J. Therm. Anal. Calorim.*, 99(3), 1005–1010.

Kan, J., Deng, L., Li, B., Huang, Q., Zhu, S., Shen, S., and Chen, Y. (2017). “Performance of co-doped Mn-Ce catalysts supported on cordierite for low concentration chlorobenzene oxidation.” *Appl. Catal. A Gen.*, 530, 21–29.

Kang, C. Y., Kusaba, H., Yahiro, H., Sasaki, K., and Teraoka, Y. (2006). “Preparation, characterization and electrical property of Mn-doped ceria-based oxides.” *Solid State Ionics*, 177(19-25 SPEC. ISS.), 1799–1802.

Kaplin, I. Y., Lokteva, E. S., Golubina, E. V., Shishova, V. V., Maslakov, K. I., Fionov, A. V., Isaikina, O. Y., and Lunin, V. V. (2019). “Efficiency of manganese modified CTAB-templated ceria-zirconia catalysts in total CO oxidation.” *Appl. Surf. Sci.*, 485, 432–440.

Kapteijn, F., Langeveld, A. D. van, Moulijn, J. A., Andreini, A., Vuurman, M. A., Turek, A. M., Jehng, J. M., and Wachs, I. E. (1994). “Alumina-supported manganese oxide catalysts. I. Characterization: Effect of precursor and loading.” *J. Catal.*, 150(1), *Ceria-Manganese Mixed Oxides as Catalyst for Soot and CO Oxidation Activity*.

94–104.

Kašpar, J., Fornasiero, P., and Graziani, M. (1999). “Use of CeO₂-based oxides in the three-way catalysis.” *Catal. Today*, 50(2), 285–298.

Katta, L., Sudarsanam, P., Thrimurthulu, G., and Reddy, B. M. (2010). “Doped nanosized ceria solid solutions for low temperature soot oxidation: Zirconium versus lanthanum promoters.” *Appl. Catal. B Environ.*, 101(1–2), 101–108.

Kharlamova, T. S., Verkhov, V. A., Kulchakovskaya, E. V., Svetlichnyi, V. A., Cadete Santos Aires, F. J., Bargiela, P., and Vodyankina, O. V. (2022). “Effect of metal-doping (Me = Fe, Ce, Sn) on phase composition, structural peculiarities, and CO oxidation catalytic activity of cryptomelane-type MnO₂.” *J. Alloys Compd.*, 917, 165504.

Kim, K., Yoo, J. Do, Lee, S., Bae, M., Bae, J., Jung, W. C., and Han, J. W. (2017). “A Simple Descriptor to Rapidly Screen CO Oxidation Activity on Rare-Earth Metal-Doped CeO₂: From Experiment to First-Principles.” *ACS Appl. Mater. Interfaces*, 9(18), 15449–15458.

Kim, S. C., and Shim, W. G. (2010). “Catalytic combustion of VOCs over a series of manganese oxide catalysts.” *Appl. Catal. B Environ.*, 98(3–4), 180–185.

Kleitz, F., Choi, S. H., and Ryoo, R. (2003). “Cubic Ia3d large mesoporous silica: Synthesis and replication to platinum nanowires, carbon nanorods and carbon nanotubes.” *Chem. Commun.*, 9(17), 2136–2137.

Krishna, K., Bueno-López, A., Makkee, M., and Moulijn, J. A. (2007a). “Potential rare earth modified CeO₂ catalysts for soot oxidation: I. Characterisation and catalytic activity with O₂.” *Appl. Catal. B Environ.*, 75(3), 189–200.

Kumar, P. A., Tanwar, M. D., Bensaïd, S., Russo, N., and Fino, D. (2012a). “Soot combustion improvement in diesel particulate filters catalyzed with ceria nanofibers.” *Chem. Eng. J.*, 207–208, 258–266.

Kumar, P. A., Tanwar, M. D., Russo, N., Pirone, R., and Fino, D. (2012b). “Synthesis and catalytic properties of CeO₂ and Co/CeO₂ nanofibres for diesel soot combustion.” *Catal. Today*, 279–287.

Laguna, O. H., Centeno, M. A., Boutonnet, M., and Odriozola, J. A. (2011). “Fe-doped ceria solids synthesized by the microemulsion method for CO oxidation reactions.” *Appl. Catal. B Environ.*, 106(3–4), 621–629.

Ceria-Manganese Mixed Oxides as Catalyst for Soot and CO Oxidation Activity.

- Lahaye, J. (1990). "Mechanisms of soot formation." *Polym. Degrad. Stab.*, 30(1), 111–121.
- Lee, C., Park, J. Il, Shul, Y. G., Einaga, H., and Teraoka, Y. (2015). "Ag supported on electrospun macro-structure CeO₂ fibrous mats for diesel soot oxidation." *Appl. Catal. B Environ.*, 174–175, 185–192.
- Lee, H. W., Muralidharan, P., and Kim, D. K. (2011). "Synthesis of one-dimensional spinel LiMn₂O₄ nanostructures as a positive electrode in lithium ion battery." *J. Korean Ceram. Soc.*, 48(5), 379–383.
- Lee, J., Lee, M. W., Kim, M. J., Lee, J. H., Lee, E. J., Jung, C. H., Choung, J. W., Kim, C. H., and Lee, K. Y. (2021). "Effects of La incorporation in catalytic activity of Ag/La-CeO₂ catalysts for soot oxidation." *J. Hazard. Mater.*, 414(November 2020), 125523.
- Lee, K. O., Seong, H., and Choi, S. M. (2013). "Detailed analysis of kinetic reactions in soot oxidation by simulated diesel exhaust emissions." *Proc. Combust. Inst.*, 34(2), 3057–3065.
- Lei, Y. C., Hwang, J. S., Chan, C. C., Lee, C. Te, and Cheng, T. J. (2005). "Enhanced oxidative stress and endothelial dysfunction in streptozotocin-diabetic rats exposed to fine particles." *Environ. Res.*, 99(3), 335–343.
- Li, B., Huang, Q., Yan, X. K., Xu, X. L., Qiu, Y., Yang, B., Chen, Y. W., Zhu, S. M., and Shen, S. B. (2014). "Low-temperature catalytic combustion of benzene over Ni-Mn/CeO₂/cordierite catalysts." *J. Ind. Eng. Chem.*, 20(4), 2359–2363.
- Li, B., Raj, A., Croiset, E., and Wen, J. Z. (2019a). "Reactive Fe-O-Ce sites in ceria catalysts for soot oxidation." *Catalysts*, 9(10), 20–22.
- Li, B., Sediako, A. D., Zhao, P., Li, J., Croiset, E., Thomson, M. J., and Wen, J. Z. (2019b). "Real-Time Observation of Carbon Oxidation by Driven Motion of Catalytic Ceria Nanoparticles within Low Pressure Oxygen." *Sci. Rep.*, 9(1), 1–12.
- Li, H., Qi, G., Tana, Zhang, X., Huang, X., Li, W., and Shen, W. (2011a). "Low-temperature oxidation of ethanol over a Mn_{0.6}Ce_{0.4}O₂ mixed oxide." *Appl. Catal. B Environ.*, 103(1–2), 54–61.
- Li, J., Lei, Y., Guo, Z., Li, G., Chen, X., and Zhou, F. (2019c). "Temperature-dependent reaction pathways of CO oxidation and the application as monolithic catalysts for Co₃O₄ nanorods." *Appl. Catal. A Gen.*, 587, 117191.

Li, L., Jing, F., Yan, J., Jing, J., and Chu, W. (2017a). “Highly effective self-propagating synthesis of CeO₂-doped MnO₂ catalysts for toluene catalytic combustion.” *Catal. Today*, 297, 167–172.

Li, L., Song, L., Fei, Z., Chu, W., Luo, X., and Yan, J. (2022). “Effect of different supports on activity of Mn–Ce binary oxides catalysts for toluene combustion.” *J. Rare Earths*, 40(4), 645–651.

Li, S., Yan, S., Xia, Y., Cui, B., Pu, Y., Ye, Y., Wang, D., Liu, Y. Q., and Chen, B. (2019d). “Oxidative reactivity enhancement for soot combustion catalysts by co-doping silver and manganese in ceria.” *Appl. Catal. A Gen.*, 570, 299–307.

Li, T. Y., Chiang, S. J., Liaw, B. J., and Chen, Y. Z. (2011b). “Catalytic oxidation of benzene over CuO/Ce_{1-x}Mn_xO₂ catalysts.” *Appl. Catal. B Environ.*

Li, Z., Wang, H., Wu, X., Ye, Q., Xu, X., Li, B., and Wang, F. (2017b). “Novel synthesis and shape-dependent catalytic performance of Cu–Mn oxides for CO oxidation.” *Appl. Surf. Sci.*, 403, 335–341.

Liang, Q., Wu, X., Weng, D., and Xu, H. (2008). “Oxygen activation on Cu/Mn-Ce mixed oxides and the role in diesel soot oxidation.” *Catal. Today*, 139(1–2), 113–118.

Liao, Y., Fu, M., Chen, L., Wu, J., Huang, B., and Ye, D. (2013). “Catalytic oxidation of toluene over nanorod-structured Mn-Ce mixed oxides.” *Catal. Today*, 216, 220–228.

Lin, X., Li, S., He, H., Wu, Z., Wu, J., Chen, L., Ye, D., and Fu, M. (2018a). “Evolution of oxygen vacancies in MnO_x-CeO₂ mixed oxides for soot oxidation.” *Appl. Catal. B Environ.*, 223, 91–102.

Liu, G., Yue, R., Jia, Y., Ni, Y., Yang, J., Liu, H., Wang, Z., Wu, X., and Chen, Y. (2013). “Catalytic oxidation of benzene over Ce-Mn oxides synthesized by flame spray pyrolysis.” *Particuology*, 11(4), 454–459.

Liu, Y., Wen, C., Guo, Y., Lu, G., and Wang, Y. (2010). “Modulated CO oxidation activity of M-doped ceria (M = Cu, Ti, Zr, and Tb): Role of the Pauling electronegativity of M.” *J. Phys. Chem. C*, 114(21), 9889–9897.

López-Fonseca, R., Elizundia, U., Landa, I., Gutiérrez-Ortiz, M. A., and González-Velasco, J. R. (2005). “Kinetic analysis of non-catalytic and Mn-catalysed combustion of diesel soot surrogates.” *Appl. Catal. B Environ.*, 61(1–2), 150–158.

López-Fonseca, R., Landa, I., Elizundia, U., Gutiérrez-Ortiz, M. A., and González-Velasco, J. R. (2005). *Ceria-Manganese Mixed Oxides as Catalyst for Soot and CO Oxidation Activity*.

- Velasco, J. R. (2006). “Thermokinetic modeling of the combustion of carbonaceous particulate matter.” *Combust. Flame*, 144(1–2), 398–406.
- Lu, H., Zhou, Y., Huang, H., Zhang, B., and Chen, Y. (2011). “In-situ synthesis of monolithic Cu-Mn-Ce/cordierite catalysts towards VOCs combustion.” *J. Rare Earths*, 29(9), 855–860.
- Lu, S., Zhang, J., Sun, Y., and Liu, H. (2017). “Preparation and characterization of CuO-CeO₂-ZrO₂/cordierite monolith catalysts.” *Ceram. Int.*, 43(8), 5957–5962.
- Lykaki, M., Pachatouridou, E., Carabineiro, S. A. C., Iliopoulou, E., Andriopoulou, C., Kallithrakas-Kontos, N., Boghosian, S., and Konsolakis, M. (2018). “Ceria nanoparticles shape effects on the structural defects and surface chemistry: Implications in CO oxidation by Cu/CeO₂ catalysts.” *Appl. Catal. B Environ.*, 230, 18–28.
- Ma, J., Fang, M., Li, P., Zhu, B., Lu, X., and Lau, N. T. (1997). “Microwave-assisted catalytic combustion of diesel soot.” *Appl. Catal. A Gen.*, 159(1–2), 211–228.
- Maini, S., Shin, C., Wen, J. Z., Li, B., Sediako, A., and Thomson, M. J. (2022). “Heterogeneous oxidation of powder and individual carbon nanoparticles catalyzed by ceria nanoparticles.” *Appl. Catal. A Gen.*, 630, 118465.
- Martínez-Munuera, J. C., Serrano-Martínez, V. M., Giménez-Mañogil, J., Yeste, M. P., and García-García, A. (2022). “Unraveling the nature of active sites onto copper/ceria-zirconia catalysts for low temperature CO oxidation.” *Catal. Today*, 384–386, 246–256.
- Meng, Y., Song, W., Huang, H., Ren, Z., Chen, S.-Y., and Suib, S. L. (2014). “Structure–Property Relationship of Bifunctional MnO₂ Nanostructures: Highly Efficient, Ultra-Stable Electrochemical Water Oxidation and Oxygen Reduction Reaction Catalysts Identified in Alkaline Media.” *J. Am. Chem. Soc.*, 136(32), 11452–11464.
- Miceli, P., Bensaid, S., Russo, N., and Fino, D. (2014). “CeO₂-based catalysts with engineered morphologies for soot oxidation to enhance soot-catalyst contact.” *Nanoscale Res. Lett.*, 9(1), 1–10.
- Mogensen, M., Sammes, N. M., and Tompsett, G. A. (2000). “Physical, chemical and electrochemical properties of pure and doped ceria.” *Solid State Ionics*, 129(1), 63–94.
- Mukherjee, D., Rao, B. G., and Reddy, B. M. (2016a). “CO and soot oxidation activity of doped ceria: Influence of dopants.” *Appl. Catal. B Environ.*, 197, 105–115.

Ceria-Manganese Mixed Oxides as Catalyst for Soot and CO Oxidation Activity.

Mukherjee, D., and Reddy, B. M. (2018). “Noble metal-free CeO₂-based mixed oxides for CO and soot oxidation.” *Catal. Today*, 309, 227–235.

Nascimento, L. F., Lima, J. F., Sousa Filho, P. C. de, and Serra, O. A. (2016). “Control of diesel particulate emission based on Ag/CeO_x/FeO_y catalysts supported on cordierite.” *Chem. Eng. J.*, 290, 454–464.

Nascimento, L. F., Lima, J. F., Sousa Filho, P. C. de, and Serra, O. A. (2018a). “Effect of lanthanum loading on nanosized CeO₂-ZnO solid catalysts supported on cordierite for diesel soot oxidation.” *J. Environ. Sci. (China)*, 73, 58–68.

Nascimento, L. F., and Serra, O. A. (2016a). “Washcoating of cordierite honeycomb with ceria-copper mixed oxides for catalytic diesel soot combustion.” *Process Saf. Environ. Prot.*, 101, 134–143.

Neeft, J. P. A., Hoornaert, F., Makkee, M., and Moulijn, J. A. (1996a). “The effects of heat and mass transfer in thermogravimetric analysis. A case study towards the catalytic oxidation of soot.” *Thermochim. Acta*.

Neeft, J. P. A., Makkee, M., and Moulijn, J. A. (1996b). “Diesel particulate emission control.” *Fuel Process. Technol.*, 47(1), 1–69.

Neyertz, C. A., Banús, E. D., Miró, E. E., and Querini, C. A. (2014). “Potassium-promoted Ce_{0.65}Zr_{0.35}O₂ monolithic catalysts for diesel soot combustion.” *Chem. Eng. J.*, 248, 394–405.

Neyertz, C. A., Miró, E. E., and Querini, C. A. (2012). “K/CeO₂ catalysts supported on cordierite monoliths: Diesel soot combustion study.” *Chem. Eng. J.*, 181–182, 93–102.

Nishu, Liu, R., Rahman, M. M., Li, C., Chai, M., Sarker, M., Wang, Y., and Cai, J. (2021). “Catalytic pyrolysis of microcrystalline cellulose extracted from rice straw for high yield of hydrocarbon over alkali modified ZSM-5.” *Fuel*, 285, 119038.

Novák, V., Kočí, P., Gregor, T., Choi, J. S., Štěpánek, F., and Marek, M. (2013). “Effect of cavities and cracks on diffusivity in coated catalyst layer.” *Catal. Today*, 216, 142–149.

Oi-Uchisawa, J., Obuchi, A., Wang, S., Nanba, T., and Ohi, A. (2003). “Catalytic performance of Pt/MO_x loaded over SiC-DPF for soot oxidation.” *Appl. Catal. B Environ.*, 43(2), 117–129.

Ozawa, T. (1992). “Estimation of activation energy by isoconversion methods.” *Ceria-Manganese Mixed Oxides as Catalyst for Soot and CO Oxidation Activity*.

Thermochim. Acta, 203, 159–165.

Palmisano, P., Russo, N., Fino, P., Fino, D., and Badini, C. (2006). “High catalytic activity of SCS-synthesized ceria towards diesel soot combustion.” *Appl. Catal. B Environ.*, 69(1–2), 85–92.

Pannone, G. M., and Mueller, J. D. (2001). “A comparison of conversion efficiency and flow restriction performance of ceramic and metallic catalyst substrates.” *SAE Tech. Pap.*, (724).

Papadopoulos, C., Kappis, K., Papavasiliou, J., Vakros, J., Kuśmierz, M., Gac, W., Georgiou, Y., Deligiannakis, Y., and Avgouropoulos, G. (2019). “Copper-promoted ceria catalysts for CO oxidation reaction.” *Catal. Today*, (June), 1–7.

Papadopoulos, C., Kappis, K., Papavasiliou, J., Vakros, J., Kuśmierz, M., Gac, W., Georgiou, Y., Deligiannakis, Y., and Avgouropoulos, G. (2020). “Copper-promoted ceria catalysts for CO oxidation reaction.” *Catal. Today*, 355, 647–653.

Patil, P., Nakate, U. T., Harish, K., Pavan, S. P., Rakesh, N. P., Selvakumar, D., and Kumar, N. S. (2020). “Au sensitized La–CeO₂ catalyst coated ceramics monoliths for toluene catalysis application.” *Mater. Chem. Phys.*, 240, 122269.

Patil, S. S., Dasari, H. P., and Dasari, H. (2019). “Effect of Nd-doping on soot oxidation activity of Ceria-based nanoparticles synthesized by Glycine Nitrate Process.” *Nano-Structures and Nano-Objects*, 20, 100388.

Pérez, V. R., and Bueno-López, A. (2015). “Catalytic regeneration of Diesel Particulate Filters: Comparison of Pt and CePr active phases.” *Chem. Eng. J.*, 279, 79–85.

Piumetti, M., Bensaid, S., Fino, D., and Russo, N. (2016). “Nanostructured ceria-zirconia catalysts for CO oxidation: Study on surface properties and reactivity.” *Appl. Catal. B Environ.*, 197, 35–46.

Piumetti, M., Bensaid, S., Russo, N., and Fino, D. (2015a). “Nanostructured ceria-based catalysts for soot combustion: Investigations on the surface sensitivity.” *Appl. Catal. B Environ.*, 165, 742–751.

Piumetti, M., Fino, D., and Russo, N. (2015b). “Mesoporous manganese oxides prepared by solution combustion synthesis as catalysts for the total oxidation of VOCs.” *Appl. Catal. B Environ.*, 163, 277–287.

Pope, C. A., Burnett, R. T., Thurston, G. D., Thun, M. J., Calle, E. E., Krewski, D., and *Ceria-Manganese Mixed Oxides as Catalyst for Soot and CO Oxidation Activity*.

Godleski, J. J. (2004). "Cardiovascular Mortality and Long-Term Exposure to Particulate Air Pollution: Epidemiological Evidence of General Pathophysiological Pathways of Disease." *Circulation*, 109(1), 71–77.

Prasad, D. H., Park, S. Y., Ji, H. I., Kim, H. R., Son, J. W., Kim, B. K., Lee, H. W., and Lee, J. H. (2012a). "Structural characterization and catalytic activity of $\text{Ce}_{0.65}\text{Zr}_{0.25}\text{RE}_{0.1}\text{O}_{2-\delta}$ nanocrystalline powders synthesized by the glycine-nitrate process." *J. Phys. Chem. C*, 116(5), 3467–3476.

Prasad, D. H., Park, S. Y., Oh, E. O., Ji, H., Kim, H. R., Yoon, K. J., Son, J. W., and Lee, J. H. (2012b). "Synthesis of nano-crystalline $\text{La}_{1-x}\text{Sr}_x\text{CoO}_{3-\delta}$ perovskite oxides by EDTA-citrate complexing process and its catalytic activity for soot oxidation." *Appl. Catal. A Gen.*, 447–448, 100–106.

Putla, S., Amin, M. H., Reddy, B. M., Nafady, A., Farhan, K. A. Al, and Bhargava, S. K. (2015a). "MnO_x Nanoparticle-Dispersed CeO₂ Nanocubes: A Remarkable Heteronanostructured System with Unusual Structural Characteristics and Superior Catalytic Performance." *ACS Appl. Mater. Interfaces*, 7(30), 16525–16535.

Qian, K., Qian, Z., Hua, Q., Jiang, Z., and Huang, W. (2013). "Structure-activity relationship of CuO/MnO₂ catalysts in CO oxidation." *Appl. Surf. Sci.*, 273, 357–363.

Raj, A., Yang, S. Y., Cha, D., Tayouo, R., and Chung, S. H. (2013). "Structural effects on the oxidation of soot particles by O₂: Experimental and theoretical study." *Combust. Flame*, 160(9), 1812–1826.

Rajvanshi, K., Patil, S. S., Lakhanlal, Dasari, H. P., Saidutta, M. B., and Dasari, H. (2020). "Promotional effect of nickel addition on soot oxidation activity of $\text{Ce}_{0.9}\text{Pr}_{0.1}\text{O}_2$ oxide catalysts." *Chem. Pap.*, 74(12), 4581–4592.

Ramdas, R., Nowicka, E., Jenkins, R., Sellick, D., and Davies, C. (2015). "Applied Catalysis B: Environmental Using real particulate matter to evaluate combustion catalysts for direct regeneration of diesel soot filters." *Applied Catal. B, Environ.*, 176–177(2), 436–443.

Ramesh, K., Chen, L., Chen, F., Liu, Y., Wang, Z., and Han, Y. F. (2008). "Re-investigating the CO oxidation mechanism over unsupported MnO, Mn₂O₃ and MnO₂ catalysts." *Catal. Today*, 131(1–4), 477–482.

Rangaswamy, A., Sudarsanam, P., and Reddy, B. M. (2015). "Rare earth metal doped Ceria-Manganese Mixed Oxides as Catalyst for Soot and CO Oxidation Activity."

CeO₂-based catalytic materials for diesel soot oxidation at lower temperatures.” *J. Rare Earths*, 33(11), 1162–1169.

Ratnayake, S. P., Mantilaka, M. M. M. G. P. G., Sandaruwan, C., Dahanayake, D., Gunasekara, Y. P., Jeyasakthy, S., Gurusinghe, N. M., Wanninayake, U. K., and Nalin de Silva, K. M. (2021). “Low-temperature thermocatalytic particulate carbon decomposition via urea solution-combustion derived CeO₂ nanostructures.” *J. Rare Earths*, 39(1), 67–74.

Raub, J. A. (1999). “Health effects of exposure to ambient carbon monoxide.” *Chemosph. - Glob. Chang. Sci.*

Raub, J. A., Mathieu-Nolf, M., Hampson, N. B., and Thom, S. R. (2000). “Carbon monoxide poisoning - A public health perspective.” *Toxicology*, 145(1), 1–14.

Reddy, M. S., and Boucher, O. (2007). “Climate impact of black carbon emitted from energy consumption in the world’s regions.” *Geophys. Res. Lett.*, 34(11), 1–5.

Ren, Z., Botu, V., Wang, S., Meng, Y., Song, W., Guo, Y., Ramprasad, R., Suib, S. L., and Gao, P. X. (2014). “Monolithically integrated Spinel M_xCo_{3-x}O₄ (M=Co, Ni, Zn) nanoarray catalysts: Scalable synthesis and cation manipulation for tunable low-temperature CH₄ and CO oxidation.” *Angew. Chemie - Int. Ed.*

Rico-Pérez, V., Aneggi, E., Bueno-López, A., and Trovarelli, A. (2016). “Synergic effect of Cu/Ce_{0.5}Pr_{0.5}O_{2-δ} and Ce_{0.5}Pr_{0.5}O_{2-δ} in soot combustion.” *Appl. Catal. B Environ.*, 197, 95–104.

Rushton, M. J. D., and Chroneos, A. (2014). “Impact of uniaxial strain and doping on oxygen diffusion in CeO₂.” *Sci. Rep.*, 4, 2–7.

Russo, N., Fino, D., Saracco, G., and Specchia, V. (2006). “Supported gold catalysts for CO oxidation.” *Catal. Today*, 117(1–3), 214–219.

Sacco, N. A., Bortolozzi, J. P., Milt, V. G., Miró, E. E., and Banús, E. D. (2022). “One step citric acid-assisted synthesis of Mn-Ce mixed oxides and their application to diesel soot combustion.” *Fuel*, 322.

Sahoo, T. R., Armandi, M., Arletti, R., Piumetti, M., Bensaid, S., Manzoli, M., Panda, S. R., and Bonelli, B. (2017). “Pure and Fe-doped CeO₂ nanoparticles obtained by microwave assisted combustion synthesis: Physico-chemical properties ruling their catalytic activity towards CO oxidation and soot combustion.” *Appl. Catal. B Environ.*, *Ceria-Manganese Mixed Oxides as Catalyst for Soot and CO Oxidation Activity*.

211, 31–45.

Sarli, V. Di, Landi, G., Benedetto, A. Di, and Lisi, L. (2021). “Synergy Between Ceria and Metals (Ag or Cu) in Catalytic Diesel Particulate Filters: Effect of the Metal Content and of the Preparation Method on the Regeneration Performance.” *Top. Catal.*, 64(3–4), 256–269.

Sarli, V. Di, Landi, G., Lisi, L., Saliva, A., and Benedetto, A. Di. (2016a). “Catalytic diesel particulate filters with highly dispersed ceria: Effect of the soot-catalyst contact on the regeneration performance.” *Appl. Catal. B Environ.*, 197, 116–124.

Sartoretti, E., Novara, C., Chiodoni, A., Giorgis, F., Piumetti, M., Bensaid, S., Russo, N., and Fino, D. (2022). “Nanostructured ceria-based catalysts doped with La and Nd: How acid-base sites and redox properties determine the oxidation mechanisms.” *Catal. Today*, 390–391, 117–134.

Sartoretti, E., Novara, C., Giorgis, F., Piumetti, M., Bensaid, S., Russo, N., and Fino, D. (2019). “In situ Raman analyses of the soot oxidation reaction over nanostructured ceria-based catalysts.” *Sci. Rep.*, 9(1), 9–13.

Sato, M., Hansen, J., Koch, D., Lacis, A., Ruedy, R., Dubovik, O., Holben, B., Chin, M., and Novakov, T. (2003). “Global atmospheric black carbon inferred from AERONET.” *Proc. Natl. Acad. Sci. U. S. A.*, 100(11), 6319–6324.

Shenoy, C. S., Patil, S. S., Govardhan, P., Shourya, A., Dasari, H. P., Saidutta, M. B., and Dasari, H. (2019). “Studies on the Solid Oxide Cell Perovskite Electrode Materials for Soot Oxidation Activity.” *Emiss. Control Sci. Technol.*, 5(4), 342–352.

Shimizu, K. I., Kawachi, H., Komai, S. I., Yoshida, K., Sasaki, Y., and Satsuma, A. (2011). “Carbon oxidation with Ag/ceria prepared by self-dispersion of Ag powder into nano-particles.” *Catal. Today*, 175(1), 93–99.

Shimizu, K. ichi, Kawachi, H., and Satsuma, A. (2010). “Study of active sites and mechanism for soot oxidation by silver-loaded ceria catalyst.” *Appl. Catal. B Environ.*, 96(1–2), 169–175.

Shourya, A., and Dasari, H. P. (2022). “Manganese doped Ceria ($\text{Ce}_{1-x}\text{Mn}_x\text{O}_{2-\delta}$ ($x = 0-0.3$)) catalysts synthesized by EDTA–Citrate method for soot oxidation activity.” *Chem. Pap.*, 76(11), 7095–7110.

Shourya, A., and Dasari, H. P. (2023). “Formation of nano-rod structures in manganese-Ceria-Manganese Mixed Oxides as Catalyst for Soot and CO Oxidation Activity.”

rich ceria–manganese mixed oxides and their soot oxidation activity.” *Nano-Structures and Nano-Objects*, 34, 100970.

Shuang, L. I. U., Xiaodong, W. U., Duan, W., and Rui, R. A. N. (2015). “Ceria-based catalysts for soot oxidation : a review.” *J. Rare Earths*, 33(6), 567–590.

Soliman, N. K. (2019). “Factors affecting CO oxidation reaction over nanosized materials: A review.” *J. Mater. Res. Technol.*, 8(2), 2395–2407.

Sonawane, R. S., Kale, B. B., and Dongare, M. K. (2004). “Preparation and photocatalytic activity of Fe-TiO₂ thin films prepared by sol-gel dip coating.” *Mater. Chem. Phys.*

Spezzati, G., Benavidez, A. D., DeLaRiva, A. T., Su, Y., Hofmann, J. P., Asahina, S., Olivier, E. J., Neethling, J. H., Miller, J. T., Datye, A. K., and Hensen, E. J. M. (2019). “CO oxidation by Pd supported on CeO₂(100) and CeO₂(111) facets.” *Appl. Catal. B Environ.*, 243, 36–46.

Stanmore, B. R., Brilhac, J. F., and Gilot, P. (2001). “The oxidation of soot: A review of experiments, mechanisms and models.” *Carbon N. Y.*, 39(15), 2247–2268.

Stegmayer, M. Á., Godoy, M. L., Múnera, J. F., Miró, E. E., and Milt, V. G. (2022a). “In situ growth of ceria nanofibers on cordierite monoliths for diesel soot combustion.” *Surf. Coatings Technol.*, 439.

Tana, Wang, F., Li, H., and Shen, W. (2011). “Influence of Au particle size on Au/CeO₂ catalysts for CO oxidation.” *Catal. Today*, 175(1), 541–545.

Tang, L., Zhao, Z., Li, K., Yu, X., Wei, Y., Liu, J., Peng, Y., Li, Y., and Chen, Y. (2020). “Highly Active Monolith Catalysts of LaKCoO₃ Perovskite-type Complex Oxide on Alumina-washcoated Diesel Particulate Filter and the Catalytic Performances for the Combustion of Soot.” *Catal. Today*, 339, 159–173.

Tang, L., Zhao, Z., Wei, Y., Liu, J., Peng, Y., and Li, K. (2017). “Study on the coating of nano-particle and 3DOM LaCoO₃ perovskite-type complex oxide on cordierite monolith and the catalytic performances for soot oxidation: The effect of washcoat materials of alumina, silica and titania.” *Catal. Today*, 297, 131–142.

Tang, Q., Du, J., Xie, B., Yang, Y., Yu, W., and Tao, C. (2018). “Rare earth metal modified three dimensionally ordered macroporous MnO_x-CeO₂ catalyst for diesel soot combustion.” *J. Rare Earths*, 36(1), 64–71.

Ceria-Manganese Mixed Oxides as Catalyst for Soot and CO Oxidation Activity.

Tang, W., Lu, X., Liu, F., Du, S., Weng, J., Hoang, S., Wang, S., Nam, C. Y., and Gao, P. X. (2019). "Ceria-based nanoflake arrays integrated on 3D cordierite honeycombs for efficient low-temperature diesel oxidation catalyst." *Appl. Catal. B Environ.*, 245, 623–634.

Tang, X., Wang, C., Gao, F., Han, W., Yi, H., Zhao, S., Zhou, Y., and Liu, Y. (2021). "Mn-Fe-Ce multiple oxides with Al₂O₃ coating supported onto honeycomb cordierite monoliths for NO catalytic oxidation." *Colloids Surfaces A Physicochem. Eng. Asp.*, 611, 125790.

Thommes, M., Kaneko, K., Neimark, A. V., Olivier, J. P., Rodriguez-Reinoso, F., Rouquerol, J., and Sing, K. S. W. (2015). "Physisorption of gases, with special reference to the evaluation of surface area and pore size distribution (IUPAC Technical Report)." *Pure and Applied Chemistry*, 87(9–10), 1051–1069.

Tikhomirov, K., Kröcher, O., Elsener, M., and Wokaun, A. (2006). "MnO_x-CeO₂ mixed oxides for the low-temperature oxidation of diesel soot." *Appl. Catal. B Environ.*, 64(1–2), 72–78.

Tiscornia, I. S., Lacoste, A. M., Gómez, L. E., and Boix, A. V. (2020). "CuO–CeO₂/SiO₂ coating on ceramic monolith: Effect of the nature of the catalyst support on CO preferential oxidation in a H₂-rich stream." *Int. J. Hydrogen Energy*, 45(11), 6636–6650.

Tomašić, V., and Jović, F. (2006). "State-of-the-art in the monolithic catalysts/reactors." *Appl. Catal. A Gen.*, 311(1–2), 112–121.

Trovarelli, A. (1996). "Catalytic properties of ceria and CeO₂-Containing materials." *Catal. Rev. - Sci. Eng.*, 38(4), 439–520.

Trovarelli, A. (1999). "Structural and oxygen storage/release properties of CeO₂-based solid solutions." *Comments Inorg. Chem.*, 20(4–6), 263–284.

Tsai, Y. C., Kwon, E., Park, Y. K., Nhat Huy, N., Lisak, G., Hsu, P. S., Hu, C., and Lin, K. Y. A. (2022). "Broccoli-like CeO₂ with Hierarchical/Porous Structures, and promoted oxygen vacancy as an enhanced catalyst for catalytic diesel soot elimination." *Sep. Purif. Technol.*, 281, 119867.

Venkataswamy, P., Jampaiah, D., Rao, K. N., and Reddy, B. M. (2014). "Nanostructured Ce_{0.7}Mn_{0.3}O_{2-δ} and Ce_{0.7}Fe_{0.3}O_{2-δ} solid solutions for diesel soot Ceria-Manganese Mixed Oxides as Catalyst for Soot and CO Oxidation Activity.

- oxidation.” *Appl. Catal. A Gen.*, 488, 1–10.
- Venkataswamy, P., Rao, K. N., Jampaiah, D., and Reddy, B. M. (2015a). “Nanostructured manganese doped ceria solid solutions for CO oxidation at lower temperatures.” *Appl. Catal. B Environ.*, 162, 122–132.
- Vergunst, T., Kapteijn, F., and Moulijn, J. A. (2001). “Monolithic catalysts - Non-uniform active phase distribution by impregnation.” *Appl. Catal. A Gen.*, 213(2), 179–187.
- Wagloehner, S., Nitzer-Noski, M., and Kureti, S. (2015). “Oxidation of soot on manganese oxide catalysts.” *Chem. Eng. J.*, 259, 492–504.
- Waikar, J. M., More, R. K., Lavande, N. R., and More, P. M. (2021). “Lattice expansion and smaller $\text{CuO}_x\text{CeO}_{2-\delta}$ particles formation by magnesium interaction for low temperature CO oxidation.” *J. Rare Earths*, 39(4), 434–439.
- Wan, J., Liu, Y., Zhou, Y., Liu, H., Wu, G., Kan, J., Li, M., Weng, D., and Wu, X. (2022). “Controllable synthesis of argentine decorated $\text{CuO}_x@\text{CeO}_2$ catalyst and its highly efficient performance for soot oxidation.” *J. Rare Earths*, 40(10), 1546–1553.
- Wang, B., Chi, C., Xu, M., Wang, C., and Meng, D. (2017). “Plasma-catalytic removal of toluene over $\text{CeO}_2\text{-MnO}_x$ catalysts in an atmosphere dielectric barrier discharge.” *Chem. Eng. J.*, 322, 679–692.
- Wang, F., Dai, H., Deng, J., Bai, G., Ji, K., and Liu, Y. (2012). “Manganese oxides with rod-, wire-, tube-, and flower-like morphologies: Highly effective catalysts for the removal of toluene.” *Environ. Sci. Technol.*, 46(7), 4034–4041.
- Wang, H., Lu, Z., Qian, D., Li, Y., and Zhang, W. (2007). “Single-crystal $\alpha\text{-MnO}_2$ nanorods: synthesis and electrochemical properties.” *Nanotechnology*, 18(11), 115616.
- Wang, J., Yang, S., Sun, H., Qiu, J., and Men, Y. (2020). “Highly improved soot combustion performance over synergetic $\text{Mn}_x\text{Ce}_{1-x}\text{O}_2$ solid solutions within mesoporous nanosheets.” *J. Colloid Interface Sci.*, 577, 355–367.
- Wang, L. C., Huang, X. S., Liu, Q., Liu, Y. M., Cao, Y., He, H. Y., Fan, K. N., and Zhuang, J. H. (2008). “Gold nanoparticles deposited on manganese(III) oxide as novel efficient catalyst for low temperature CO oxidation.” *J. Catal.*, 259(1), 66–74.
- Wang, Q., Yeung, K. L., and Bañares, M. A. (2019). “Ceria and its related materials for VOC catalytic combustion: A review.” *Catal. Today*, (April), 0–1.

Wang, W., Liu, Y., Wang, L., Zhan, W., Guo, Y., and Guo, Y. (2021). "Soot combustion over Ag catalysts supported on shape-controlled CeO₂." *Catal. Today*, 376, 9–18.

Wasalathanthri, N. D., SantaMaria, T. M., Kriz, D. A., Dissanayake, S. L., Kuo, C. H., Biswas, S., and Suib, S. L. (2017). "Mesoporous manganese oxides for NO₂ assisted catalytic soot oxidation." *Appl. Catal. B Environ.*, 201(2), 543–551.

Wheeler, D. W., and Khan, I. (2014). "Vibrational Spectroscopy A Raman spectroscopy study of cerium oxide in a cerium – 5 wt .% lanthanum alloy." *Vib. Spectrosc.*, 70, 200–206.

Williams, J. L. (2001). "Monolith structures, materials, properties and uses." *Catal. Today*, 69(1–4), 3–9.

Wu, X., Lin, F., Wang, L., Weng, D., and Zhou, Z. (2011a). "Preparation methods and thermal stability of Ba-Mn-Ce oxide catalyst for NO_x-assisted soot oxidation." *J. Environ. Sci.*, 23(7), 1205–1210.

Wu, X., Lin, F., Xu, H., and Weng, D. (2010). "Effects of adsorbed and gaseous NO_x species on catalytic oxidation of diesel soot with MnO_x-CeO₂ mixed oxides." *Appl. Catal. B Environ.*, 96(1–2), 101–109.

Wu, X., Liu, S., Weng, D., and Lin, F. (2011b). "Textural-structural properties and soot oxidation activity of MnO_x-CeO₂ mixed oxides." *Catal. Commun.*, 12(5), 345–348.

Wu, X., Yu, H., Weng, D., Liu, S., and Fan, J. (2013). "Synergistic effect between MnO and CeO₂ in the physical mixture: Electronic interaction and NO oxidation activity." *J. Rare Earths*, 31(12), 1141–1147.

Wu, Z., Li, M., and Overbury, S. H. (2012). "On the structure dependence of CO oxidation over CeO₂ nanocrystals with well-defined surface planes." *J. Catal.*, 285(1), 61–73.

Xiao, G., Li, S., Li, H., and Chen, L. (2009). "Synthesis of doped ceria with mesoporous flowerlike morphology and its catalytic performance for CO oxidation." *Microporous Mesoporous Mater.*, 120(3), 426–431.

Xu, J., Deng, Y. Q., Luo, Y., Mao, W., Yang, X. J., and Han, Y. F. (2013a). "Operando Raman spectroscopy and kinetic study of low-temperature CO oxidation on an α -Mn₂O₃ nanocatalyst." *J. Catal.*, 300(x), 225–234.

Ceria-Manganese Mixed Oxides as Catalyst for Soot and CO Oxidation Activity.

- Xu, J., Li, P., Song, X., He, C., Yu, J., and Han, Y. F. (2010). “Operando Raman spectroscopy for determining the active phase in one-dimensional $\text{Mn}_{1-x}\text{Ce}_x\text{O}_{2+y}$ nanorod catalysts during methane combustion.” *J. Phys. Chem. Lett.*, 1(10), 1648–1654.
- Yan, X., Huang, Q., Li, B., Xu, X., Chen, Y., Zhu, S., and Shen, S. (2013). “Catalytic performance of $\text{LaCo}_{0.5}\text{M}_{0.5}\text{O}_3$ (M=Mn, Cr, Fe, Ni, Cu) perovskite-type oxides and $\text{LaCo}_{0.5}\text{Mn}_{0.5}\text{O}_3$ supported on cordierite for CO oxidation.” *J. Ind. Eng. Chem.*, 19(2), 561–565.
- Yang, Y., Fang, J., Meng, Z., Pu, P., Zhang, Q., Yi, C., Pan, S., and Li, Y. (2022). “Catalytic activity and influence factors of Mn-Ce mixed oxides by hydrothermal method on diesel soot combustion.” *Mol. Catal.*, 524, 112334.
- Yang, J., Holt, E. M., Blanco-García, P., Wagland, A., Hounslow, M. J., and Salman, A. D. (2016). “A novel technique for quantifying the cohesive strength of washcoat.” *Chem. Eng. Res. Des.*, 110, 108–113.
- Yang, Y., Zhao, D., Gao, Z., Tian, Y., Ding, T., Zhang, J., Jiang, Z., and Li, X. (2021). “Interface interaction induced oxygen activation of cactus-like $\text{Co}_3\text{O}_4/\text{OMS-2}$ nanorod catalysts in situ grown on monolithic cordierite for diesel soot combustion.” *Appl. Catal. B Environ.*, 286, 119932.
- Yu, D., Peng, C., Yu, X., Wang, L., Li, K., Zhao, Z., and Li, Z. (2022). “Facile preparation of amorphous Ce_nMnO_x catalysts and their good catalytic performance for soot combustion.” *Fuel*, 307, 121803.
- Yuan, J., Zhao, K., Cai, T., Gao, Z., Yang, L., and He, D. (2016). “One-step dip-coating of uniform $\gamma\text{-Al}_2\text{O}_3$ layers on cordierite honeycombs and its environmental applications.” *Ceram. Int.*, 42(13), 14384–14390.
- Zagaynov, I. V., Naumkin, A. V., and Grigoriev, Y. V. (2018). “Perspective intermediate temperature ceria based catalysts for CO oxidation.” *Appl. Catal. B Environ.*, 236, 171–175.
- Zagaynov, I. V., Shelepin, I. V., Konovalov, A. A., Obraztsova, E. A., Naumkin, A. V., Bykov, A. V., and Leontiev, V. G. (2021). “Gd-Bi-M-Ce-O (M = Cu, Zr, Ni, Co, Mn) ceria-based solid solutions for low temperature CO oxidation.” *Ceram. Int.*, 47(6), 8142–8149.

Zhang, H., Wang, J., Cao, Y., Wang, Y., Gong, M., and Chen, Y. (2015). "Effect of Y on improving the thermal stability of $\text{MnO}_x\text{-CeO}_2$ catalysts for diesel soot oxidation." *Cuihua Xuebao/Chinese J. Catal.*, 36(8), 1333–1341.

Zhang, T., Hing, P., Huang, H., and Kilner, J. (2002). "Sintering study on commercial CeO_2 powder with small amount of MnO_2 doping." *Mater. Lett.*, 57(2), 507–512.

Zhang, X., Wei, J., Yang, H., Liu, X., Liu, W., Zhang, C., and Yang, Y. (2013). "One-pot synthesis of mn-doped CeO_2 nanospheres for CO oxidation." *Eur. J. Inorg. Chem.*, (25), 4443–4449.

Zhang, X., and Wu, D. (2016). "Ceramic monolith supported Mn–Ce–M ternary mixed-oxide (M=Cu, Ni or Co) catalyst for VOCs catalytic oxidation." *Ceram. Int.*, 42(15), 16563–16570.

Zhang, Y., Chen, M., Zhang, Z., Jiang, Z., Shangguan, W., and Einaga, H. (2019). "Simultaneously catalytic decomposition of formaldehyde and ozone over manganese cerium oxides at room temperature: Promotional effect of relative humidity on the MnCeO_x solid solution." *Catal. Today*, 327, 323–333.

Zhang, Y., Yao, Y., Ren, J., Kong, H., Wang, B., Wang, Z., Zhang, Z., and Wang, J. (2020). " MnO_2 as an effective sintering aid for difficult-to-sinter LiTaO_3 -based ceramics: Densification and dielectric properties." *J. Alloys Compd.*, 829.

Zhang, Z. H., Cheung, C. S., Chan, T. L., and Yao, C. D. (2010). "Experimental investigation of regulated and unregulated emissions from a diesel engine fueled with Euro V diesel fuel and fumigation methanol." *Atmos. Environ.*, 44(8), 1054–1061.

Zhang, Z., Xin, Y., Qu, N., Han, D., Jia, J., Wang, J., and Zhang, Z. (2023). "In situ growth of ZnO nanorods on monolithic diesel particulate filters and supporting potassium for catalytic soot combustion." *Chem. Phys. Impact*, 6, 100174.

Zhao, H., Zhou, X., Wang, M., Xie, Z., Chen, H., and Shi, J. (2017). "Highly active $\text{MnO}_x\text{-CeO}_2$ catalyst for diesel soot combustion." *RSC Adv.*, 7(6), 3233–3239.

Zheng, Y., Li, K., Wang, H., Wang, Y., Tian, D., Wei, Y., Zhu, X., Zeng, C., and Luo, Y. (2016a). "Structure dependence and reaction mechanism of CO oxidation: A model study on macroporous CeO_2 and $\text{CeO}_2\text{-ZrO}_2$ catalysts." *J. Catal.*, 344, 365–377.

Zhou, B., Xi, K., Fan, L., Zhou, Y., Wang, Y., Zhu, Q., and Lu, H. (2018). "Applied Catalysis A , General A comparative study on Ce – Pr and Ce – Mn mixed oxide Ceria-Manganese Mixed Oxides as Catalyst for Soot and CO Oxidation Activity.

- catalysts toward soot catalytic combustion.” *Appl. Catal. A, Gen.*, 562, 1–10.
- Zhou, G., Lan, H., Gao, T., and Xie, H. (2014). “Influence of Ce/Cu ratio on the performance of ordered mesoporous CeCu composite oxide catalysts.” *Chem. Eng. J.*, 246, 53–63.
- Zhou, H., Li, K., Zhao, B., Deng, W., Su, Y., and Zhong, F. (2017). “Surface properties and reactivity of Fe/Al₂O₃/cordierite catalysts for NO reduction by C₂H₆: Effects of calcination temperature.” *Chem. Eng. J.*, 326(x), 737–744.
- Zhou, H., Su, Y., Liao, W., Deng, W., and Zhong, F. (2015). “Preparation, characterization, and properties of monolithic Fe/Al₂O₃/cordierite catalysts for NO reduction with C₂H₆.” *Appl. Catal. A Gen.*, 505, 402–409.
- Zhou, T., Li, L., Cheng, J., and Hao, Z. (2010). “Preparation of binary washcoat deposited on cordierite substrate for catalytic applications.” *Ceram. Int.*, 36(2), 529–534.
- Zhu, A., Zhou, Y., Wang, Y., Zhu, Q., Liu, H., Zhang, Z., and Lu, H. (2018). “Catalytic combustion of VOCs on Pt/CuMnCe and Pt/CeY honeycomb monolithic catalysts.” *J. Rare Earths*, 36(12), 1272–1277.
- Zhu, H., Xu, J., Yichuan, Y., Wang, Z., Gao, Y., Liu, W., and Yin, H. (2017a). “Catalytic oxidation of soot on mesoporous ceria-based mixed oxides with cetyltrimethyl ammonium bromide (CTAB)-assisted synthesis.” *J. Colloid Interface Sci.*, 508, 1–13.
- Zhu, J., Zhang, W., Qi, Q., Zhang, H., Zhang, Y., Sun, D., and Liang, P. (2019). “Catalytic oxidation of toluene, ethyl acetate and chlorobenzene over Ag/MnO₂-cordierite molded catalyst.” *Sci. Rep.*, 9(1), 1–10.
- Zhu, L., Yu, J., and Wang, X. (2007). “Oxidation treatment of diesel soot particulate on Ce_xZr_{1-x}O₂.” *J. Hazard. Mater.*, 140(1–2), 205–210.
- Zhu, M., Wen, Y., Shi, L., Tan, Z., Shen, Y., Yin, K., and Sun, L. (2022a). “Revealing the promoting effect of multiple Mn valences on the catalytic activity of CeO₂ nanorods toward soot oxidation.” *Nanoscale*, 14(33), 11963–11971.
- Zhu, Y., Wang, Q., Lan, L., Chen, S., and Zhang, J. (2022b). “Effect of surface manganese oxide species on soot catalytic combustion of Ce–Mn–O catalyst.” *J. Rare Earths*, 40(8), 1238–1246.

PUBLICATIONS

International peer-reviewed journals (from thesis)

Accepted

1. “Manganese doped Ceria ($Ce_{1-x}Mn_xO_{2-\delta}$ ($x = 0$ to 0.3)) Catalysts Synthesized by EDTA-Citrate Method for Soot Oxidation Activity” Shourya, A., and Dasari, H. P., Chem. Pap. 76 (2022) 7095–7110. <https://doi.org/10.1007/s11696-022-02386-8>.
2. “Formation of nano-rod structures in Manganese-rich Ceria-Manganese mixed oxides and its Soot oxidation activity” Shourya, A., and Dasari, H. P., Nano-Structures and Nano-Objects. 34 (2023) 100970. <https://doi.org/10.1016/j.nanoso.2023.100970>.
3. “Dip coating of Ceria-Manganese mixed oxides on Cordierite and its CO oxidation activity” Shourya, A., Dasari, H.P. & Wagay, A.A., Chem. Pap. 78, 5113–5129 (2024). <https://doi.org/10.1007/s11696-024-03457-8>

Papers published apart from the thesis

1. “Effect of Ag loading on Praseodymium doped Ceria Catalyst for Soot Oxidation Activity” Govardhan, P., Anantharaman, A. P., Patil, S. S., Dasari, H. P., Dasari, H., and Shourya, A., *Korean J. Chem. Eng.* (2022), 39(2), 328–342.
2. “Studies on the solid oxide cell perovskite electrode materials for soot oxidation activity” Shenoy, C. S., Patil, S. S., Govardhan, P., Shourya, A., Dasari, H. P., Saidutta, M. B., and Dasari, H., *Emiss. Control Sci. Technol.* (2019), 5(4), 342–352.

Patents

1. “A Method and Composition for Soot Oxidation in a Diesel Particulate Filter” Hari Prasad Dasari, Chaithra Shenoy, Atmuri Shourya

Conferences attended (flash talk and poster presentation)

“Coating and Characterization of Brewer’s yeast template-based synthesis of Ceria/Cordierite” at IIT Guwahati Dec 2022 in BSBB- 2022

Won the best flash talk and poster presentation.

BIODATA

Name : Atmuri Shourya

Personal details

Date of Birth : 17 MAY 1990

Address : Flat no. 511, Srinivasam appts, KLU road, Kunchanapalli Village, Tadepalli Mandal, Guntur district, AP-522501

Contact number : 7702672783

Email Id : atmuri.may17@gmail.com

EDUCATION

Degree	Specialization/Area	Institute/board	Percentage /Cgpa	Year of passing
Ph.D.	Ceria-based automobile exhaust catalysts	NITK Surathkal	9.43	2024
M.Tech.	Industrial Pollution Control	NITK Surathkal	7.72	2016
B.E.	Mechanical Engineering	P.S.N.A CET, Dindigul	82.81%	2011
XII th (CBSE)	Maths, Physics and Chemistry	MVM Sr. Sec School Chennai	84.00%	2007
X th (CBSE)		MVM Sr. Sec School Chennai	82.20%	2005